SOLAR RADIATIVE FLUXES FOR REALISTIC EXTENDED BROKEN CLOUD FIELDS ABOVE REFLECTING SURFACES

by

HOWARD W. BARKER

A Thesis

Submitted to the School of Graduate Studies

in Partial Fulfilment of the Requirements

of the Degree

Doctor of Philosophy

McMaster University

SOLAR RADIATIVE FLUXES FOR EXTENDED BROKEN CLOUD FIELDS

DOCTOR OF PHILOSOPHY (1991)
(Geography)

McMASTER UNIVERSITY
Hamilton, Ontario

TITLE:	Solar Radiative Fluxes for Realistic Extended Broken Cloud Fields Above Reflecting Surfaces
AUTHOR:	Howard W. Barker, B.Sc. (University of Toronto) M.Sc. (McMaster University)
SUPERVISOR:	Professor John A. Davies
NUMBER OF PAGES:	xviii, 257

Abstract

Structural properties and solar radiative fluxes for broken, inhomogeneous cloud fields (primarily fairweather cumulus) are examined from the point of view of sub–grid parameterization for global climate models (GCMs). AVHRR satellite visible and infrared radiances (256x256 km images) display almost identical one and two–dimensional wavenumber spectra. For scales greater than ~4 km, radiance spectra follow k^{-1} to $k^{-5/3}$ where k is wavenumber (at scales greater than ~40 km, radiance spectra for stratocumulus and stratocumulus of open polygonal cells behave as white noise). At scales between ~4 km and ~2 km, spectra follow $\sim k^{-4}$. Aircraft observations of cloud microphysics and temperature, however, suggest that these fields follow closely Kolmogorov's classic $k^{-5/3}$ law down to at least ~120 m. The dramatic scaling change in radiance fields may, therefore, be due to horizontal variation in the vertical integral of liquid water content.

Based on the empirical data, a phenomonological scaling cloud field model which produces three different forms of a cloud field is developed and demonstrated. The cloud fields produced by this model are used ultimately in a three–dimensional atmospheric Monte Carlo photon transport model which is developed and validated. Also, two methods of including an underlying reflecting surface are developed and validated.

Using the models mentioned above, fluxes for various scaling, random,

regular, and plane–parallel broken cloud fields are compared. Scaling cloud fields span a spectrum from white noise fields to plane–parallel. If most cloud fields scale between $k^{-0.5}$ and $k^{-5/3}$ over regions the size of GCM grids, as they probably do, neither the plane–parallel nor the random array models yield adequate flux estimates.

If a scaling cloud field with horizontally variable optical depth is transformed so that all cells with optical depth greater than zero are replaced by cells with optical depth equal to grid–averaged optical depth, reflectance is increased by 10 to 20%. This is due to the non–linearity of radiative transfer and the fact that photons are more likely to encounter liquid water in the homogenized case. Accounting for variable geometric depth of cloud may be important in warm regions where substantial towering clouds occur regularly. Also, at GCM gridbox scales it is probably just as important to account for low frequency whitish noise in cloud fields as it is to account for high frequency smoothing at scales below typical cloud cell diameter.

The convenient Lambertian surface approximation is probably adequate for most broken cloud scenarios. Expected errors in fluxes probably will not exceed a few percent. A method is developed for calculating cloudbase reflectance in a Monte Carlo simulation. For the widely used geometric sum formulae for flux calculation to be applicable, cloudbase reflectance must be independent of the number of internal reflections. For broken scaling clouds, however, this is violated. Fortuitously and fortunately, if cloudbase reflectance in the geometric sum formulae is set to the spherical albedo of the cloud field, errors in flux estimates should be small ($\lesssim$ 5%) in most cases. Finally, it is shown analytically that reduction in system albedo due to the introduction of broken, non–absorbing clouds is possible but highly unlikely to occur with any importance on Earth.

ACKNOWLEDGEMENTS

This study, and to some extent my life, were supported by grants from the Natural Science and Engineering Research Council of Canada and the Ontario Graduate Scholarship Fund.

I should like to express my deepest gratitude to my primary supervisor Dr. John A. Davies. I am particularly thankful for his invaluable editing, patience through my wandering phase of the degree, and financial support for the Lille/Paris conferences in August, 1988 and for the period from September, 1990 to April, 1991.

My deepest gratitude is also extended to my secondary supervisor Dr. Jean–Pierre Blanchet of AES. His encouragement and suggestions are indispensable and always welcome. Through particularly isolated times, he served as my main link to the outside world.

I should also like to acknowledge the following people for helping make parts of this thesis possible. In chronologic order of my encountering them, they are: Dr. Wayne Rouse (McMaster) for encouragement and proof–reading; Dr. Shawn Lovejoy (McGill University) for many long phone discussions; Wai Lau and Dave Steenbergen (AES) for helping extract AVHRR satellite data; Dr. Richard Leaitch (AES) for providing cloud microphysical data; Dr. John Kuenher (McMaster) for his laser printer program; and Dr. Robert Cahalan (NASA) for several discussions and proof–reading of manuscripts.

Finally, and most importantly, I express my love, respect, and thanks to my wife Liz. Her patience, acceptance, and support continually give value to being.

TABLE OF CONTENTS

LIST OF ILLUSTRATIONS

LIST OF TABLES

CHAPTER 1

Introduction

1.1 Background

Global Climate Models (GCMs) indicate that climatic change and stability are intimately related to Earth's radiation budget (Ramanathan, 1987, 1988; Mitchell, 1989) which itself is dominated by clouds. In turn, clouds are governed by Earth's radiation budget and thus by climate (Somerville and Remer, 1984; Roeckner, 1988; Mitchell *et al.*, 1990). The potential importance of this feedback has initiated research to develop accurate and computationally quick methods for calculating cloud dynamics and radiation transfer through clouds. However, different GCMs have different cloud–radiative dynamics (Cess and Potter *et al.*, 1989) which produce different climatic equilibrium (and presumably transient) responses to perturbations.

The differences between cloud–radiation interactions within existing GCMs is compounded by the complexity and non–linearity of climate and GCMs. Both probably contain chaotic tendencies (Lorenz, 1969; Somerville, 1987). If so, the small scale detail of the climate system should not be ignored, for in chaotic systems small scale variability can modulate significantly the overall state of the system (Ruelle, 1989). The current generation of GCMs, however, has horizontal resolutions typically between 60 to 600 km. Hence, there is much unresolved physics. Clouds are observed to be extremely variable over large ranges of scale.

Recent studies (e.g. Stephens, 1985) suggest that solar radiative transfer in clouds depends very much on the distribution of liquid water. One of the pressing problems in climate modelling, therefore, is the description of sub–grid spatial structure of realistic cloud fields and the efficient calculation of radiative transfer through them.

At present, many climate models compute the fraction of cloud in a grid using the gridbox's value of relative humidity RH as

$$A_c = \begin{cases} \left[\dfrac{RH - RH_c}{1 - RH_c}\right]^{\eta} & RH \geq RH_c \\ 0 & RH < RH_c \end{cases}, \tag{1.1}$$

where RH_c is clear–sky relative humidity. If $\eta = 1$, RH being becomes a linear weighted average of relative humidity in the cloudless and cloudy (saturated) portions of the grid. Both RH_c and η, and Eq.(1.1) for that matter, are *ad hoc* and probably very scale dependent. Typical values of RH_c and η are 0.9 and 1 or 2, respectively (e.g. Slingo *et al.*, 1989).

Once A_c is determined, cloud liquid water content (LWC) and effective radius of cloud droplet size distribution are calculated by semi–empirical functions of humidity and temperature (e.g. Fouquart *et al.*, 1990). More realistic parameterizations of cloud fraction and attributes treat liquid water as a prognostic variable. Such models are still in the formative stage and not widely used (Sasamori, 1975; Sunqvist, 1978; Smith, 1990).

Climate modellers have yet to address the problem of sub–grid geometry (distribution) of cloud. Not only is this due to lack of theory, but it has only been during the last ten years that detailed observation of cloud geometry has come into

vogue. Even if techniques existed for describing cloud geometry, there are no radiative transfer procedures which could use the information. In the meantime, climate modellers assume that clouds are 'fractionally' plane–parallel and use multi–layer, plane–parallel solutions of the radiative transfer equation to compute solar fluxes (e.g. Wiscombe, 1977; Fouquart and Bonnel, 1980; Blanchet and Morcrette, 1985).

Plane–parallel clouds are flat, homogeneous slabs of infinite horizontal extent. Fluxes for a gridbox containing plane–parallel clouds are calculated as

$$F = A_c F_{pp} \ , \tag{1.2}$$

where F_{pp} comes from a plane–parallel radiative flux model (see Meador and Weaver, 1980 and Zdunkowski *et al.*, 1980 for reviews). Although many plane–parallel flux models are computationally efficient and accurate (King and Harshvardhan, 1986), their true accuracy is limited because clouds are *never* plane–parallel.

One route for investigating the radiative properties of non–planar clouds is to solve the radiative transfer equation with appropriate boundary conditions. Davies (1978), Bradley (1981), and Preisendorfer and Stephens (1984) have derived solutions that describe the radiance fields of isolated, homogeneous cuboidal clouds. Smith (1988) has developed the mathematical foundation for an analytic radiance solution for isolated cylindrical clouds. Stephens (1988) has derived a two–dimensional Fourier expansion/interaction principle (Grant and Hunt, 1969) solution which in principle could handle arrays of variable cloud. To study radiative transfer in clouds that are extremely inhomogeneous in three–dimensions, Lovejoy *et al.* (1990) and Gabriel *et al.* (1990) constructed semi–analytic models based on a three–dimensional form of the interaction

principle. While the analytic models developed so far are potentially useful for detailed studies of various samplings of cloud radiation fields, they are too limited and cumbersome for studying extensive cloud fields and too computationally demanding for use in climate models.

The Monte Carlo method of photon transport offers a different approach to studying radiative transfer in non–planar, inhomogeneous clouds. The roots of this procedure lie in neutron transport theory for nuclear reactors (e.g. Spanier and Gelbard, 1969). To date, most studies of radiative transfer for inhomogeneous cloud have been conducted with Monte Carlo methods. They allow fluxes and radiances to be computed fairly easily for any cloud geometry. As such, Monte Carlo models can provide a wealth of information on how cloud inhomogeneity at various scales affects radiative transfer. The primary drawback with Monte Carlo simulations is the excessive computation demands. Although Monte Carlo models may never appear in climate models, the latter may well incorporate parameterizations of Monte Carlo results.

The first Monte Carlo simulations of photon transport in non–planar clouds focused on fluxes due to isolated, homogeneous clouds (e.g. Busygin *et al.*, 1973; McKee and Cox, 1974; Davies, 1978). They showed that radiative fluxes for finite clouds can differ greatly from those due to plane–parallel clouds because finite clouds have sides that intercept and leak photons. During the same period, Van Blerkhom (1971) and Wendling (1976) showed that regular striations (turrets) appended to the top of plane–parallel clouds reduce cloud albedo below that due to plane–parallel clouds with equal vertical optical depth.

Attention then shifted to the middleground between plane–parallel and isolated finite clouds: regular arrays of identical, homogeneous clouds. The original studies by Busygin *et al.* (1973) and Aida (1977) (nine cubic clouds) suggested that enhanced illuminated area, cloud–cloud interaction of photons, and cloud

shadowing are important for flux calculations. Similar investigations where conducted by Claussen (1982), Wienman and Harshvardhan (1982), Schmetz (1984), Harshvardhan and Thomas (1984), Welch and Wielicki (1984) and others. These studies confirmed and elaborated on the importance of enhanced illumination, cloud–cloud interactions, and shadowing for fluxes in regular cloud arrays. Kobayashi (1988) extended these findings to include arrays of various cloud forms positioned at random in a 10x10 checkerboard. These studies have shown that, at high sun, non–planar clouds reflect less radiation than plane–parallel clouds while at low sun they reflect more.

Kite (1987) (see Rawlins (1990) for corrections) and Cretel *et al.* (1988) examined how a cloud size distribution placed in a regular array affects solar fluxes. These studies followed from the work by Welch and Zdunkowski (1981) and observational studies (Plank, 1969; Wielicki and Welch, 1986). The results of Cretel *et al.* and Rawlins imply that cloud reflectance is not very sensitive to cloud size distribution.

In general, Monte Carlo results of photon transport for regular arrays of clouds show that plane–parallel models are at best only a first order approximation that introduces biased radiative forcing at various spatial and temporal scales. Given that the climate system is a vast network of non–linear feedback processes, it is impossible to speculate on how fundamental systematic biases involving clouds and radiative transfer manifest themselves and cascade through the system.

In contrast to broken cloud fields examined thus far, most cloud fields the size of GCM gridboxes are as distinct from regular and random arrays of homogeneous clouds as they are from plane–parallel. Rather, clouds (LWC) tend to clump and cluster at all scales: cloudy patches, with optically thickest regions towards the centers, separated at times by large tracts of cloud–free space. Theory

maintains that over a vast range of scales the lower atmosphere is often in a turbulent state (e.g. Richardson, 1926; Kolmogorov, 1941). Wind and temperature observations confirm this (e.g. Gage and Nastrom, 1986). Liquid water concentration depends very much on temperature and over many scales can be considered as a passive variable that is shunted around by the wind field. Thus, it is not surprising that cloud observations (*in situ* sampling and satellite radiances) exhibit features intrinsic to chaotic turbulence: random fractal properties (Mandelbrot, 1974; Lovejoy, 1982; Gabriel *et al.*, 1986; Cahalan, 1989; and Cahalan and Joseph, 1989); and continuous wavenumber spectra that decay algebraically as a function of wavenumber (frequency) (King *et al.*, 1982; Cahalan and Snider, 1989). Clouds exhibit 'scaling' or spatial autocorrelative structure as is clearly visible at all scales in the form of clumping and clustering.

In response to theoretical and observational evidence which links clouds and turbulence, Davis *et al.* (1990) used a simple random mono–fractal cascade model to simulate highly irregular isolated cubic clouds and overcast clouds. Radiative fluxes were calculated with a simplified discrete (six) angle approach for overhead sun only. They demonstrated that compared with plane–parallel clouds, three–dimensional inhomogeneity can dramatically reduce cloud reflectance. They suggested that this might explain the long standing disagreement between theory and observation regarding anomalous absorption of solar radiation by clouds (Wiscombe *et al.*, 1984). Cahalan (1989) used a two–dimensional Monte Carlo model to simulate photon transport in quasi–fractal, two–dimensional, horizontally inhomogeneous overcast cloud. His results are similar to those of Davis *et al.* Thus, inter–cloud inhomogeneity reduces cloud albedo. A simple qualitative proof of this statement is given in Appendix A. As yet, however, properties of radiative transfer for GCM grid size cloud fields that exhibit realistic autocorrelative structure have not been studied.

1.2 Purpose and Outline of Study

The purpose of this thesis is to explore properties of solar radiative transfer transfer (fluxes) for large arrays of realistic, scaling, broken clouds (fairweather cumulus) above reflecting surfaces. Using satellite radiances and *in situ* aircraft measurements within cloud fields as empirical guides, realistic cloud fields are generated stochastically. Then, their grid–averaged solar fluxes are determined by the Monte Carlo technique of photon transport.

The second chapter reviews Fourier spectral analysis and the scaling and fractal nature of atmospheric turbulence. Then, several satellite radiance and aircraft datasets are analysed for spectral properties. Last. three phenomonological scaling cloud field models are developed and demonstrated.

In chapter three, a three–dimensional Monte Carlo atmospheric radiative transfer model is developed. Also, two general procedures to account for an underlying reflecting surface are presented. These models are validated in chapter four.

The fifth chapter contains results on the statistical significance of fluxes for large arrays of cloud; representativeness of single realizations of the cloud field models; intercomparison of fluxes for various kinds of broken cloud fields; and analysis of radiative properties of scaling cloud fields. Finally, some properties of fluxes for broken clouds above reflecting surfaces are examined.

CHAPTER 2

Scaling Cloud Fields: Observational Evidence and Model Development

This chapter consists of four main sections. The first section, briefly reviews one– and two–dimensional discrete Fourier transforms and power spectra. The second section presents a qualitative model of two–dimensional turbulence (Frisch *et al.*, 1978) which demonstrates the scaling nature of turbulence and the relation between scaling and fractal geometry. In the third section, observational evidence is given to support the hypothesis that the distribution of cloud liquid water is scaling. The last section presents and demonstrates three simple phenomonological scaling cumulus cloud field models. Cloud fields generated by these models are used ultimately as boundary conditions in the Monte Carlo radiative transfer model which is presented and discussed in the next chapter.

2.1 Discrete Fourier Transformations and Power Spectra

In this thesis, extensive use is made of one– and two–dimensional Fourier analysis. This section introduces discrete Fourier analysis.

First, consider one–dimensional fields. Assume that a function f(x) is defined on $-\infty < x < \infty$, where x may be time or distance. This function can also be expressed as a superposition of waves with frequency ω (either Hertz or inverse wavelength). The amplitudes of the waves characterizing f(x) are given by the

continuous Fourier transform:

$$F_c(\omega) = \int_{-\infty}^{\infty} f(x)\exp\left[-2\pi i\omega x\right]dx \ , \quad -\infty < \omega < \infty \ , \tag{2.1}$$

which has an inverse of

$$f(x) = \int_{-\infty}^{\infty} F_c(\omega)\exp\left[2\pi i\omega x\right]d\omega \ , \tag{2.2}$$

where $i = \sqrt{-1}$. Suppose we have a sequence of N 'observations' of f(x), denoted as f_n (n = 0,...,N–1), and that the observations are defined as either

$$f_n = \frac{1}{\Delta}\int_{x_n}^{x_{n+1}} f(x)dx \ , \quad (n = 0,...,N-1) \ . \tag{2.3a}$$

or

$$f_n = f(n\Delta) \ , \tag{2.3b}$$

where

$$\Delta = x_{n+1} - x_n \ , \tag{2.3c}$$

which is constant and referred to as the sampling frequency. At this point it is assumed that f(x) on $x \in [0,(N-1)\Delta]$ is representative of the entire function f(x). This is because f_n is assumed to be periodic with wavelength $N\Delta$. The discrete frequencies of the waves making up f_n are

$$\omega_k = k/(N\Delta) \ , \quad (k = 0,...,N-1) \ , \tag{2.4}$$

where k is wavenumber (the number of complete sine and cosine waves in the interval $[0,(N-1)\Delta]$). Therefore, the continuous transform in Eq.(2.1) is approximated as

$$F_c(\omega) = \int_{-\infty}^{\infty} f(x)\exp\left[-2\pi i\omega x\right]dx \simeq \Delta \sum_{n=0}^{N-1} f_n \exp\left[-\frac{2\pi i\, nk}{N}\right] \ . \qquad (2.5)$$

The discrete Fourier transform is then defined as

$$\begin{aligned} F_k &= \sum_{n=0}^{N-1} f_n \exp\left[-\frac{2\pi i\, nk}{N}\right] \\ &= u_k + iv_k \ , \qquad (k = 0,\ldots,N-1) \ , \end{aligned} \qquad (2.6)$$

where u_k and v_k are the amplitudes of the cosine and sine waves of wavenumber k. Therefore, the discrete and continuous transforms are related by

$$F_k \simeq \Delta F(\omega_k) \ . \qquad (2.7)$$

The inverse of F_k is

$$f_n = \frac{1}{N} \sum_{k=0}^{N-1} F_k \exp\left[\frac{2\pi i\, nk}{N}\right] \ , \quad (n = 0,\ldots,N-1) \ . \qquad (2.8)$$

Efficient computation of Eq.(2.6) and Eq.(2.8) is performed by standard Fast Fourier Transform (FFT) programs (e.g. Press *et al.*, 1986).

Note that

$$F_0 = \sum_{n=0}^{N-1} f_n = N\langle f \rangle \ , \tag{2.9}$$

where $\langle f \rangle$ is the mean of f_n. Furthermore, it is straightforward to show that when $f_n \in \mathbb{R}$,

$$F_k = F^*_{N-k} \ , \quad (k = 1,...,N/2-1) \ , \tag{2.10}$$

where the asterisk denotes complex conjugate. Thus, F_k is conjugate symmetric about $k = N/2$ which is the wavenumber associated with the Nyquist critical frequency given by $1/(2\Delta)$ [see Eq.(2.4)].

The discrete power spectrum of f_n is defined simply as

$$S_k = |F_k|^2 \ , \tag{2.11}$$

where the vertical bars represent the modulus of the complex number F_k. Note that when $f_n \in \mathbb{R}$, Eq.(2.10) implies that

$$S_k = S_{N-k} \ , \quad (k = 1,...,N/2-1) \ . \tag{2.12}$$

Thus, the power spectrum is symmetric about the Nyquist frequency.

One form of the Wiener–Khintchin theorem is now stated without proof (Bergé *et al.*, 1988). Define the discrete autocorrelation function of f_n as

$$\psi_m = \frac{1}{N} \sum_{j=0}^{N-1} f_j f_{j+m} \quad . \tag{2.13}$$

It can be shown that the Fourier transform of ψ_m is equal to the power spectrum S_k of f_n. This implies that the power spectrum of a function that is correlated with f_n will have some similarities with S_k.

By extension, consider a two–dimensional field f_{mn} which has forward and backward discrete Fourier transforms (Rosenfeld and Kak, 1982) defined as

$$F_{kl} = \sum_{m=0}^{N-1} \sum_{n=0}^{N-1} f_{mn} \exp\left[-2\pi i \left[\frac{mk + nl}{N}\right]\right] \tag{2.14a}$$

$$= u_{kl} + i v_{kl} \quad ,$$

and

$$f_{mn} = N^{-2} \sum_{k=0}^{N-1} \sum_{l=0}^{N-1} F_{kl} \exp\left[2\pi i \left[\frac{mk + nl}{N}\right]\right] \quad , \tag{2.14b}$$

where k and l are orthogonal wavenumbers making up the wave vector $\mathbf{k} = k\hat{\mathbf{i}} + l\hat{\mathbf{j}}$. Two–dimensional FFTs efficiently evaluate Eq.(2.14a and b). For example, for N=256 they reduce CPU time from hours to seconds.

This study uses two methods for computing power spectra of a two–dimensional field. First, an ensemble of one–dimensional spectra (transects across a field) are computed and averaged to yield a smoothed spectrum denoted as $\langle S_k \rangle$. This provides an estimate of the typical one–dimensional power spectrum one would expect to measure along a transect of f_{mn}. The second method involves finding the total power as a function of modulus of wavenumber $|\mathbf{k}|$ and as such is an integration over all directions, not just one direction as is the case in the first

method. Thus, define the continuous two–dimensional power spectrum as a function of $|\mathbf{k}|$ as the line integral

$$\check{S}_{|\mathbf{k}|} = \oint_{c} |F_{\mathbf{k}'l'}|^2 d|\mathbf{k}'| \ , \tag{2.15}$$

where c represents closed curves about the origin in Fourier space. If the field is isotropic, c represents circles of radius $|\mathbf{k}|$. If the field is anisotropic, c may represent an ellipse. In fact for some fields, c may represent some homotopic set of curves. For discrete, isotropic data, $\check{S}_{|\mathbf{k}|}$ may be approximated as

$$\check{S}_{|\mathbf{k}_i|} \simeq \frac{\sum\limits_{|\mathbf{k}_{i-1}| \le |\mathbf{k}'| \le |\mathbf{k}_i|} |F_{\mathbf{k}'l'}|^2}{N_i} \ , \tag{2.16}$$

where N_i is the number of terms in the annulus defined beneath the summation sign.

2.2 The Scaling Nature of Turbulence

This section introduces the concept of scaling by showing how it arises in fully developed, two–dimensional, homogeneous turbulence, and how it is related to fractal geometry of sets. A field is said to be scaling if typical fluctuations at different scales of observation are related by a scale changing factor only. This section is essential to acquaint the reader with properties of scaling fields since such fields are referred to extensively in this thesis. The formulation of the turbulent scaling law is essentially the simple dynamical model of Frisch *et al.* (1978) which relies implicitly on rather complex derivations found in Kraichnan (1967).

Schertzer and Lovejoy (1985) have convincingly argued that there is no transition scale below which the atmosphere *is* three–dimensional and above which it *is* two–dimensional. The manner in which Frisch *et al.*'s model is presented, however, assumes that the atmosphere is two–dimensional at scales greater than about 0.5 km (Kraichnan, 1967; Charney, 1971; Gage and Nastrom, 1986).

For simplicity, consider the size of turbulent eddies to be defined for a sequence of space scales

$$\ell_n = \ell_0 2^{-n} \quad , \quad (n = 0,1,2,...,N) \quad , \tag{2.17}$$

where ℓ_N is the scale at which energy is injected into the system (e.g. by convective cells). Thus, the sequence of wavenumbers for which eddies are defined is $k_n = \ell_n^{-1}$. Define the kinetic energy/unit mass at scales $\sim\ell_n$ to be

$$E_n = \int_{k_n}^{k_{n+1}} E(k)dk \quad , \tag{2.18}$$

where E(k) is the energy spectrum describing the distribution of kinetic energy per unit mass per unit wavenumber. Assuming statistically stationary turbulence, energy is introduced at scales $\sim\ell_N$ and is transferred to successively smaller wavenumbers (downward cascade) by local shear deformation of the velocity field. Also, assume that at all scales, eddies fill the available space. Thus, intermittancy of energy transfer is neglected. Then, the kinetic energy per unit mass of n–scale eddies is

$$E_n \sim \Delta v^2(\ell_n) \quad , \tag{2.19}$$

where $\Delta v(\ell_n)$ represents the typical velocity difference across a distance ℓ_n with the frame of reference being that of the largest eddies. The eddy turnover time is defined as

$$t_n \sim \frac{\ell_n}{\Delta v(\ell_n)} , \tag{2.20}$$

where t_n^{-1} is the typical rate at which energy is fed from eddies of size ℓ_n into eddies of size ℓ_{n-1}. In other words, t_n is the typical lifetime of n–eddies.

In the energy inertial range of fully developed, two–dimensional, homogeneous turbulence, the rate at which energy/unit mass is transferred from one scale to the next is

$$\epsilon_n \sim \frac{E_n}{t_n} \sim \frac{\Delta v^2(\ell_n)}{t_n} \sim \frac{\Delta v^3(\ell_n)}{\ell_n} , \tag{2.21}$$

with insignificant loss of energy due to viscous dissipation. Since no energy is lost

$$\epsilon_n = \bar{\epsilon} \ , \ \forall n \ , \tag{2.22}$$

where $\bar{\epsilon}$ may be thought of as either the rate of energy injection or the rate of energy transfer down the cascade. Manipulation of Eq.(2.21) yields

$$\Delta v(\ell_n) \sim \bar{\epsilon}^{1/3} \ell_n^{1/3} , \tag{2.23a}$$

and

$$E_n \sim \bar{\epsilon}^{2/3} \ell_n^{2/3} . \tag{2.23b}$$

These relations imply that typical fluctuations at scale ℓ_n in velocity and energy per unit mass are proportional to $\ell_n^{1/3}$ and $\ell_n^{2/3}$ respectively. Since $k_n = \ell_n^{-1}$, Eq.(2.23b) becomes

$$E_n \sim \bar{\epsilon}^{2/3} k_n^{-2/3} \quad , \tag{2.24a}$$

which upon substitution into Eq.(2.18) yields

$$E(k_n) \sim \bar{\epsilon}^{2/3} k_n^{-5/3} \quad , \tag{2.24b}$$

which is the Kolmogorov 5/3 scaling law for kinetic energy cascade in turbulent flow. Note that this is also the power spectrum of the velocity field. This formulation works equally well for fully developed, isotropic, three–dimensional turbulence with the exception that energy cascades upwards in k to the dissipation scale.

This law is also expected to apply to the concentration of a 'passive scalar' riding on the turbulent eddies. A passive scalar is a scalar, such as liquid water, whose concentration differences are due largely to advection only and whose non–linear effects on turbulence are negligible.

Making the above results more general (Schertzer and Lovejoy, 1987), any field f that exhibits typical fluctuations at scale ℓ like

$$\Delta f_\ell \sim \ell^H \quad , \tag{2.25a}$$

has a power spectrum

$$S_k \sim k^{-(2H+1)} \quad . \tag{2.25b}$$

Thus, the relations

$$\begin{aligned} \Delta f_{\lambda \ell} &= \lambda^{H} \Delta f_{\ell} \\ S_{\lambda k} &= \lambda^{-(2H+1)} S_{k} \end{aligned} , \tag{2.26}$$

immediately follow and demonstrate unambiguously the nature of scaling. Hence, it is clear that for a scaling variable, the statistics at one scale ℓ are related to the statistics at another scale $\lambda\ell$ by a scale dependent multiple λ^{H} only. This result can now be compared to the definition of a fractal set.

Assume that a set of points $\mathscr{S}$ is imbedded in a region of D–dimensional space of size ℓ_0. Divide this region into D–dimensional 'cubes' of size $\ell_n = \ell_0 \lambda^n$ where $\lambda<1$ and $n \geq 1$. Hence, the region is divided into a total of $N_T(\ell_n) = \lambda^{-nD}$ D–dimensional cubes. Let the total number of cubes required to 'cover' $\mathscr{S}$ at scale ℓ_n be $N(\ell_n)$. If $N(\ell_n) \sim \lambda^{-nd}$ as $n \to \infty$ and d is noninteger, then $\mathscr{S}$ is a fractal set and has a Haussdorf dimension of d. Note that the scale dependent probability of a cube covering $\mathscr{S}$ is

$$\frac{N(\ell_n)}{N_T(\ell_n)} = \Pr\left[\mathscr{S}(\ell_n)\right] = \frac{\lambda^{-nd}}{\lambda^{-nD}} = (\lambda^{-n})^{D-d} = \lambda^{-nc} , \tag{2.27}$$

where c is the codimension of $\mathscr{S}$. Thus, the probabilities of $\mathscr{S}$ being covered by a D–dimensional cube at ℓ_m and ℓ_n are related by

$$\Pr\left[\mathscr{S}(\ell_m)\right] = (\lambda^{-m+n})^{c} \Pr\left[\mathscr{S}(\ell_n)\right] , \tag{2.28}$$

which follows immediately from Eq.(2.27) and where λ^{-m+n} is the ratio between scale ℓ_m and ℓ_n. This is the same form as Eq.(2.26). Therefore, if a variable

exhibits scaling over a range, it is fractal–like in that range. Hence, the velocity field in turbulent flow and its power spectrum are fractal–like over a finite range of space scales. By the same token, a fractal object exhibits scaling over an infinite range of scales. Not surprisingly, observations have shown that cloud fields (passive scalars) have fractal–like area–to–perimeter relationships and scaling liquid water content (e.g. Lovejoy, 1982; Welch *et al.*, 1988; Cahalan and Joseph, 1989; Cahalan and Snider, 1989).

2.3 Evidence That Horizontal Distribution of Cloud Liquid Water is Scaling

Satellite images and aircraft datasets are analyzed for scaling properties. The two types of data are presented and discussed in turn. These data are used primarily because of availability but also because they are reliable and span about 3.5 orders of magnitude.

2.3.1 Satellite Image Analysis

The satellite images discussed here are 256x256 pixel arrays obtained by the Advanced Very High Resolution Radiometer (AVHRR) onboard the NOAA–9 satellite. This instrument has five narrowband radiometers all of which have a nominal resolution of about 1 km at nadir viewing. This study utilizes the 0.63 μm visible (VIS) and 11.5 μm (IR) thermal bands. Data were extracted and calibrated at the Aerospace Division of AES. Eight images were examined. The images are for areas 500 – 1000 km off the east coast of North America extending from Florida to Labrador. The data were recorded during the first half of March, 1986. Results of three representative images are presented here in detail. These images are shown in Figs.2.1 – 2.3 using the AVHRR VIS band and a relative grey scale. Satellite tracking direction is towards the top of the page. This is approximately

Table 2.1

NOAA–9 (AVHRR) satellite information

	Scene A	Scene B	Scene C
Date	5/3/86	8/3/86	13/3/86
Time (GMT)	1939	1909	1637
Orbit Number	6325	6367	6436
Latitude (N)	29.5°	36.0°	54.0°
Longitude (W)	75.0°	69.5°	40.5°
Solar Zenith Angle	50.7°	52.9°	61.7°
Viewing Zen. Angle	32.6°	26.4°	6.0°
Relative Azimuth	31.8°	35.8°	45.4°

due north for NOAA–9 is a polar orbiting satellite. Information pertaining to these images are summarized in Table 2.1. Following Garand's (1986) examples, scene A is of scattered cumulus; scene B appears to be stratocumulus; and scene C appears to be something between stratocumulus and open polygonal cells.

2.3.1.1 Spatial Coherence Analysis

Since information about layered cloud fields is sought, the first stage of the analysis is to establish whether a satellite image is of a single layer of clouds only. This is achieved by applying the spatial coherence method (Coakley and Bretherton, 1982) to the AVHRR IR band.

In the spatial coherence method, pixel radiances are grouped together into n×n arrays. The mean and standard deviation of the radiances in the n×n arrays are calculated and plotted as ordered pairs in Cartesian co–ordinates with the mean on the x–axis. If the sea–surface temperature and the cloud–top temperatures do not vary much over the image, the pattern of ordered pairs will be a broad arch with two well defined 'feet'. The reasons for this are as follows. Pixel arrays with no cloud have a large mean radiance (warm ocean; warm foot of arch) and negligible variance amongst the constituent pixel radiances. Similarly, a pixel array of completely overcast sky will have a small mean radiance (cool cloud–tops; cool foot of arch) with little variance amongst the constituents. Pixel arrays that contain similar patterns of broken cloud in each constituent pixel will have an intermediate mean and moderate variance (lower mid–arch). Lastly, pixel arrays with highly variable broken cloud will have an intermediate mean and large variance (upper mid–arch). Figures 2.1 – 2.3 show IR spatial coherence scatter–plots for the three respective images using 4x4 pixel arrays. Clearly, each image gives rise to a single broad arch with two fairly well–defined feet thus

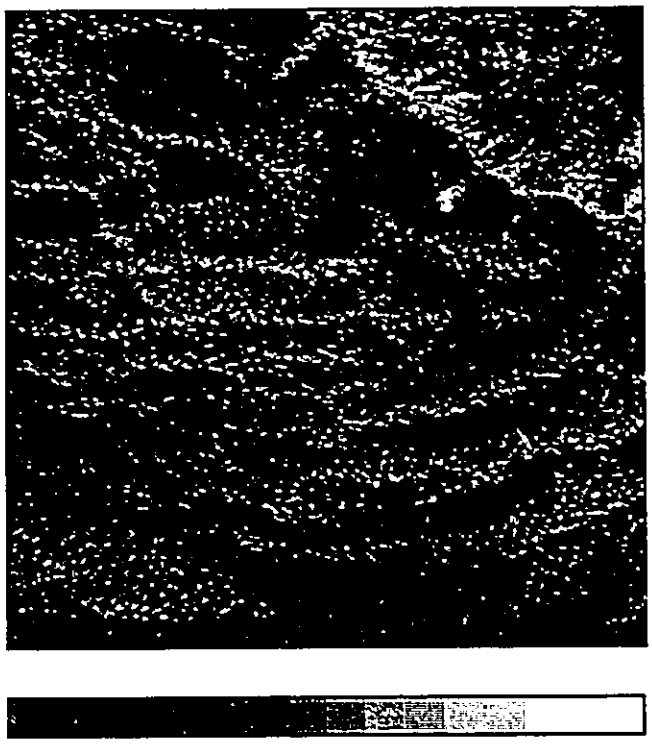

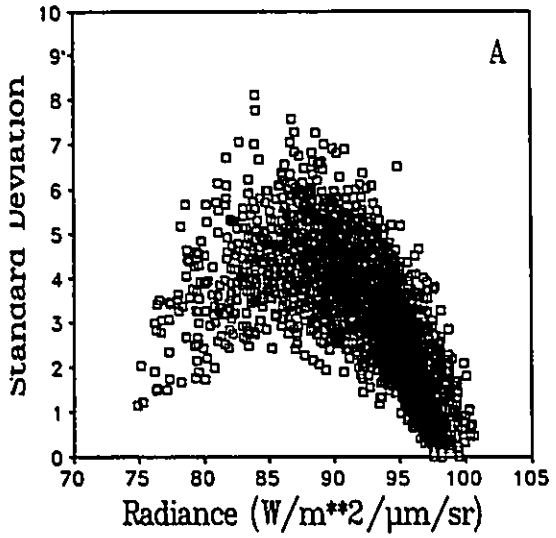

Fig.2.1. (a) Relative brightness image of scene A using AVHRR VIS data. Minimum and maximum reflectances are 0.031 and 0.561. Below the image is its spatial coherence scatter–plot using AVHRR IR imagery. 4x4 pixel arrays have been used.

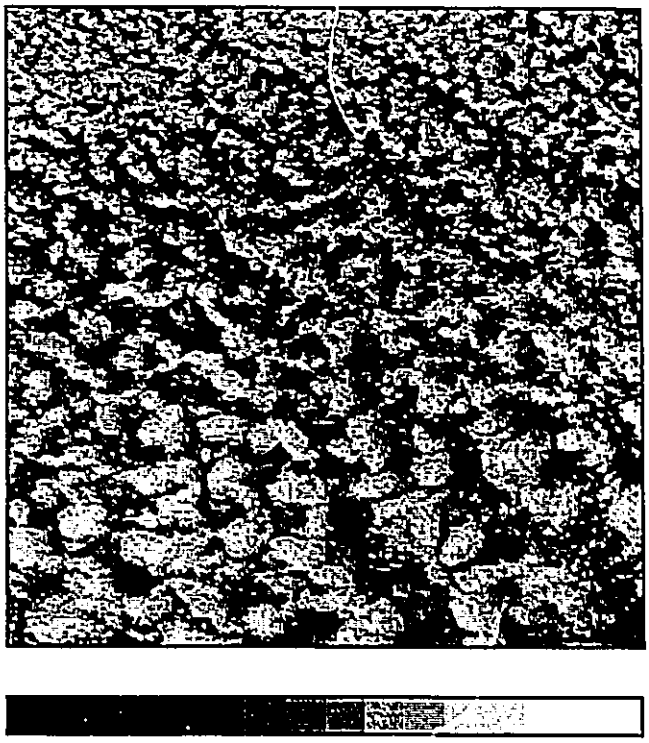

Fig.2.1. (b) As in (a) except for scene B where minimum and maximum reflectances are 0.039 and 0.652.

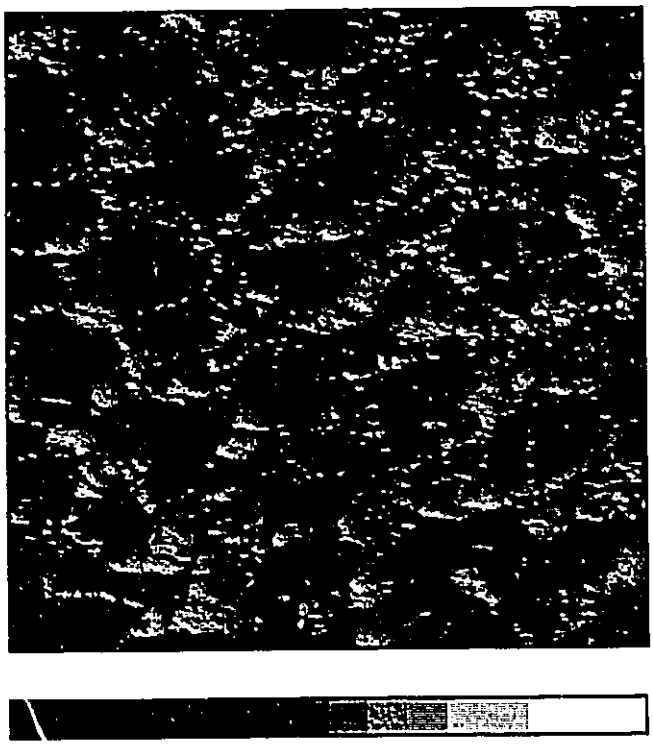

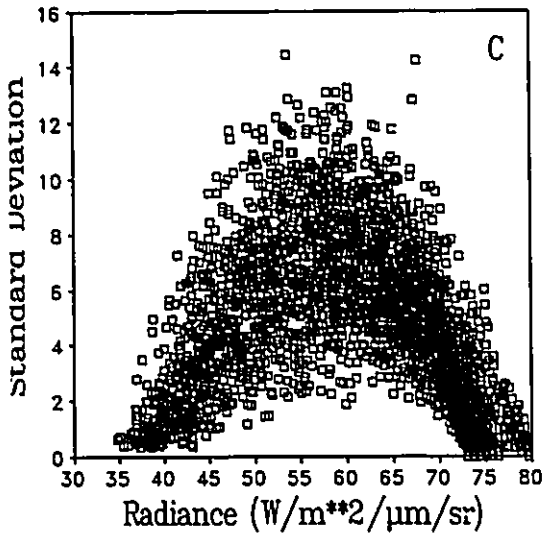

Fig.2.1. (c) As in (a) except for scene C where minimum and maximum are 0.02 and 0.588.

signifying a single layer of cloud. Had a second cloud layer been present, another foot would have appeared at the base of a second arch emanating from the first arch (Coakley, 1983).

Let $I_c \pm \Delta I_c$ be the IR radiance associated with the warm foot of the arch (clear–sky) and $I_o \pm \Delta I_o$ be the cold foot's IR radiance (cloud tops). ΔI_c and ΔI_o are errors in I_c and I_o. Their magnitudes are determined by the dispersion of points at the base of the arches. Making the extreme assumption that when clouds occur they are unconditionally very thick in the IR, the average (measured) radiance of the image is

$$I = (1 - A_s)I_c + A_s I_o \ , \tag{2.29}$$

where A_s is cloud cover fraction presented to the satellite. Hence, inferred cloud fraction of the image is

$$A_s = \frac{I - I_c}{I_o - I_c} \ . \tag{2.30}$$

The error associated with A_s is

$$\Delta A_s = \pm \frac{A_s}{I - I_c} \left\{ \left[\Delta I_c (1 - A_s) \right]^2 + \left[\Delta I_o A_s \right]^2 \right\}^{1/2} \ . \tag{2.31}$$

A_s for the images in Figs. 2.1 – 2.3 are listed, along with other spatial coherence information, in Table 2.2. The problem, however, with this approach is that cloud fields are inhomogeneous and parts of clouds, unresolved by AVHRR, have very

Table 2.2

Summary of Spatial Coherence Analyses of Scenes A, B, and C

	Scene A	Scene B	Scene C
I_c	99.9±0.5	93.6±0.9	78.3±0.8
I_o	76.9±1.8	54.2±0.3	37.3±0.9
σ_{crit}	0.378	0.728	0.764
N_c	190	146	282
N_o	10	268	335
A_s	0.28±0.06	0.77±0.02	0.38±0.02

I_c: Clear–sky radiance ($W/m^2/\mu m/sr$)

I_o: Overcast radiance ($W/m^2/\mu m/sr$)

σ_{crit}: Maximum standard deviation a collection of pixels may have to be considered as being a constituent of one of the arch's feet

N_c: Number of points in clear–sky foot of arch

N_o: Number of points in overcast foot of arch

A_s: Inferred cloud fraction using Eq.(2.30)

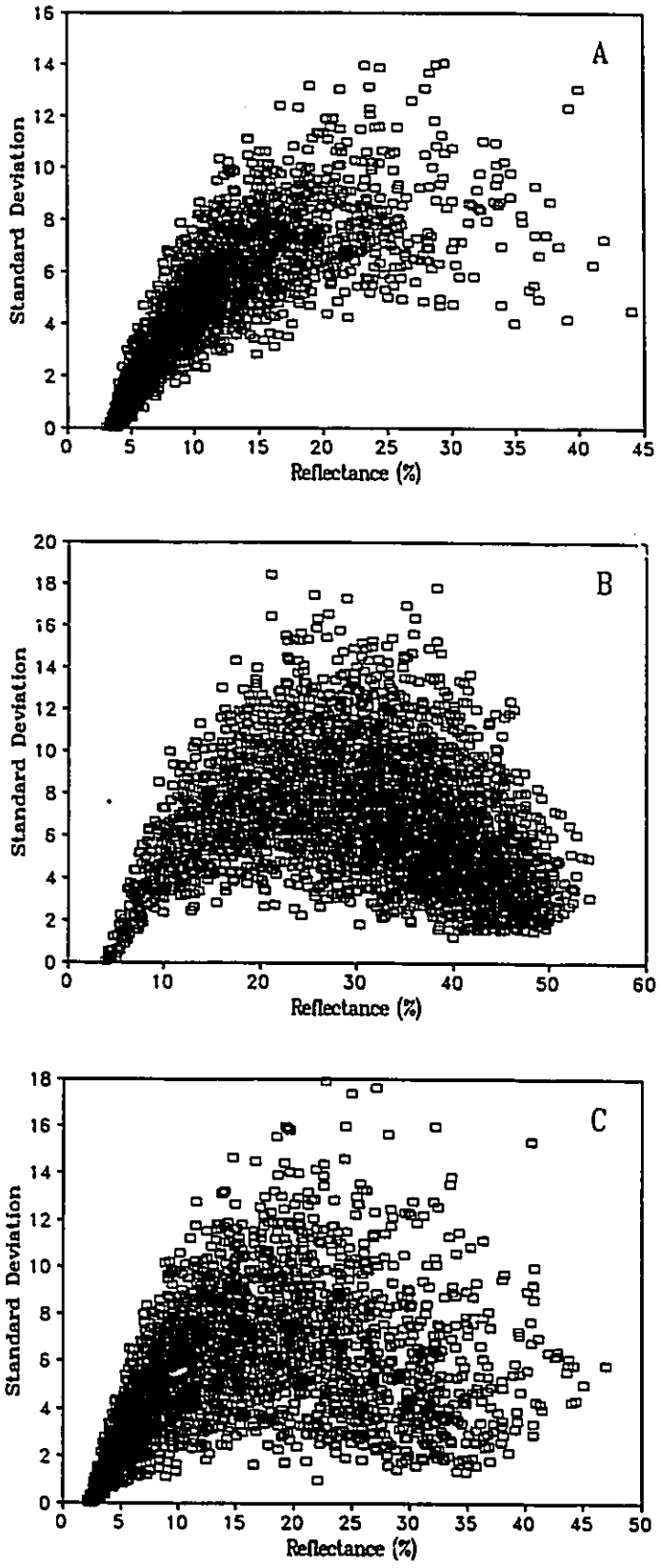

Fig.2.2. Spatial coherence scatter–plots for scenes A, B, and C using AVHRR VIS imagery (reflectance in %). 4x4 pixel arrays have been used.

thin regions that are not thick in the IR (see Parker *et al.*, 1986). Since the surface is detected to some extent through thin cloud, A_s estimated by Eq.(2.30) will be too low by an unknown amount (see Appendix B for a proof of this statement).

Horizontal variability in vertically integrated cloud mass is not very apparent in the IR due to limited multiple scattering of photons by cloud droplets and the very rapid reduction in transmittance with increasing cloud optical depth τ above $\sim$1. In the visible, however, horizontal variability is apparent. Using the AVHRR 0.63 μm (VIS) band this time, the spatial coherence procedure is repeated for the three images. The resulting VIS scatter–plots are shown in Fig. 2.2. It is immediately clear that sea–surface albedo is very well defined in all cases (equal to about 0.04), yet there is no characteristic cloud albedo; standard deviation does not taper off as reflectance increases. This implies high variability in horizontal distribution of cloud thickness (mass).

2.3.1.2 Spectral Analysis of Satellite Images

The next step is to determine an ensemble averaged one–dimensional power spectrum $\langle S_k \rangle$ for each of the images. This is achieved by taking ten horizontal and vertical lines of pixels from the images, finding the power spectrum for each line, and averaging the twenty spectra to give one representative smoothed spectrum. Cahalan and Snider (1989) applied a similar method for two 60x60 km LANDSAT visible images (30 m resolution) from July 7, 1987 off the coast of Southern California.

Figure 2.3 shows the smoothed spectra[1] for the VIS band of the images in Fig.s 2.1 – 2.3. None of the spectra display dominant peaks. This implies that the images are quite isotropic (not much orientation). The most distinguishing feature

[1]All spectra plotted in this thesis are normalized by the total power in the image.

Fig.2.3. Ensemble averaged one–dimensional power spectra for scenes A, B, and C. Solid and dashed lines are for VIS and IR imagery respectively. Spectra are normalized to the total power in the image. The IR spectra are shifted up one decade. Straight lines that are labelled are best–fit lines.

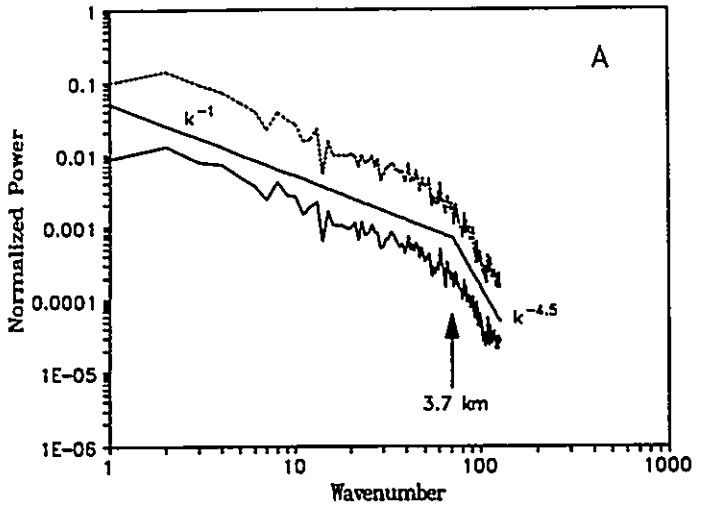
A
Normalized Power
1
0.1
0.01
0.001
0.0001
1E-05
1E-06
k^-1
k^-4.5
3.7 km
1
10
100
1000
Wavenumber

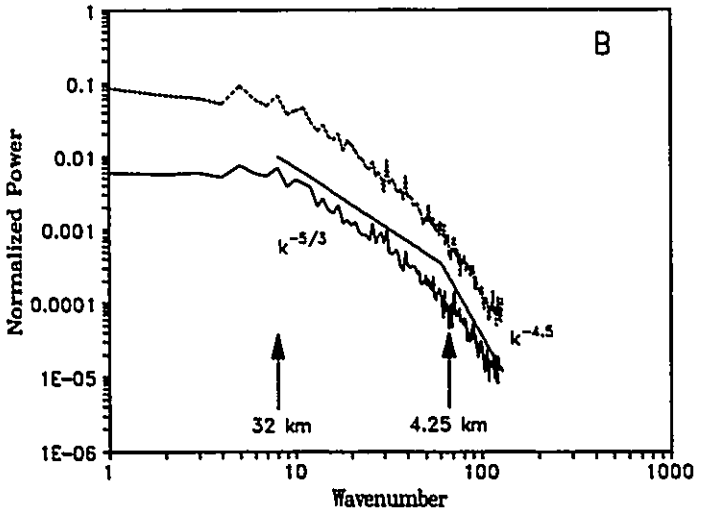
B
Normalized Power
1
0.1
0.01
0.001
0.0001
1E-05
1E-06
k^-5/3
k^-4.5
32 km
4.25 km
1
10
100
1000
Wavenumber

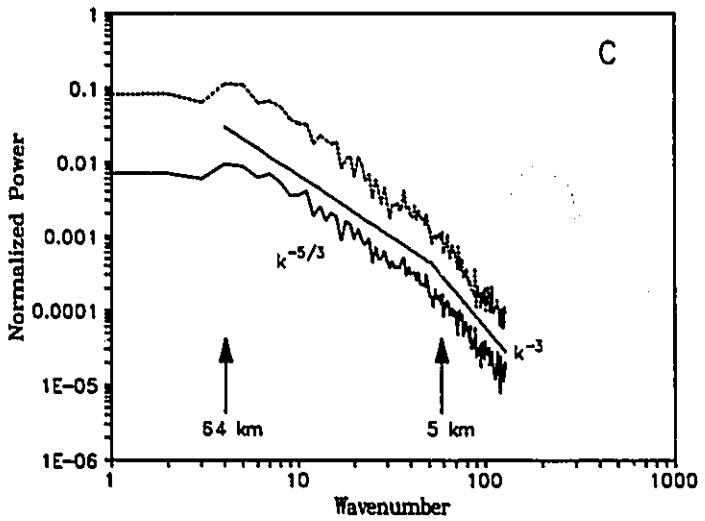
C
Normalized Power
1
0.1
0.01
0.001
0.0001
1E-05
1E-06
k^-5/3
k^-3
64 km
5 km
1
10
100
1000
Wavenumber

in all three plots in Fig.2.3 is the unmistakable change in scaling at about 4 km (k $\simeq 60 - 70$). Examination of the images reveals that 4 km is approximately typical cloud cell size. Furthermore, many of the larger clouds ($\gg$ 4 km) appear to be conglomerates of bright cells which measure about 4 km in diameter. For scenes A and B, the spectra follow $k^{-4.5}$ approximately for scales less than about 4 km. Over the same range of scales, the spectrum for scene C follows k^{-3}. For scales between about $4 - 30$ km and $5 - 60$ km for scenes B and C respectively, the spectra follow $k^{-5/3}$. For scales larger than those just mentioned, the spectra of scenes B and C appear to imply random (white noise) fields of reflected radiance; k^{-0}. The spectrum for scene A follows k^{-1} (1/f–noise) from about 4 km to at least 256 km.

These results are very similar to Cahalan and Snider's results. Though the two $\langle S_k \rangle$ radiance spectra they showed ranged only from 60 m to about 15 km, their scattered cumulus case followed $k^{-0.6}$ down to about 0.5 km and k^{-3} for smaller scales, and the stratocumulus case followed $k^{-5/3}$ down to about 200 m and then followed $k^{-3.6}$. For their scattered cumulus case it is clear that typical cloud size is about 0.5 km. Hence, the steeper portion of the spectra correspond to radiance variance across cloud cells. It is interesting that similar cloud types in different oceans and different seasons show very similar scaling exponents before and after the break in scaling. Especially since the scaling breaks in scenes A, B, and C occur at a space scale about one order of magnitude greater than in Cahalan and Snider's cases. This, however, is consistent with diurnal observations of clouds (e.g. Plank, 1969); small clouds in the morning (LANDSAT) and larger conglomerated clouds in the afternoon (AVHRR).

Cahalan and Snider also showed the spectrum of vertically integrated liquid water for the July 7 stratocumulus obtained by an uplooking microwave radiometer on San Nicolas Island, California which was near the LANDSAT

tracking line. Assuming frozen turbulence (advected turbulent field), the spectrum followed $k^{-5/3}$ for scales between about 600 m to at least 100 km; the same as for stratocumulus reflected radiance. This appears to verify that for large scales the structure of the reflected radiance and liquid water fields are very similar. If *all* clouds behaved as isolated plane–parallel media, this result would not be interesting because reflectance would be a one–to–one function of, and highly correlated with, liquid water amount. Hence, by the Wiener–Khintchin theorem, the power spectra of reflectance and liquid water would be expected to be largely similar. Reflectance of real clouds, however, depends on the local three–dimensional distribution of liquid water and, thus, a unique relation between reflectance and liquid water is not expected.

The important point regarding many of the scaling exponents just mentioned is that they arise in the theory of two– and three–dimensional homogeneous, space–filling turbulence (e.g. Kolmogorov, 1941; Kraichnan, 1967). Following Cahalan and Snider's reasoning, a possible explanation for the reflected radiance scaling patterns may be that convective energy is injected at scales of about 4 km (in their two cases about 0.5 km), energy cascades downwards in k (up in real space) following a $k^{-5/3}$ two–dimensional turbulence law and enstrophy (vorticity squared) cascades upwards in k following approximately a k^{-3} two–dimensional turbulence law (Kraichnan, 1967; 1970). Assuming cloud droplets to be passive scalars in the range of satellite resolution, cloud structure would then follow a scaling law similar to the turbulent field which in turn would give rise to a reflectance field with again similar scaling. For scales less than about 5 km, however, it is difficult to see how two–dimensional turbulence theory can describe atmospheric motion. At this stage it is difficult to attribute dynamical mechanisms to the k^{-1} and $k^{-4.5}$ regimes.

Regarding Cahalan and Snider's results, Wiscombe (personal communication, 1990) has hypothesized that the change to the –3 to –4 power laws for scales below typical cloud size may possibly be due to photon transport rather than to a structural change in cloud liquid water distribution. The basis of his argument is that multiple scattering of photons serves to make inhomogeneous cloud look smooth (more homogeneous) and this leads to a rapid reduction in the amplitude (power) of waves, of wavelength less than typical cloud diameter, which make up the radiance field. This argument simply recognizes that multiple scattering of photons acts as a low–pass filter suppressing detail and, thus, high frequency wave amplitudes.

If the breaks in scaling of the VIS fields are due to dynamics (cloud liquid water) rather than multiple scattering, a similar break in scaling might appear in the power spectrum of an image's corresponding IR radiances. This is because of limited multiple scattering and short photon mean–free (absorption) pathlength at thermal wavelengths. Therefore, using the lines of pixels used to create the VIS spectra in Fig.2.3, smoothed power spectra of the IR fields are shown on the same plots. VIS and IR spectra have much in common. This was expected for the low wavenumber regime (where they are almost identical), but the break in scaling at $\sim$ 4 km to a new regime is clear in the IR fields too: the slopes are the same, but with minor differences in detailed structure. It appears, however, that the scale changing transition is less abrupt in the IR case than in the VIS case. Thus, in all three cases, it appears that the breaks in scaling are not due to the smoothing effects of multiple scattering of photons. If the changes in scaling are due to dynamics, the nature of the dynamics is as of yet unclear. Similar results where obtained for six other satellite images analysed (see Appendix C).

Assuming that the IR radiance of the $(ij)^{th}$ pixel I_{ij} is approximated by Eq.(2.29) with A_s replaced by the cloud fraction in the pixel, implies that Fourier

transforms of I_{ij} and cloud fraction [Eq.(2.30)] are equal to within a constant factor. Therefore, if cloud amount was the only variable modulating clear–sky IR emission to space, the results in Fig.2.3, imply that cloud amount is scaling. While cloud amount is certainly not the only variable modulating IR to space, this is a reasonable suggestion since observations show that clouds tend to clump together and that clumps are separated by substantial cloud–free areas (see Randall and Huffman, 1980; Fouquart *et al.*, 1990). In fact, this is the reason why the spatial coherence method works at different scales. However, as mentioned above, the problem is compounded beyond cloud fraction by horizontal variation in cloud optical thickness. Unfortunately, there seems no way to directly and simultaneously assess the impact of cloud fraction and optical depth on radiance fields.

IR radiance is also modulated by changes in cloud temperature with height. A general idea of the magnitude of this effect is attainable. Following Cahalan and Snider (1990), begin by calculating the cumulative frequency of the IR images (see Fig.2.4). Then, find the radiance that exceeds $100A_s$ % of the radiances in the image where A_s is the image averaged cloud fraction as determined by the spatial coherence method. This radiance is a first order estimate of the cloud–base radiance (temperature) I_b. Using the AVHRR radiance–to–temperature conversion, one has an idea of the range of cloud temperature which is approximately proportional to $I_b - I_o$. Using the values of I_o (Table 2.2) and I_b (Fig.2.4), the cloud–tops in Figs.2.1 – 2.3 may vary in temperature by up to 15 K. Assuming cloud temperature decreases with height along a moist adiabat, cloud geometric thickness (assuming a constant lifting condensation level) may vary by as much as 2 km. As such, much of the variation in cloud reflectance and emittance across an image may be explained by variations in cloud geometric, and thus optical, thickness. Perhaps cloud liquid water content scales similar to $k^{-5/3}$

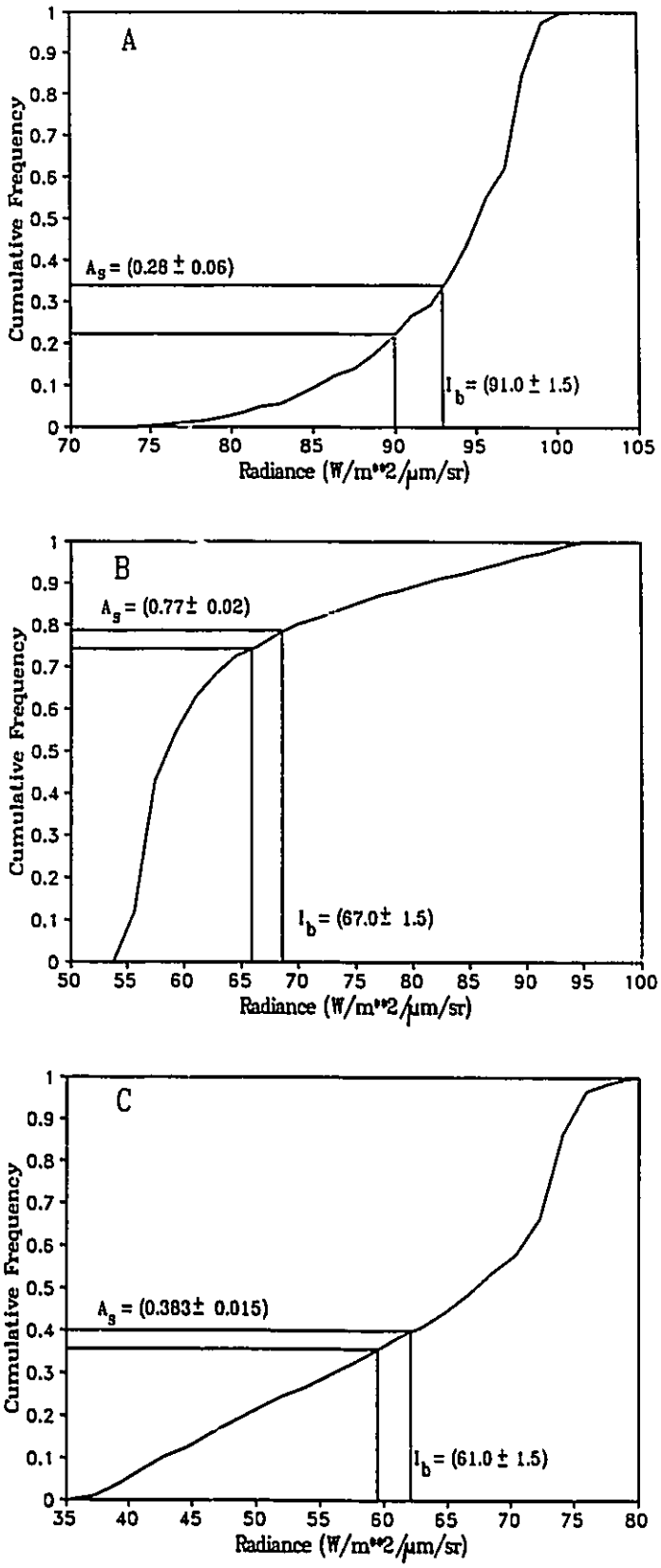

Fig.2.4. Cumulative frequency of AVHRR IR imagery for scenes A, B, and C. A_S is cloud amount estimated from the IR spatial coherence scatter–plots and I_b is estimated cloudbase radiance.

Fig.2.5. Directionally integrated two–dimensional power spectra for scenes A, B, and C. Solid and dashed curves are for VIS and IR imagery respectively. Spectra are normalized to the total power in the image. The IR spectra are shifted up one decade. Straight lines that are labelled are best–fit lines.

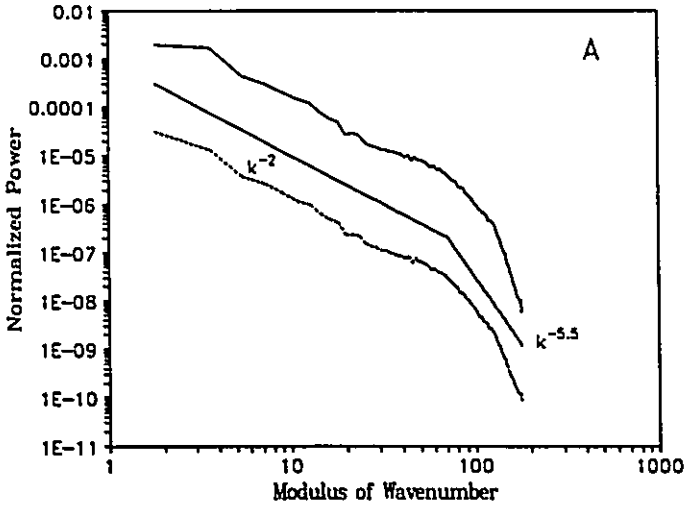
A
Normalized Power
0.01
0.001
0.0001
1E-05
1E-06
1E-07
1E-08
1E-09
1E-10
1E-11
k^-2
k^-5.5
1
10
100
1000
Modulus of Wavenumber

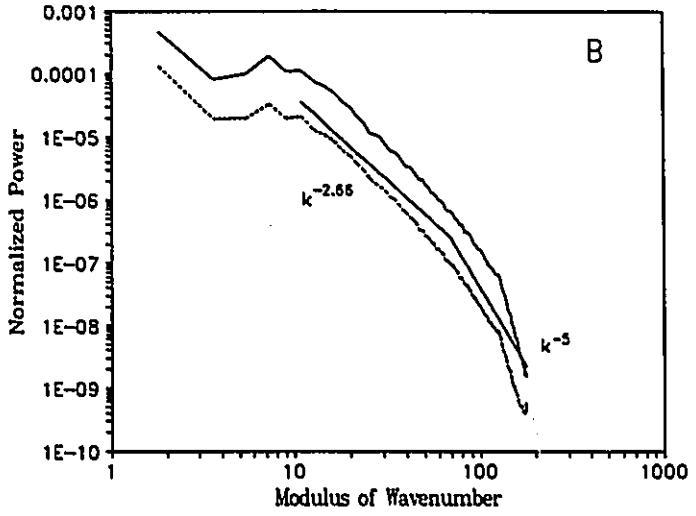
B
Normalized Power
0.001
0.0001
1E-05
1E-06
1E-07
1E-08
1E-09
1E-10
k^-2.65
k^-5
1
10
100
1000
Modulus of Wavenumber

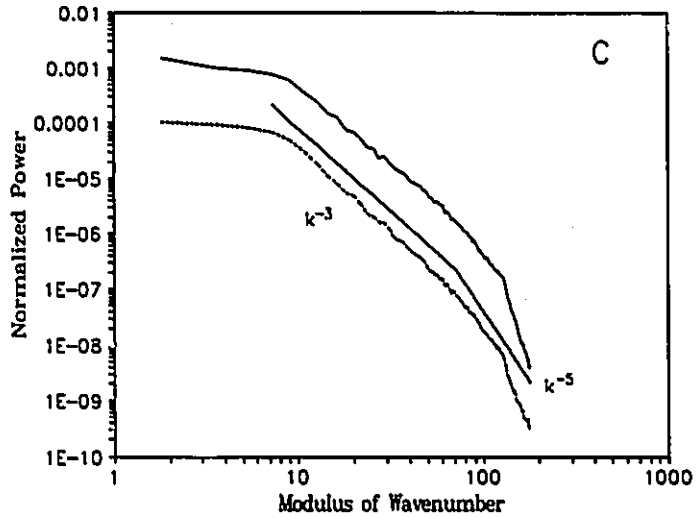
C
Normalized Power
0.01
0.001
0.0001
1E-05
1E-06
1E-07
1E-08
1E-09
1E-10
k^-3
k^-5
1
10
100
1000
Modulus of Wavenumber

in three–dimensions and the vertical integral of liquid water is smoother and scales more like k^{-4}. Exploration of this hypothesis is beyond the scope of this thesis.

This analysis supports the claim that the scaling break is due to dynamical effects and not radiation effects only. Again, however, it is stressed that the scaling changes in Cahalan and Snider's examples occur below 1 km which is both below the resolution of AVHRR data and closer to the average photon mean–free pathlength in the visible. Thus, the results presented here do not necessarily negate Wiscombe's hypothesis. Better confirmation will come with a comparison of LANDSAT visible and IR spectra.

As a final note regarding power spectra of satellite imagery, consider the directionally integrated spectrum $\check{S}_{|\mathbf{k}|}$. Figure 2.5 shows $\check{S}_{|\mathbf{k}|}$ for the VIS and IR fields of scenes A, B, and C. These spectra bear many expected similarities to their one–dimensional counterparts shown in Fig.2.3. In the intermediate $|\mathbf{k}|$ and k ranges, all spectra for scene A scale approximately as $|\mathbf{k}|^{-2}$ and k^{-1}, respectively, while for scenes B and C they scale approximately as $|\mathbf{k}|^{-8/3}$ and $k^{-5/3}$. It is interesting that all spectra in Fig.2.5 show gentle, gradual increases in slope over the range where spectra in Fig.2.3 shows distinct changes in slope. Furthermore, the spectra in Fig.2.5 display distinct changes in slope at $|\mathbf{k}| \simeq 128$ and follow straight lines up to $|\mathbf{k}| = \sqrt{2} \cdot 128$.

2.3.1.3 Multifractal Analysis of Satellite Images

In addition to Fourier analysis, cloud and radiation fields can be examined with fractal concepts. The relation between scaling and mono–fractal sets has been alluded to already in Section 2.2. The radiation field in a satellite image, however, defines a three–dimensional graph and not a set; two dimensions for location and one for magnitude. Thus, the first problem is to transform the three–dimensional graph into sets by imposeing radiance exceedance thresholds: if a radiance exceeds

the threshold it is in the set, otherwise it is not. This casts the problem into the standard fractal framework.

With fractals, one is concerned with what sets look like at various scales of measure. Therefore, attention must be directed towards what a field looks like at different scales; that is, when measured at different resolutions. As resolution decreases, a variable field appears smoother since it is averaged over larger areas. Conversely, as resolution increases, the field may become more variable. Hence, care must be taken when imposing exceedance thresholds on an image at various scales because specific thresholds have different meanings at different scales. Furthermore, one may generally expect that the low and high intensity regions of an image scale differently. This gives rise to multifractals which are characterized by many (perhaps an infinity of) codimensions (Frisch and Parisi, 1985; Schertzer and Lovejoy, 1986).

Schertzer and Lovejoy (1986) and Lovejoy and Schertzer (1990) have stressed the use of simple, phenomonological multiplicative cascade models to simulate turbulent and random multifractal fields. A multiplicative cascade model begins with a homogeneous field of size ℓ_0 which is then repeatedly subdivided. Upon each subdivision, the value of offspring cells (eddies) equals the value of the parent cell times a number whose value is determined by a well defined probability rule. Schertzer and Lovejoy (1986) showed that as the size of cells ℓ, and thus the scale factor $\lambda = \ell/\ell_0$, decrease, the resulting 'bare' quantities of the cascade f_ℓ tend to cluster and behave like $f_\ell \sim \ell^{-\gamma}$ where γ is an order of singularity. In other words, the emerging field develops a hierarchy of singularities. As such, the ensemble average of realizations of a multiplicative cascade yields the approximate relation

$$\Pr\left[f_\ell \geq \ell^{-\gamma}\right] \simeq \ell^{c(\gamma)} , \qquad (2.32)$$

where Pr is probability and $c(\gamma)$ is the scale independent co–dimension function. In non–dimensional form, Eq.(2.32) is

$$\Pr\left[f_\lambda \geq \langle f \rangle \lambda^{-\gamma}\right] \simeq \lambda^{c(\gamma)} \quad , \tag{2.33}$$

where $\langle f \rangle$ is the mean of f over the image (which is independent of scale). Note the similarity between Eq.(2.33) and Eq.(2.27) and also that the exceedance thresholds $\langle f \rangle \lambda^{-\gamma}$ depend on scale. Schertzer and Lovejoy (1986) also showed that

$$c(\gamma) = c_o\left[\frac{\gamma}{\gamma_o} + 1\right]^{\alpha} \quad , \tag{2.34}$$

where c_o, γ_o, and α are constants. Hence, for multiplicative processes, the scale independent co–dimension function is a power function of γ, the parameter that governs the magnitude of the scale dependent thresholds used to form sets out of the field.

It is important to note that Eq.(2.33) applies to the ensemble average of the so–called 'bare' quantities of the cascade. If a cascade is allowed to develop to its inner scale λ_i, Eq.(2.33) does not strictly apply to the 'dressed' quantities: the fully developed bare quantities averaged (measured) at scales $\lambda > \lambda_i$. If atmospheric turbulence is assumed to behave as a multiplicative cascade with liquid water for the most part being a passive scalar, observations with the 1 km resolution AVHRR instrument (and even the SPOT satellite with ~10 m resolution) are well above the viscous cut–off (inner scale of turbulent cascade) and are thus substantially dressed. Furthermore, radiation fields are surrogate measures of the cloud field. Thus, the inferred $c(\gamma)$ function of a satellite image depends on wavelength of radiation and viewing and illumination geometry. This

complicates the problem for relations between $c(\gamma)$ for remotely sensed radiation and the corresponding cloud field are unknown. Nevertheless, Gabriel *et al.* (1988) and Lovejoy and Schertzer (1990) have shown that visible and IR satellite radiances of mostly overcast scenes of northeast North America have well defined $c(\gamma)$ functions over scales from 8 to 256 km.

Now, consider estimation of $c(\gamma)$ with the Probability Distribution/ Multiple Scaling (PDMS) method (Lovejoy and Schertzer, 1990). For the time being, assume that Eq.(2.32) is an equality. It may, therefore, be rearranged as

$$c(\gamma) = \frac{\ln\left\{\Pr\left[\gamma \geq \dfrac{\ln(f_\lambda/\langle f\rangle)}{\ln(\lambda)}\right]\right\}}{\ln(\lambda)} \quad . \tag{2.35}$$

This equation is calculated (histograms are tabulated) for many values of γ and λ (by averaging, and thus degrading, the satellite data). Figure 2.6 shows Eq.(2.35) averaged for λ = 1/256, 2/256, 4/256, 16/256, and 32/256 for the VIS images in Fig.s 2.1 – 2.3. Also plotted are estimated best–fit curves of $c(\gamma)$ in the form of Eq.(2.34). The constants for Eq.(2.34) are listed on the plot. The obvious method for finding c_0, γ_0, and α is non–linear regression, but often this was unsatisfactory. So too was the graphical method presented by Lovejoy and Schertzer (1990). A new graphical method was, therefore, developed (see Appendix D) and used in this study. It worked fairly well in the cases used. Evaluations of Eq.(2.35) at λ = 8/256 were excluded demonstrate that $c(\gamma)$ can be applied to a scale not used to derive it.

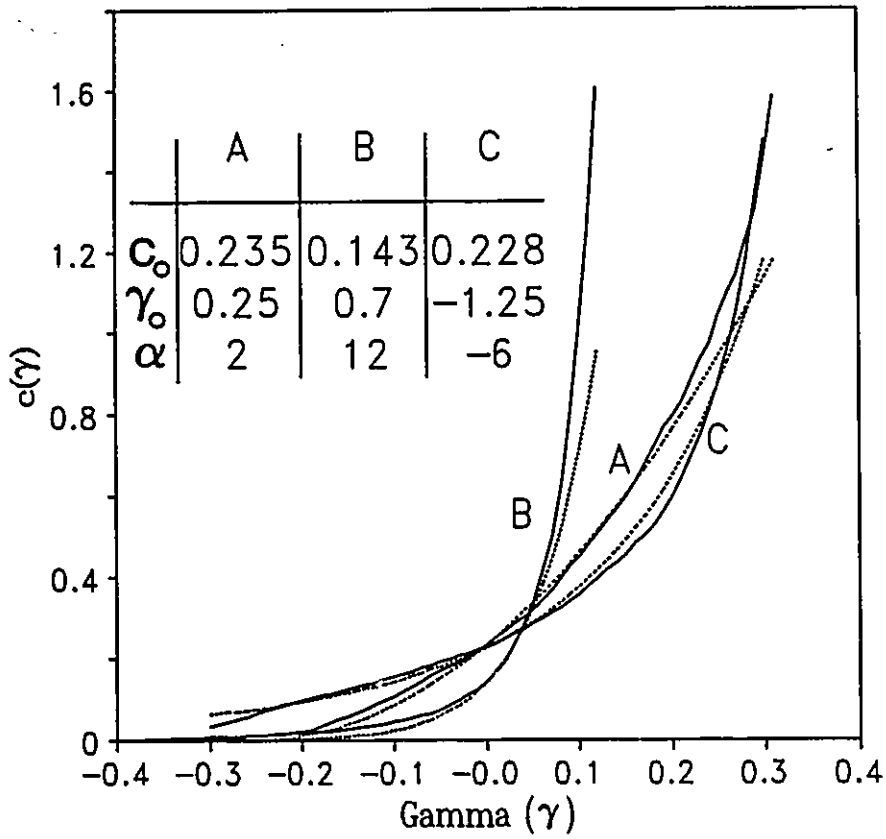

Fig.2.6. Estimated co–dimension functions for the VIS images of scenes A, B, and C. Solid lines are mean values obtained from Eq.(2.35). Dashed lines are best–fit curves to the solid lines. The parameters of Eq.(2.34) corresponding to the dashed lines are listed in the inset table.

Equation (2.33) can be written as

$$\int_{\langle f\rangle\lambda^{-\gamma}}^{\infty} p_\lambda(f_\lambda)df_\lambda \simeq \lambda^{c(\gamma)} \quad , \tag{2.36}$$

where $p_\lambda(f_\lambda)$ is a normalized, scale dependent density function of radiance measured at scale λ. Assuming that Eq.(2.36) is an equality and $f_\lambda = \langle f\rangle\lambda^{-\gamma}$, $p_\lambda(f_\lambda)$ is defined as

$$p_\lambda(f_\lambda) = \frac{\alpha \ln(\lambda) c(f_\lambda)\lambda^{c(f_\lambda)}}{f_\lambda\left[\gamma_0 \ln(\lambda) - \ln(f_\lambda/\langle f\rangle)\right]} \quad . \tag{2.37}$$

Figure 2.7 shows p_λ at $\lambda = 8/256$ using the constants listed in Fig.2.6. Also plotted in Fig.2.7 are the derivatives of the cumulative density functions of the VIS images in Fig.s 2.1 – 2.3 as averaged at 8 km resolution. Clearly, the theoretical descriptions are excellent given that $\lambda = 8/256$ was not used to estimate $c(\gamma)$ and that only one realization of the cascade, not an ensemble average, is being considered. These examples show, for apparently the first time, that radiances from single layer, non–overcast (broken) cloud fields may at times be characterized by multifractals.

Finally, it should be mentioned that the multifractal framework provides a potentially attractive approach to parameterization of sub–grid processes in climate models. The scale independent co–dimension function may provide a way of getting around re–tuning parameterizations as the resolution of a climate model changes. Currently, many parameterizations are bogged down with parameters that are seemingly very dependent on model resolution. If the parameters in the

Fig.2.7. Cumulative frequency curves of AVHRR VIS imagery averaged at 8 km resolution for scenes A, B, and C (solid lines). Thus, they are approximations to the radiance density functions at 8 km resolution. The dashed lines are theoretical density functions predicted by Eq.(2.37) using $\lambda=8/256$ and the parameters listed in Fig.2.6.

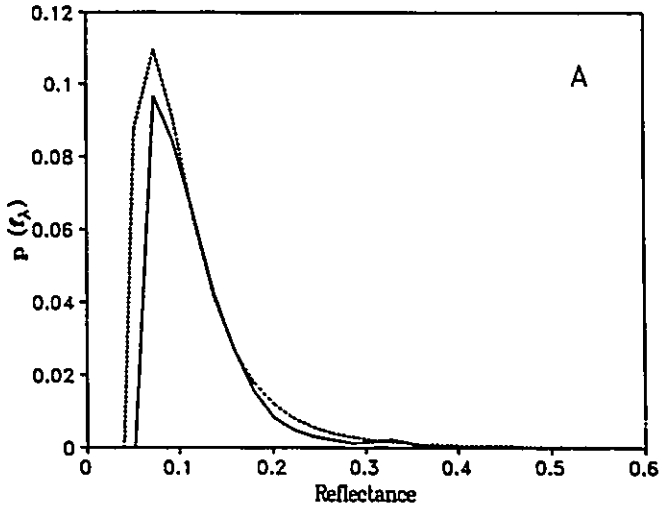
A
0.12
0.1
0.08
0.06
0.04
0.02
0
p (r_λ)
0 0.1 0.2 0.3 0.4 0.5 0.6
Reflectance

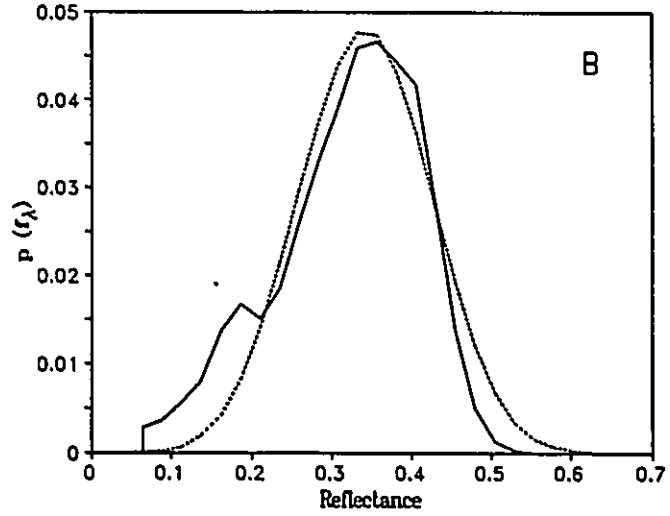
B
0.05
0.04
0.03
0.02
0.01
0
p (r_λ)
0 0.1 0.2 0.3 0.4 0.5 0.6 0.7
Reflectance

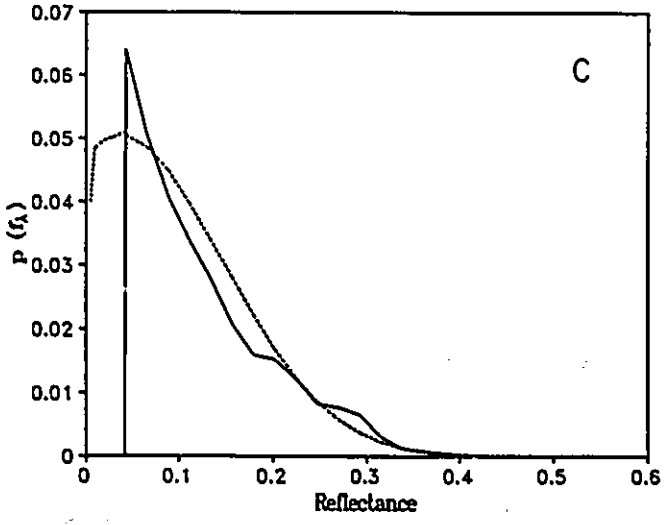
C
0.07
0.06
0.05
0.04
0.03
0.02
0.01
0
p (r_λ)
0 0.1 0.2 0.3 0.4 0.5 0.6
Reflectance

codimension function can be estimated and explained physically, $c(\gamma)$ may become a useful diagnostic variable in climate modelling of sub–grid phenomena.

2.3.2 Aircraft Data Analysis

Attention is now turned toward *in situ* observations of cumulus cloud fields as measured by instruments mounted on an aircraft. Four level flights between Muskoka and Dorset, Ontario (45°N, 79°W) through scattered cumulus during August, 1988 are considered. All data were measured by the Cloud Physics Division of AES (personal communication; Dr. R. Leaitch, 1990). Table 2.3 lists flight data. The Twin Otter aircraft flew at approximately 60 ms^{-1}. All data are one second integrations, hence, their resolution is about 60 m. This study makes use of air temperature, liquid water content (LWC), and up–welling and down–welling ultra–violet (UV) solar radiation. Liquid water content measurements for flights 25, 32, and 49 were obtained with a forward scattering spectrometer probe (FSSP) while for flight 43 a hot–wire probe was used. UV radiation was measured with a quartz–domed radiometer active at wavelengths between 0.29 and 0.385 μm and accurate to within ±2% at solar zenith angles less than 80°.

Figure 2.8 shows composite time series of LWC and temperature. The series are superimposed such that the following implication holds approximately:

$$T_n \gtrless T_{crit} \Rightarrow LWC_n \lessgtr 0 \ , \tag{2.38}$$

where T_n and LWC_n are the values at the n^{th} second and T_{crit} is approximately the upper bound of temperature for which a measurable amount of liquid water exists. For flights 25, 32, and 43, T_{crit} is about 8.8°, 13.0°, and 12.7°C, respectively. The correlation implied by Eq.(2.38) is especially good for flight 32

Table 2.3

AES Twin Otter flight information

	flight 25	flight 32	flight 43	flight 49
Date	6/8/88	15/8/88	24/8/88	29/8/88
Start Time (GMT)	1643	1942	1528	1841
Altitude (m)	2000	1240	1100	2180
Pressure (mb)	792	870	880	780

Fig.2.8. (a) Flight 25 time series of simultaneously measured cloud liquid water content (LWC), temperature, and upwelling UV radiative flux. For the upper plot, solid and dashed lines are temperature and LWC.

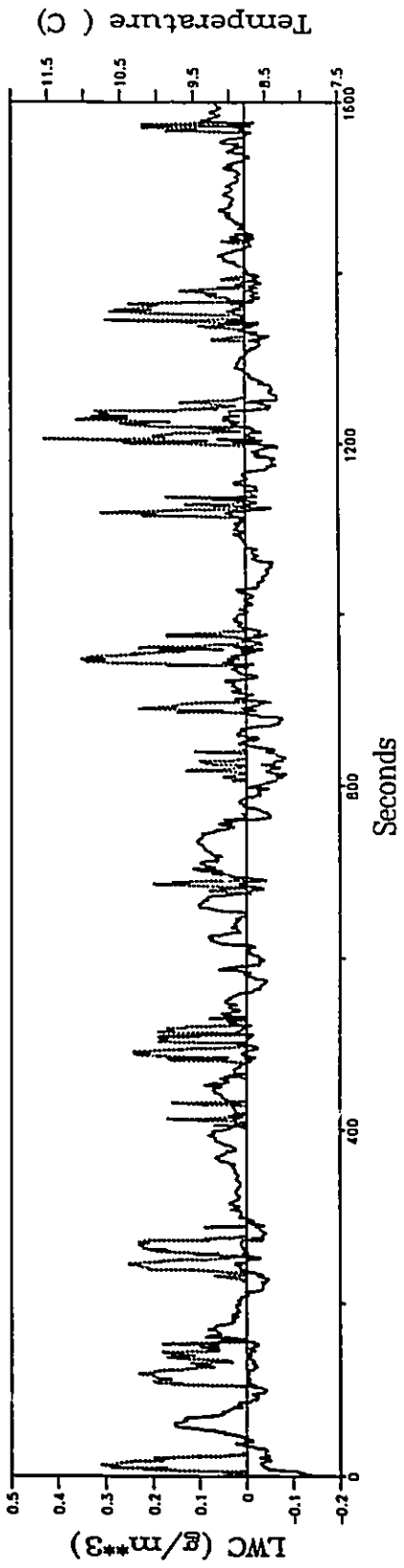
Temperature (C)
11.5
10.5
9.5
8.5
7.5
1600
1200
800
400
0
Seconds
LWC (g/m**3)
0.5
0.4
0.3
0.2
0.1
0
-0.1
-0.2

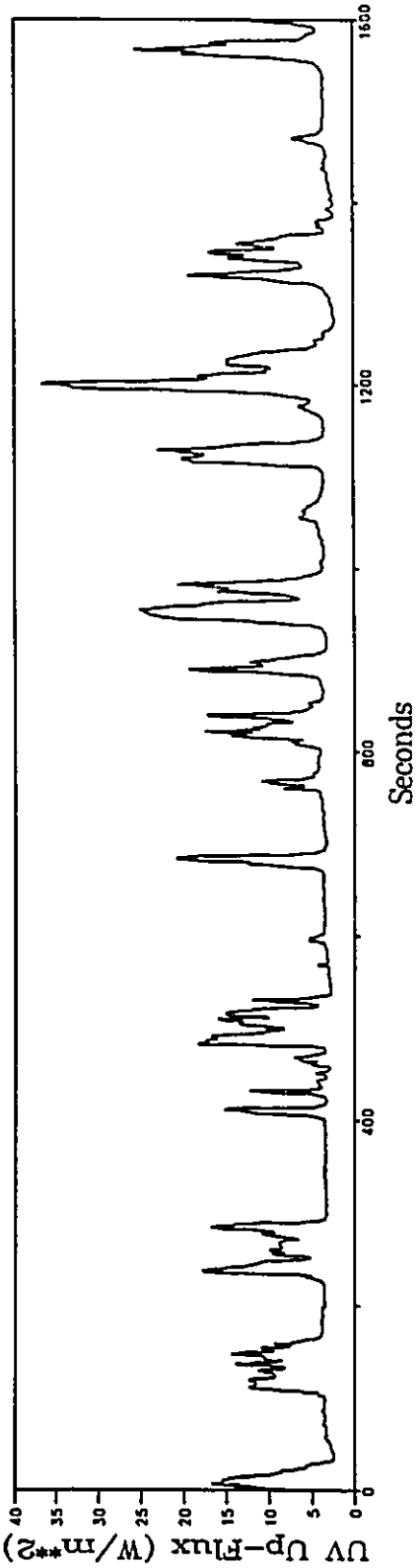
1600
1200
800
400
0
Seconds
UV Up-Flux (W/m**2)
40
35
30
25
20
15
10
5
0

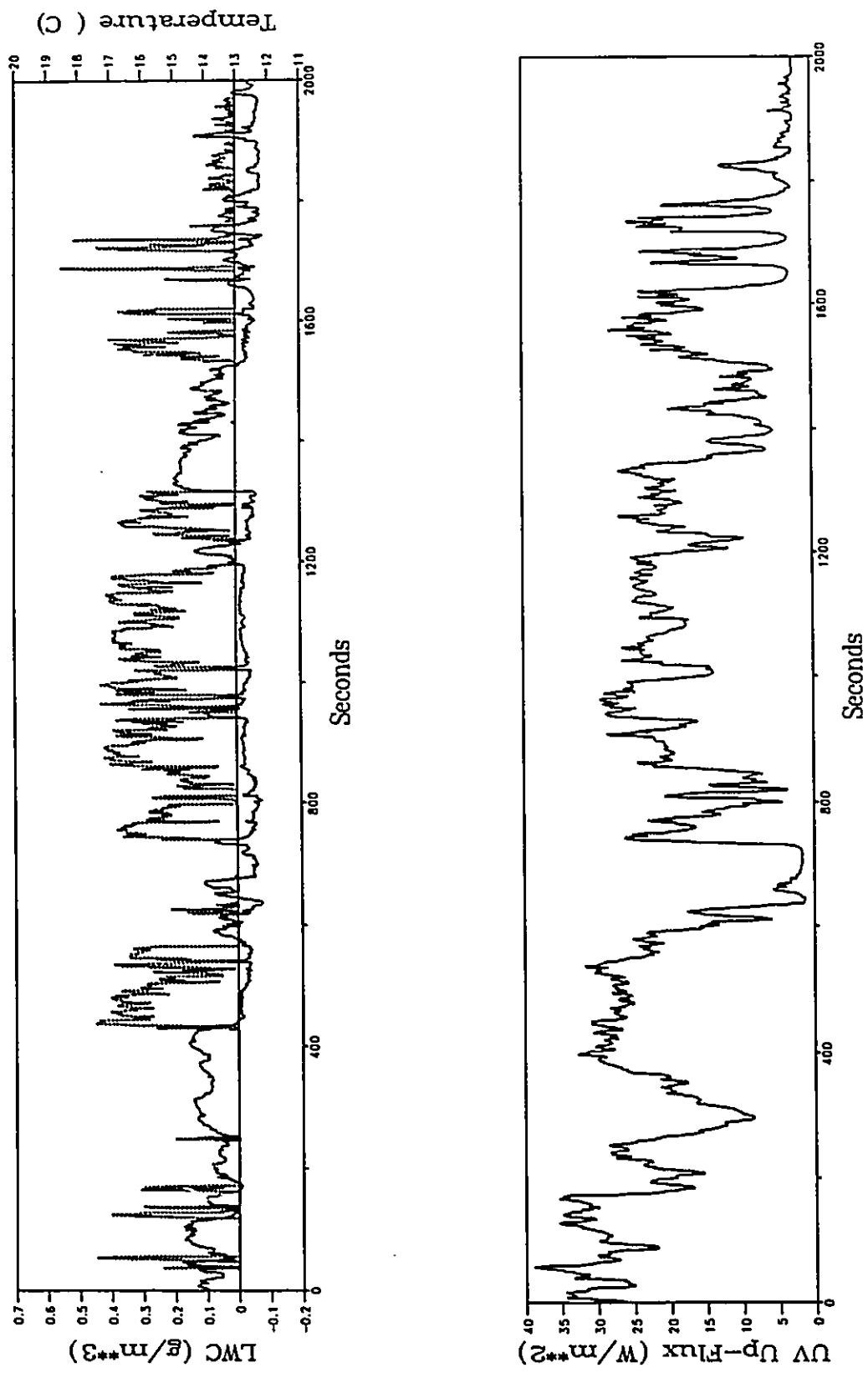

Fig.2.8. (b) As in (a) except for flight 32.

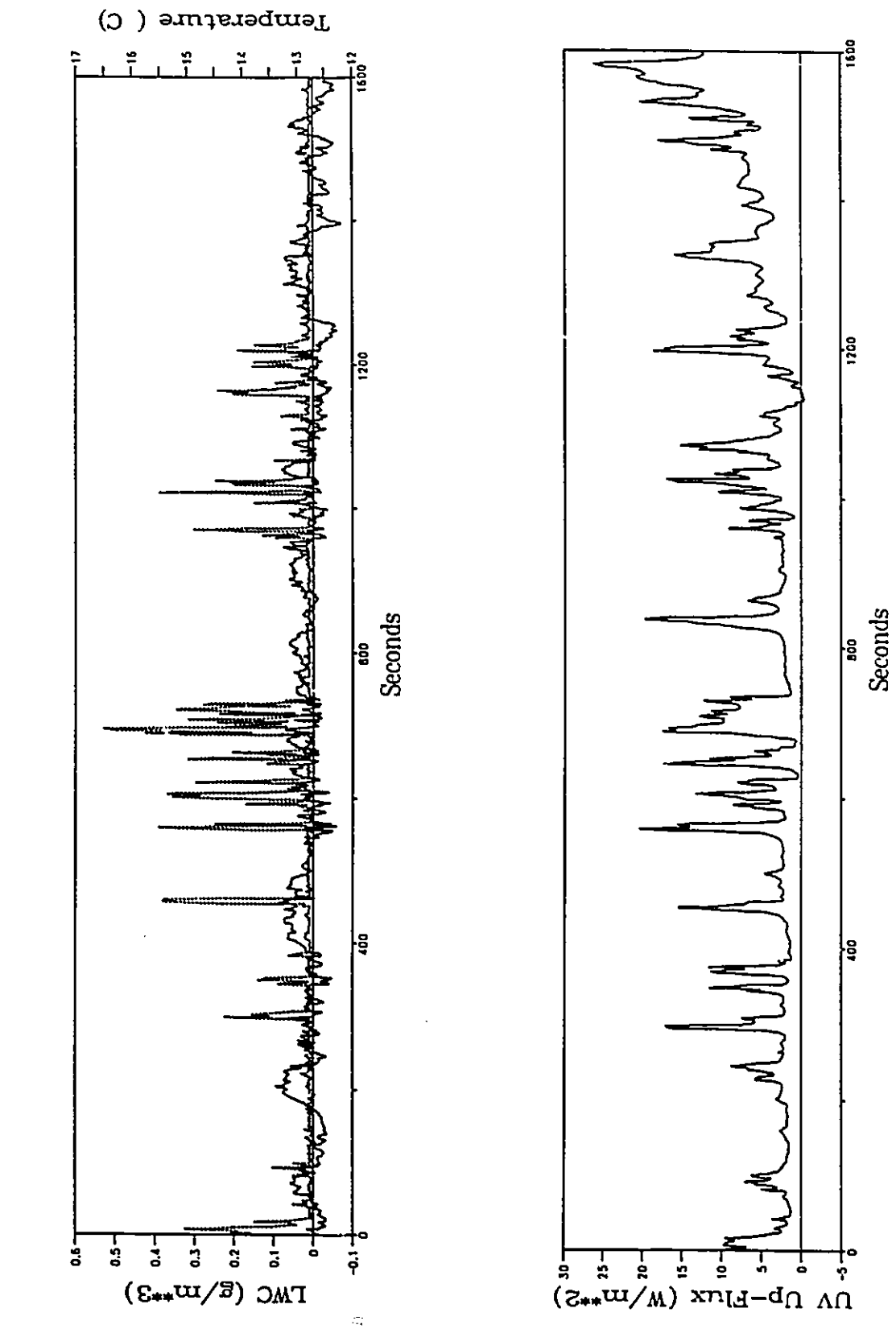

Fig.2.8. (c) As in (a) except for flight 43.

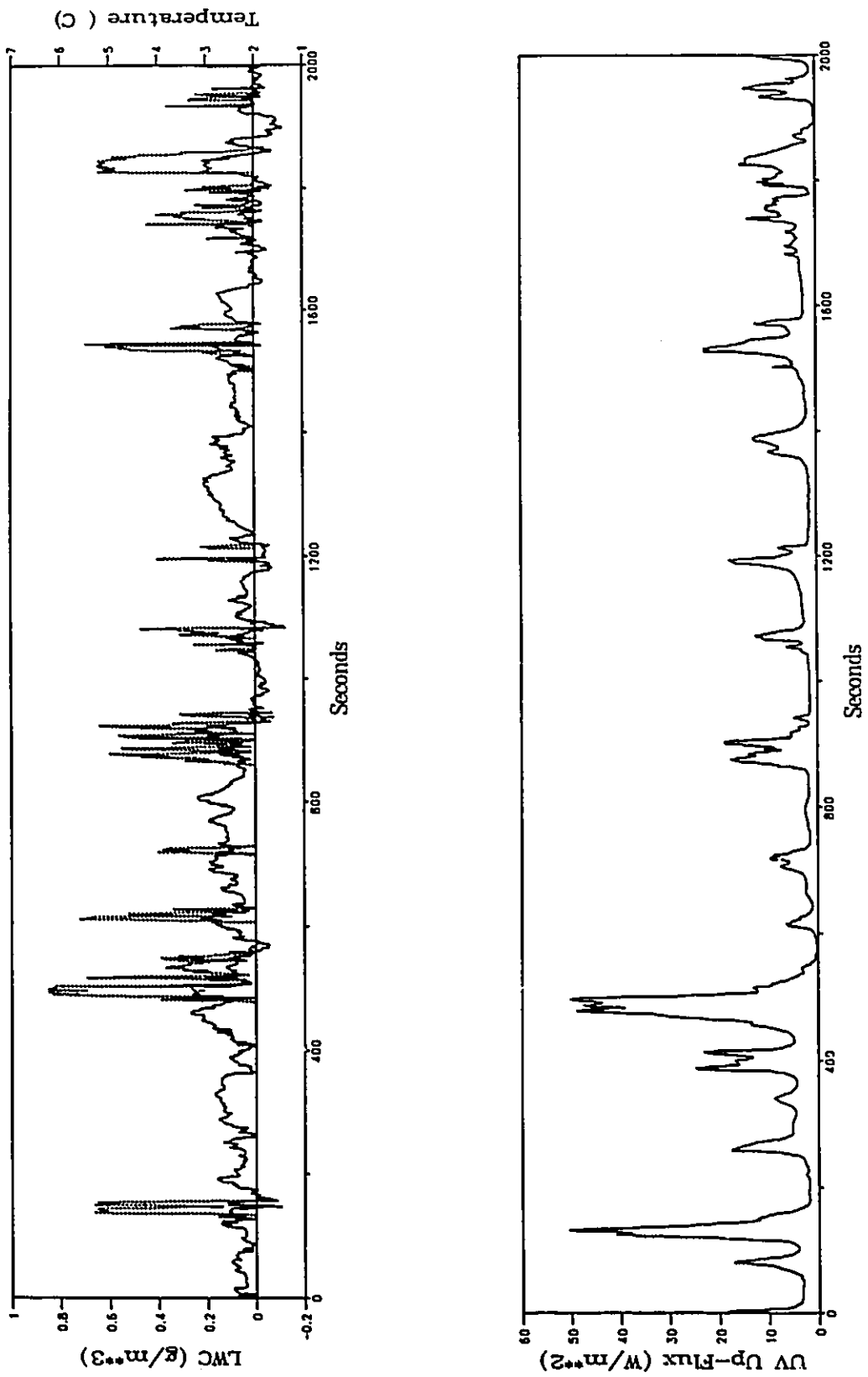

Fig.2.8. (d) As in (a) except for flight 49.

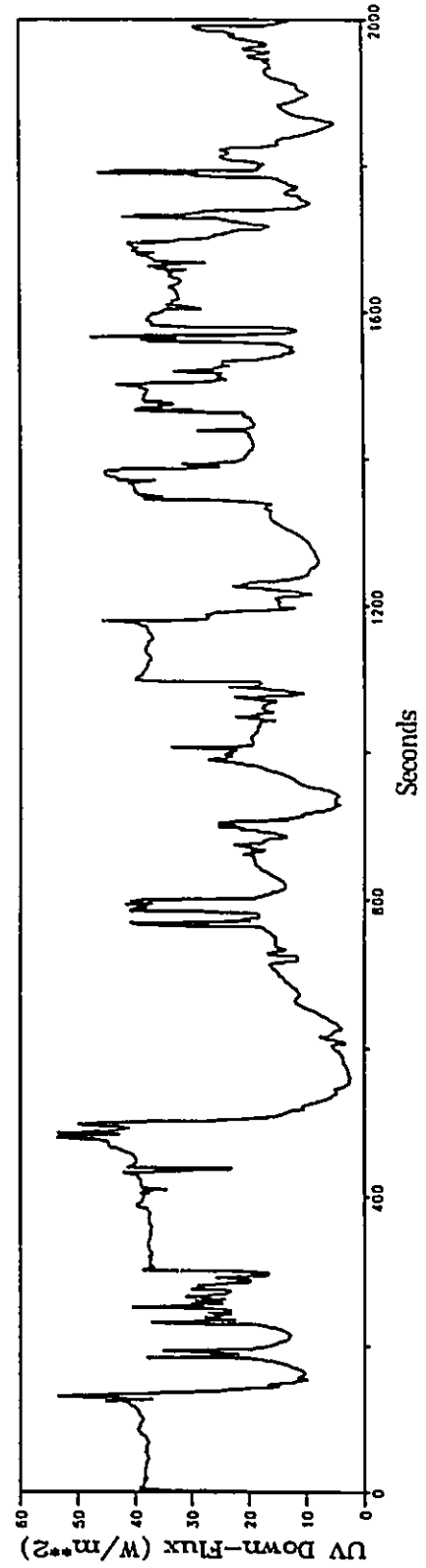

Fig.2.8. (e) Flight 49 time series of downwelling UV radiative flux.

where with few exceptions, LWC = 0 when T > 13.0° C. Note that for flight 49 a well defined T_{crit} value does not exist (~ 2° C was the closest).

Assuming frozen turbulence (Taylor's hypothesis), one should expect that temperature measured at a stationary point on the flight–path would produce a time series very similar to those shown in Fig. 2.8. This is the case with temperature measured at a point slightly above Earth's surface (Oke, 1978). Near the surface in unstable conditions, however, temperature enhancements are associated with rising eddies while reductions are due to descending eddies. Figure 2.8 shows that the reverse can be true at cloud altitudes. Cumulus clouds form when bouyant eddies ascend past the lifting condensation level. Hence, clouds form in updrafts. Therefore, the time series indicate that, at a given level, cool temperatures are associated with updrafts and warm temperatures are associated with space between clouds or holes in clouds which are most likely regions of downdraft given anti–cyclonic synoptic conditions. Similar results have been presented elsewhere. For example, Warner (1969) showed simultaneous time series of LWC and vertical wind speed (Pruppacher and Klett, 1978). His results are qualitatively the same as those inferred above in that they show a strong correlation of the form: updraft ⇒ LWC > 0; downdraft ⇒ LWC = 0.

An explanation for the form of Eq.(2.38) is as follows. Air leaving cloud tops and sides is much drier than it was during it's condensation phase (ascent). Hence, as the air descends outside the clouds, it warms at the dry adiabatic lapse rate. Thus, at a given level, an eddy's temperature upon descent is greater than it was on ascent for then it was cooling along a moist adiabat.

The time series for flight 49 (Fig. 2.8d,e) suggest that the lower atmosphere was very unstable relative to the other flights and characterized in spots by relatively deep convection. The down–welling radiation time series (Fig.2.8e)

shows that high and low fluxes can be be measured within a few seconds of each other. This is due to direct solar beam and scattered radiation from the side of an approaching towering cloud reaching the radiometer just before the radiometer enters the cloud. Also, there are several simultaneous occurrences of large up–welling and down–welling fluxes and LWC = 0. This is due to cloudtops below the flight path. Evidently, the reasoning used in the previous paragraph to explain the temperature series for flights 25, 32, and 43 and the existence of T_{crit} does not apply well in the case of flight 49.

Figure 2.9 shows wavenumber spectra of the temperature time series (curve A) in Figs. 2.8. The temperature spectra for flights 25, 32, and 43 follow very closely the $k^{-5/3}$ law for all k in the first two flights and for $k < 200$ in the last. For scales between about 300 m and 120 m (Nyquist frequency), the temperature spectrum for flight 43 follows k^{-3}. These results are similar to those of Gage and Nastrom (1986) and Nastrom and Gage (1985) who used data from over 6900 commercial aircraft flights to show that the spectral signatures of wind and potential temperature are both very close to $k^{-5/3}$ over scales from ~ 1000 km to 2 km regardless of altitude and geographic location. The temperature spectrum for flight 49 is close to k^{-1} for $k \leq 10$ and $k^{-1.8}$ for smaller scales. This is similar to the k^{-2} spectrum for vertical wind measured by Warner (1969).

Also plotted in Fig. 2.9 are spectra for LWC (curve C) and the following truncated temperature series:

$$\mathcal{T}_n = \begin{cases} T_{crit} \; ; \; T_n \geq T_{crit} \\ T_n \; ; \; T_n < T_{crit} \end{cases} . \tag{2.39}$$

$\mathcal{T}$ is spectrally analyzed because for flights 25, 32, and 43 it is the part of the temperature field associated with non–zero LWC.

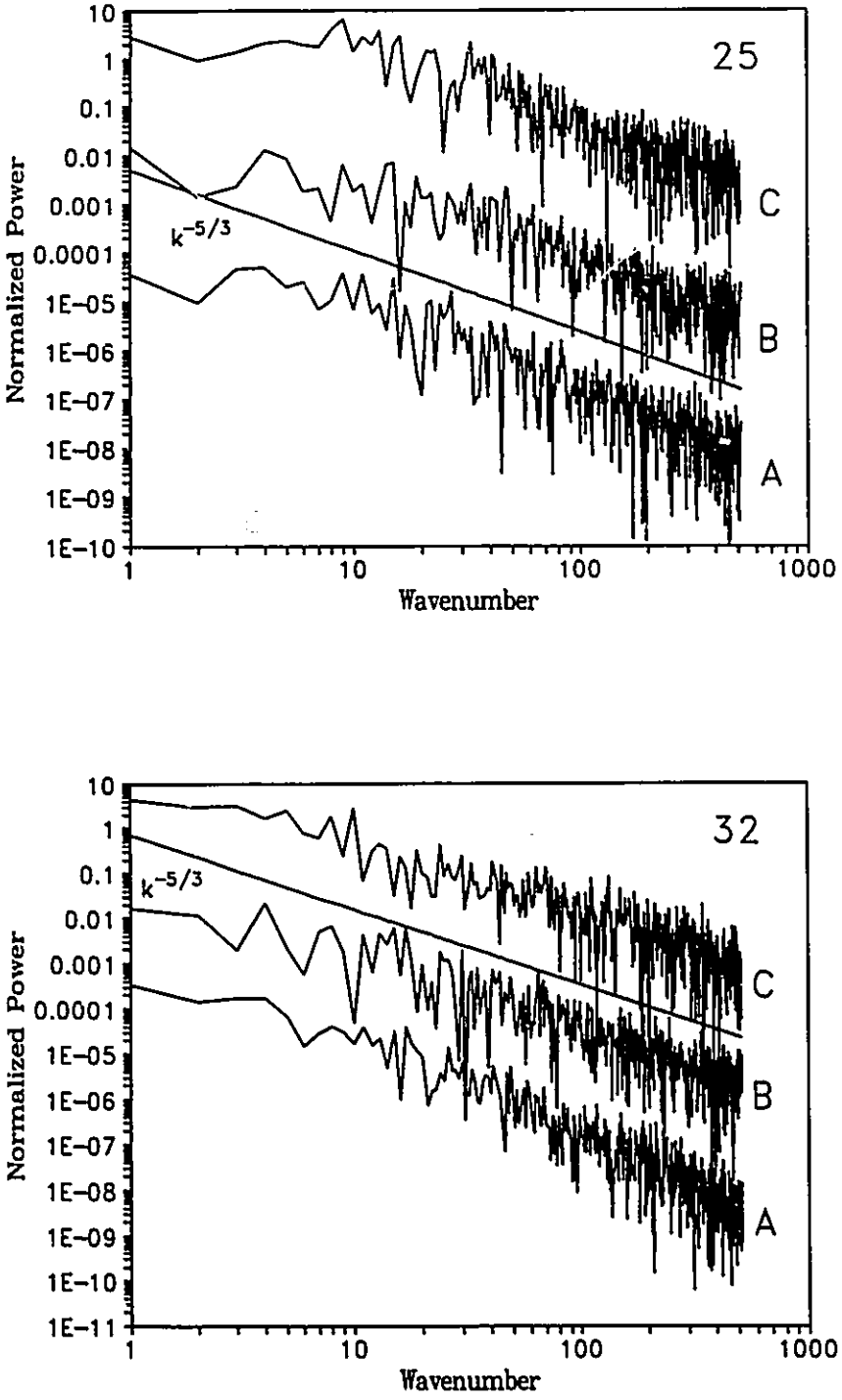

Fig.2.9. One–dimensional power spectra for time series of temperature (A), truncated temperature (B), and liquid water content (C). Spectra (B) and (C) are shifted up one and two decades respectively. Labelled straight lines are best–fit lines. Flight number is indicated in the upper right corner of the plots...

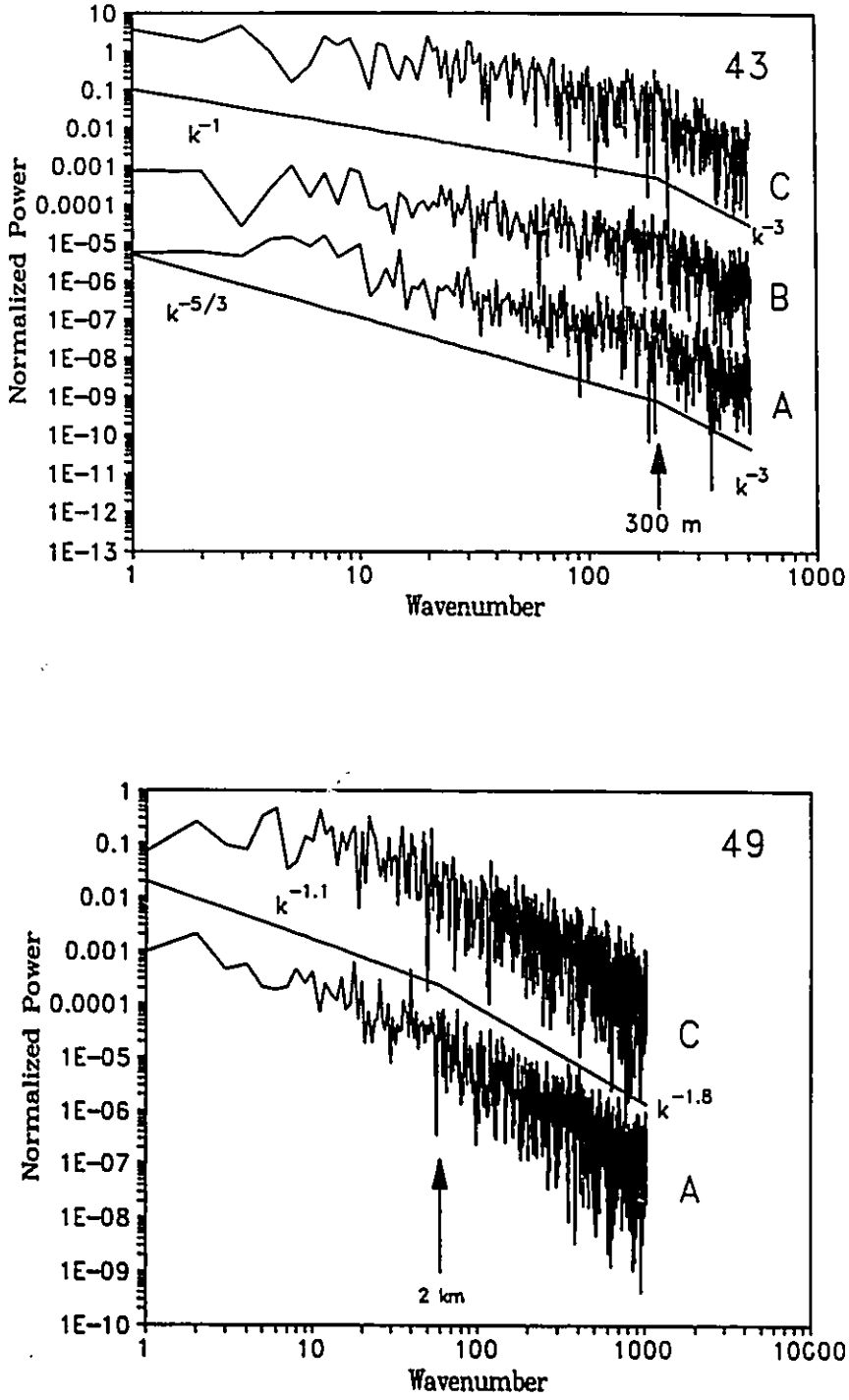

Fig.2.9. continued.

For flights 25, 32 and 49, LWC spectra (and the spectrum of $\mathcal{T}$ for flights 25 and 32) have nearly identical slopes and structure to their respective temperature spectra (save for the low k regime of flight 49 where for LWC $S_k \sim k^0$). In fact, the slope of the LWC spectra for flight 49 is almost identical to that measured by King *et al.* (1982) for scales between 2 m and 45 m. For flight 43, spectra for LWC and $\mathcal{T}$ are similar for scales greater than about 300 m where they closely approximate k^{-1}. For scales less than 300 m, the $\mathcal{T}$ field seems to continue with k^{-1} while the LWC field scales similar to the full temperature field at k^{-3}. Thus, at most scales for flight 43, LWC and $\mathcal{T}$ are less smooth than the full temperature field. This is interesting for it suggests that fields of liquid water (cloud) with distributions that do not abide by standard theories of turbulence may exist in a temperature (wind) field that scales in accordance with classical turbulence theory. This may be what is occurring in the cumulus satellite image of Cahalan and Snider (1989) as well as in scenes A, B, and C; especially scene A. Furthermore, note that breaks in the power spectra of LWC and T are less pronounced (if they exist at all) than breaks in the power spectra of the satellite images. This result, coupled with the fact that spectra of satellite IR and VIS radiances show similar scaling behaviour, supports the hypothesis mentioned earlier regarding the smoothness of the vertical integral of liquid water relative to that of liquid water content.

2.3.2.1 Time Series of Up–welling UV Fluxes

Consider the time series of up–welling UV radiation fluxes (Fig. 2.8). Although it is one–dimensional data, it is the projection of a three–dimensional field. Unlike temperature or LWC, up–welling flux at a point can be influenced strongly by clouds far from the flight–line. Furthermore, a cloud within the field of view of a radiometer influences several sequential measurements uniquely.

Conversely, deep inside a cloud the flux is largely independent of neigbouring clouds and governed primarily by the clouds three–dimensional distribution of liquid water, solar illumination and the position of the aircraft in the cloud. For the cases considered in this study, surface reflection should have minimal influence on the structure of the flux times series. Though the scaling pattern of shadows on the ground cast by clouds may introduce some variance, the surface is quite dark and homogeneous (mixed deciduous/coniferous forest and lakes) and the aircraft is too high for any significant high frequency oscillations to exist. The time series show that up–welling flux from the surface and lower atmosphere is generally between 2 to 4 Wm^{-2} for all flights. To remove as much of the surface signal as possible, all fluxes less than 3 Wm^{-2} were set to this value.

Figure 2.10 shows the power spectra of the four up–welling flux time series. They exhibit some remarkable similarities. For scales greater than about 5 km for flights 25 and 43 and 10 km for flight 49 ($k \lesssim 15$) the spectra are nearly horizontal implying white noise. Then, for about an order of magnitude increase in wavenumber (up to $k \sim 150$), the three spectra exhibit an increasingly precipitous fall which reaches a $k^{-3.5}$ to k^{-4} scaling. Flights 25 and 43 reach $k^{-3.8}$ for scales less than about 600 m while flight 49 reaches $k^{-3.6}$ for scales less than about 1 km. The power spectrum for flight 32 is significantly different. The decrease in slope at scales greater than about 3 km is more gradual and eventually reaches $k^{-2.3}$ for smaller scales.

In their study on holes in clouds, Parker *et al.* (1986) made the point that time series of LWC cannot yield information on the size of clouds or holes in clouds. This is because when LWC goes to zero, one cannot be sure whether a hole in the cloud or a space between two individual clouds has been encountered.

Since the up–welling flux from the surface has been largely removed (set to 3 Wm^{-2}), the flux spectra at large wavenumbers is associated with the interior of

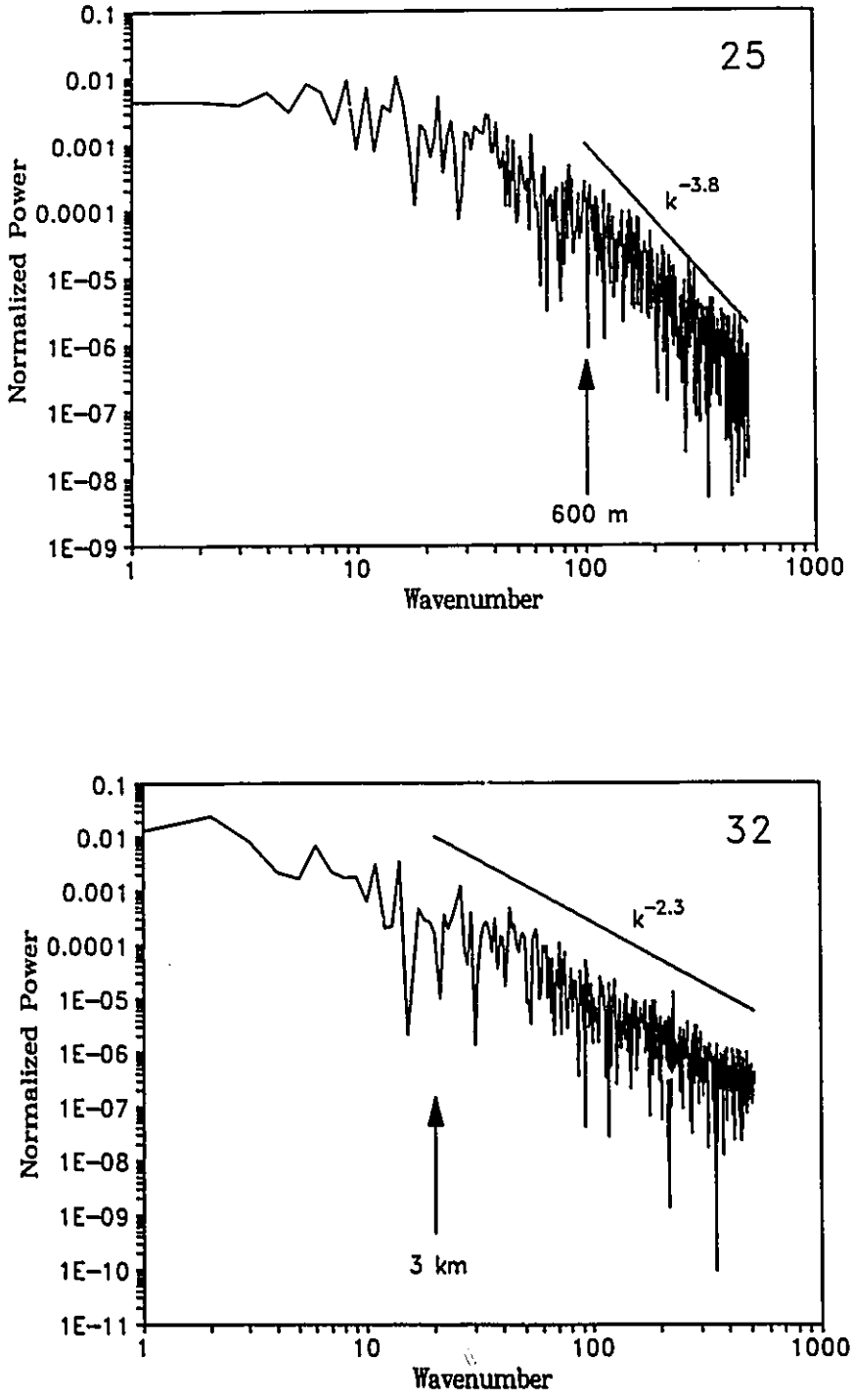

Fig.2.10. One–dimensional power spectra for time series of up welling UV radiative flux. Straight lines that are labelled are best–fit lines. Flight number is indicated in the upper right corner of the plots...

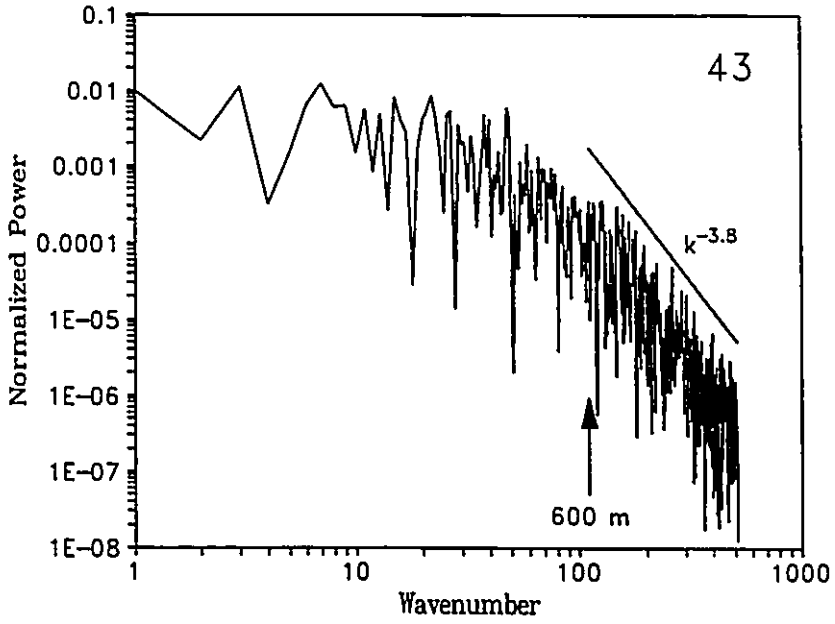

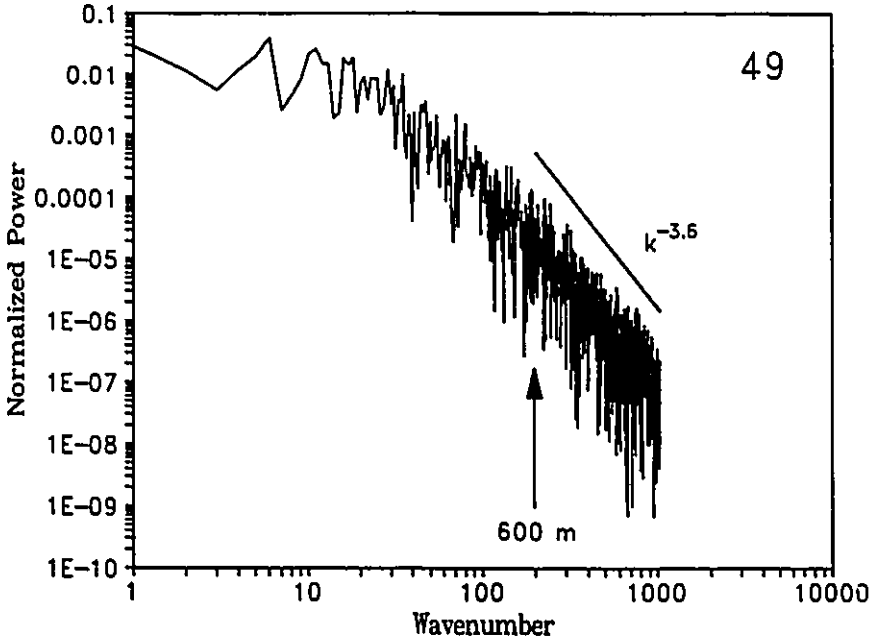

Fig.2.10. Continued.

clouds. Flux inside clouds is expected to be a slowly varying field (the diffusion domain), and consequently, the spectra are steep. In the cases examined here, the steep, constant slope, regime of the up–welling flux spectra starts at about 0.5 to 1.0 km. It is interesting that virtually the same large scaling exponent beginning at the same space scale occurs for both the inter–cloud fluxes examined here and cumulus LANDSAT scene examined by Cahalan and Snider (1989). As mentioned before, the space scale at which the change to the steep spectrum occurred in their case was indeed about typical cloud size. Thus, while time series of LWC cannot yield information on cloud size, perhaps inter–cloud up–welling flux can; particularly if the flight line is near cloudbase.

The similarity between power spectra for up–welling inter–cloud flux and satellite radiances may be coincidental. What is interesting, however, is that this may help to support Wiscombe's hypothesis regarding smoothing of the visible radiation field due to multiple scattering. Obviously, work still needs to be done to clarify the nature of the scaling changes observed in satellite radiance spectra.

Parts of this discussion are speculative since the structure of cloud bi–directional reflectance fields has not been related to cloud–top and inter–cloud flux fields for inhomogeneous cloud fields; all three are profoundly different samplings of the visible radiation field. The consistency of the inter–cloud flux spectral slopes in the small space scale regime, however, may be of value when validating Monte Carlo radiation codes applied to inhomogeneous cloud. This type of model validation is certainly much more accessible then validation using satellite data since far fewer photons are required to get statistically significant fluxes than statistically significant radiances.

2.4 Model Development: Two–Dimensional Scaling Cloud Fields

Data presented in the previous sections have suggested strongly that distributions of cloud liquid water are scaling. Therefore, a phenomonological model is presented which produces cloud fields characterized by continuous power spectra. Attention is restricted to producing cumulus–like cloud fields. This section begins by developing a one–dimensional version of the initial stage of the cloud model. This helps significantly in understanding the cloud model.

2.4.1 One–Dimensional Example

The intention is to produce a sequence of measurements f_n which has a power spectrum like

$$S_k \sim k^{-d} \quad , \tag{2.40}$$

where $d > 0$. This does not mean that S_k is a straight line. Rather, S(k) is quite noisy with k^{-d} as a best–fit line.

The method used in this thesis for producing a stochastic sequence f_n that is scaling, begins by distributing two white noises γ_1 and γ_2 over half the domain in Fourier space (e.g. Schertzer and Lovejoy, 1986); one each for u_k and v_k:

$$\tilde{F}_k = \gamma_1(k) + i\gamma_2(k) \quad , \quad (k = 1,...,N/2) \quad . \tag{2.41}$$

The only restriction on the noises is that they are symmetric about zero. To ensure that the mean of f_n is zero also, set $\tilde{F}_0 = 0$ [see Eq.(2.9)]. At this stage, the power spectrum of $\tilde{F}_k$ follows k^{-0}. Hence, inverse transformation would produce a field with no autocorrelation; white noise.

The next step is to invest the process with autocorrelation. This is achieved by multiplying (filtering) $\tilde{F}_k$ by $k^{-d/2}$ where $-d$ is the desired slope of the power spectrum of f_n when plotted on a log–log graph. Then, the new power spectrum is

$$S_k \sim |F_k|^2 = |\tilde{F}_k\, k^{-d/2}|^2 \sim k^{-d} \quad . \tag{2.42}$$

S_k has a best–fit line of the form k^{-d} because $\tilde{F}_k$ varies about zero with constant variance and is independent of k. Note that filtering the white noises with a negative power function of k suppresses the amplitude of high frequency waves. The final step is to assign values to the other half of the domain in Fourier space as $F_{N-k} = F_k^*$ [Eq.(2.10)], and then substitute F_k into Eq.(2.8) and inverse transform to get f_n. Figure 2.11 shows the result of this process using $d = 5/3$. Therefore, the sequence of f_n in Fig.2.11 is qualitatively similar to time sequences of wind speed, temperature, etc... This example shows clearly that f_n has a high degree of autocorrelation.

2.4.2 Cloud Model Development

The cloud pattern model begins with the above procedure except that it is done in two–dimensions. The ultimate intention is to produce a field of broken clouds with vertically integrated optical depth varying in the horizontal. The first intention, however, is to produce an NxN array of $f_{mn} \in \mathbb{R}$ (m=0,...,N–1 and n=0,...,N–1) which has forward and backward two–dimensional discrete Fourier transforms given by Eq.(2.14).

Basically, the kinds of cloud fields sought after are those for which transects across them ($f_{m=const,n}$ and $f_{m,n=const}$) yield $\langle S_k \rangle$ and $\check{S}_{|\mathbf{k}|}$ of vertically integrated optical depth that follow k^{-d} and $|\mathbf{k}|^{-(d+1)}$. Thus, the process begins by distributing noises in Fourier space. This time, however, the noises, still with

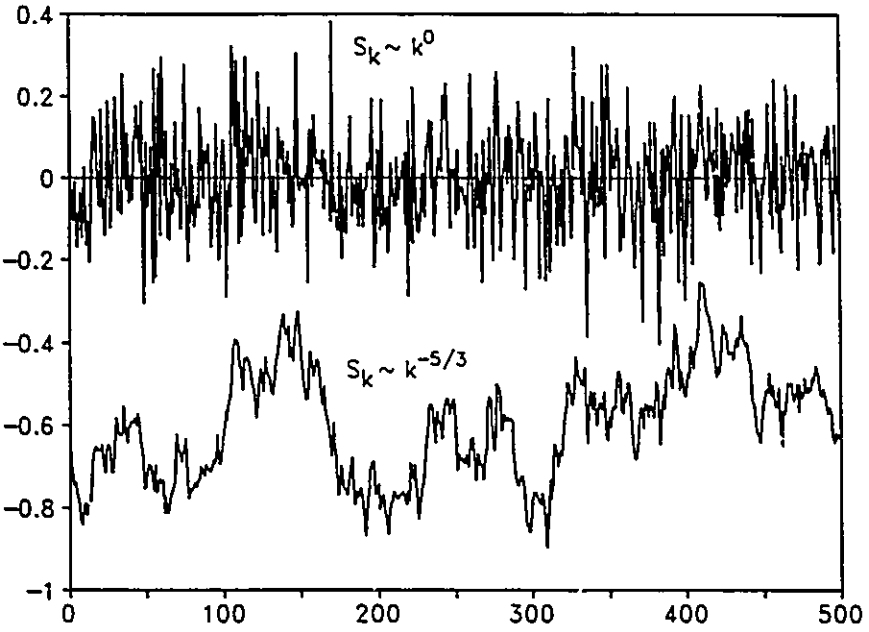

Fig.2.11. Sequences of data points generated by scaling a white noise in Fourier space such that their power spectra go like k^{-0} and k^{-1} [66].

means of zero, are generated in the upper–half of the complex matrix $\tilde{F}_{kl} = \tilde{u}_{kl} + i\tilde{v}_{kl}$ for k = 0,...,N/2 and l = 0,...,N–1. Furthermore, $\tilde{F}_{00} = 0$ ensures that $\langle f_{mn} \rangle = 0$. (The end product appears quite insensitive to the kind of noise used. A Gaussian noise with mean of zero and unit variance is used throughout this study). Then, $\tilde{F}_{kl}$ is scaled (filtered), depending on radial distance from the origin [generalization of Eq.(2.42)], by

$$J_{kl} = \left\{ \left[k^2 + L^2 \right]^{1/2} \right\}^{-\left[\frac{d+1}{2}\right]} , \tag{2.43a}$$

where

$$L = \begin{cases} l \; ; & l \in [0, N/2] \\ N-l \; ; & l \in [N/2+1, N-1] \end{cases} , \tag{2.43b}$$

which gives

$$F_{kl} = J_{kl} \tilde{F}_{kl} \; . \tag{2.43c}$$

Thus, fields produced with this procedure are isotropic and tend to lack dominant frequencies and, therefore, orientation. Note that the term in braces in Eq.(2.43a) is just the modulus of the wave vector $k\hat{i} + l\hat{j}$. In general, more than one scaling can be applied to the white noise matrix. However, if one wishes the power spectrum to be piecewise continuous, care must be taken to ensure that additional scalings are multiplied by the correct constant factors.

The reason why the noises are distributed into the upper–half matrix only is for the same reason as in the one–dimensional case: symmetry laws must be obeyed in order that $f_{mn} \in \mathbb{R}$. Therefore, the following assignments are performed which map the upper–half of F_{kl} into the lower–half and carry out other necessary symmetry relations:

for $k = 1,...,N/2-1$ and $l = 1,...,N/2-1$:

$$F_{0,N/2+l} = F^{*}_{0,N/2-l}$$

$$F_{N/2+k,0} = F^{*}_{N/2-k,0}$$

$$F_{N/2,N/2+l} = F^{*}_{N/2,N/2-l} \tag{2.44}$$

$$F_{N/2+k,N/2} = F^{*}_{N/2-k,N/2}$$

$$F_{N/2+k,N/2\pm l} = F^{*}_{N/2-k,N/2\mp l}$$

Substituting F_{kl} into Eq.(2.14b) and evaluating yields the scaled field f_{mn}.

At this stage, the field f_{mn} may be thought of roughly as a representative of either the vertical wind speed ($f_{mn} > 0 \Rightarrow$ updraft) or temperature averaged through a layer of the atmosphere. Based on the findings within aircraft data presented earlier, truncation of f_{mn} at a critical value f_{crit}, such that if $f_{mn} < f_{crit}$ conditions are not conducive for condensation, or maintenance, of cloud droplets, should produce two–dimensional fields of vertically integrated optical depth that resemble real cloud fields. Hence, f_{crit} can be thought of roughly as a kind of moisture parameter; the drier the air, the larger is f_{crit}.

Thus, the next step is to find the value of f_{crit} such that the vertically projected cloud fraction is

$$A_c = \frac{\sum_{m=0}^{N-1} \sum_{n=0}^{N-1} \phi\left[f_{mn} - f_{crit}\right]}{N^2}, \tag{2.45}$$

where

$$\phi[z] = \begin{cases} 0 \; ; z \leq 0 \\ 1 \; ; z > 0 \end{cases} , \tag{2.46}$$

is the Heavyside step function which in this case behaves as a threshold or cut function. Since by definition the mean of f_{mn} is zero and the white noises making up $\tilde{F}_{kl}$ are distributed equally around the origin in the complex plane, $f_{crit} = 0$ leads to $A_c = 0.5$ on average. Given a particular value of A_c, f_{crit} must be found using Eq.(2.45) iteratively. This is achieved using Brent's root finding method (Press *et al.*, 1986).

Next, having obtained f_{crit}, f_{mn} is transformed into h_{mn} such that all f_{mn} less than f_{crit} are zero and all f_{mn} greater than f_{crit} are proportional to $f_{mn} - f_{crit}$:

$$h_{mn} = (f_{mn} - f_{crit})\phi\left[f_{mn} - f_{crit}\right] . \tag{2.47}$$

Define the mean of h_{mn} when it exceeds zero as

$$\bar{h} = \frac{\sum_{m=0}^{N-1} \sum_{n=0}^{N-1} h_{mn}}{\sum_{m=0}^{N-1} \sum_{n=0}^{N-1} \phi\left[f_{mn} - f_{crit}\right]} = \frac{\sum_{m=0}^{N-1} \sum_{n=0}^{N-1} h_{mn}}{N^2 A_c} . \tag{2.48}$$

By the Wiener–Khintchin theorem [Eq.(2.13)], the fact that h_{mn} can be highly correlated with f_{mn} implies that their power spectra can be similar. The resemblance between the power spectra of f_{mn} and h_{mn}, denoted as $|F_{kl}|^2$ and $|H_{kl}|^2$ respectively, depends, however, on the magnitude of f_{crit} and on the form

of f_{mn}. For example, if f_{crit} is near the maximum of $\{f_{mn}\}$, most $h_{mn} = 0$. Therefore, regardless of the form of f_{mn}, h_{mn} and f_{mn} will often have little in common. The same goes for their power spectra. Likewise, if f_{mn} is dominated by low frequency oscillations [large d in Eq.(2.43)], most values of f_{crit} will cause $|H_{kl}|^2$ to differ significantly from $|F_{kl}|^2$ due to loss of information upon application of Eq.(2.47). If, on the other hand, d is small ($< \sim 1$) which implies that f_{mn} has substantial high frequency oscillations, one might expect $|H_{kl}|^2$ to resemble $|F_{kl}|^2$ for values of f_{crit} significantly greater than the minimum of $\{f_{mn}\}$. As will be shown later, this statement holds for $d \simeq 1$ to the extent that for $A_c \simeq 0.2$ (80% of f_{mn} set to zero), the ensemble average of one–dimensional power spectra of f_{mn} and h_{mn} often have very similar structure and slopes.

a) Cloud Model 1: Horizontally Inhomogeneous, Single Layer

This model produces a horizontally inhomogeneous single layer cloud field. Thus, all clouds in the field have the same vertical geometric extent yet the horizontal density of LWC can vary significantly. Thus, cumulus cloud fields represented by this model are those which form over cool continents and oceans.

Designate the mean extinction coefficient of clouds in the field to be $\bar{\beta}$ (km^{-1}). Like A_c, the value of $\bar{\beta}$ is set. Using Eq.(2.47) and Eq.(2.48), the extinction coefficient of the $(mn)^{th}$ cell is

$$\beta_{mn} = \left[\frac{h_{mn}}{\bar{h}}\right]\bar{\beta} \ . \qquad (2.49)$$

Note that for cells with $f_{mn} \leq f_{crit}$, $\beta_{mn} = 0$ and the cell is cloudless. Otherwise, the cell is assumed to be filled with cloud with extinction coefficient of β_{mn}. Power spectra of β_{mn} and h_{mn} are identical, to within a constant of proportionality.

The vertical optical depth of the $(mn)^{th}$ cell is just β_{mn} multiplied by the vertical geometric thickness of the cloud layer. As such, it is assumed that clouds are vertically homogeneous and of constant vertical extent. Cloud fields generated with this model are referred to as 'variable cloud'.

Frequent use will be made of a cloud field's 'identical cloud' format. In this case, the extinction coefficient of a cell is either zero or $\bar{\beta}$ only. This is achieved by masking β_{mn} [defined in Eq.(2.49)] as

$$\beta_{mn} = \bar{\beta}\,\phi\left[\beta_{mn}\right] \quad . \tag{2.50}$$

Regardless of whether the cloud field is defined by Eq.(2.49) or Eq.(2.50), cloud amount and mass of liquid water in the entire grid are the same. Thus, comparing solar fluxes obtained by the two cases will illustrate some effects of horizontal inhomogeneity of vertically integrated optical depth in irregular cloud fields.

b) Cloud Model 2: Variable Vertical Extent

This model produces three–dimensional fields of clouds which have similar extinction coefficient, identical cloudbase elevation (constant lifting condensation level), but vertical geometric extent varies horizontally. Thus, vertically integrated extinction coefficient (total vertical optical depth) varies horizontally as well. The types of cumulus cloud fields represented by this model are common over warm continents and tropical seas.

As cited previously, vertical velocity is a scaling field over many orders of scale. Thus, this model assumes that cloud vertical extent is scaling also. Therefore, beginning with Eq.(2.47), assume that the cloud field is composed of cubes. This time, however, the mean number of unit cloud cubes in the vertical is $\bar{h}$ and the $(mn)^{th}$ grid cell is discretized such that it is

$$\mathcal{N}_{mn} = \mathrm{INT}(h_{mn} + 1 - \epsilon) \ , \tag{2.51}$$

cells thick where ϵ is a small number and INT( ) indicates rounding down to the nearest integer. Designate the uppermost layer of the cloud field to be k = 1 and the bottom layer to be k = NL where NL is the maximum number of vertical cells in the field (this k is not to be confused with wavenumber). If β is the average extinction coefficient per cube, the cloud field matrix is filled up as follows:

$$\beta_{mnk} = \begin{cases} 0 \quad ; \quad k = 1, \ldots, (NL - \mathcal{N}_{mn}) \\ \dfrac{\beta h_{mn}}{\mathcal{N}_{mn}} \ ; \ k = (NL - \mathcal{N}_{mn} + 1), \ldots, NL \end{cases} . \tag{2.52}$$

Hence, the tallest cloud in the field has vertical optical depth of $NL\beta\ell_z$ where ℓ_z is the geometric length of the side of a cube. Cloud fields produced by this model will be referred to as 'textured cloud'.

If the β_{mnk} field is collapsed down to a single layer with geometric thickness ℓ_z, the cell extinction coefficients are

$$\beta_{mn} = \mathcal{N}_{mn}\beta_{mnk} \ . \tag{2.53}$$

This field is equivalent to that produced with Eq.(2.49). Consequently, an identical cloud field could be produced from Eq.(2.53) by applying Eq.(2.50). As such, all three cloud fields have identical vertically projected cloud fraction and average vertical optical depth.

2.4.3 Properties of the Cloud Models

This section examines some properties of the cloud models. Figures 2.12 to 2.14 are examples of both the variable cloud model [Eq.(2.49)] and the corresponding identical cloud model [(Eq.(2.50)]. Each field consists of 256x256 cells. Though unintentional, the variable cloud images are similar to satellite IR imagery where bright areas (large β) are cold cloud–tops and dark areas (small β) are thin cloud or ocean. However, the images in Figs. 2.12 – 2.14 are just choropleth maps of vertically integrated optical depth.

Comparing the full scaling images to the identical cloud images reveals some interesting properties which are not clear from the variable cloud images alone. First, small clouds tend to have small optical depth. This is consistent with three–dimensional homogeneous turbulence where eddies are close to spherical. Second, large clouds have thin edges with maximal optical depth in their interior. Third, as the magnitude of the scaling exponent increases, clustering or clumping becomes more prevalent. Fourth, holes in the interior of large clouds are not rare.

Figure 2.15 shows the one– and two–dimensional power spectra of the images shown in Figs. 2.12 – 2.14. Figure 2.15a,b shows that for $d = 1.0$ with A_c as low as 0.25, the intended scaling properties are retained well. The image in Fig.2.13 was created with $d = 1.0$ for $|\mathbf{k}| < 70$ and $d = 5.0$ for $|\mathbf{k}| \geq 70$ and $A_c = 0.5$. Comparing Fig.2.12 to Fig.2.13 shows that the rapid attenuation in power of high frequency waves results in smoother edged clouds. The two–dimensional spectra in Fig.2.15c,d shows abrupt breaks in scaling. These breaks in scaling show up well in the corresponding one–dimensional spectra, however, they are slightly smeared relative to that observed in the two–dimensional counterpart. Figures 2.15a,b,c,d show that the truncation in Eq.(2.47) unintentionally 'whitens' the image for large $|\mathbf{k}|$. The image in Fig.2.14 was created with $d = 0$ for $|\mathbf{k}| \leq 10$ and $d = 3$ for $|\mathbf{k}| > 10$, and $A_c = 0.5$. The spectra in Fig.2.15e,f show clearly the

Fig.2.12. (a) False grey image (256x256 pixels) of vertically integrated optical depth. This image was produced by Eq.(2.49) and has $\langle S_k \rangle \sim k^{-1} \; \forall \; k$, $A_c = 0.25$, and average β of 10 km^{-1}. Assuming cloud geometric thickness is 1 km, minimum and maximum optical depths are 0 and 60. Note that this field, and all other fields created with the scaling cloud models, all periodic. (b) Identical cloud version of (a). Black regions signify no cloud and white regions signify optical depth of 10.

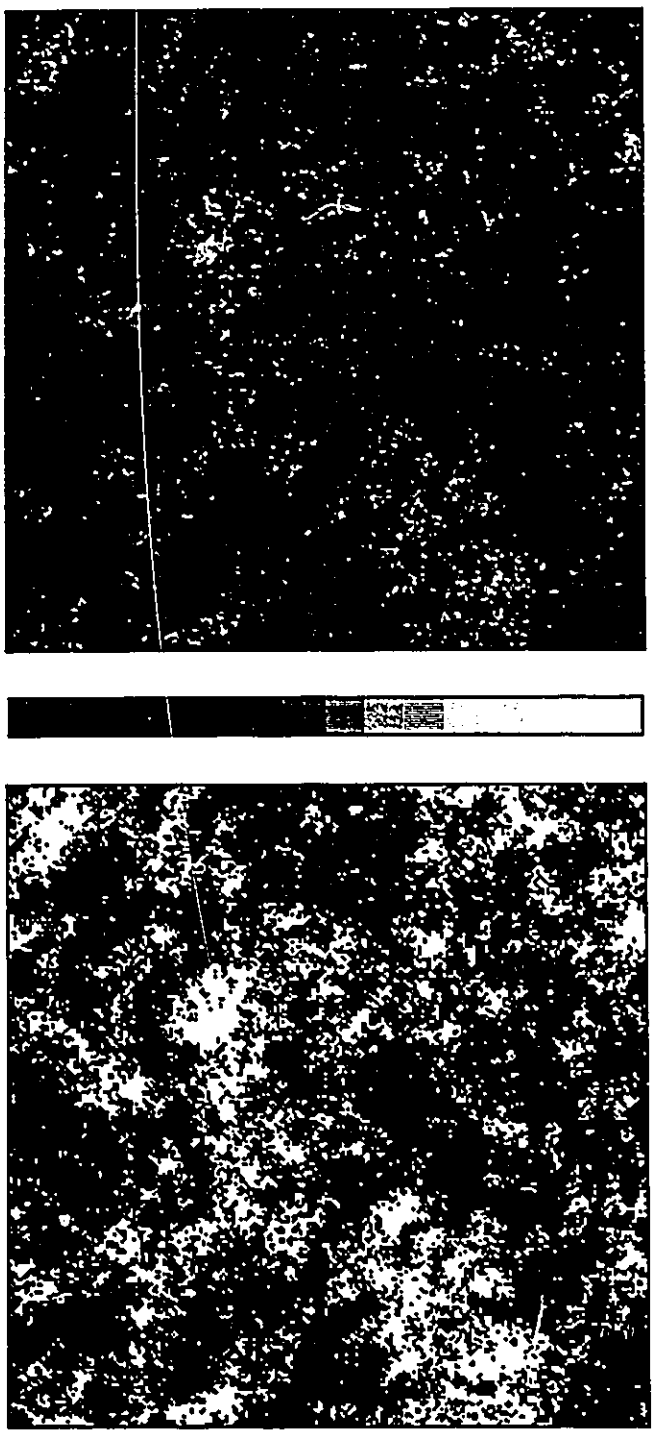

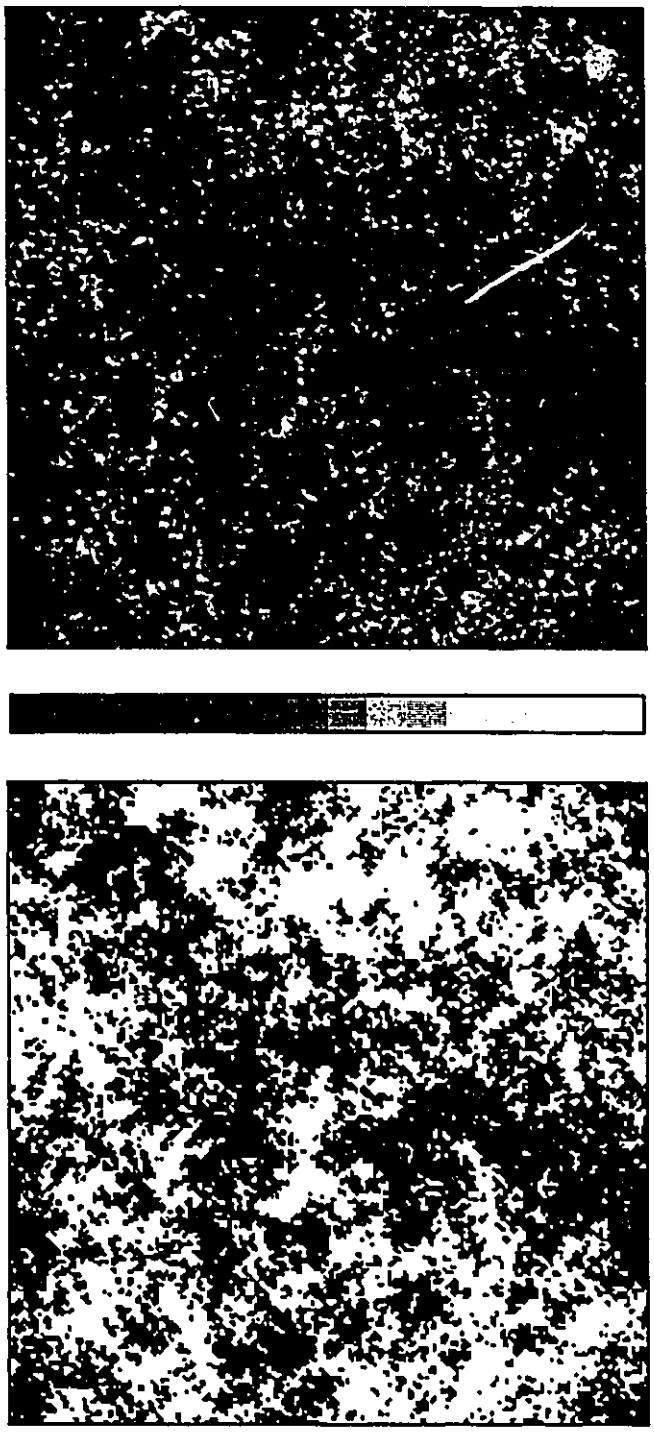

Fig.2.13. (a) As in Fig.2.12a except $\langle S_k \rangle \sim k^{-1}$ for $k < 70$ and k^{-5} for $k \geq 70$, and $A_c = 0.5$. Minimum and Maximum optical depths are 0 and 49. (b) As in Fig.2.12b.

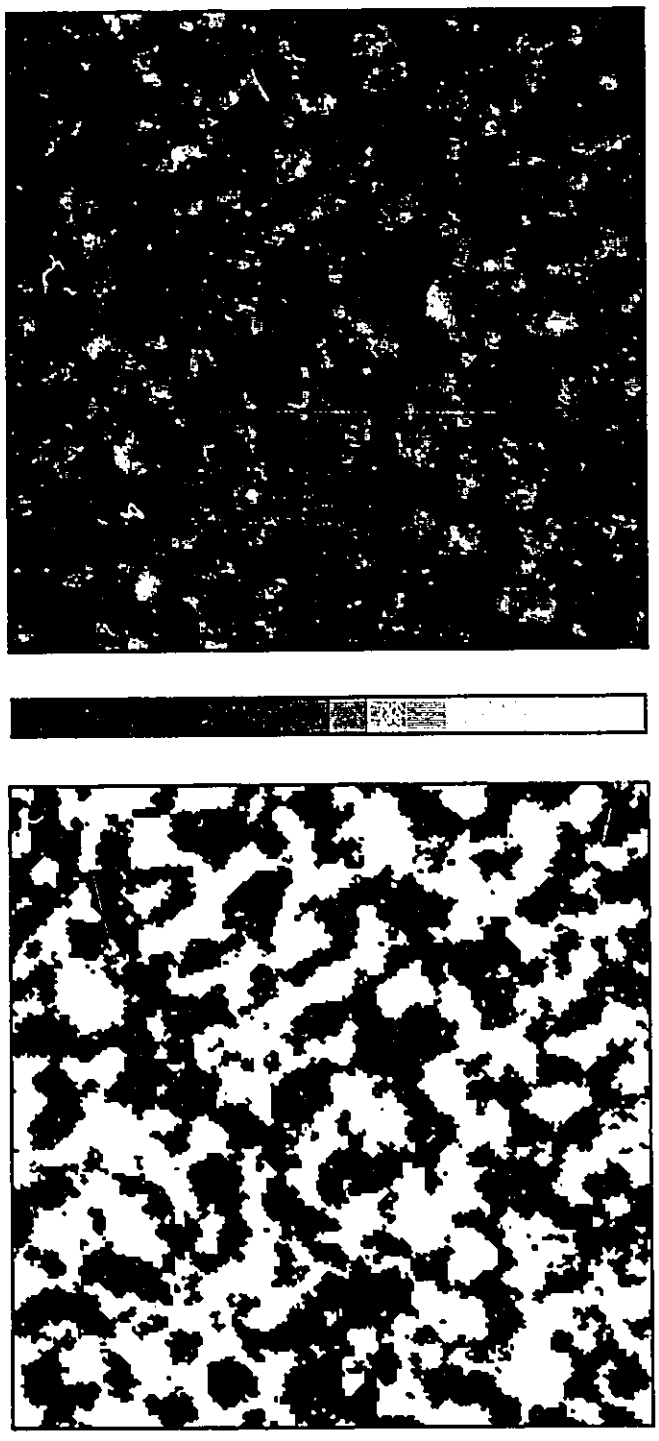

Fig.2.14. (a) As in Fig2.12a except $\langle S_k \rangle \sim k^{-0}$ for $k \leq 10$ and k^{-3} for $k > 10$, and $A_c = 0.5$. Minimum and maximum optical depths are 0 and 53. (b) As in Fig.2.12b.

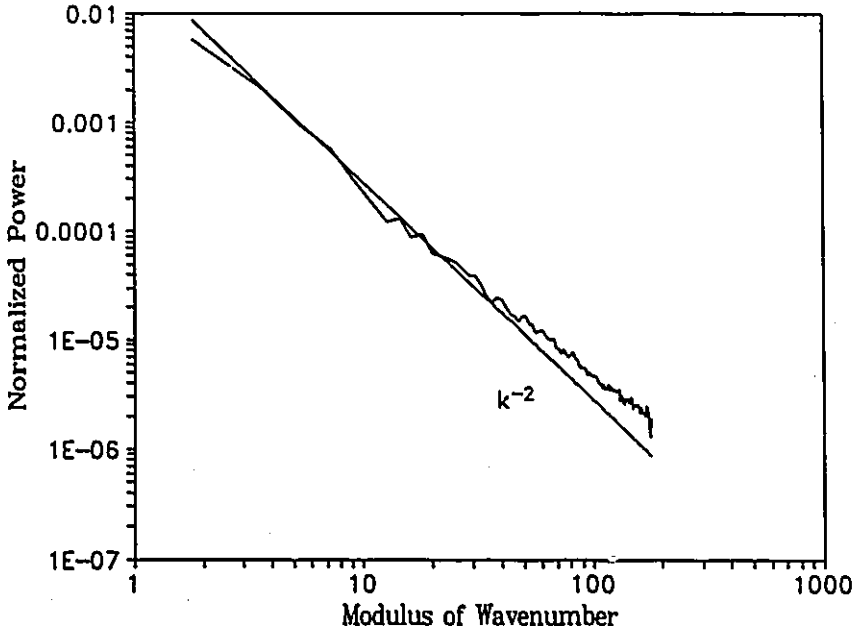

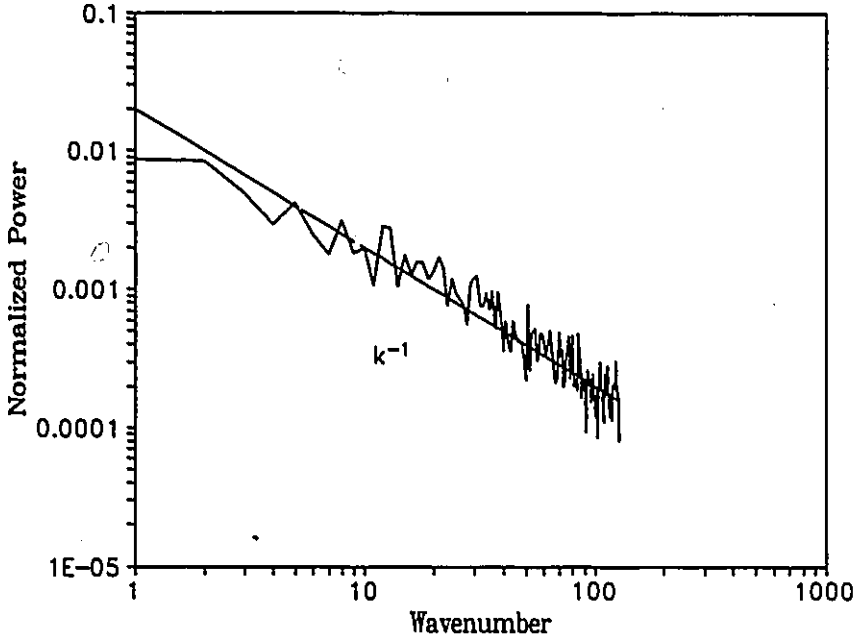

Fig.2.15. (a) Directionally integrated two–dimensional power spectrum for the image in Fig.2.12a. (b) Ensemble averaged one–dimensional power spectrum (10 samples) of the image in Fig.2.12a.

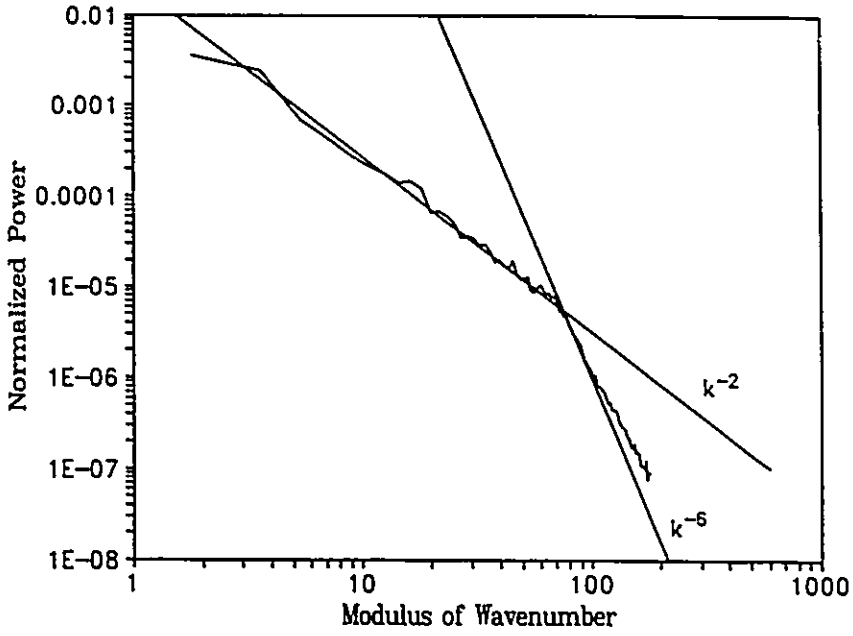

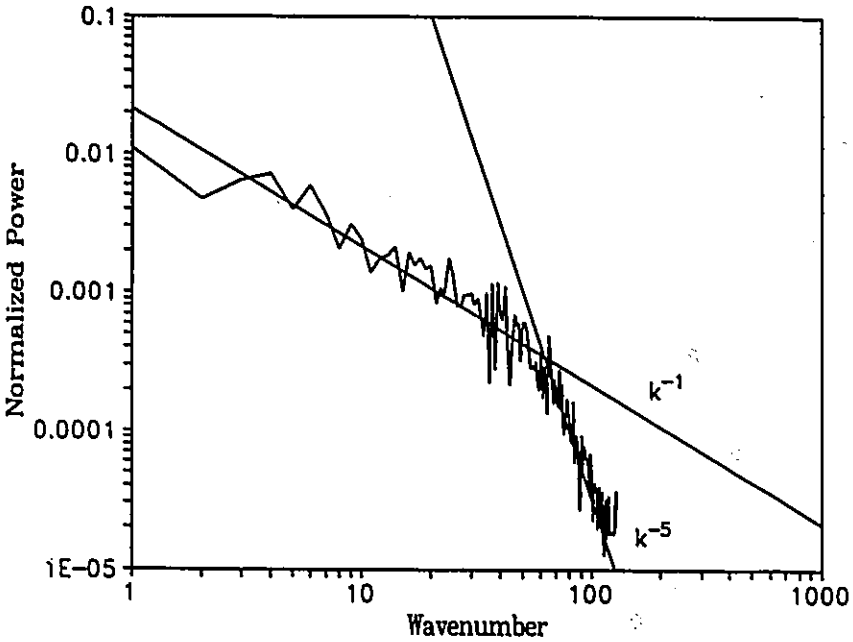

Fig.2.15 (c) As in (a) except for image in Fig.2.13a. (d) As in (b) except for image in Fig.2.13a.

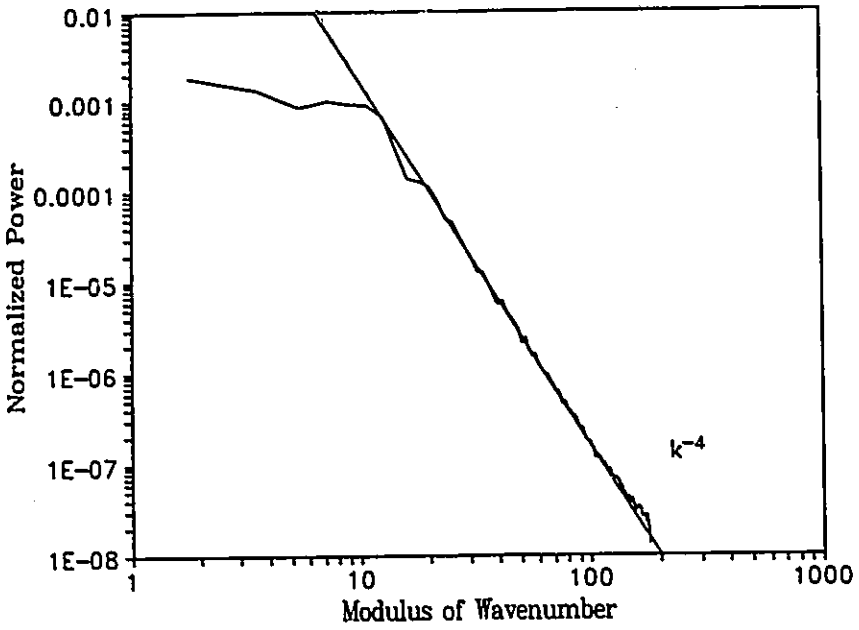

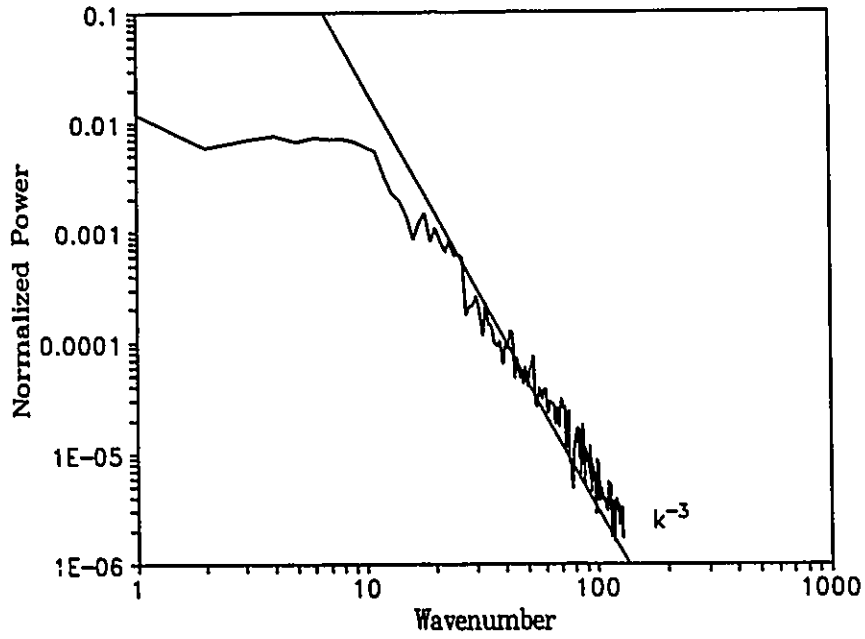

Fig.2.15. (e) As in (a) except for image in Fig.2.14a. (f) As in (b) except for image in Fig.2.14a.

Fig.2.16. Perspective plots of the textured version of the lower left 100x100 pixels of Fig.2.12a. Tallest cloud is five cells high. Viewing zenith angles are (a) 80° and (b) 60°.

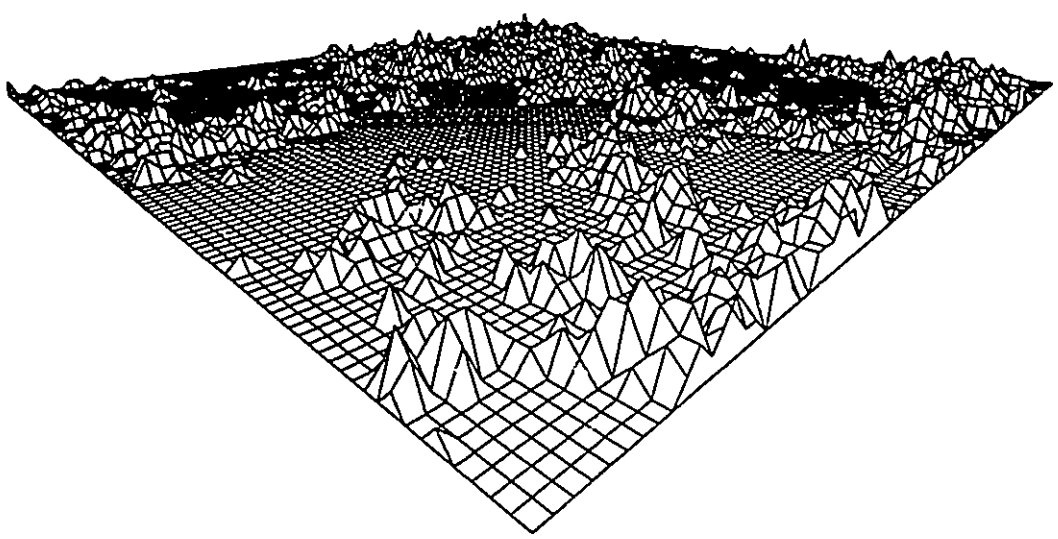

a

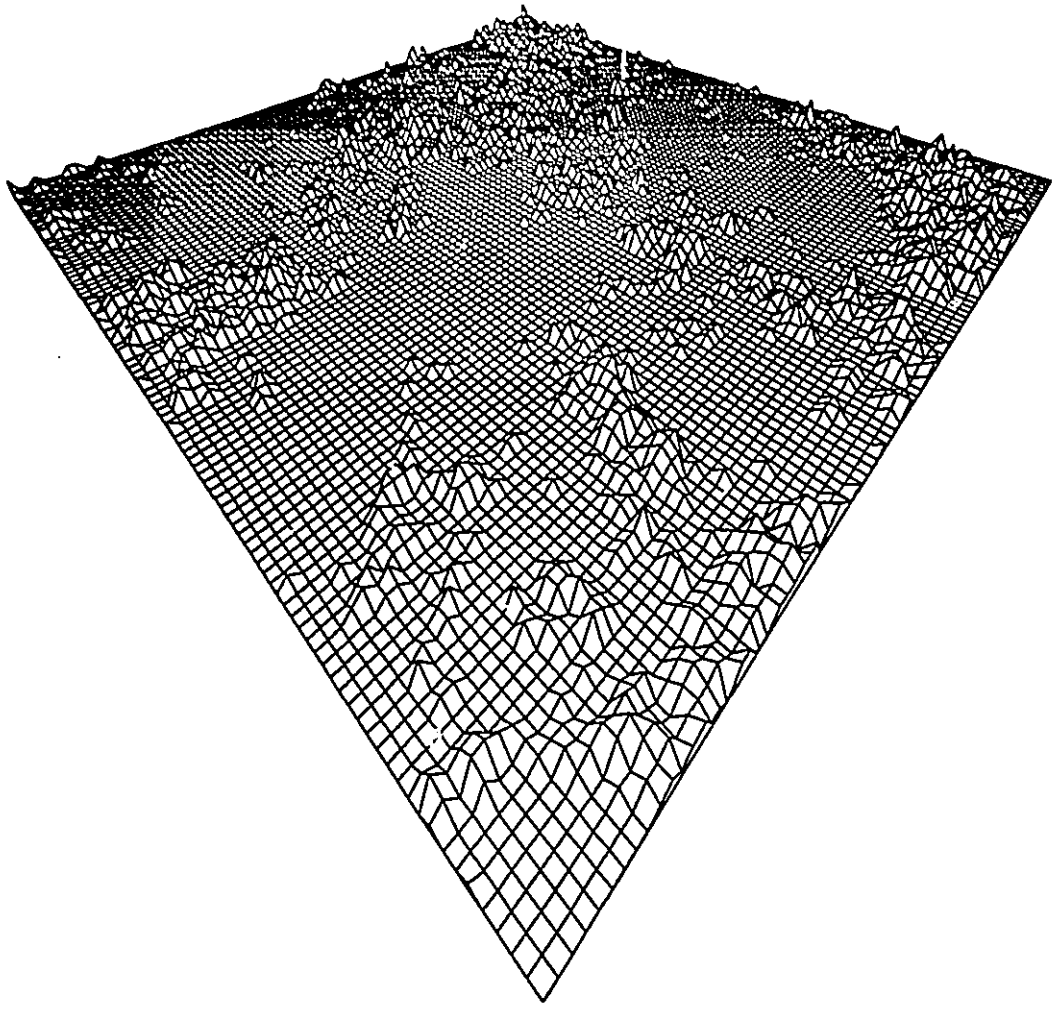

b

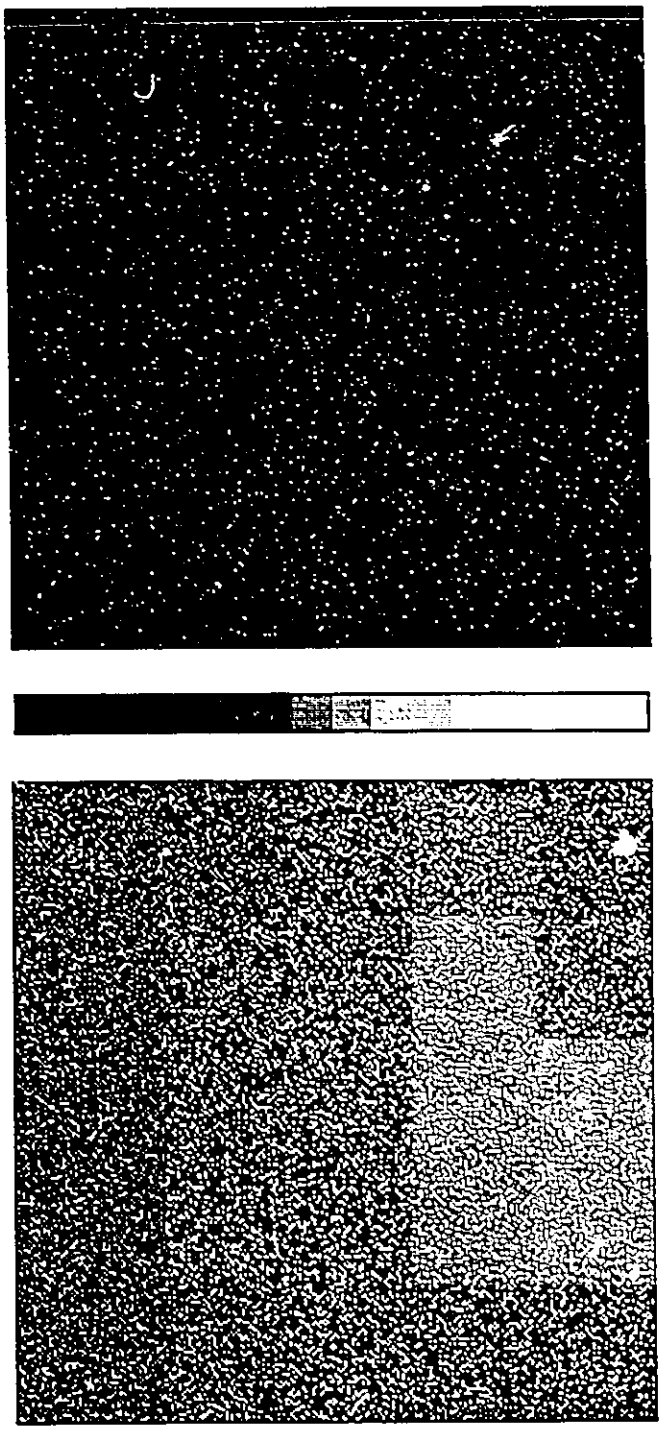

Fig.2.17. (a) As in Fig.2.12a except $\langle S_k \rangle \sim k^{-0}$ ∀ k (white noise). Minimum and maximum optical depths are 0 and 69.5.

break at $|\mathbf{k}|$ and k at 10.

Figure 2.16 shows two perspective plots of the textured cloud model. The field is the lower left quarter of Fig.2.12 (100x100 array). The view in Fig.2.16 is from the lower left corner of Fig.2.12 towards it's center. Maximum cloud thickness is five cells thick. Note that for the larger viewing zenith angle significantly less clear–sky is visible.

Figure 2.17 shows a white noise field of β. The cloud fraction and mass in this field are identical to those in Fig.2.12. The white noise field, however, displays no pattern, coherence, or clumping. Indeed, if real cloud fields resembled this pattern, the spatial coherence method would not work (most points on the scatter–plot would be near the top of the arch). Clearly, application of this cloud field to GCM grid boxes measuring hundreds of kilometers is a serious error. It is conceivable, however, that portions of grid boxes could have white noise arrangements of scattered cumulus. Similarly, one can imagine what a regular array of cloud would look like and if applied to a GCM grid box would also be in serious error.

In summary, this chapter has reviewed Fourier analysis, shown the relation between turbulence, scaling, and fractals, presented empirical evidence that broken cumulus cloud fields exhibit scaling structure, and presented and demonstrated three phenomonological scaling cloud models. In the next two chapters, Monte Carlo photon transport models are developed and validated. In Chapter 5 output from the cloud models will be used as input to the Monte Carlo codes.

CHAPTER 3

Monte Carlo Photon Transport: Model Development

This chapter develops the physical and computational structure of the three–dimensional Monte Carlo atmospheric/underlying reflecting surface radiative transfer model to be used in this study. The model is presented in five sections. First, the fundamental structure is described. Second, the physics and numerical modelling procedures of photon transport through an inhomogeneous atmosphere are discussed. Third, a general theory for implementing realistic underlying reflecting surfaces is developed. Forth, two methods of accounting for absorption of radiation by particles and surfaces are presented. Last, some straightforward extensions of the model, not implemented in this study, are discussed.

3.1 Basic Architecture

In this Monte Carlo simulation study, all photons in a single simulation have the same wavelength λ which is unaltered by collisions with particles. Therefore, only elastic, monochromatic radiative transfer is considered.

The fundamental elements of the model atmosphere are homogeneous cuboids of scattering and absorbing particles. All particles are assumed to be spherical cloud droplets. A cloud or cloud field is made up of many elemental cuboids of geometric size ℓ_x, ℓ_y, and ℓ_z in the x, y, and z Cartesian directions. Each

cuboid is assigned a volume scattering coefficient β_{ijk}, where i, j, and k are cell indices. Note that β_{ijk} may be obtained from the cloud models presented in the previous chapter or directly input such as in the case of regular arrays of clouds. If a single layer of clouds is used, the set of coefficients take the form β_{ij1}. The orthogonal scattering optical depths of a cell are defined as

$$\begin{aligned} \tau_{i'jk} &= \beta_{ijk}\ell_x \\ \tau_{ij'k} &= \beta_{ijk}\ell_y \\ \tau_{ijk'} &= \beta_{ijk}\ell_z \ . \end{aligned} \tag{3.1}$$

Clouds and cloud fields consist of cuboids which act as homogeneous cloud blocks ($\beta_{ijk} \neq 0$) or empty blocks ($\beta_{ijk} = 0$).

Figure 3.1 shows the right–handed Cartesian co–ordinate system to be used as well as a rectangular region $\mathcal{R}$ having N_x, N_y, and N_z cuboids in the $\hat{i}$, $\hat{j}$, and $\hat{k}$ directions. The model may interpret $\mathcal{R}$ either as an isolated region of the atmosphere or as the 'generator' of a horizontally infinite array of connected (periodic) regions $\mathcal{R}$. The first case is referred to as *open boundary conditions* while the second case is referred to as *cyclic boundary conditions.* These cases are considered in turn.

3.1.1. Open Boundary Conditions

Open boundary conditions are used to obtain information about the radiative characteristics of an individual cloud or isolated group of clouds. Because the region is isolated, it must be uniformly irradiated by photons on the top face and at least one of the side faces when the solar zenith angle $\theta_\bullet > 0°$. Figure 3.1 shows the photon injection plane. The ratio of the areas of sub–surface 1 and 2 on the injection plane defines the fraction of photons to be injected into the top and

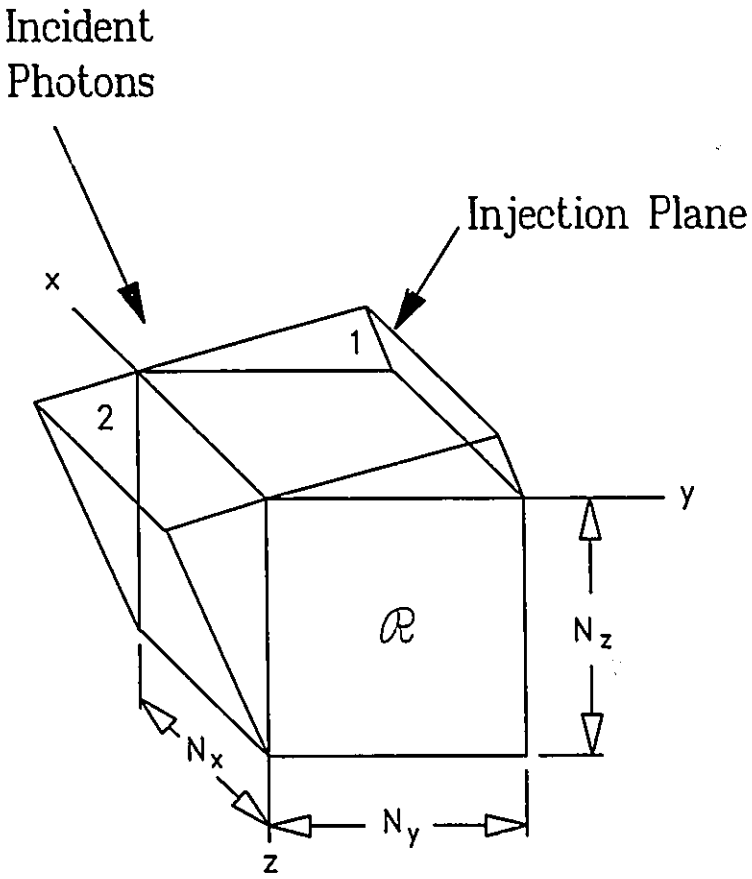

Fig.3.1. $\mathcal{R}$ is an isolated region of atmosphere (open boundary conditions) with N_x, N_y, and N_z elementary cells in the x (i), y (j), and z (k) directions. θ_0 is solar zenith angle. Incident photons are uniformly distributed over the Injection Plane.

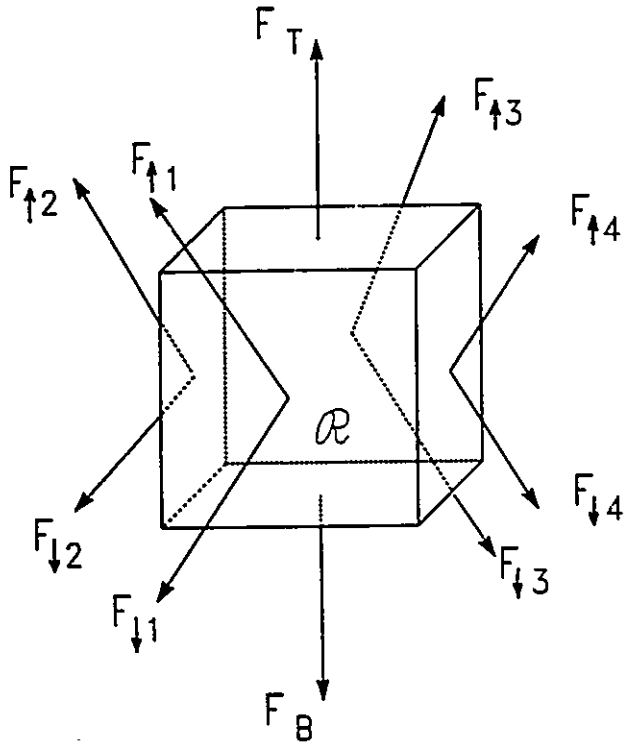

Fig.3.2. Ten bins into which photons exiting $\mathcal{R}$ (open boundary conditions) are accumulated for flux calculations.

side of $\mathcal{R}$. Therefore, if N photons are injected, the number of photons injected into the top face is

$$N_{top} = INT\left[\frac{N}{1 + \frac{\ell_z N_z}{\ell_y N_y} \tan\theta_o}\right] , \tag{3.2}$$

where INT indicates rounding down to the nearest integer. The remaining $N-N_{top}$ photons are then injected into the side of $\mathcal{R}$. The co–ordinates of the photon entry points on $\mathcal{R}$ are given by position vectors

$$\mathbf{x}_o = (x_o, y_o, z_o)^t = \begin{cases} (RN \cdot \ell_x N_x,\ RN \cdot \ell_y N_y,\ 0)^t \ ; & N_{top} \text{ times} \\ (RN \cdot \ell_x N_x,\ 0\ ,\ RN \cdot \ell_z N_z)^t \ ; & N - N_{top} \text{ times} \end{cases} \tag{3.3}$$

where RN are pseudo–random generated numbers uniformly distributed on (0, 1) and 't' denotes transpose. The random number generator used throughout much of this study is the RND() intrinsic function in Lahey's 32–bit extended memory FORTRAN compiler.

The underlying surface in open boundary conditions is assumed to be black. Therefore, after a photon exits $\mathcal{R}$, it cannot re–enter. A photon's point of exit and the zenith angle of it's trajectory determine which flux bin it goes into. Figure 3.2 shows the bins associated with open boundary conditions. The fractions of the total incident flux leaving $\mathcal{R}$ in the upward direction (reflectance) and downward direction (transmittance) are calculated from

$$F_{\uparrow} = F_T + \sum_{i=1}^{4} F_{\uparrow,i} \ , \tag{3.4}$$

and

$$F_{\downarrow} = F_B + \sum_{i=1}^{4} F_{\downarrow,i} \ , \tag{3.5}$$

where the components on the RHS of Eq.(3.4) and (3.5) are identified in Fig.3.2.

3.1.2. Cyclic Boundary Conditions

Cyclic boundary conditions are used to obtain radiative characteristics of extensive cloud fields. Unlike open boundary conditions, an underlying reflecting surface is included. Cyclic cloud fields are simulated by allowing the region $\mathcal{R}$ (Fig.3.1) to be repeated infinitely many times in all four horizontal directions. The resulting region is denoted as $\mathcal{R}^{\infty}$. Because $\mathcal{R}^{\infty}$ lacks sides, photons can enter the experiment through the top face of $\mathcal{R}$ and exit through the upper and lower faces of $\mathcal{R}$. Thus, in cyclic conditions, photon entry points $\mathbf{x}_0$ into $\mathcal{R}$ are described by the top row of Eq.(3.3) with $N_{top} = N$.

Cyclic boundary conditions are simple to model. To begin, assume that $\mathcal{R}$ in Fig.3.1 is a generator for a cyclic cloud field $\mathcal{R}^{\infty}$. If a photon trajectory contains a point which is in the set

$$\mathcal{P} = \left\{ (X,y,z)^t, (x,Y,z)^t \;\middle|\; \begin{array}{c} X=0,\ell_x N_x;\ Y=0,\ell_y N_y \\ x\in(0,\ell_x N_x)\ ;\ y\in(0,\ell_y N_y);\ \ z\in(0,\ell_z N_z) \end{array} \right\} \subset \mathcal{R}, \tag{3.6}$$

which makes up the sides of $\mathcal{R}$, the photon is transferred into an adjacent cell which takes it outside $\mathcal{R}$ but still within $\mathcal{R}^{\infty}$. When this occurs, the capitalized co–ordinate of the point in $\mathcal{P}$ is changed to its other value. All else in the

experiment remains the same. This mirror reflection process is illustrated in Fig.3.3. It is important to realize that in both cyclic and open boundary conditions, photons may enter and exit the sides, top, and base of a cloud if the cloud is a subset of $\mathcal{R}$.

3.2 Photon Transport: Scattering and Tracking

In this section, theoretical and modelling aspects of photon transport are presented. This includes: initial photon injection, determination of free pathlength between scattering events, photon tracking, and scattering geometry. For simplicity, in this section, droplets are assumed to be non–absorbing. Unless specified, the material presented here applies to both open and cyclic boundary conditions.

We begin with some definitions. The 'number' of a cell containing a photon can be defined by the position of the photon. If a photon is at any point $\mathbf{x} = (x,y,z)^t \in \mathcal{R}$ (and $\mathcal{R}^\infty$), it is in cell number

$$(i,j,k) = \left[\mathrm{INT}(x/\ell_x + 1), \mathrm{INT}(y/\ell_y + 1), \mathrm{INT}(z/\ell_z + 1)\right]. \tag{3.7}$$

Define the angle between any photon trajectory and the x–, y–, and z–axes as θ_x, θ_y, and θ_z. The cosine of these angles are denoted as μ_x, μ_y, and μ_z respectively. These are direction cosines of the photon's trajectory and have the property

$$\mu_x^2 + \mu_y^2 + \mu_z^2 = 1 \ . \tag{3.8}$$

A useful way of interpreting direction cosines is to consider them as the $\hat{\mathbf{i}}$, $\hat{\mathbf{j}}$, and $\hat{\mathbf{k}}$

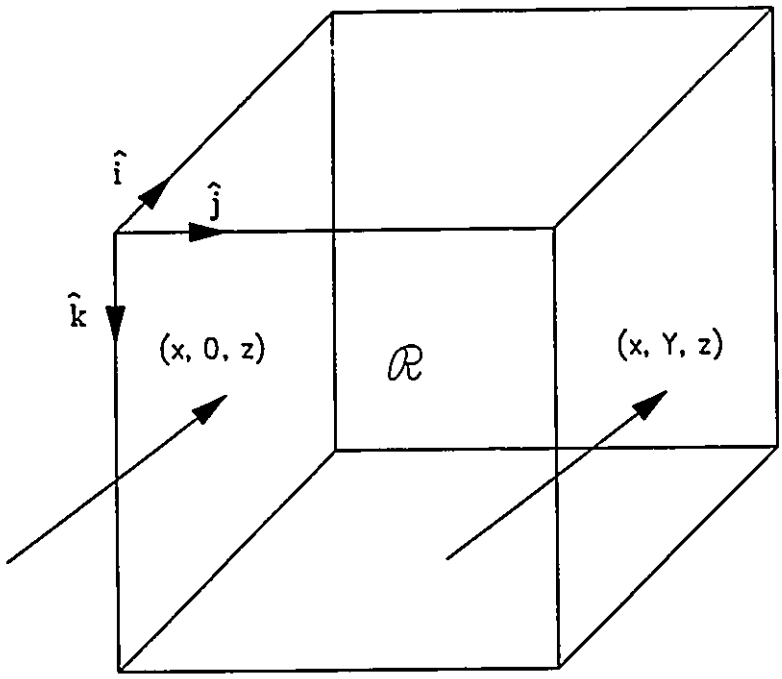

Fig.3.3. Schematic diagram showing the trajectory vector of a photon when cyclic boundary conditions are used. Photon exits $\mathcal{R}$ through the y = Y plane at $(x,Y,z)^t$ and is reinjected into $\mathcal{R}$ through the y = 0 plane at $(x,0,z)^t$. Note that the photon's direction cosines do not change.

co–ordinates of photon trajectory vectors (see Fig.3.4). The convention in this thesis maintains that downward directed photons have $\mu_z > 0$ and upward directed photons have $\mu_z < 0$. By the definitions set forth in the last section, initial photon trajectory vectors are of the form

$$\mu_o = \sin\theta_o\cos\varphi_o\hat{i} + \sin\theta_o\sin\varphi_o\hat{j} + \cos\theta_o\hat{k} \ , \tag{3.9}$$

where φ_o is the solar azimuth angle measured clockwise form the x–axis while looking down from the zenith.

Once the entry point $\mathbf{x}_o \in \mathcal{R}$ is defined, the photon travels into the cloud a distance f_p before being scattered by a cloud droplet. This distance is a stochastic function of the volume scattering coefficient associated with the cell containing $\mathbf{x}_o$ and is determined exactly as free–pathlengths between scattering events are determined. Since the latter procedure is more general, it is presented in detail while recognizing that the initial entry, or pre–scattering, distance is a special case in which the entry point $\mathbf{x}_o$ may be considered as the first scattering event.

The essence of determining photon free–pathlengths between scattering events rests on the assumption that cloud droplets in any cuboid are distributed at random. Hence, the probability that a photon will traverse an optical length τ greater than τ' before encountering a droplet is exactly the same as the probability that a photon will travel an optical distance τ' (Beer's law):

$$\Pr[\, \tau > \tau' \,] = e^{-\tau'} \ , \tag{3.10}$$

where

$$\tau' = \beta_{ijk} f_p \ , \tag{3.11}$$

and f_p is the corresponding geometric length. It can be shown using Eq.(3.10) that

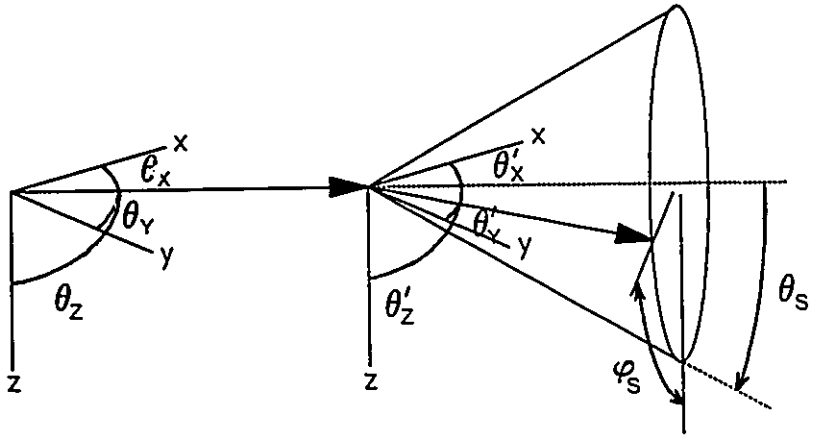

Fig.3.4. Photon trajectory and scattering geometry. Lines with large arrowheads indicate photon path. Initial photon direction angles are θ_x, θ_y, and θ_z. Scattering deflection angle is θ_s and scattering azimuth angle is φ_s. New direction angles are θ'_x, θ'_y, and θ'_z.

the mean of f_p in cell number (i,j,k) (photon mean free–pathlength) is β_{ijk}^{-1}. For example, the photon mean free–path in a typical fairweather cumulus cloud is thought to be about 20 m (Welch *et al*, 1980). Assume that a photon in cell number (i,j,k) is scattered at $\mathbf{x} = (x,y,z)^t$ into direction $\mu = (\mu_x,\mu_y,\mu_z)^t$. Choosing a random number RNϵ(0,1) to represent Pr[$\tau > \tau'$] in Eq.(3.10), and solve for f_p as

$$f_p = -\frac{\log(RN)}{\beta_{i\,j\,k}} \ , \tag{3.12}$$

the tentative point at which the next scattering event takes place is given by

$$\mathbf{x}_{tent} = \mathbf{x} + f_p\mu \ . \tag{3.13}$$

To avoid division by zero in Eq.(3.12), empty cells have β_{ijk} set to an arbitrarily small value of 0.00001 km^{-1}. If the number of the cell containing $\mathbf{x}_{tent}$ is (i,j,k), the next scattering event will be at $\mathbf{x}_{tent}$. In general, however, the trajectory from $\mathbf{x}$ to $\mathbf{x}_{tent}$ will take the photon through N cells, each having a unique scattering coefficient. In this case, Eq.(3.10) becomes

$$RN = e^{-\tau'} = \exp\left[-\sum_{n=1}^{N} f_n\left[\beta_{ijk}\right]_n \right] \ , \tag{3.14}$$

where f_n and $\left[\beta_{ijk}\right]_n$ are the geometric pathlength through and the associated scattering coefficient of the n^{th} cell traversed by the photon. Note that we are accumulating scattering coefficient–weighted pathlength until the random generated transmittance r is attained. When stepping through Eq.(3.14), two

possibilities exist: either the photon exits $\mathcal{R}$ or $\mathcal{R}^m$ before RN is accumulated, or RN is achieved in the N^{th} cell and the next scattering event occurs. Directly solving for N in Eq.(3.14) within the code would be especially difficult. Therefore, pathlength is accumulated by iteratively moving and checking each photon's position.

If it is established that the photon scattered at $\mathbf{x}$ is to move outside the cell containing $\mathbf{x}$, the photon is moved in direction μ to an infinitesimal distance past the exit point of cell (i,j,k). This is achieved by recognizing that the distance to the edge of the cuboid and the plane containing the exit point is the minimum distance to three planes, which form half the cuboid's boundary, that the photons trajectory line passes through. The three planes of concern are dictated by the signs of the components of μ. For example, if the $\hat{\mathbf{i}}$ component of μ is positive, the photon will not intersect the yz–plane defined by $x = \ell_x(i - 1)$. Rather, it will intersect the yz–plane defined by $x = \ell_x(i)$. The opposite holds if $\mu_x < 0$. If $\mu_x = 0$, the photon is travelling parallel to all yz–planes. Likewise for the other co–ordinates. Figure 3.5 illustrates this three–plane trajectory intersection theorem. Therefore, the equations of the planes that are of interest upon exiting a cell are

$$\begin{aligned} x_p &= \mathrm{INT}(x/\ell_x + 1) + \hat{\phi}(\mu_x) \\ y_p &= \mathrm{INT}(y/\ell_y + 1) + \hat{\phi}(\mu_y) \\ z_p &= \mathrm{INT}(z/\ell_z + 1) + \hat{\phi}(\mu_z) \end{aligned} \tag{3.15}$$

where

$$\hat{\phi}(x) = \begin{cases} 0 : x > 0 \\ M : x = 0 \\ -1 : x < 0 \end{cases},$$

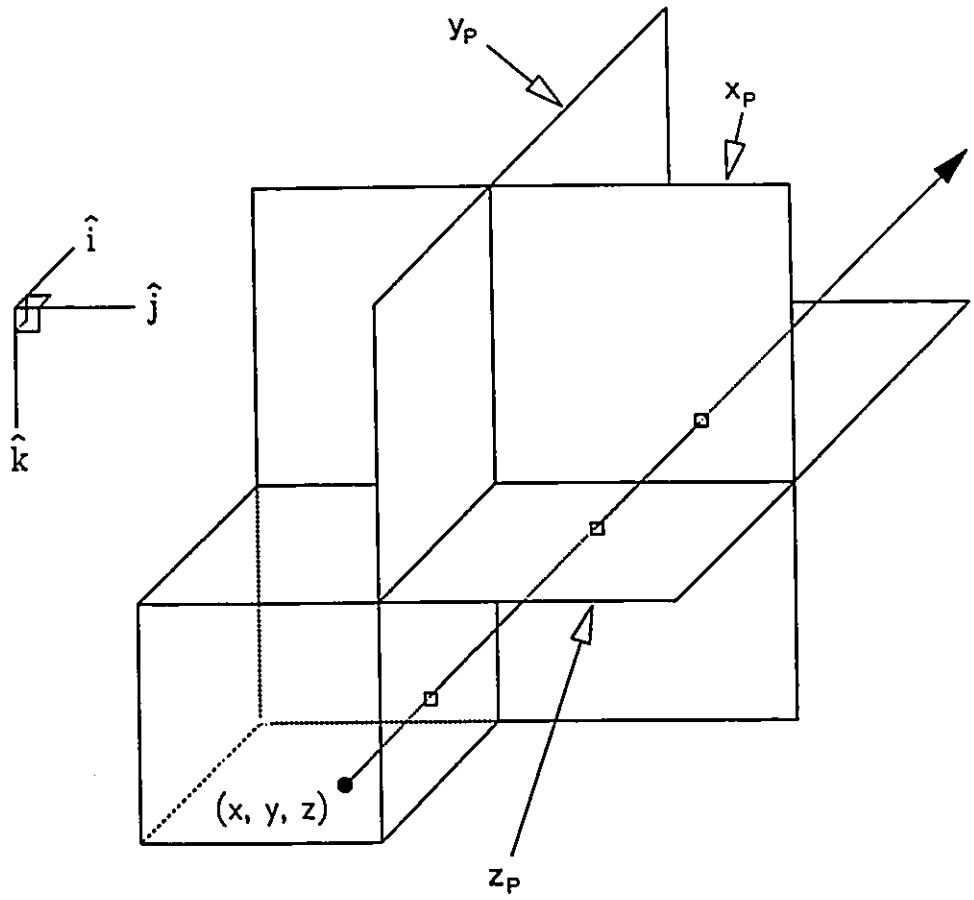

Fig.3.5. Three–plane theorem: In this example, a photon is scattered at $(x,y,z)^t$ with resulting trajectory vector $(\mu_x>0,\mu_y>0,\mu_z<0)^t$ and a free path that takes it outside of the cell in which it was scattered. Hence, the planes making up the cell containing $(x,y,z)^t$ which are intersected by the extended photon trajectory are $x_p = \ell_x[INT(x/\ell_x+1)]$; $y_p = \ell_y[INT(y/\ell_y+1)]$; and $z_p = \ell_z[INT(z/\ell_z+1)-1]$. The y_p plane is the one of concern because it is intersected first. Therefore, the photon is moved to the point on the y_p plane, the optical pathlength through the cell containing $(x,y,z)^t$ is accumulated, and the remaining pathlength is determined to see if the next scattering event should be in the newly entered cell.

in which M is an arbitrarily large number. Thus, defining $\mathbf{p} = (x_p, y_p, z_p)^t$, we have the system

$$\mathbf{p} = \mathbf{x} + \mathbf{D}\mu \ , \tag{3.16a}$$

where

$$\mathbf{D} = \begin{bmatrix} f_x & 0 & 0 \\ 0 & f_y & 0 \\ 0 & 0 & f_z \end{bmatrix} \ , \tag{3.16b}$$

in which the main diagonal entries are the distances from $\mathbf{x}$ to the planes x_p, y_p, and z_p. These distances are solved for as

$$f_x = \frac{x_p - x}{\mu_x} \ ,$$

$$f_y = \frac{y_p - y}{\mu_y} \ , \tag{3.17}$$

and

$$f_z = \frac{z_p - z}{\mu_z} \ .$$

Hence, using the three plane theorem, the distance to just outside the cell containing $\mathbf{x}$ in the μ direction is

$$f_1 = \text{MIN}(f_x, f_y, f_z) \pm \epsilon \ , \tag{3.18}$$

where ϵ is arbitrarily small and used to *nudge* the photon an infinitesimal distance out of the cell containing $\mathbf{x}$. The new position of the photon is, therefore,

$$x_1 = x + f_1\mu \ , \tag{3.19}$$

where subscript 1 refers to the first time the process of updating position is executed. At this point we have accumulated a weighted pathlength of $f_1\left[\beta_{ijk}\right]_1$.

Assume that this process of moving just beyond cell boundaries in direction μ is repeated N times. The residual pathlength left to go before scattering , obtained by decomposing and rearranging Eq.(3.14), is

$$f_{res} = \frac{-\ln(RN) - \sum_{n=1}^{N} f_n\left[\beta_{ijk}\right]_n}{\left[\beta_{ijk}\right]_{N+1}} \ , \tag{3.20}$$

where f_n is distance travelled through the n^{th} cell and $\left[\beta_{ijk}\right]_{N+1}$ is the scattering coefficient of the cell containing the photon. The current position of the photon, given by repeated application of Eq.(3.19), is

$$x_N = x + \mu\left[\sum_{n=1}^{N} f_n\right] \ . \tag{3.21}$$

If the number of the cell containing x_N equals the number of the cell containing

$$x_{N+1} = x_N + f_{res}\mu \ , \tag{3.22}$$

there is a scattering event at x_{N+1} for the required optical pathlength has then been obtained. If the cell numbers do not match, f_{res} is discarded and the updating

process is again repeated. Note that this checking procedure is done at every incremental movement f_n of the photon.

To illustrate the process, three simplified examples are considered. The first case is for homogeneous $\mathcal{R}$ with scattering coefficient β_o in every cell. The equation defining residual pathlength is

$$f_{res} = \frac{-\ln(RN) - \beta_o \sum_{n=1}^{N} f_n}{\beta_o} = f_p - \sum_{n=1}^{N} f_n \ . \tag{3.23}$$

Here it is clear that the photon is just crossing through cells until f_p, calculated by Eq.(3.12), is accumulated. In this case, the scattering event will take place at $\mathbf{x}_{tent}$ given by Eq.(3.13) provided $\mathbf{x}_{tent} \in \mathcal{R}$ ($\mathcal{R}^{\infty}$). Next, consider what happens when an empty cell ($\beta_{ijk} \simeq 0$) is encountered. From Eq.(3.20), f_{res} is very large, hence, the cell is traversed. The optical depth accumulated by crossing this cell is $f_n\left[\beta_{ijk}\right]_n \simeq 0$ and contributes almost nothing to the accumulated optical depth. Finally, assume that $\left[\beta_{ijk}\right]_{N+1}$ is large enough that $f_{res} \simeq 0$. Therefore, $\mathbf{x}_{N+1}$ is almost certainly in the same cell as $\mathbf{x}_N$. In fact, by Eq.(3.22), $\mathbf{x}_N \simeq \mathbf{x}_{N+1}$; the scattering event occurs shortly after entering this cell because of the small mean free–pathlength.

Once the photon accumulates the required optical pathlength (whether before the initial scattering event or between scattering events), a scattering event occurs and the trajectory vector is updated. These two processes are now discussed in the order just mentioned.

The radius of most cloud droplets is significantly larger than the wavelengths of solar radiation. Hence, scattering of solar radiation by cloud

droplets is due mostly to diffraction, refraction, and reflection, and thus, is approximated well by conventional Mie theory. Single–scattering patterns are characterized by strong forward scattering (due primarily to diffraction). The distribution of radiation scattered by a cloud droplet depends on λ and droplet size, shape, and refractive indices. Scattering functions are determined by solving the three–dimensional wave equation in spherical co–ordinates (Mie, 1908; van de Hulst, 1957; Wiscombe, 1979). The probability of a scattering angle being between θ and $\theta+d\theta$ and around the resulting cone with an azimuth angle between φ and $\varphi+d\varphi$ (see Fig.3.4) is

$$\Pr[\theta,\varphi] = \frac{1}{4\pi} p(\theta,\varphi)\sin\theta d\theta d\varphi \ , \tag{3.24}$$

where $p(\theta,\varphi)$, called the scattering phase function, is obtained from Mie theory. Note that $p(\theta,\varphi)$ is for monochromatic radiation integrated over the number size distribution of cloud droplets. The factor 4π is for normalization over the sphere and $\sin\theta$ represents the circumference of a cone of angle θ. If Eq.(3.24) is integrated over $\varphi \in [0, 2\pi]$, the probability of scattering with an angle between θ and $\theta+d\theta$ is

$$\Pr[\theta] = \frac{1}{2} p(\theta)\sin\theta d\theta \ , \tag{3.25a}$$

where

$$p(\theta) = \frac{1}{2\pi}\int_0^{2\pi} p(\theta,\varphi)d\varphi \ , \tag{2.25b}$$

is the azimuthally averaged phase function. Integration of Eq.(3.25a) over $\theta \in [0, \pi]$ yields the phase function normalization condition (conservation of energy):

$$\frac{1}{2}\int_0^{\pi} p(\theta)\sin\theta d\theta = 1 \quad , \tag{3.26a}$$

or

$$\frac{1}{2}\int_{-1}^{1} p(\mu)d\mu = 1 \quad , \tag{3.26b}$$

where $\mu = \cos\theta$.

$p(\mu)$ can be represented as

$$p(\mu) = \sum_{n=0}^{N} \omega_n P_n(\mu) \quad , \tag{3.27a}$$

where $P_n(\mu)$ is the n^{th} order Legendre polynomial, and

$$\omega_n = \frac{2n + 1}{2}\int_{-1}^{1} p(\mu)P_n(\mu)d\mu \quad . \tag{3.27b}$$

Substituting $n = 0$ in Eq.(3.27b) gives $\omega_0 = 1$ due to Eq.(3.26b). If $\omega_0 \neq 1$, this implies that $1 - \omega_0$ of the incident radiation is absorbed by the droplet. Thus, ω_0 is the single–scattering albedo. Hereafter, we will denote ω_0 as ω_o. Substituting $n = 1$ into Eq.(3.27b) yields the first moment of $p(\mu)$:

$$g \equiv \frac{\omega_1}{3} = \frac{1}{2}\int_{-1}^{1} \mu p(\mu)d\mu \quad . \tag{3.28}$$

g is referred to as the asymmetry factor. It is the mean value of the cosine of the scattering angle for the phase function $p(\mu)$.

The scattering deflection angle θ_s (Fig.3.4) is computed in the Monte Carlo

code by solving [see Eq.(3.26b)]

$$RN = \frac{1}{2} \int_{\cos\theta_s}^{1} p(\mu) d\mu \ . \tag{3.29}$$

Solving Eq.(3.29) for θ_s amounts to inverting the cumulative density function of $p(\mu)$. Cloud droplet phase functions obtained by Mie theory are non–analytic and often require $n > 200$ in Eq.(3.27a) to capture much of the detail (e.g. King and Harshvardhan, 1986). If these kinds of phase functions are used in Monte Carlo codes, the inverse of Eq.(3.29) must be either tabulated or approximated by a function before the simulations are done. It is common in atmospheric radiative transfer studies, however, to approximate $p(\mu)$ with an analytic phase function. In this study, the Henyey–Greenstein phase function $P_{HG}(\mu)$ is used (Henyey and Greenstein, 1941). It is given as

$$P_{HG}(\mu) = \frac{1 - g^2}{\left[1 + g^2 - 2g\mu\right]^{3/2}} \ . \tag{3.30}$$

In a later chapter it is shown that use of $P_{HG}(\mu)$ rather than a full Mie function amounts to only slight differences in radiative flux estimates. The attractiveness of using $P_{HG}(\mu)$, beyond giving accurate flux estimates, is two–fold. First, it depends on only one free parameter; the asymmetry factor g. Second, substitution of $P_{HG}(\mu)$ into Eq.(3.29) leads to

$$\cos\theta_s = P - \frac{Q}{(RN - R)^2} \ , \tag{3.31}$$

where

$$P = \frac{1 + g^2}{2g} ,$$

$$Q = \frac{(1 - g^2)^2}{(2g)^3} ,$$

and

$$R = \frac{1 + g}{2g} .$$

g, and thus P, Q, and R, remain constant during a simulation. Hence, Eq.(3.31) is very efficient for computing θ_s. This expression for $\cos\theta_s$ is similar to one used by Harshvardhan and Thomas (1984). Their equation, however, facilitates $g\epsilon(0,1)$, while Eq.(2.31) facilitates $g\epsilon\{(-1,0) \cup (0,1)\}$. Using L'Hopital's rule, it can be shown that $\lim_{g \to 0\pm} \cos\theta_s = 1 - 2(RN)$.

A cone of angle θ_s has now been defined into which the photon is scattered. Because the phase function exhibits azimuthal symmetry, all points on the cone occur with equal probability. Thus, the azimuthal angle of scattering (see Fig.3.4) is simply

$$\varphi_s = 2\pi(RN) , \tag{3.32}$$

where again, RN is a uniform random number on (0,1).

Having determined the scattering angles θ_s and φ_s, the direction cosines of the scattered photon may now be adjusted (see Fig.3.4). Recall that the photon trajectory vector before scattering is $\mu = (\mu_x,\mu_y,\mu_z)^t$. Using spherical trigonometry, the components of the trajectory vector $\mu' = (\mu'_x,\mu'_y,\mu'_z)^t$ after scattering are

$$\left.\begin{aligned} \mu'_x &= \sin\theta_s\cos\varphi_s \\ \mu'_y &= \sin\theta_s\sin\varphi_s \\ \mu'_z &= \mu_z\cos\theta_s \end{aligned}\right\} \mu_z = \pm 1 \ , \tag{3.33a}$$

and for all other μ_z

$$\mu'_x = \mu_x\cos\theta_s - \frac{\left[\ \mu_y\sin\varphi_s + \mu_x\mu_z\cos\varphi_s\ \right]\sin\theta_s}{\left[\ 1 - \mu_z^2\ \right]^{1/2}} \ ,$$

$$\mu'_y = \mu_y\cos\theta_s + \frac{\left[\ \mu_x\sin\varphi_s - \mu_y\mu_z\cos\varphi_s\ \right]\sin\theta_s}{\left[\ 1 - \mu_z^2\ \right]^{1/2}} \ , \tag{3.33b}$$

$$\mu'_z = \mu_z\cos\theta_s + \left[\ 1-\mu_z^2\ \right]^{1/2}\cos\varphi_s\sin\theta_s \ .$$

3.3 Including Underlying Reflecting Surfaces

Most previous Monte Carlo studies of radiative transfer in broken clouds assumed a black underlying surface. This is to approximate clouds over dark oceans. Only the studies of Welch and Wielicki (1989) and Kobayashi (1989) have considered in depth the effects of underlying reflecting surfaces on radiative fluxes for broken clouds. Both studies, however, used the same erroneous representation of a Lambertian surface. This section develops general methods for including realistic underlying reflecting surfaces in Monte Carlo atmospheric radiative models.

Surfaces generally exhibit complex albedo (e.g. Barker and Davies, 1989; Cess and Vulis, 1989) and bi–directional reflectance functions which depend on the

direction of incident radiation. For each incident direction, there exists a unique probability function for emerging directions into the up–facing hemisphere. Mathematical and computational representation of this trait complicates the task of including realistic surfaces in Monte Carlo codes.

There are three obvious methods of accounting for realistic surfaces in Monte Carlo photon transport simulations. First, the surface can be viewed as a simple extension of the atmospheric model: photons enter the surface and are scattered and absorbed by surface elements accordingly. Second, if analytic functions for bi–directional reflectance and albedo are known *a priori*, reflectance angles could be obtained by a statistical method similar to the one used to compute scattering angles in Section 2.2. Third, if there are enough bi–directional reflectance measurements for one surface, a tabular look–up approach may be feasible. This is not the case at present, however.

This section has three main parts. First, two general methods for including a lower boundary condition in an atmospheric Monte Carlo radiative transfer model are developed: the Monte Carlo and statistical bi–directional methods mentioned above. In the second section, the statistical bi–directional method is applied to the highly idealized Lambertian and Fresnelian surfaces. Also in this section, it is shown that Welch and Wielicki (1989) and Kobayashi (1989) used a surface quite different from Lambertian. Third, the bi–directional method is developed for non–vegetated land surfaces composed of particles.

3.3.1 Method 1: Monte Carlo Photon Transport

In both the Monte Carlo and bi–directional methods, $\mathcal{A}$ signifies the plane–parallel surface below an atmospheric region $\mathcal{R}$ which is the generator of cyclic region $\mathcal{R}^{\infty}$ (see section 3.1.2). In the Monte Carlo method, $\mathcal{A}'$ signifies the sub–surface below $\mathcal{A}$.

Let an incident photon at the surface pass through a point like $(x, y, \ell_z N_z)$ and have a trajectory vector of the form $(\mu_x, \mu_y, \mu_z > 0)$. These are the components of the trajectory vectors with which photons begin their trace through $\mathcal{A}'$. Photon mean–free pathlengths between scattering events by surface particles and scattering geometry are calculated as in Eq's.(3.12), (3.31),and (3.32) respectively. If, however, we assume the surface to be semi–infinite, pathlength becomes arbitrary and we can neglect the scattering coefficient β and set it to unity. However, the single–scattering albedo and phase function of surface particles are required.

Since the surface is assumed to be semi–infinite and plane–parallel, few checks regarding photon position are required. The only necessary checks are: photon exittance across $\mathcal{A}$; and photon absorption. Thus, photon trajectories are calculated much faster than in the inhomogeneous atmosphere model. Note that only vertical depth in $\mathcal{A}'$ need be monitored. As such, it is assumed that photons exit and re–enter the atmosphere at the same point on $\mathcal{A}$. This approximation is entirely adequate since the smallest scale of atmospheric homogeneity considered in this thesis is on the order of hundred of metres. If and when a photon emerges from $\mathcal{A}'$, the only specific condition attached to the new trajectory vector is $\mu_z < 0$. This method allows for horizontally inhomogeneous surfaces (Diner and Martonchik, 1984).

The *opposition effect* applies to single–scattered photons that undergo near perfect backscatter (Hapke, 1981). These photons are in essence no longer part of the transport process for they exit the media along almost the exact path by which they entered. This effect, however, is not restricted to single–scattered photons. Rather, it applies to all photons at all times whenever near perfect backscatter occurs. However, since only fluxes are being considered in this study, *all* opposition effects are neglected.

3.3.2 Method 2: Statistical Bi–directional Reflectance Functions

This section establishes a general procedure to be used in a Monte Carlo code for determining statistically the trajectory vector of a photon as it is scattered and reflected by an underlying surface. Assume a beam of photons arrive at the surface with zenith angle θ_z [$\equiv \arccos(\mu_z)$] and azimuth φ_z (relative to the x–axis). If the photon (beam) has unit intensity and cross–sectional area, then the incident energy per unit area is simply the projection; μ_z. Denote the reflected radiance from the surface into the unit solid angle around the direction $(-\mu,\varphi)$ as $I(-\mu,\varphi;\mu_z,\varphi_z)$. The reflected radiance per unit solid angle per unit surface area is, therefore, $\mu I(-\mu,\varphi;\mu_z,\varphi_z)$ (see Fig.3.6). The directional surface albedo, defined as the ratio between total reflected radiation/unit area and incident radiation/unit area, is then given as

$$\alpha_s(\mu_z,\varphi_z) = \frac{1}{\mu_z}\int_0^{2\pi}\int_0^1 \mu I(-\mu,\varphi;\mu_z,\varphi_z)\,d\mu\,d\varphi \ . \tag{3.34}$$

Note that both φ and φ_z are relative to the x–axis. The first step, therefore, is to determine whether a photon incident at the surface is reflected or absorbed. If RN is a random number generated between 0 and 1, and $\alpha_s(\mu_z,\varphi_z) <$ RN, the photon is absorbed and a new one injected. If $\alpha_s(\mu_z,\varphi_z) >$ RN, the reflected angles (θ,φ) are determined as follows.

Defining the total radiance reflected into a narrow azimuthal band as

$$\hat{I}(-\mu;\mu_z,\varphi_z) = \int_0^{2\pi} I(-\mu,\varphi;\mu_z,\varphi_z)\,d\varphi \ , \tag{3.35}$$

leads to

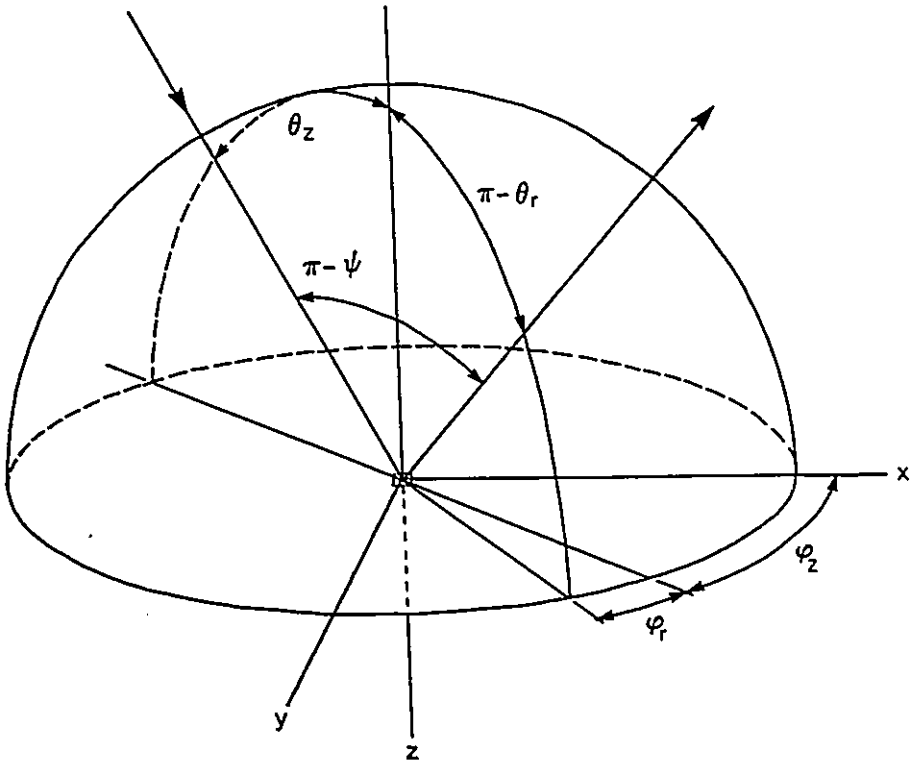

Fig.3.6. Surface reflection geometry. Photon trajectory is indicated by the line with the large arrowhead. Photon is incident with a zenith angle θ_z and azimuth angle relative to the x–axis of φ_z. Upon emerging from the surface, the photon has a zenith angle of θ_r and azimuth of $\varphi_z+\varphi_r$. Scattering angle is ψ. Note that the photon emerges from the surface at the same point it entered.

$$\alpha_s(\mu_z,\varphi_z) = \frac{1}{\mu_z}\int_0^1 \mu\hat{I}(-\mu;\mu_z,\varphi_z)d\mu \ . \tag{3.36}$$

Therefore, the conditional cumulative probability density function of μ, given μ_z and φ_z, is

$$P_c(-\mu|\mu_z,\varphi_z) = \frac{\int_0^{\mu} \mu'\hat{I}(-\mu';\mu_z,\varphi_z)d\mu'}{\int_0^1 \mu'\hat{I}(-\mu';\mu_z,\varphi_z)d\mu'} \ , \tag{3.37a}$$

or

$$P_c(-\mu|\mu_z,\varphi_z) = \frac{\int_0^{\mu} \mu'\hat{I}(-\mu';\mu_z,\varphi_z)d\mu'}{\mu_z\alpha_s(\mu_z,\varphi_z)} \ . \tag{3.37b}$$

Equation (3.37) essentially defines the conditional probability of a photon being reflected from the surface at a zenith angle whose cosine is greater than $-\mu$. By setting $P_c(-\mu|\mu_z,\varphi_z)$ equal to a uniform random number RN generated on the interval (0,1), and solving for $-\mu$ gives the zenith angle of the reflected photon, as

$$\theta_r = \arccos(-\mu) \ . \tag{3.38}$$

If RN = 0 ($P_c = 0$), $-\mu$ in Eq.(3.37) is also 0 and the photon is reflected along the horizon with $\theta_r = \pi/2$. Similarly, if RN = 1, $-\mu = -1$ and the photon is reflected towards the zenith with $\theta_r = \pi$.

The azimuth angle φ_r of the reflected photon is obtained in a similar manner. By assigning the cumulative probability function of φ_r, given $-\mu$ [which is now known from Eq.(3.37)], μ_z, and φ_z, a value of RN (a random number), we get, in a slightly rearranged and more direct form than Eq.(3.37),

$$\int_0^{\varphi_r} I(-\mu,\varphi';\mu_z,\varphi_z)d\varphi' = RN\int_0^{2\pi} I(-\mu,\varphi';\mu_z,\varphi_z)d\varphi' \quad , \tag{3.39}$$

which is then solved for φ_r. Again, if RN = 0 or 1, $\varphi_r = 0$ or 2π and the photon is scattered forward in conjunction to the Sun. All other values of RN result in off–forward scattering.

From the definitions given in section 3.2, the incident azimuth angle relative to the x–axis is given by

$$\varphi_z = \arccos\left[\frac{\mu_x}{\sin\theta_z}\right] = \frac{\pi}{2} + \arccos\left[\frac{\mu_y}{\sin\theta_z}\right] \quad . \tag{3.40}$$

Therefore, the direction cosines of the photons reflected by the surface are given by

$$\begin{aligned} \mu_x &= \sin\theta_r\cos(\varphi_z + \varphi_r) \\ \mu_y &= \sin\theta_r\cos(\varphi_z + \varphi_r - \tfrac{\pi}{2}) \\ \mu_z &= \cos\theta_r \quad , \end{aligned} \tag{3.41}$$

where θ_r and φ_r are determined from Eq's.(3.38) and (3.40).

While this procedure is straightforward, it is difficult to implement. There is no reason to assume that real surfaces have functional forms of $I(-\mu,\varphi;\mu_z,\varphi_z)$, and even the simplest realistic analytic forms lead to substantial amounts of model computation or prior parameterization as will be seen later. For now, however, two highly idealized surfaces are considered in the general framework; Lambertian and Fresnelian surfaces. The later surface is theoretically justifiable but rarely observed, and the former surface is theoretically unjustifiable but is often a good first order approximation in plane–parallel cloud conditions.

3.3.2.1 Lambertian Surface

If a surface is irradiated by a collimated beam from an arbitrary direction and the reflected intensity field is equal in all directions, the surface is Lambertian (Lenoble, 1977). Because of this simplicity, it is the surface of choice in most climate studies. Equal in all directions implies that I and $\hat{I}$ in Eq's.(3.34) through (3.37) and Eq.(3.39) are constant. Hence, from Eq.(3.34), the intensity function associated with the Lambertian surface is

$$I_L(-\mu,\varphi;\mu_z,\varphi_z) = \frac{\mu_\circ \alpha_s}{\pi} \ , \tag{3.42}$$

where the incident beam has unit intensity. This property is occasionally relaxed in climate studies to the extent of having solar zenith angle dependent albedos $\alpha_s(\mu_z)$, though it does violate principles of reciprocity (see Lenoble, 1977). The procedure begins by generating a random number RN and if α_s < RN reflection takes place, otherwise the photon is absorbed.

Letting Eq.(3.37) equal a random number RN, and substitution of Eq.(3.42) into Eq.(3.37) reduces Eq.(3.37) to

$$\frac{\int_0^{\mu} \mu' \, d\mu'}{\int_0^{1} \mu' \, d\mu'} = RN \ , \tag{3.43}$$

which leads to reflected zenith angle of

$$\theta_r = \arccos(-RN^{1/2}) \ . \tag{3.44}$$

Inserting I_L into Eq.(3.39) leads to the simple solution

$$\varphi_r = 2\pi(\mathrm{RN}) \quad . \tag{3.45}$$

The new direction cosines are calculated using Eq.(3.41). Thus, including a Lambertian surface in Monte Carlo models is computationally extremely efficient.

Welch and Wielicki (1989) and Kobayashi (1989) claimed to have used a Lambertian surface in their studies of fluxes in broken cloud fields. Both, however, used something different. What they did [personal communication, Dr. Ron Welch, 1990; and Kobayashi's Eq.(11)] was to assign the trajectory angles of reflected photons using an even distribution of φ_r *and* θ_r:

$$\left.\begin{aligned} \theta_r &= \tfrac{\pi}{2}(1 + \mathrm{RN}) \\ \varphi_r &= 2\pi(\mathrm{RN}) \end{aligned}\right\} \quad . \tag{3.46}$$

At first glance, this set of assignments appear to make logical sense with respect to the 'equal in all directions' requirement of the Lambertian surface. However, working backwards using Eq's.(3.46), (3.37) and (3.38) shows that the intensity function implicit in Eq.(3.46) is given by

$$I_\theta(-\mu,\mu_z) = \frac{\alpha_s \mu_z}{\pi^2 \mu \sqrt{1 - \mu^2}} \quad . \tag{3.47}$$

Compared with I_L, reflected radiance is underestimated when I_θ is used for reflected zenith angles between ~ 110° and 160° and overestimated for all others. In essence, I_θ fails to account for surface projection and proportional circumference on the hemisphere as a function of zenith angle.

The validity of Eq.(3.42) can be demonstrated simply. Assume a cloud field is irradiated by a field of radiation whose intensity $I(\mu)$ depends on zenith angle only. If $R_c(\mu)$ is the azimuthally averaged zenith angle dependent reflectance of the cloud field to radiation incident from the $\theta = \cos^{-1}\mu$ direction, cloud field reflectance to the entire field of radiation is

$$\langle r \rangle = \frac{\int_0^1 R_c(\mu) I(\mu) \mu d\mu}{\int_0^1 I(\mu) \mu d\mu} \quad . \tag{3.48}$$

If $I(\mu)$ is constant, the field is isotropic and Eq.(3.48) reduces to the familiar Bond (spherical) albedo given by

$$\langle r \rangle = 2 \int_0^1 R_c(\mu) \mu d\mu \quad , \tag{3.49}$$

which is usually used to represent sky reflectance to surface reflected radiation (Lacis and Hansen, 1974). Note that insertion of I_L into Eq.(3.48) yields precisely Eq.(3.49) (denote as $\langle r \rangle_L$) as it should since Lambertian is synonymous with isotropic. Insertion of I_θ into Eq.(3.48), however, yields

$$\langle r \rangle_\theta = \frac{2}{\pi} \int_0^{\pi/2} R_c(\theta) d\theta \quad . \tag{3.50}$$

A correction can be assigned to Welch and Wielicki's and Kobayashi's non–Lambertian based results. Defining the difference between Eq.(3.49) and

Eq.(3.50) as $\Delta\langle r\rangle = \langle r\rangle_L - \langle r\rangle_\theta$ and expressing $R_c(\mu)$ in a power series expansion as

$$R_c(\mu) = \sum_{n=0}^{\infty} a_n \mu^n \ , \tag{3.51}$$

where a_n are constants, it can be shown that

$$\Delta\langle r\rangle = \sum_{n=0}^{\infty} a_n \left[\frac{2}{n+2} - \frac{\Gamma(\frac{n+1}{2})}{\sqrt{\pi}\ \Gamma(\frac{n+2}{2})} \right] \ , \tag{3.52}$$

where $\Gamma(x)$ is the gamma function. In most cases, an excellent approximation of $R_c(\mu)$ is

$$R_c(\mu) \simeq a_0 + a_1\mu + a_2\mu^2 + a_3\mu^3 \ , \tag{3.53a}$$

with

$$\left.\begin{aligned} a_0 &= \lim_{\mu \to 0} R_c(\mu) \\ a_1 &= \lim_{\mu \to 0} \frac{\partial R_c}{\partial \mu}(\mu) \end{aligned}\right\} . \tag{3.53a}$$

The other coefficients have less straightforward meanings. Using Eq.(3.53a), Eq.(3.52) is approximated as

$$\Delta\langle r\rangle \simeq 0.03a_1 - 0.02a_3 \ . \tag{3.54}$$

Assume that the cloud–surface system reflectance after infinitely many internal reflections is

$$R(\mu_o) = R_c(\mu_o) + \frac{[1 - R_c(\mu_o)][1 - \langle r\rangle]\alpha_s}{1 - \alpha_s\langle r\rangle} \quad . \tag{3.55}$$

Later on it is shown that this expression is valid for regular arrays of cubes with base height of 1 km (as used by Welch and Wielicki). Differentiating Eq.(3.55) with respect to $\langle r\rangle$ and substituting Eq.(3.54) for $\Delta\langle r\rangle$ approximates closely the error in system reflectance due to use of I_θ as

$$\Delta R(\mu_o) \simeq \frac{-\alpha_s(1 - \alpha_s)[1 - R_c(\mu_o)]}{(1 - \alpha_s\langle r\rangle)^2}(0.03a_1 - 0.02a_3) \quad . \tag{3.56}$$

In all cases tested, $\Delta R(\mu_o)$ was negative meaning that use of I_θ rather than I_L reduces system albedo. Though this correction is almost always less than 5% of $R(\mu_o)$, it is often enough to nullify the phenomenon noted by Welch and Wielicki (1989) that non–absorbing clouds act to reduce system albedo.

3.3.2.2 Fresnelian Surface

The second ideal surface is the Fresnelian surface. It is characterized by perfect specular reflection and has an intensity function

$$I_F(-\mu,\varphi;\mu_z,\varphi_z) = f(\mu_z)\delta(\mu-\mu_z)\delta(\varphi-\varphi_z) \quad , \tag{3.57}$$

where $f(\mu_z)$ is the zenith angle dependent albedo (van de Hulst, 1957). This is the case for perfectly flat, clear, deep water. Again, a random number RN is generated and if $f(\mu_z) < RN$ the photon is reflected. Inserting Eq.(3.57) into Eq.(3.37) leads to

$$\frac{\int_0^{\mu} \mu' \, \delta(\mu' - \mu_z) d\mu'}{\mu_z} = \mathrm{RN} \ , \tag{3.58}$$

which results in the following set of implications:

$$\begin{aligned} &\mu < \mu_z \Leftrightarrow r = 0 \\ &\mu > \mu_z \Leftrightarrow r = 1 \\ &\mu = \mu_z \Leftrightarrow r \in (0,1) \ . \end{aligned} \tag{3.59}$$

Since the probability of generating RN = 0 or 1 is essentially zero, all reflected angles are $\theta_z = \arccos(-\mu_z) = \pi - \theta_z$.

Furthermore, it is implicit in Eq.(3.56) that $\varphi_r = 0$. The new direction cosines are calculated using Eq.(3.41).

3.3.3 General Solution for a Particulate Surface

The radiation intensity field emerging from a surface consisting of particles, irradiated by direct beam from the $(\mu_z, \varphi_z) \equiv \Omega_z$ direction, has been extensively documented by Chandrasekhar (1960) and Hapke (1981). For convenience, much of the general solution, neglecting the opposition effects (preferential escape), is derived here.

Consider a volume element of soil at depth z which is irradiated by radiation from all directions. Denote the amount of radiation incident from the Ω' direction as

$$J(z,\Omega') = \sum_{n=0}^{\infty} J_n(z,\Omega') \ , \tag{3.60}$$

where J_n is the amount of radiation making up J that has already undergone n scattering events. We wish to know how much of J will be scattered by the elemental volume of soil into the Ω direction. If μ is the cosine of the zenith angle of the scattered beam, β_s is the soil volume scattering coefficient, and dz is the vertical thickness of the elemental volume, then the amount of radiation scattered from Ω' to Ω is

$$dJ''(z,\Omega',\Omega) = J(z,\Omega') \frac{P_s(\Omega',\Omega)}{4\pi} \beta_s \frac{dz}{\mu} d\Omega' \quad , \tag{3.61}$$

where P_s is the soil scattering phase function defining the probability of radiation scattered from the Ω' direction into the Ω direction. Assuming the soil particles are randomly packed, the probability of $dJ''(z,\Omega',\Omega)$ getting out of the soil is $\exp(-\beta_e z/\mu)$ where β_e is soil volume extinction coefficient. Thus, the amount of radiation exiting the soil in direction Ω which was travelling in direction Ω' at depth z is

$$dJ'(\tau,\Omega',\Omega) = \frac{\omega_s}{4\pi} P_s(\Omega',\Omega) J(\tau,\Omega') e^{-\tau/\mu} \frac{d\tau}{\mu} d\Omega' \quad , \tag{3.62}$$

where $d\tau = \beta_e dz$ ($\tau = \beta_e z$) is optical depth, and ω_s is soil particle single–scattering albedo. Integrating Eq.(3.62) over all Ω' gives the amount of radiation incident on the volume element at depth τ that exits the soil in direction Ω as

$$dJ(\tau,\Omega) = \frac{\omega_s}{4\pi} e^{-\tau/\mu} \frac{d\tau}{\mu} \int_{4\pi} J(\tau,\Omega') P_s(\Omega',\Omega) d\Omega' \quad , \tag{3.63}$$

Finally, integrating Eq.(3.63) over all depths gives the total amount of

radiation exiting the soil in the direction Ω as

$$I(\Omega,\Omega_z) = \frac{\omega_s}{4\pi}\int_0^\infty e^{-\tau/\mu}\int_{4\pi} J(\tau,\Omega')P_s(\Omega',\Omega)\frac{d\Omega'}{\mu}\,d\tau \ . \qquad (3.64a)$$

Substituting Eq.(3.60) into Eq.(3.64a) gives

$$I(\Omega,\Omega_z) = \frac{\omega_s}{4\pi}\left\{\int_0^\infty J_0(\tau,\Omega_z)e^{-\tau/\mu}\frac{d\tau}{\mu}P_s(\Omega_z,\Omega) + \sum_{n=1}^{\infty}\left[\int_0^\infty e^{-\tau/\mu}\int_{4\pi} J_n(\tau,\Omega')P_s(\Omega',\Omega)\frac{d\Omega'}{\mu}\,d\tau\right]\right\} \qquad (3.64b)$$

$$= \hat{I}_s(\Omega,\Omega_z) + \hat{I}_m(\Omega,\Omega_z) \ , .$$

where $\hat{I}_s$ and $\hat{I}_m$ are the single and multiple scattering contributions to $I(\Omega,\Omega_z)$. $J_0(\tau,\Omega_z)$ is the fraction of the direct beam incident at the surface that arrives unscattered at depth τ. It is given as

$$J_0(\tau,\Omega_z) = e^{-\tau/\mu_z} \ , \qquad (3.65)$$

where μ_z is the cosine of solar zenith angle of the incident photon. Substituting Eq.(3.65) into Eq.(3.64b) and evaluating the integral yields

$$\hat{I}_s(\Omega,\Omega_z) = \frac{\omega_\bullet}{4\pi}\frac{\mu_z}{\mu_z + \mu}P_s(\Omega_z,\Omega) \ . \qquad (3.66)$$

The $\hat{I}_m$ term in Eq.(3.64b) represents radiation exiting in the Ω direction that

has already been scattered at least once before undergoing it's final scattering event. Assuming $P_s(\Omega) = 1.0$ (isotropic scattering particles), Chandrasekhar (1960) showed that

$$\hat{I}_m(\Omega,\Omega_z) = \frac{\omega_s}{4\pi}\frac{\mu_z}{\mu_z + \mu}\left[H(\mu_z)H(\mu) - 1 \right] , \tag{3.67}$$

where

$$H(\mu) = 1 + \tfrac{1}{2}\,\omega_s\mu H(\mu)\int_0^1 \frac{H(\mu')}{\mu + \mu'}\,d\mu' \quad . \tag{3.68}$$

This is an exact solution but must be solved numerically. Hapke (1981) showed that if $\hat{I}_m(\Omega,\Omega_z)$ is solved by the two–stream approximation (Coakley and Chýlek, 1975) with $P_s(\Omega) = 1.0$, the result is again Eq.(3.67) but with

$$H(\mu) = \frac{1 + 2\mu}{1 + 2\gamma\mu} , \tag{3.69a}$$

where

$$\gamma = (1 - \omega_s)^{1/2} \quad . \tag{3.69b}$$

For our purposes ($\omega_s < 0.7$), Hapke's formulae are satisfactory. Problems are apparent, however, near $\omega_s = 1.0$ where it becomes clear that conservation of energy is violated when particle asymmetric phase functions are used.

Substituting Eq.s (3.66) and (3.67) into Eq.(3.64b) yields

$$I(\Omega,\Omega_z) = I(\mu,\varphi;\mu_z,\varphi_z) = \frac{\omega_s}{4\pi}\frac{\mu_z}{\mu_z + \mu}\left[P_s(\Omega,\Omega_z) + H(\mu_z)H(\mu) - 1 \right] , \tag{3.70}$$

where (Ω,Ω_z) represents the scattering angle ψ, which, by spherical trigonometry, can be written as $\cos\psi = -\mu\mu_z+\sqrt{(1-\mu^2)(1-\mu_z^2)}\cos\varphi_r$ (see Fig.3.6).

In order to relate the scattering angle ψ to the zenith and azimuth angles, $P_s(\cos\psi)$ is expanded in a series of Legendre polynomials and the addition theorem of spherical harmonics is used to give

$$P_s(\cos\psi) = \sum_{n=0}^{\infty} \omega_n \left[\sum_{m=0}^{n} (-1)^{n+m} (2-\delta_{0m}) \frac{(n-m)!}{(n+m)!} P_n^m(\mu_z) P_n^m(\mu) \cos(m\varphi) \right] , \tag{3.71}$$

where ω_n are phase function expansion coefficients (ω_0=1; ω_1=3g) and $P_n^m(\mu)$ is the associated Legendre polynomial of order n and degree m. Here, the relation $P_n^m(-\mu) = (-1)^{n+m}P_n^m(\mu)$ has been used since all μ of concern are of opposite sign to μ_z. Inserting Eq.s (3.33) and (3.32) into Eq.(3.4) gives

$$\frac{\displaystyle\int_0^{\mu} \frac{\mu'}{\mu'+\mu_z} \left[H(\mu_z)H(\mu') + \sum_{n=1}^{\infty} (-1)^n \omega_n P_n(\mu_z) P_n(\mu') \right] d\mu'}{\displaystyle\int_0^{1} \frac{\mu'}{\mu'+\mu_z} \left[H(\mu_z)H(\mu') + \sum_{n=1}^{\infty} (-1)^n \omega_n P_n(\mu_z) P_n(\mu') \right] d\mu'} = RN \ . \tag{3.72}$$

Note that upon integration around the full azimuth, the m > 0 terms in Eq.(3.71) vanish. Unfortunately, no useful simplifications appear possible in Eq.(3.72). An analytic solution was found for the integrals involving the H–functions when $H(\mu)$ is given by Hapke's formula. The solution, however, consists of two unruly functions; the choice of which to use depends on values of ω_s and μ_z. For this reason Eq.(3.72) is left as it is in unsolved form. If the commonly cited

Henyey–Greenstein phase function is assumed to apply to soil grains, $\omega_n = (2n + 1)g^n$ where g is asymmetry factor (Joseph *et al.*, 1976).

Due to the obvious complexity of Eq.(3.72), this study is limited to phase functions with $\omega_n = 0$ for $n > 1$. In this case, Eq.(3.72) becomes

$$\frac{\int_0^{\mu} \frac{\mu'}{\mu' + \mu_z} \left[H(\mu_z)H(\mu') - \omega_1 \mu' \mu_z \right] d\mu'}{\int_0^{1} \frac{\mu'}{\mu' + \mu_z} \left[H(\mu_z)H(\mu') - \omega_1 \mu' \mu_z \right] d\mu'} = RN \ , \qquad (3.73)$$

which simplifies to

$$\frac{\int_0^{\mu} \frac{\mu' H(\mu_z)H(\mu')}{\mu' + \mu_z} d\mu' - A(\mu_z)}{\int_0^{1} \frac{\mu' H(\mu_z)H(\mu')}{\mu' + \mu_z} d\mu' - A(\mu_z)} = RN \ , \qquad (3.74a)$$

where

$$A(\mu_z) = \omega_1 \mu_z \left[\frac{1}{2} - \mu_z + \mu_o^2 \ln\left[\frac{1 + \mu_z}{\mu_z} \right] \right] \ . \qquad (3.74b)$$

For isotropic scattering particles, Eq.(3.73) is used except with $\omega_1 = 0$. Since the objective is to choose RN and solve for μ, Eq.(3.73) must be solved either numerically, or by parameterization. This problem is addressed in Chapter 4. Regardless of how μ is obtained, the conventional transformation is applied to it to get reflected angle: $\theta_r = \pi - \arccos(\mu)$.

Having solved for θ_r, we must now solve for φ_r. Inserting Eq's.(3.70) and (3.71) into Eq.(3.39) gives the general solution as

$$RN = \frac{\varphi_r}{2\pi} + \frac{2\sum_{n=1}^{\infty}\omega_n\left[\sum_{m=1}^{n}(-1)^{n+m}\frac{(n-m)!}{(n+m)!}P_n^m(\mu_z)P_n^m(\mu)\frac{\sin(m\varphi_r)}{m}\right]}{2\pi\left[H(\mu_z)H(\mu) + \sum_{n=1}^{\infty}(-1)^n\omega_n P_n(\mu_z)P_n(\mu)\right]} . \tag{3.75}$$

For the most complex case considered here, Eq.(3.75) becomes

$$RN = \frac{1}{2\pi}\left\{\varphi_r + \omega_1\frac{\sqrt{(1-\mu^2)(1-\mu_z^2)}\,\sin\varphi_r}{H(\mu_z)H(\mu) - \omega_1\mu_z\mu}\right\} . \tag{3.76}$$

This equation, like Eq.(3.73), can be solved either by parameterization or numerically. Note that if $P_s(\cos\psi) = 1$ the Lambertian solution is retrieved:

$$\varphi_r = 2\pi(RN) . \tag{3.77}$$

3.4 Absorption of Radiation by Droplets and Surfaces

Absorption of photons by droplets or the underlying surface can be computed by either the *on–line* or *off–line* technique. Choice of which technique to use depends on the type of experiment being conducted. The techniques are discussed in turn and followed by a proof of their statistical equivalence.

On–line absorption is characterized by explicit absorption events. Assume the single–scattering albedo of droplets (or soil particles) is ω_0. At each scattering event, before the scattering angles are determined, a uniform random number $RN\epsilon(0,1)$ is generated. If $RN < \omega_0$ the scattering event is carried through. If $RN \geq \omega_0$ the photon is absorbed, its trajectory terminated, the cloud absorption counter

is incremented, and a new photon is injected. Similarly, assume a photon arrives at the surface with a cosine of zenith angle μ_z and that the zenith angle dependent surface albedo is $\alpha_s(\mu_z)$. As in the droplet case, RN is generated before the reflectance angles are determined. If RN $< \alpha_s(\mu_z)$ the photon is reflected, but if RN $\geq \alpha_s(\mu_z)$ it is absorbed.

Separate bins are used to accumulate photons absorbed by droplets and the surface. Thus, if one wishes to know system reflectance, transmittance, and cloud and surface absorptance, the on–line method is used. Furthermore, if surface albedo is a function of incident zenith angle or if ω_o varies in space, the on–line method must be used. With this method, system reflectance is calculated as

$$R = 1.0 - A_{atmos} - A_{surf} \ , \tag{3.78}$$

where A_{atmos} and A_{surf} are atmosphere and surface absorptance (defined by the ratio of absorbed photons to the total number of photons injected). For non–uniform or zenith angle dependent surface albedo, total transmittance, or surface irradiance, is

$$T = \frac{1}{N} \sum_{i=1}^{N} m_i \ , \tag{3.79}$$

where m_i is the number of times the i^{th} photon encountered the surface. Hence, grid–averaged surface albedo of a simulation is

$$\alpha_s = 1 - \frac{A_{surf}}{T} \ . \tag{3.80}$$

The drawback of using the on–line technique is that the results of a simulation apply only to that simulation.

In the off–line technique, photons are represented as ensembles of many photons to a greater extent than in the on–line technique. Simulations are conducted with $\alpha_s = \omega_o = 1.0$; no absorption takes place during the simulation. The algorithm keeps track of the total number of droplet and surface scattering events experienced by each ensemble of photons. Each ensemble begins with unit weight (as in the on–line method). When the ensemble encounters a droplet or the surface, fractions ω_o and α_s of the photons in the ensemble are assumed to be absorbed. Thus, when the i^{th} ensemble of photons emerges from the system, its weight is

$$w_i = \omega_o^{n_i} \alpha_s^{m_i} , \tag{3.81}$$

where n_i and m_i are the total number of droplet and surface scattering events. The system reflectance is given as

$$R = \frac{1}{N} \sum_{i=1}^{N} w_i . \tag{3.82}$$

If open boundary conditions are used, all fluxes shown in Fig.3.2 are weighted like Eq.(3.82) except $m_i = 0$ for all i. The drawback of this method is that with cyclic boundary conditions, overall system reflectance and absorptance are the only quantities that can be obtained with confidence. Also, only unrealistic surfaces with albedo independent of incident zenith angle are admissible (e.g. Lambertian). Furthermore, this method can take significantly longer to run than

the on–line method. The attractive aspect of this technique is that for a single simulation with $\alpha_s = \omega_o = 1.0$, results may be efficiently generated for any number of combinations of $\alpha_s \leq 1.0$ and $\omega_o \leq 1.0$ since n_i and m_i are stored.

It is now shown that the on–line and off–line methods are statistical equivalent for cases in which $\alpha_s(\mu) = \alpha_s$ and ω_o does not vary in space. First, consider the on–line method. Each time a photon strikes a droplet or the surface it has a probability of success (scattering) ω_o or α_s. All interactions are mutually exclusive. If all numbers of droplet and surface scattering events, n and m respectively, are possible for a given photon, we can define the conditional probabilities P(n|m) (read as: the probability of a photon having n droplet scattering events given that it had m surface encounters). The mean survival (system reflectance) is thus given by

$$R = \sum_{n=0}^{\infty} \sum_{m=0}^{\infty} P(n|m)\left[\omega_o^n \cdot \alpha_s^m\right] \quad . \tag{3.83}$$

Assume that N photons are used and that

$$P(n|m) \simeq \frac{1}{N} \sum_{i=1}^{N} \delta_{nn_i} \delta_{mm_i} \quad , \tag{3.84}$$

where n_i and m_i are the number of droplet and surface encounters of the i^{th} photon. Substituting Eq.(3.84) into Eq.(3.83) yields

$$R = \frac{1}{N}\Big[\left(N_0^0 + N_1^0\omega_o + \cdots \right) + \left(N_0^1\alpha_s + N_1^1\omega_o\alpha_s + \cdots \right) + \left(N_0^m\alpha_s^m + N_1^m\omega_o\alpha_s^m + \cdots + N_n^m\omega_o^n\alpha_s^m + \cdots \right) + \cdots \Big] \quad , \tag{3.85}$$

where N_i^j are the number of occurrences of photons that had i and j droplet and surface scattering events. Upon careful consideration of Eq.(3.85) one sees that it is equivalent to Eq.(3.82) and this concludes the proof. In Chapter 4 the statistical equivalence of the two techniques is demonstrated numerically using a variety of demanding simulations.

3.5 Extensions of the Model

The purpose of this section is to document some of the capabilities of the Monte Carlo model. The capabilities outlined here are not crucial to understanding the remainder of the thesis. Therefore, this section may be bypassed. What this section does provide, however, are indications of the models versatility and possible future applications.

First, the geometric pathlength traversed by each photon is saved just as the number of scattering events and surface encounters are saved. This is necessary if one wishes to investigate the effect on fluxes due to variable amounts of water vapour in and around clouds. Assuming a homogeneous distribution of water vapour, system reflectance is given as [see Eq.(3.82)]

$$R = \frac{1}{N} \sum_{i=1}^{N} \omega_o^{n_i} \alpha_s^{m_i} Tr(p_i) \ , \tag{3.86}$$

where p_i is the pathlength traversed by the i^{th} photon and Tr is a spectral H_2O vapour transmittance function. With only minor modification to the code, variable vapour concentration and temperature and pressure effects on spectral line shapes can be included. This would be useful for testing gaseous absorption routines used in climate models (e.g. Fouquart and Bonnel, 1980; Kratz and Cess, 1986) if and when parameterizations of broken cloud are incorporated into climate models.

Another intriguing possibility is spatial variability of cloud drop size distributions. For example, the effective radius of droplets in cumuliform clouds is greatest in the core and at the top due to coalescence and radiative cooling. Droplets tend to be smallest at the cloud sides due to entrainment of dry (cloud–free) air (Rogers, 1976). Changes in drop size distribution enter the Monte Carlo code through the scattering coefficient, ω_o, and g. If ω_o varied from cell–to–cell, on–line absorption is required. If one were to avoid droplet absorption bands, however, and only let g vary, the off–line technique would be suitable. This would require parameterizing g as a function of drop size only.

It would be a relatively straightforward, though tedious, exercise to include the effects of air molecules and ozone above cloud tops (Welch and Wielicki, 1985). Total reflected solar flux at the top of the atmosphere could be approximated by running only two simulations. Drop size integrated g for a cloud drop distribution are often closely approximated by (e.g. Wiscombe *et al.*, 1984): $g \simeq 0.85$ for $2.0\mu m < \lambda < 1.5\mu m$, and $g \simeq 0.95$ for $1.5\mu m < \lambda < 2.0\mu m$. Because ω_o, O_3, and water vapour absorption are rapidly varying functions of λ, spectrally integrated net solar reflectance at the top of the atmosphere could be approximated as

$$\langle R(\mu_o)\rangle \simeq \left\{\left[S(\lambda_L) - S(\lambda_1)\right]N\right\}^{-1} \sum_{\ell=1}^{L} \left\{\left[S(\lambda_{\ell+1}) - S(\lambda_\ell)\right] \times \right.$$

$$\sum_{i=1}^{N} \exp[-\beta_{O_3}(\hat{\lambda})(\mu_o^{-1} + \mu_i^{-1})D]\, \omega_o(\hat{\lambda})^{n_i} \alpha_s(\hat{\lambda})^{m_i} \exp[-\beta_{H_2O}(\hat{\lambda})p_i] \times$$

$$\left.\left[1 - R_r(\hat{\lambda},\mu_o)\right]\left[1 - R_r(\hat{\lambda},\mu_i)\right] + R_r(\hat{\lambda},\mu_o)\right\}, \qquad (3.87)$$

where

$$\hat{\lambda} = \frac{\lambda_{\ell+1} + \lambda_\ell}{2},$$

N is the number of photons used, β_{O_3} and β_{H_2O} are ozone and water vapour spectral absorption coefficients, D is vertical depth of O_3, L is the number of spectral intervals, $S(\lambda)$ is the fraction of the solar constant at the top of the atmosphere at wavelengths less than λ, R_r is reflectance of the Rayleigh atmosphere and μ_i is the cosine of the zenith angle at which the i^{th} photon leaves cloud top. All other variables are as previously defined. Note that multiple reflections of photons between the upper molecular atmosphere and clouds have been neglected.

CHAPTER 4

Monte Carlo Photon Transport: Error Analysis and Model Validation

This chapter consists of three main sections. First, a method for assigning statistical error to radiative fluxes determined by a Monte Carlo code is derived. Second, the Monte Carlo code, presented in the previous chapter, is validated by comparing its flux estimates with published estimates for standard cloud configurations. Also, the model's ability to handle underlying reflecting surfaces is tested and the equivalence of the on–line and off–line droplet/surface absorption methods are demonstrate numerically. Third, a minor weakness of the code which was exposed by 'failure testing' the model is documented.

4.1 Error Analysis

In principle, the Monte Carlo technique of modelling radiative transfer is an *exact* method (Lenoble, 1977). On the other hand, it is essentially a statistical method; finite number of photons lead to random unbiased error in flux estimates. In this section, a simple method for predicting errors in Monte Carlo estimates of radiative flux is developed (Spanier and Gelbard, 1969; Davies, 1978).

Assuming that each photon history can be viewed as a Bernouili trial, this implies

1. that photons (trials) are statistically independent,
2. that photons have two possible outcomes: *succeeding* with probability p (exiting the cloud at a specific region and direction); *failing* with probability $1-p$ (the complement of a success),
3. that the probability of success remains constant for all trials (constant boundary conditions).

Assume that N photons are injected into the cloud or cloud field. Thus, the set of photons represent a random sample of size N. The values of the sample x_1, x_2, $\cdots$, x_N may be interpreted as respective values of a set of independent random variables $X_1, X_2, \cdots, X_N$ such that

$$X_i = \begin{cases} 0\,; \text{failure} \\ 1\,; \text{success} \end{cases} . \tag{4.1}$$

In random sampling, the density functions of all X_i equal the density function of the population. Hence, the sample mean, or best estimator, is also a random variable which is denoted and given by

$$E(X_i) \equiv \hat{P} = \frac{1}{N} \sum_{i=1}^{N} X_i = 1 \cdot p + 0 \cdot (1-p) = p \ , \tag{4.2}$$

The expected value of $\hat{P}$ is, therefore,

$$E(\hat{P}) = E\left[\frac{1}{N} \sum_{i=1}^{N} X_i \right] = \frac{1}{N} E\left[\sum_{i=1}^{N} X_i \right] \ , \tag{4.3}$$

which from Eq.(4.2) becomes

$$E(\hat{P}) = \frac{1}{N} Np = p \quad . \tag{4.4}$$

Since $\hat{P}$ is a random variable, its standard deviation is

$$\sigma(\hat{P}) = \left[\mathrm{Var}\left[\frac{1}{N} \sum_{i=1}^{N} X_i \right] \right]^{1/2} = \frac{1}{N} \left[\mathrm{Var}\left[\sum_{i=1}^{N} X_i \right] \right]^{1/2} \quad . \tag{4.5}$$

This can be further reduced to

$$\sigma(\hat{P}) = \frac{1}{N} \left[\sum_{i=1}^{N} \mathrm{Var}(X_i) \right]^{1/2} = \frac{1}{N} \left\{ \sum_{i=1}^{N} \left[E(X_i^2) - E^2(X_i) \right] \right\}^{1/2} \quad . \tag{4.6}$$

From Eq.(4.2) it is clear that $E^2(X_i) = p^2$. Also, since $X_i = 0$ or 1, so too does X_i^2. Hence, $E(X_i^2) = p$ and Eq.(4.6) simplifies to

$$\sigma(\hat{P}) = \frac{1}{N} \left[Np - Np^2 \right]^{1/2} = \left[\frac{p(1 - p)}{N} \right]^{1/2} \quad . \tag{4.7}$$

By virtue of the central limit theorem, when N is large, $\hat{P}$ will be distributed Gaussian–wise about p, the population mean, with standard deviation

$$\sigma(\hat{P}) \simeq \left[\frac{\hat{p}(1 - \hat{p})}{N} \right]^{1/2} \quad , \tag{4.8}$$

where $\hat{p}$ is the model predicted fractional flux. Equation (4.8) still holds when droplet and surface absorption are considered. $\sigma(\hat{P})$ is concave down, has a

maximum of $(4N)^{-1/2}$ at $\hat{p} = 0.5$, and a minimum of 0 at $\hat{p} = 0$ and 1. Equation (4.8) may be used as an indication of error around the estimated fractional flux. In this study, errors are expressed as $\hat{p} \pm \sigma(\hat{P})$.

Fractional error is defined as

$$f(\hat{P}) = \frac{\sigma(\hat{P})}{\hat{p}} = \left[\frac{1 - \hat{p}}{N\hat{p}}\right]^{1/2} . \qquad (4.9)$$

It is 0 at $\hat{p} = 1.0$ and infinite at $\hat{p} = 0$. A rough indication of the maximum fractional error encountered in this study is for $\hat{p} = 0.1$ and $N = 15{,}000$. This yields about a 2.7% error. Most often, however, the fractional error is less than 1.5%.

As pointed out by Davies (1978), Eq.(4.8) may be solved for N if one wishes to set an upper bound to $\sigma(\hat{P})$. For example, if one desires $\sigma(\hat{P})$ to be at most 0.001, this requires at least 250,000 photons/simulation.

4.2 Model Validation

The objective of this section is to validate the Monte Carlo code developed in this study. This is done by comparing its flux estimates with previously published Monte Carlo estimates. A series of increasingly elaborate tests are conducted in which each test incorporates and extends the previous test. The tests span a wide range of optical conditions and cloud configurations including tests of the model's ability to represent an underlying reflecting surface. The effects of droplet absorption on fluxes, however, have not been systematically studied. Therefore, droplet absorption is validated by comparing fluxes computed with the on–line (physical) and off–line (statistical) techniques (see section 3.4).

4.2.1 Isolated, Homogeneous Clouds

a) Cubic Clouds

The essence of the Monte Carlo code used in this study is photon transfer through individual, homogeneous, non–absorbing, cuboidal clouds. Two studies, frequently quoted as benchmark studies, that considered these conditions are those due to McKee and Cox (1974) and Davies (1978). McKee and Cox considered θ_0 of 0°, 30°, and 60° while Davies used 0° and 60° only. There are two minor differences among the three models. First, all three models use different single–scattering phase functions. This model utilizes the Henyey–Greenstein scattering phase function (see section 2.2). McKee and Cox used the non–analytic Dermendjian (1969) C.1 function which is an exact solution of Mie scattering for radiation at 0.45 μm incident on a droplet size distribution representative of fair weather cumulus. The asymmetry factor of the C.1 function at 0.45 μm is about 0.859. Davies employed the double Henyey–Greenstein phase function given by

$$P_{DHG}(\mu) = bP_{HG}(\mu, g_1) + (1 - b)P_{HG}(\mu, g_2) \quad , \tag{4.10}$$

with $b = 0.98$, $g_1 = 0.89$, and $g_2 = -0.66$ which gives an asymmetry factor of 0.859. Davies used this to mimic the strong forward scattering and slight backward scattering peaks displayed by the C.1 function. Due to the non–analytic equation which results from substituting their phase functions into Eq.(2.29), both McKee and Cox and Davies must have computed scattering angles based on either look–up tables or regression of the cumulative density function of scattering angle. Figure 4.1 shows a plot of $P_{DHG}(\mu)$ (which has gross features similar to the C.1 function though it lacks the narrow forward peak) used by Davies and $P_{HG}(\mu)$ with $g = 0.86$ used here by our model. The important differences are that $P_{DHG}(\mu)$ has more pronounced forward and backward scattering peaks and less

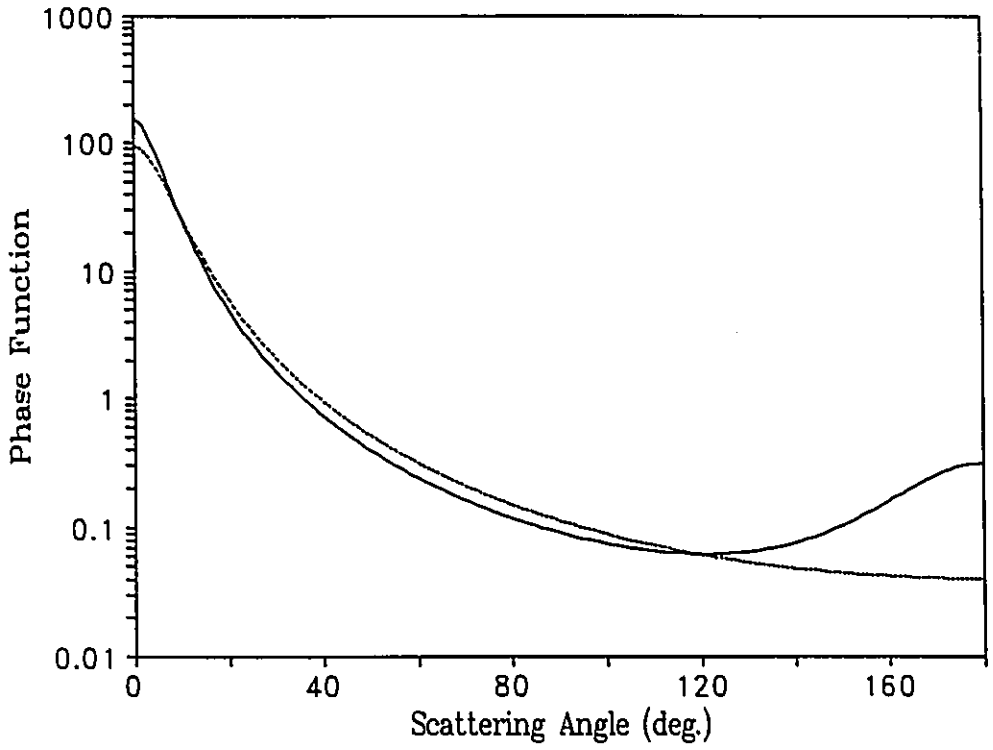

Fig.4.1. Solid line and dashed line are double Henyey–Greenstein phase function at g_1=0.89, g_2=–0.66, and b=0.98, and Henyey–Greenstein phase function at g=0.86 plotted as a function of scattering angle.

side scatter than does $P_{HG}(\mu)$. Second, McKee and Cox (1974) failed to accounted for photons that traverse the cloud space without encountering a single droplet. That is, they neglected direct beam transmittance. This is critically important at small cloud optical depth. The implications of this omission are apparent in their Figures 4, 5, and 6 where for $\tau \leq 10$ the total flux exiting the six cloud faces is less than unity. This violates conservation of energy since they used unit irradiance and $\omega_o = 1$. Also, for decreasing $\tau \leq 10$ with $\theta_0 = 60°$, their estimates of flux through the cloud sides decrease well below 0.60, while Davies's corresponding results remain constant at about 0.63. For $\tau \geq 20$ these problems are alleviated for McKee and Cox's and Davies's results agree. We, therefore, prefer to use Davies (1978) as the standard test for isolated clouds.

Table 4.1 contains results from nine tests of which the first six apply to cubic clouds. Listed are values of flux estimates obtained by our Monte Carlo code as well as the corresponding values read from Davies's Fig.4–7. The error associated with Davies's estimates as listed in Table 4.1, due to reading them from his figures, is about ±0.01. Each of our simulations used 25,000 photons. This usually leads to relative uncertainties in flux estimates of less than 1%. For $g = 0$ (isotropic scatter) with overhead sun and $\tau = 1.0$ (test 1) and 10.0 (test 2), there are no noticeable differences between the two models estimates. This validates the code in extreme scattering conditions. For $g = 0.86$, $\mu_0 = 1.0$, and $\tau = 5.0$ (test 3), there are marked differences between our results and those due to Davies (which are very similar to those of McKee and Cox). Our estimates of flux out the top and base of the cloud are significantly less than Davies's estimates. Subsequently, our estimate of total flux out the sides exceeds Davies's estimates. These differences can be explained by referring to differences in the phase functions (see Fig. 4.1). Evidently, at small τ, multiple scattering of photons is unable to completely eliminate subtle differences between phase functions.

Table 4.1

Radiative fluxes for isolated, homogeneous clouds predicted by the Monte Carlo code developed in this study (MONTE CARLO) and by Davies's (1978) Monte Carlo code (DAVIES). Errors associated with DAVIES are approximately ±0.01. τ_v and τ_h are vertical and horizontal cloud optical depths. τ_{cell} is optical depth of the cubes which makeup parallelepiped clouds in MONTE CARLO. For a list of the flux symbols see Fig.3.2. Note that $F_{S\uparrow} = \sum_i F_{\uparrow,i}$ and $F_{S\downarrow} = \sum_i F_{\downarrow,i}$

Test 1: $g = 0$; $\mu_\circ = 1.0$; $\tau = 1.0$; cube

Flux	MONTE CARLO	DAVIES
F_T	0.1234 ± 0.0021	0.12
F_B	0.4558 ± 0.0031	0.46
$F_{S\uparrow}$	0.1978 ± 0.0025	
$F_{S\downarrow}$	0.2230 ± 0.0026	
F_S	0.4208 ± 0.0031	0.42
$F_\uparrow$	0.3211 ± 0.0030	
$F_\downarrow$	0.6789 ± 0.0030	

Test 2: $g = 0$; $\mu_\circ = 1.0$; $\tau = 10.0$; cube

Flux	MONTE CARLO	DAVIES
F_T	0.5059 ± 0.0032	0.50
F_B	0.0165 ± 0.0008	0.015
$F_{S\uparrow}$	0.2142 ± 0.0026	
$F_{S\downarrow}$	0.2634 ± 0.0028	
F_S	0.4776 ± 0.0032	0.48
$F_\uparrow$	0.7201 ± 0.0028	
$F_\downarrow$	0.2799 ± 0.0028	

Table 4.1 (cont'n)

Test 3: g = 0.86; $\mu_\bullet = 1.0$; $\tau = 5.0$; cube

Flux	MONTE CARLO	DAVIES
F_T	0.0497 ± 0.0014	0.07
F_B	0.3697 ± 0.0031	0.40
$F_{S\uparrow}$	0.1140 ± 0.0020	
$F_{S\downarrow}$	0.4666 ± 0.0032	
F_S	0.5806 ± 0.0031	0.53
$F_\uparrow$	0.1637 ± 0.0023	
$F_\downarrow$	0.8363 ± 0.0023	

Test 4: g = 0.86; $\mu_\bullet = 1.0$; $\tau = 20.0$; cube

Flux	MONTE CARLO	DAVIES
F_T	0.1984 ± 0.0025	0.22
F_B	0.0727 ± 0.0016	0.08
$F_{S\uparrow}$	0.2369 ± 0.0027	
$F_{S\downarrow}$	0.4920 ± 0.0032	
F_S	0.7289 ± 0.0028	0.70
$F_\uparrow$	0.4353 ± 0.0031	
$F_\downarrow$	0.5647 ± 0.0031	

Test 5: g = 0.86; $\mu_\bullet = 0.5$; $\tau = 5.0$; cube

Flux	MONTE CARLO	DAVIES
F_T	0.0618 ± 0.0015	0.065
F_B	0.3086 ± 0.0029	0.31
$F_{S\uparrow}$	0.1453 ± 0.0022	0.14
$F_{S\downarrow}$	0.4843 ± 0.0032	
F_S	0.6296 ± 0.0031	0.63
$F_\uparrow$	0.2071 ± 0.0026	0.205
$F_\downarrow$	0.7929 ± 0.0026	

Table 4.1 (cont'n)

Test 6: g = 0.86; $\mu_\circ = 0.5$; $\tau = 20.0$; cube

Flux	MONTE CARLO	DAVIES
F_T	0.1708 ± 0.0024	0.17
F_B	0.2046 ± 0.0026	0.20
$F_{S\uparrow}$	0.2355 ± 0.0027	0.24
$F_{S\downarrow}$	0.3873 ± 0.0031	
F_S	0.6228 ± 0.0031	0.63
$F_{\uparrow}$	0.4063 ± 0.0031	0.41
$F_{\downarrow}$	0.5937 ± 0.0031	

Test 7: g = 0.86; $\mu_\circ = 1.0$; $\tau_{cell} = 5.0$, $\tau_v = 10.0$, $\tau_h = 100.0$

Flux	MONTE CARLO	DAVIES
F_T	0.3511 ± 0.0030	0.35
F_B	0.5197 ± 0.0032	0.52
$F_{S\uparrow}$	0.0444 ± 0.0013	
$F_{S\downarrow}$	0.0848 ± 0.0018	
F_S	0.1292 ± 0.0021	0.125
$F_{\uparrow}$	0.3955 ± 0.0031	
$F_{\downarrow}$	0.6045 ± 0.0031	

Test 8: g = 0.86; $\mu_\circ = 0.5$; $\tau_{cell} = 10.0$, $\tau_v = 50.0$, $\tau_h = 20.0$

Flux	MONTE CARLO	DAVIES
F_T	0.0910 ± 0.0018	0.09
F_B	0.1035 ± 0.0019	0.105
$F_{S\uparrow}$	0.3312 ± 0.0030	0.33
$F_{S\downarrow}$	0.4743 ± 0.0032	
F_S	0.8055 ± 0.0025	0.805
$F_{\uparrow}$	0.4222 ± 0.0031	
$F_{\downarrow}$	0.5778 ± 0.0031	

Table 4.1 (cont'n)

Test 9: g = 0.86; $\mu_\bullet = 0.5$; $\tau_{cell} = 1.0$, $\tau_v = 50.0$, $\tau_h = 20.0$

Flux	MONTE CARLO	DAVIES
F_T	0.0911 ± 0.0018	0.09
F_B	0.1019 ± 0.0019	0.105
$F_{S\uparrow}$	0.3299 ± 0.0030	0.33
$F_{S\downarrow}$	0.4770 ± 0.0032	
F_S	0.8070 ± 0.0025	0.805
$F_\uparrow$	0.4210 ± 0.0031	
$F_\downarrow$	0.5790 ± 0.0031	

Test 4 shows that if τ is increased to 20 with all else as in Test 3, the differences in fluxes predicted by the models are preserved qualitatively but their magnitudes have diminished significantly. It appears reasonable to assume that this trend is due to enhanced multiple scattering. On the other hand, returning to $\tau = 5.0$ but with $\mu_0 = 0.5$ (test 5), our estimates are virtually identical to Davies's estimates. This implies that for off–normal solar incidence, subtle differences in single–scattering phase functions are not important for flux calculations. With respect to test 5 conditions, McKee and Cox's estimates of flux out the base and sides of the cloud are significantly less than the other two model estimates. This is caused by neglect of direct transmittance which is important near the thin cloud edges. When τ is increased to 20 (test 6), however, significantly thin edges account for very little area and all three models are in excellent agreement.

b) Rectangular Clouds

Photon transfer in isolated, homogeneous, rectangular clouds is now considered. Reference is made to Davies's (1978) results exclusively since McKee and Cox (1974) only considered cubes. The following tests examine the ability of the Monte Carlo code to transport photons in media composed of contiguous, identical elemental cubes. Thus, we are testing both radiative transfer in a general cuboidal cloud as well as that part of the code which handles movement of photons amongst cubes. In all cases g = 0.86.

In the first case (test 7), radiation is normally incident on a moderately deep and horizontally extensive cloud (vertical optical depth $\tau_v = 10$; horizontal optical depth $\tau_h = 100$ in both directions). The cloud consists of cubes of optical depth 5.0; two cell layers thick and 20 cells in each horizontal direction (800 cubes in total). Our model and Davies's model are in excellent agreement. Note that clouds in Davies's model are single rectangular blocks and not constructed of

elementary cubes. Our model was re–run using individual rectangular clouds and the results (not shown) were statistically identical to those shown in Table 4.1. Tests 8 and 9 in Table 4.1 are for a deep, narrow cloud with $\tau_v = 50.0$ and $\tau_h = 20$ in both horizontal directions and $\mu_0 = 0.5$. The cloud in test 8 consists of 20 cubes of optical depth 10.0. The cloud in test 9 consists of 20,000 cubes of optical depth 1.0. The fluxes estimated using both cloud compositions agree with Davies's results to within experimental error. Test 9, however, required 46% more computer time than did Test 8.

In this section, it has been demonstrated that our Monte Carlo code can reproduce Davies's (1978) benchmark results for a wide variety of isolated cuboidal cloud forms irradiated at solar zenith angles of 0° and 60°. Though the model results tend to diverge in the case of solar radiation normally incident on cubic clouds of small optical depth, this divergence can be attributed to subtle differences in single–scattering phase functions.

4.2.2 Horizontally Infinite Arrays of Homogeneous Broken Cloud Above Reflecting Surfaces

In this section, the ability of the Monte Carlo code to compute reflected fluxes in horizontally infinite arrays of broken cloud above a reflecting surface is tested. This validates the cyclic boundary conditions of the code as well as the code's ability to represent photon transfer between clouds and the surface.

Welch and Wielicki (1989) and Kobayashi (1989) are the only Monte Carlo cloud/radiation studies that have focused on how surfaces affect fluxes for broken cloud. If their surface reflection function [Eq.(3.47)] is included in our code, it should reproduce their results. We refer exclusively to Welch and Wielicki's work on account of their more straightforward presentation of results. Welch and Wielicki's Monte Carlo model was constructed to specifically examine horizontally

infinite regular arrays of clouds (see Fig.4.2). As such, their code is very different from ours in that it contains one cloud, a cloudless region around the cloud, and a well defined shadow region on the clouds side cast by the neighbouring cloud. They used $\omega_0 = 1.0$ and Henyey–Greenstein phase function at g = 0.86. Their clouds were 1 km cubes of optical depth between 5 and 50 with constant base height of 1 km. Solar zenith angles were 0° and 60°. Scattering and absorption by atmospheric gases were neglected. Welch and Wielicki did not indicate how many photons/simulation they used. In our simulations 15,000 photons are used in the off–line absorption mode.

Twenty different conditions are considered: $\mu_0 = 1.0$, 0.5, and $\alpha_s = 0$, 0.1, 0.2, 0.3, 0.5 for $\tau = 5$ with $A_c = 0.735$, and $\tau = 20$ with $A_c = 0.25$. Table 4.2 lists the results of the comparison. Welch and Wielicki's values were read from their Fig.3. We, therefore, assume an error of about ±0.01. The comparison shows that the models agree on reflected fluxes to within experimental error for a wide variety of cloud and surface albedo scenarios.

4.2.3 Equivalence of On–Line and Off–Line Absorption

Three examples are used to demonstrate numerically the statistical equivalence of the on–line and off–line methods of accounting for absorption of radiation by droplets and the surface (see section 3.4).

All clouds are 1 km homogeneous cubes with base height of 1 km over a simple reflecting surface of the type used by Welch and Wielicki (1989) and Kobayashi (1989). Table 4.3 shows the cloud field generators used in the tests and lists the experimental attributes and results for both on–line and off–line techniques. Clearly, both techniques yield statistically identical results.

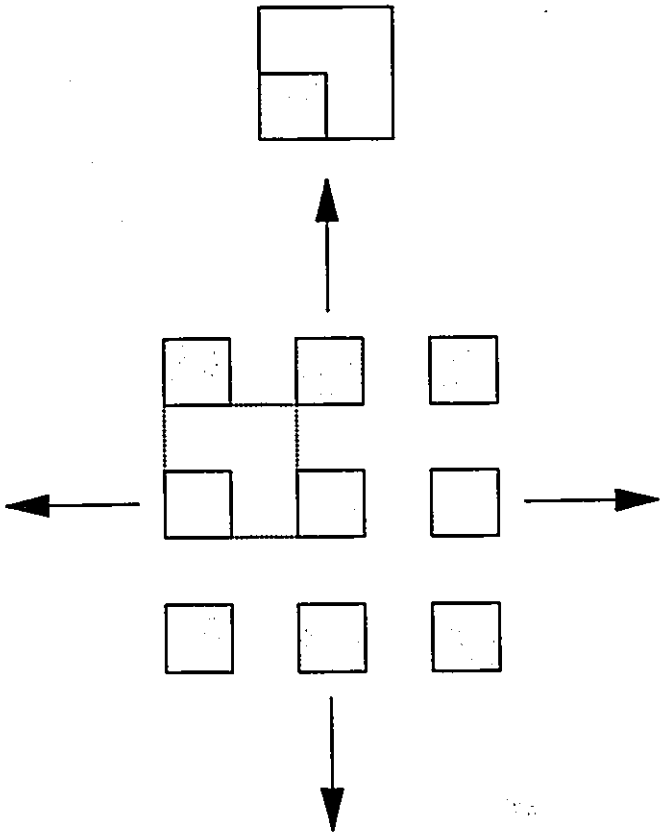

Fig.4.2. Diagram at the top is a schematic of a cyclic generator $\mathcal{R}$ for a regular array of cuboidial clouds (shaded region). If $\mathcal{R}$ is repeated infinitely many times in all horizontal directions, $\mathcal{R}^{\infty}$ is generated of which only a portion is shown in the lower part of the diagram.

Table 4.2

Reflected fluxes predicted by this study's model (MONTE CARLO) and Welch and Wielicki's (1989) model (WW). Clouds are 1 km cubes with $\omega_0 = 1$ and 1 km base height arranged in an infinite regular array above the surface defined by Eq.(3.46). Errors associated with WW are approximately ±0.01.

1. $\tau = 20$, $A_c = 0.25$

	$\mu_s = 1.0$	
Surface Albedo	MONTE CARLO	WW
0.0	0.118 ± 0.003	0.12
0.1	0.189 ± 0.003	0.19
0.2	0.263 ± 0.004	0.26
0.3	0.339 ± 0.004	0.33
0.5	0.503 ± 0.004	0.49

	$\mu_s = 0.5$	
Surface Albedo	MONTE CARLO	WW
0.0	0.266 ± 0.004	0.26
0.1	0.324 ± 0.004	0.31
0.2	0.383 ± 0.004	0.38
0.3	0.446 ± 0.004	0.44
0.5	0.580 ± 0.004	0.57

Table 4.2 (cont'n)

2. $\tau = 5$, $A_c = 0.735$

	$\mu_\bullet = 1.0$	
Surface Albedo	MONTE CARLO	WW
0.0	0.145 ± 0.003	0.14
0.1	0.206 ± 0.003	0.20
0.2	0.270 ± 0.004	0.27
0.3	0.339 ± 0.004	0.34
0.5	0.493 ± 0.004	0.49

	$\mu_\bullet = 0.5$	
Surface Albedo	MONTE CARLO	WW
0.0	0.341 ± 0.004	0.35
0.1	0.386 ± 0.004	0.38
0.2	0.435 ± 0.004	0.43
0.3	0.487 ± 0.004	0.49
0.5	0.605 ± 0.004	0.60

Table 4.3

Reflected radiative fluxes estimated using the on–line and off–line absorption techniques. The conditions in simulation A, B, and C are listed below the table.

simulation	1 (on–line)	2 (off–line)
A	0.5653 ± 0.0040	0.5613 ± 0.0041
B	0.3021 ± 0.0037	0.2985 ± 0.0037
C	0.2403 ± 0.0035	0.2353 ± 0.0035

A	B	C
$\omega_o = 0.99$	$\omega_o = 0.9$	$\omega_o = 0.99$
$\tau = 10$	$\tau = 30$	$\tau = 5$
$A_c = 0.5$	$A_c = 0.25$	$A_c = 1.0$
$\mu_o = 0.5$	$\mu_o = 0.5$	$\mu_o = 1.0$
$\alpha_s = 0.5$	$\alpha_s = 0.75$	$\alpha_s = 0.1$

4.3. Failure Testing

Johnson (1976) maintained that validation of a numerical model is only partially fulfilled by comparing its performance with existing results. Even if the comparison is perfect, conditional typographical, numerical, and logical errors may still exist in the code. Furthermore, fundamental logical errors in the approach to modelling the processes may exist and go unnoticed indefinitely in an otherwise working code. Johnson proposed that the code should be *pushed* to unrealistic extremes, for often logic can predict what the outcome should be. If the code fails, either something is wrong with the logic used to construct the code, or something is wrong with the logical deduction of what the extreme outcome should be. The Monte Carlo code was pushed in a number of extreme directions and only one logical shortcoming was found.

The extreme and unrealistic cases reported here have to do with unconditional forward and backward scattering particles. There is no problem with perfectly forward scattering particles (g=1.0). The transmittance predicted by the Monte Carlo code is identical, within experimental error, to that which leads directly from the radiative transfer equation:

$$T(\omega_0,\mu_0,\tau) = e^{-(1-\omega_0)\tau/\mu_0} \quad . \tag{4.11}$$

Reflectance predicted by the Monte Carlo code is, as expected, zero.

When g=–1.0, particles are completely backscattering. In this case, common sense leads to expression for transmittance and reflectance of

$$T(\omega_0,\mu_0,\tau) = e^{-\tau/\mu_0} \quad , \tag{4.12a}$$

and

$$R(\omega_0,\mu_0,\tau) = \omega_0\left[1 - e^{-\tau/\mu_0}\right] \quad . \tag{4.12b}$$

Since photons are either absorbed or scattered directly backwards, the only photons that penetrate to cloudbase are those that do not interact with matter. Hence, transmittance must follow Beer's Law. The reflectance expression is rationalized as follows: photons that are not directly transmitted [the bracketed term in Eq.(4.12b)] and survive their one and only collision (with probability of ω_0) will escape unattenuated back along their line of entry. This is an extreme case of the opposition effect. This, however, is not what occurs in the Monte Carlo code. Instead, a photon that is not directly transmitted to cloudbase penetrates the cloud to random depth s where it undergoes a scattering event. The photon is scattered backwards and traverses a random length s′. If s′ < s, a second scattering event occurs and the photon is scattered back into the cloud along it's original path. If s′ > s, the photon escapes by the preferential escape mechanism. In general, a photon will trace out a *jittery* back and forth trajectory along a line–of–sight before emerging from the cloud. Note that photons can escape through cloudbase after undergoing many scattering events. This contradicts the logic which lead to Eq.(4.12b). In fact, reflectance and transmittance are independent of τ.

The magnitude of this logical oversight decreases sharply with increasing g. Since g ≃ 0.85 for clouds, we expect no difficulty (see Fig.4.1). It does, however, suggest that a small correction should be made to the model: if the scattering angle θ_s is close to 180°, instead of moving the photon a random distance, it should be moved directly back to its previous scattering event and rescattered. This may be important for Monte Carlo simulations of radiation transport in stars.

In summary, this chapter established a means of assigning statistical error to radiative fluxes predicted by a Monte Carlo code. Also, an extensive validation process was carried out on the Monte Carlo code which was developed in the previous chapters. In all of the tests, ranging from simple isolated cubic clouds to fields of interacting clouds, the model was able to reproduce published results to within experimental error which is generally less than 1%. Furthermore, when our model was equipped with the surface used by Welch and Wielicki (1989) [and Kobayashi (1989)], it reproduced their results to within experimental error. The equivalence of the on–line and the off–line techniques of accounting for droplet and surface absorption was demonstrated numerically. Finally, we discussed the performance of the code to *failure testing* and showed that it is logically unsound in the regime of near–perfect backscattering. While the problem is trivial for our purposes, the failure testing process nevertheless exposed a conditional logic error in the code.

CHAPTER 5

Results and Discussion

The models presented in this thesis are employed in this chapter to calculate solar radiative fluxes for various cloud fields. This chapter consists of three main sections. The first section addresses concerns regarding statistical significance of fluxes for extensive model cloud fields and the representativeness of individual realizations of the scaling cloud field models. The second section presents results of an intercomparison of fluxes for various cumuloform cloud field configurations. Also, it examines some radiative properties associated with the scaling cumulus cloud models. In the third section, some properties of fluxes for broken cloud above reflecting surfaces are examined.

5.1 Statistical Considerations

5.1.1 Required Number of Photons per Simulation

Whenever analytic solutions are abandoned and Monte Carlo simulations adopted, experimental accessibility is gained at the expense of computation (CPU) time. Therefore, before experimentation, one should try to assess how many photons per simulation are required to achieve satisfactory estimates of fluxes.

The number of photons per simulation used in previous studies varies from 1,000 to 100,000. In Chapter 4, the Monte Carlo code was validated using 15,000 – 25,000 photons per simulation. Such a small number was justified since the

reference data were either computed with a similar number of photons per simulation or read from graphs which incurred a fairly large error. The simulations proposed in this chapter involve cloud fields consisting of up to 65,536 pixels (256x256 arrays) in a horizontal plane. Since 10^5 photons per simulation injected into a 256x256 array means that on average each cell is irradiated by about 1.5 photons only, one may be concerned whether adequately sampling of the fields is tractable.

To test sampling adequacy, ten simulations with 10^5 photons/simulation were conducted using a very irregular 256x256x1 cloud field array produced by the variable cloud model [Eq.(2.49)]. Figure 5.1 shows the inhomogeneous cloud field and two horizontal transects. The field was produced such that at large scales ($k \leq 10$) vertical optical depth is approximately white noise while at smaller scales ($k > 10$) $\langle S_k \rangle$ follows $k^{-1.25}$. Each pixel represents a cube with an average cloud optical depth of 10 (maximum is 60). Normal projected cloud amount is 0.5. Single–scattering albedo and asymmetry factor for cloud droplets are 1.0 and 0.86. Two cases are considered: $\theta_0 = 0°$ and 60°. During each simulation, reflectance was calculated every 10^3 photons. Then, the average and standard deviation of the ten simulations were computed after every 10^3 photons.

Figure 5.2 shows the mean reflectances plus and minus experimental standard deviation (solid lines) and theoretical standard deviation (dashed lines). Theoretical standard deviations were calculated by assuming that each photon is a Bernoulli trial [see Eq.(4.8)]. The plots suggest that the fields are sampled adequately for the experimental errors are systematically *less* than the theoretical errors. Figure 5.3 shows the theoretical and experimental standard deviations. In theory, the standard deviation is proportional to $N^{-1/2}$, where N is the number of photons injected. Figure 5.3 suggests that experimental error decreases faster with respect to N ($\sim N^{-0.6}$) than does the theoretical error. Similar results were

Fig.5.1. (a) False grey image of a variable cloud field with $\langle S_k \rangle \sim k^{-0}$ for $k \leq 10$ and $k^{-1.25}$ for $k > 10$. $A_c = 0.5$ and average optical depth is 10. (b) Transects of optical depth along scan lines indicated on (a). Transects start at the base of the image.

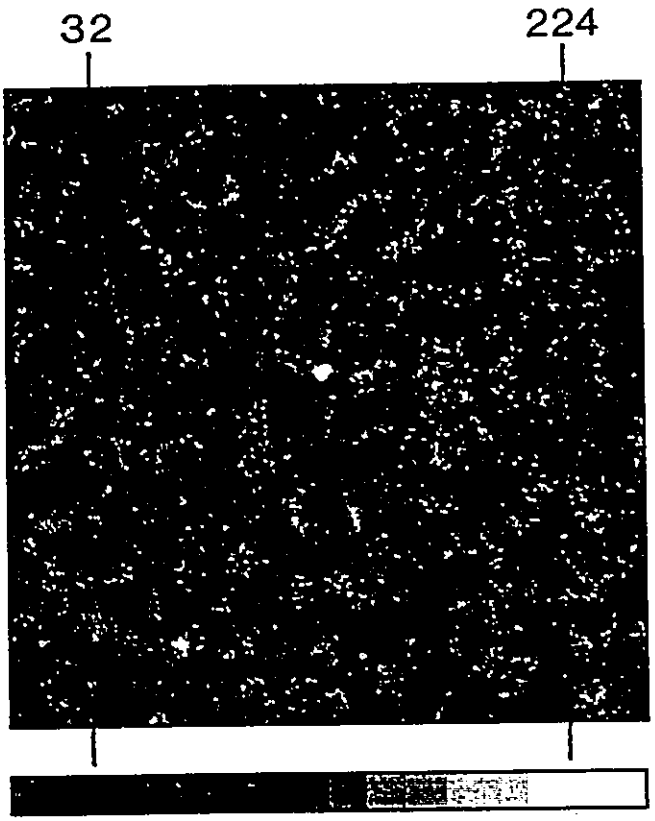
32
224

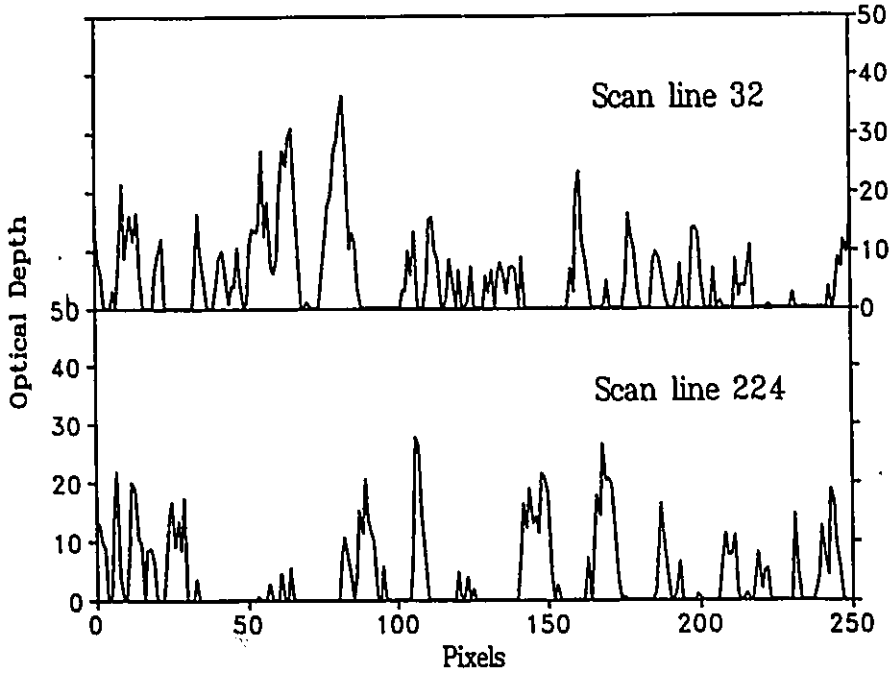
Optical Depth
Scan line 32
Scan line 224
0
10
20
30
40
50
0
50
100
150
200
250
Pixels

Fig.5.2. (a) Mean reflectance (centre line) for ten simulations using the cloud field shown in Fig.5.1a. Solid lines on either side of the mean indicate the width of one standard deviation for the ten reflectances. Dashed lines represent the width of the standard Monte Carlo error as expressed in Eq.(4.8). Solar zenith angle is 0°. (b) As in (a) except solar zenith angle is 60°.

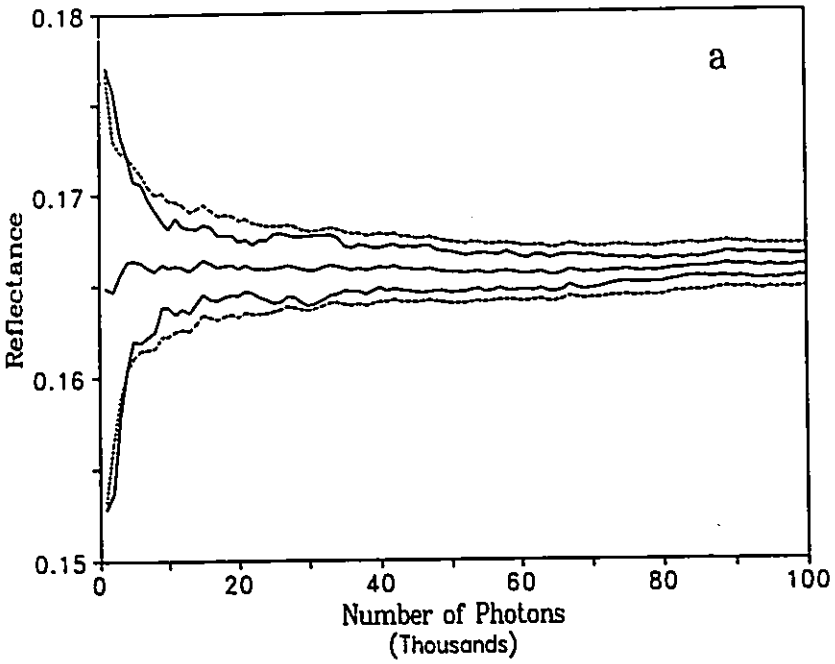
a
Reflectance
0.18
0.17
0.16
0.15
0
20
40
60
80
100
Number of Photons
(Thousands)

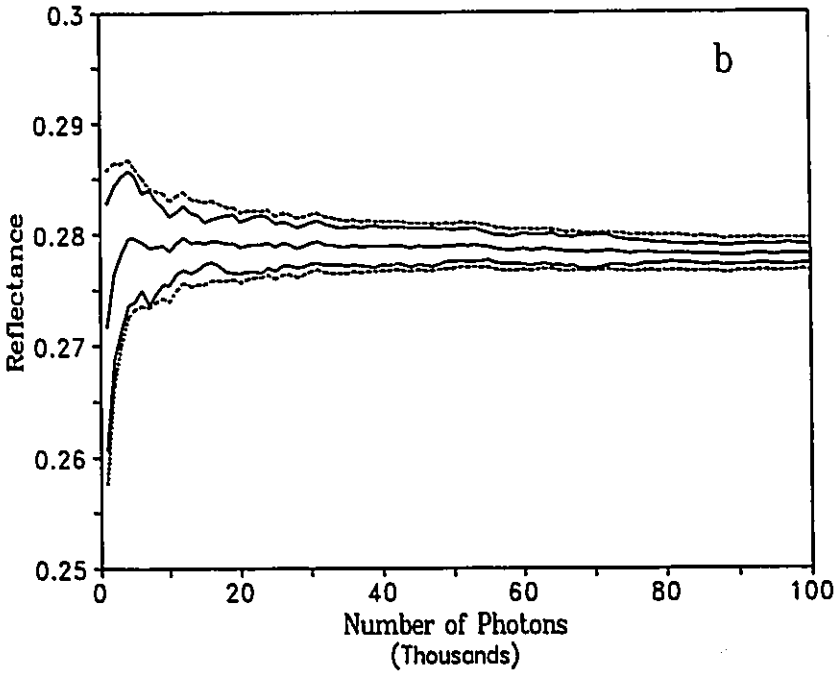
b
Reflectance
0.3
0.29
0.28
0.27
0.26
0.25
0
20
40
60
80
100
Number of Photons
(Thousands)

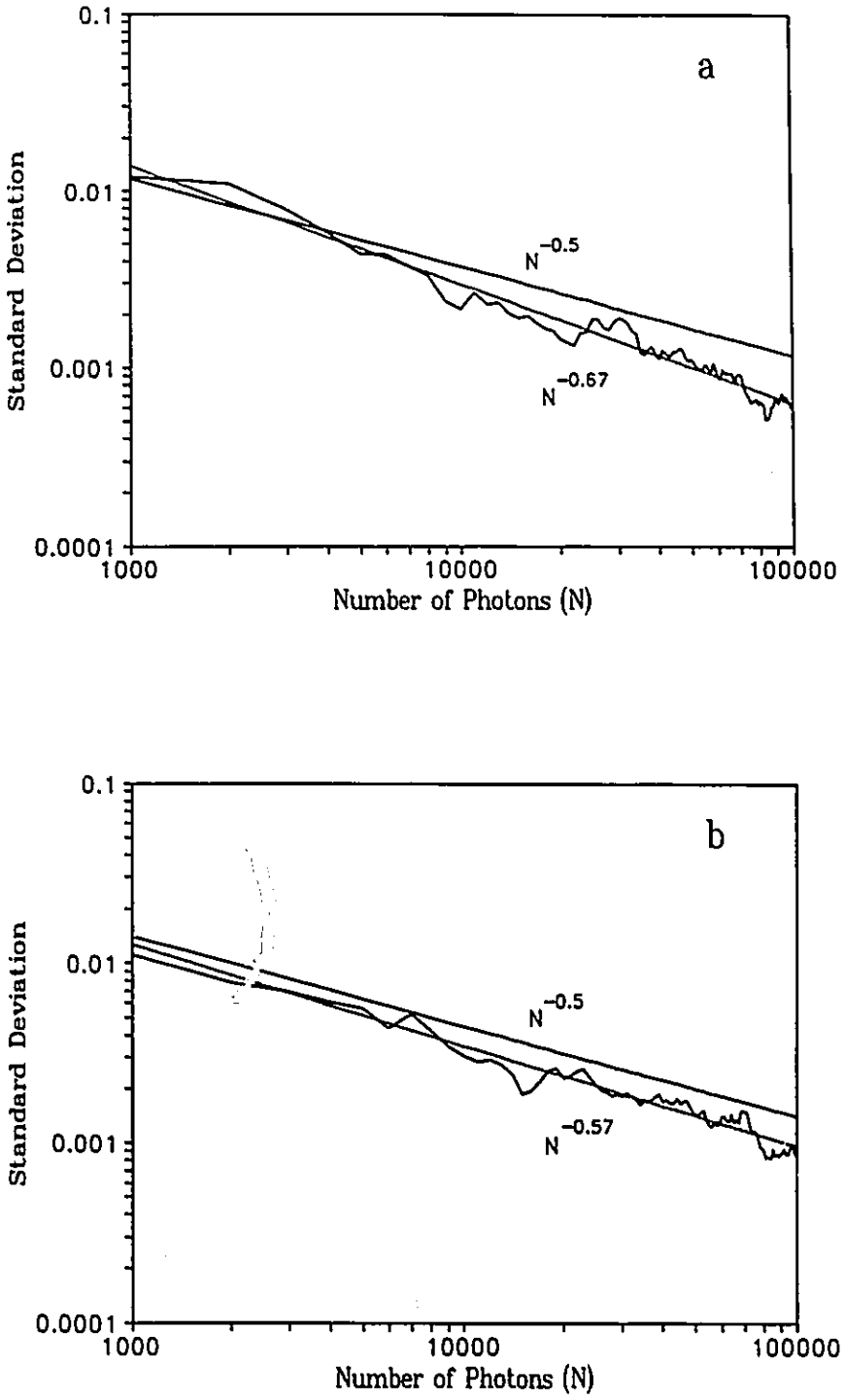

Fig.5.3. (a) Variation of standard deviation of reflectance as a function number of photons injected. Solid straight line is the theoretical standard deviation of reflectance for the ten simulations in Fig.5.2a. Jagged curve is the experimental standard deviation and the dashed line is its best–fit line. (b) As in (a) except refers to Fig.5.2b.

obtained for other experiments. Thus, it appears that satisfactory flux calculations for detailed cloud fields can be achieved using as few as 50,000 photons per simulation. This is an important result which should dispell the myth (e.g. Fouquart *et al.*, 1990) that Monte Carlo simulations are restricted to studies of regular arrays of clouds.

5.1.2 Representativeness of a Single Realization of the Cloud Model

The cloud models presented and used in this study are essentially stochastic. Therefore, several cloud fields generated by the same scaling filter, and having the same vertically projected cloud amount and mass of liquid water, can have different configurations. It would be convenient, especially for parameterization purposes, if all realizations of a particular cloud field yield statistically the same radiative fluxes. One method for testing whether this is the case involves; (1) generating several cloud fields all of which have the same spectral properties, liquid water mass, and cloud amount; (2) computing reflectance for each field; (3) calculating the standard deviation of reflectances; and (4) comparing it with the theoretical standard deviation for a single experiment [Eq.(4.8)]. If they are comparable in magnitude, individual realizations of a cloud field adequately represent the typical cloud field.

This procedure was carried out using ten realizations of two substantially different cloud fields. The first set of clouds were generated using $\langle S_k \rangle \sim k^{-1} \; \forall \; k$, $A_c = 0.25$, and $\langle \tau \rangle = 10$. The second set of clouds has $\langle S_k \rangle \sim k^{-0}$ for $k \leq 5$ and $k^{-1.3}$ elsewhere, $A_c = 0.4$, and $\langle \tau \rangle = 15$. In both cases, individual clouds are cubes and the fields are of the variable cloud type. Figure 5.4 shows mean reflectance plus and minus the standard deviation for the two experiments. Each simulation used 50,000 photons. The magnitude of the reflectance standard deviations are almost identical to the theoretical standard deviations associated

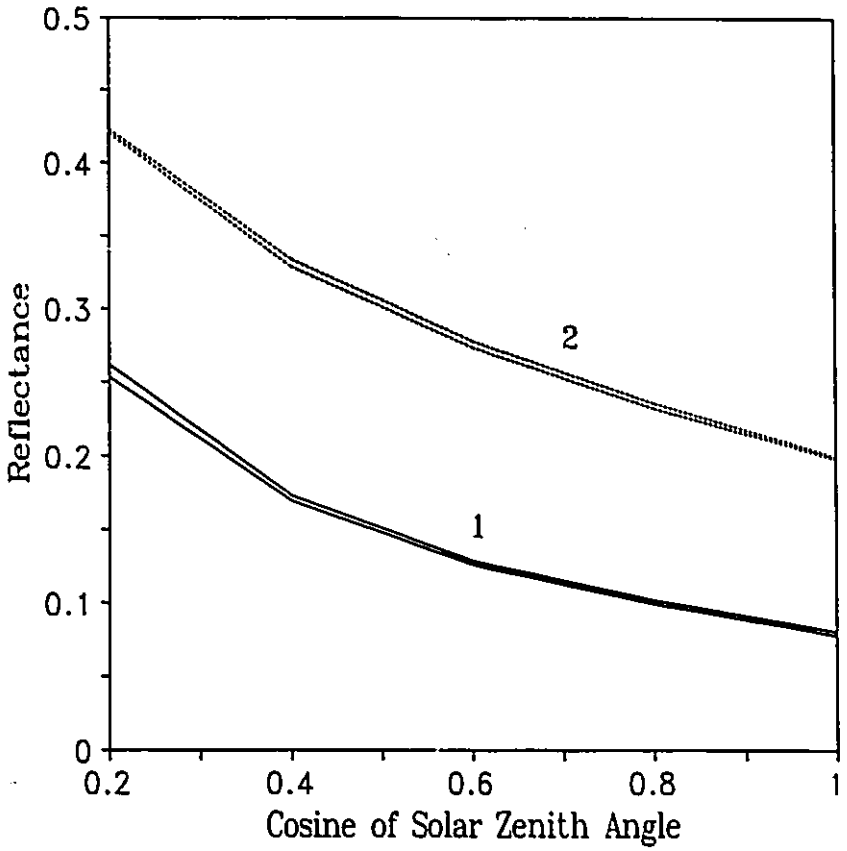

Fig.5.4. Solid curves indicate the width of one standard deviation about the mean reflectance of ten realizations of the variable cloud field model in which the cloud fields are all characterized by $\langle S_k \rangle \sim k^{-1} \; \forall \; k$, $A_c = 0.25$, and average optical depth of 10. Dashed curves are the same as the solid curves except they apply to cloud fields with $\langle S_k \rangle \sim k^{-0}$ for $k \leq 5$ and $k^{-1.3}$ for $k > 5$, $A_c = 0.4$, and average optical depth of 15.

with the Monte Carlo simulation of one realization (0.0015 and 0.002 for curves 1 and 2). This suggests that the fluxes for a single realization of a particular cloud field should be representative of all realizations.

A more demanding test for the representativeness of a single realization involves comparing fluxes associated with a cloud field produced by one of the models presented in Chapter 2 with fluxes associated with a cloud field produced by an altogether different model where both fields have similar attributes. The alternate model used here is a modified version of the two–dimensional discrete mono–fractal β–model (Mandelbrot, 1974). This model begins with a uniform region which is subdivided successively such that after M subdivisions $(2)^{2M}$ cells exist. As each parent cell divides into four off–spring, the probability of an off–spring surviving (not setting extinction coefficient to zero) is $(0.5)^c$ where c is the co–dimension of the fractal set that would emerge if $M \to \infty$. Figure 5.5a and b show realizations of the β–model ($c = 0.25$) and the identical cloud model in which both fields have $A_c = 0.27$ and $\langle S_k \rangle \sim k^{-0.88}$. Although the fields in Fig.5.5 have similar spatial statistics, they look different.

Figure 5.6 shows reflectances for the fields shown in Fig.5.5. The curves labelled 1 refer to cloud cells as cubes with $\tau = 10$ while the values for curves labelled 2 were computed using the cells as rectangles with horizontal and vertical optical depths of 3 and 10 respectively. Hence the cloud fields in simulation 2 have effective aspect ratios over three times those in simulation 1. For each value of μ_o, 50,000 photons were injected and the solar azimuth was allowed to vary randomly. The fact that both fields produce almost identical reflectances suggests that solar radiative fluxes are fairly insensitive to specific arrangements of cloud. These results are remaniscent of statistical mechanics where different configurations of a systems elcmentary constituents (cloud cells) do not influence macroscopic properties (fluxes).

Fig.5.5. (a) Single realization of the identical scaling cloud model in which $A_c = 0.27$ and $\langle S_k \rangle \sim k^{-0.88}$. All cloudy pixels (white) have optical depth of 10. (b) As in (a) except the field was produced with the modified mono–fractal model using $c = 0.25$.

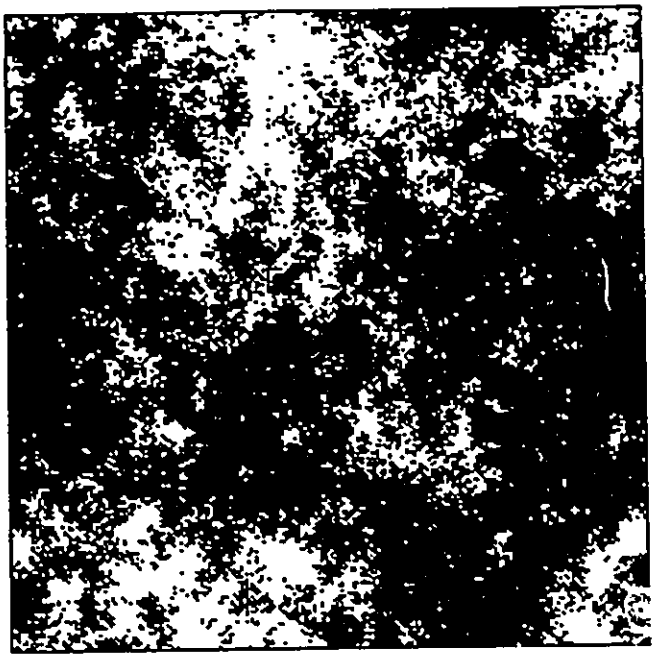

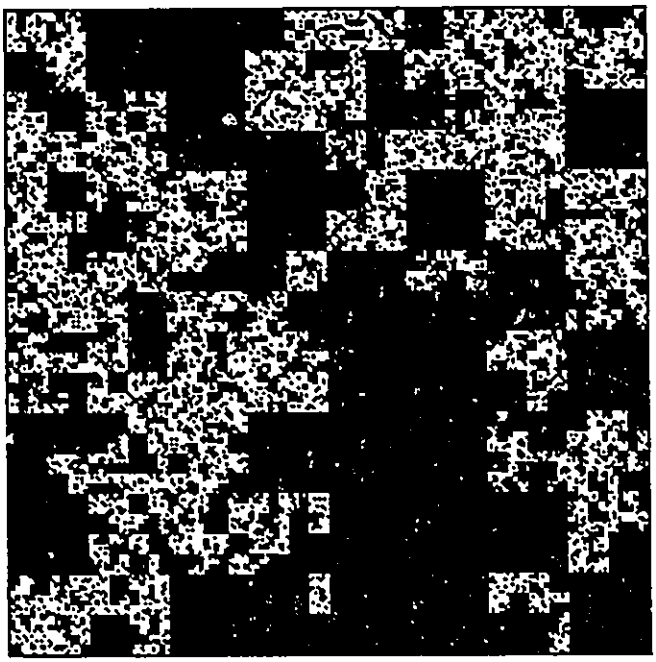

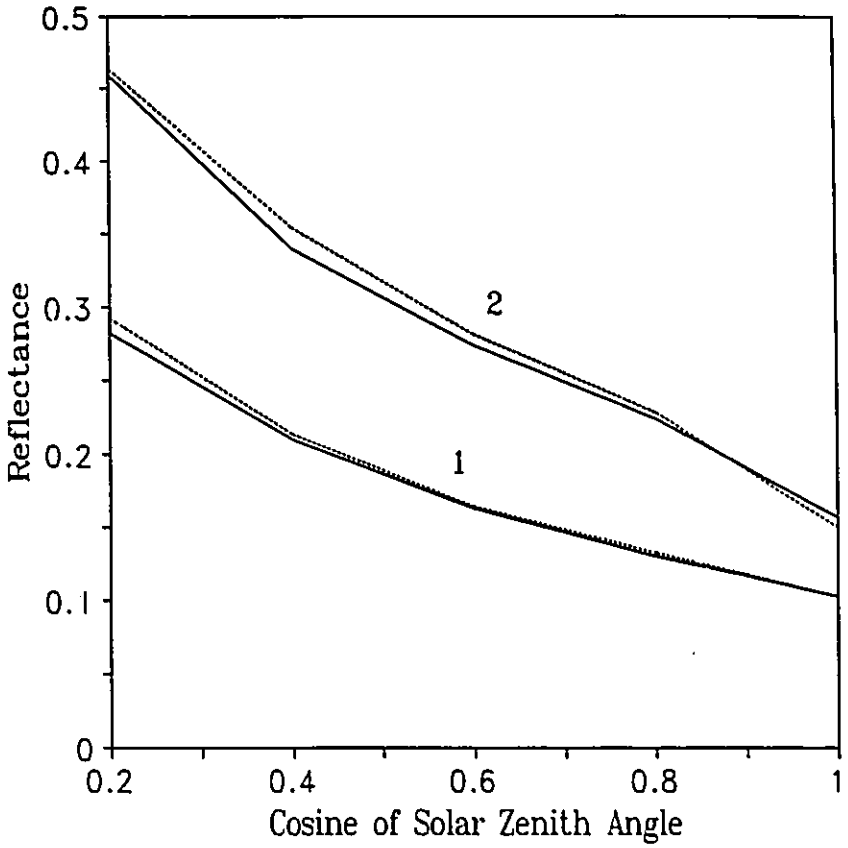

Fig.5.6. Reflectances of the cloud fields shown in Fig.5.5 as a function of μ_0. Dashed and solid lines are for the β–model and the identical scaling model respectively. The pair of curves labelled (1) are for individual cloud cells as cubes with $\tau = 10$. Curves labelled (2) are for rectangular cloud cells with aspect ratio 3.33 and vertical optical depth still 10.

5.2 Solar Radiative Fluxes Associated with Broken, Scaling Cloud Fields

This section has two main parts. First, radiative fluxes due to scaling cumulus cloud fields are compared with fluxes associated with broken cloud models used in previous studies. Second, properties of fluxes for broken, scaling cloud fields are examined in detail.

5.2.1 Intercomparison of Fluxes for Various Broken Cloud Models

Cloud fields examined in this section are plane–parallel, regular (e.g. Welch and Wielicki, 1984), random (e.g. Kobayashi, 1988), and scaling [Eqs. (2.49) and (2.50)] arrays. The potential range of experiments involving these few types of cloud geometry is vast and an exhaustive investigation is not attempted here. Instead, this section presents a limited, yet representative, set of results highlighting the important differences and similarities between fluxes predicted for the various cloud geometries. Attention is restricted to fields that are homogeneous at scales less than about 0.3 km. Therefore, internal variability of clouds is not considered. Inclusion of small scale variability appears to be very important (Davis *et al.*, 1990) and is presently being investigated by the author outside the realm of this thesis.

All cloud fields in a single intercomparison have the same vertically projected cloud fraction and all cells in a cloud field with $\beta \neq 0$ are assumed to be uniformly filled with the same cloud droplet size distribution. Hence, differences in optical depth of cells are attributed to variable density of liquid water; this implies that ω_0 and g do not vary from cell to cell. In all cases $\omega_0 = 1.0$, $g = 0.86$, and the Henyey–Greenstein phase function is used. Also, in a single experiment all non–plane–parallel geometries have the same total mass of liquid water in the field and are characterized by cyclic boundary conditions. This, taken with the restriction on vertically projected cloud fraction, implies that all geometries have

the same vertically integrated optical depth averaged over the entire field. By definition, plane–parallel clouds have infinite mass and no sides. Thus, when they are used as an approximation to broken cloud, their fluxes are calculated with the average optical depth of cloud in the truely broken cloud cases and multiplied by the vertically projected cloud fraction. In this study, all plane–parallel fluxes are calculated with the delta–Eddington model (Joseph *et al.*, 1976) because it is computationally efficient and used throughout climate studies. These specifications ensure that only differences in cloud field geometry are being compared.

Wielicki and Welch (1986) used high resolution (~ 30m) LANDSAT data to show that in large images (greater than about 150x150 km) containing cumulus, clouds with diamters less than about 0.5 km often contribute little to the total cloud amount. Therefore, it may be expected that small clouds often contribute little to radiative fluxes for the cloud field also. Thus, because of Wielicki and Welch's results, the aims of the thesis to study clouds fields about the size of GCM grid–boxes, and computer limitations, standard photon transport experiments will be conducted with no more than 256x256 (cyclic) arrays of cells with each cell representing about 0.3 to 1.0 km horizontally. In actuality, specification of the spatial scale is irrelevant here since extinction coefficient is arbitrarily variable and the radiative transfer process does not depend directly on geometric length. The only reason space scales are mentioned is because of the aims of the study, and because, to some extent, cloud fields will be generated to loosely mimic the AVHRR results of Section 2.4.

First, before beginning the full intercomparison, consider the following example which illustrates the wealth of unexplored (or unreported) radiative properties of broken cloud. It involves the simple, commonly studied, regular array of identical cubic clouds. Experimenters have shone the sun down the clear streets between clouds with a solar azimuth of $\varphi_0 = n\pi/2$ (n=0,1,2,...). Figure 5.7 shows

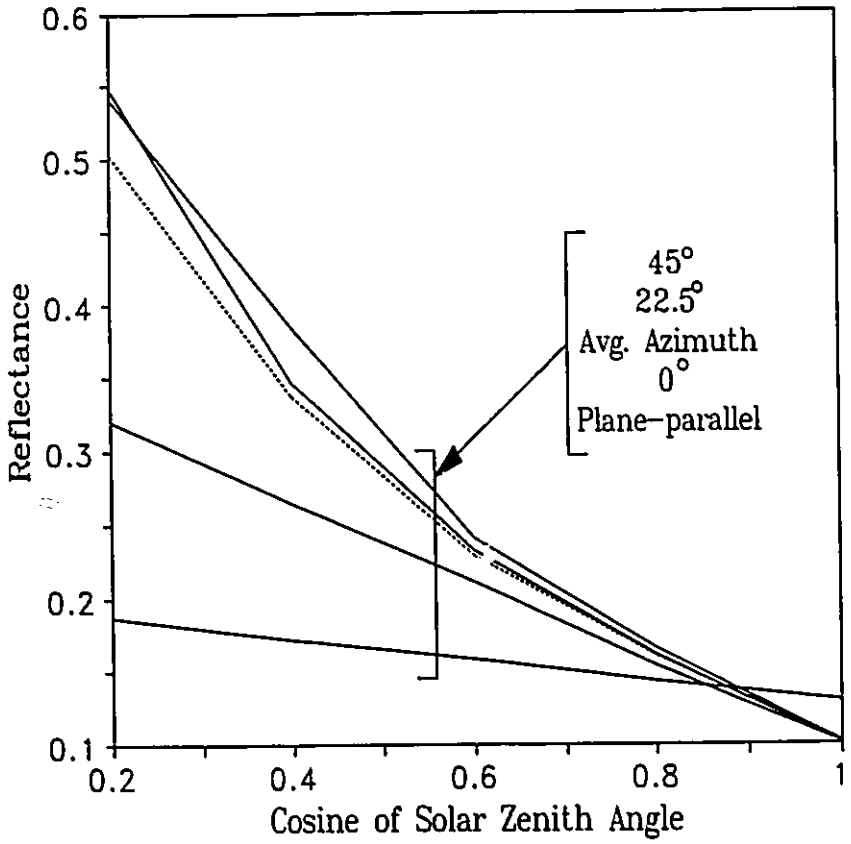

Fig.5.7. Reflectance as a function of solar zenith angle at several solar azimuth angles for a regular array of cubic clouds with optical depth 15 and A_c = 0.25.

an example of how reflectance for a regular array varies with φ_0. The cloud field is periodic and symmetric in φ_0 with period $\pi/2$ rds. Hence, $\varphi_0 = 0$, $\pi/8$, $\pi/4$, and the azimuthally averaged case are shown. At $\mu_0 \leq 0.5$, reflectances for $\varphi_0 = 0$ exceed plane–parallel estimates by about the same amount that they are exceeded by the azimuthally averaged case. Since the azimuthally averaged case may be interpreted as the typical case, it is doubtful that results from previous studies satisfactorily represent fluxes for regular arrays of cubes. Therefore, even simple regular arrays exhibit *much* more variability than has been recognized previously.

The first experiments in this intercomparison examine the effects that different cloud patterns have on reflected fluxes. Thus, the identical scaling cloud model will be used and horizontal variability is not considered. Figure 5.8 shows reflectances as a function of μ_0 with $A_c = 0.25$ and 0.45 and $\tau = 10$ and 50 for two different scaling fields ($\langle S_k \rangle \sim k^{-1}$ and $k^{-5/3}$); a random array (k^{-0}); a regular array ($\varphi_0 = 0$) of cubes; and plane–parallel clouds. Some common features of the plots are now discussed.

At overhead sun, the regular array always has the smallest reflectance while the plane–parallel cloud has the largest; all scaling fields have reflectances between these extremes with reflectance increasing with the magnitude of the scaling exponent. Within the regular array, all clouds have four exposed side faces and thus the effective cloud aspect ratio averaged over the field is 1.0. Davies (1978) and Welch and Wielicki (1984) showed that the larger a cloud's aspect ratio, the greater the proportion of radiation that escapes through the sides. Also, most of the escaping photons travel downward and either pass to the surface and are absorbed or are intercepted near the base of neighbouring clouds and thus stand a strong chance of being transmitted to the surface. Thus, due to a large area of cloud sides, regular arrays of clouds are very effective in channelling photons to the surface at high sun. Plane–parallel clouds, on the other hand, have no sides so

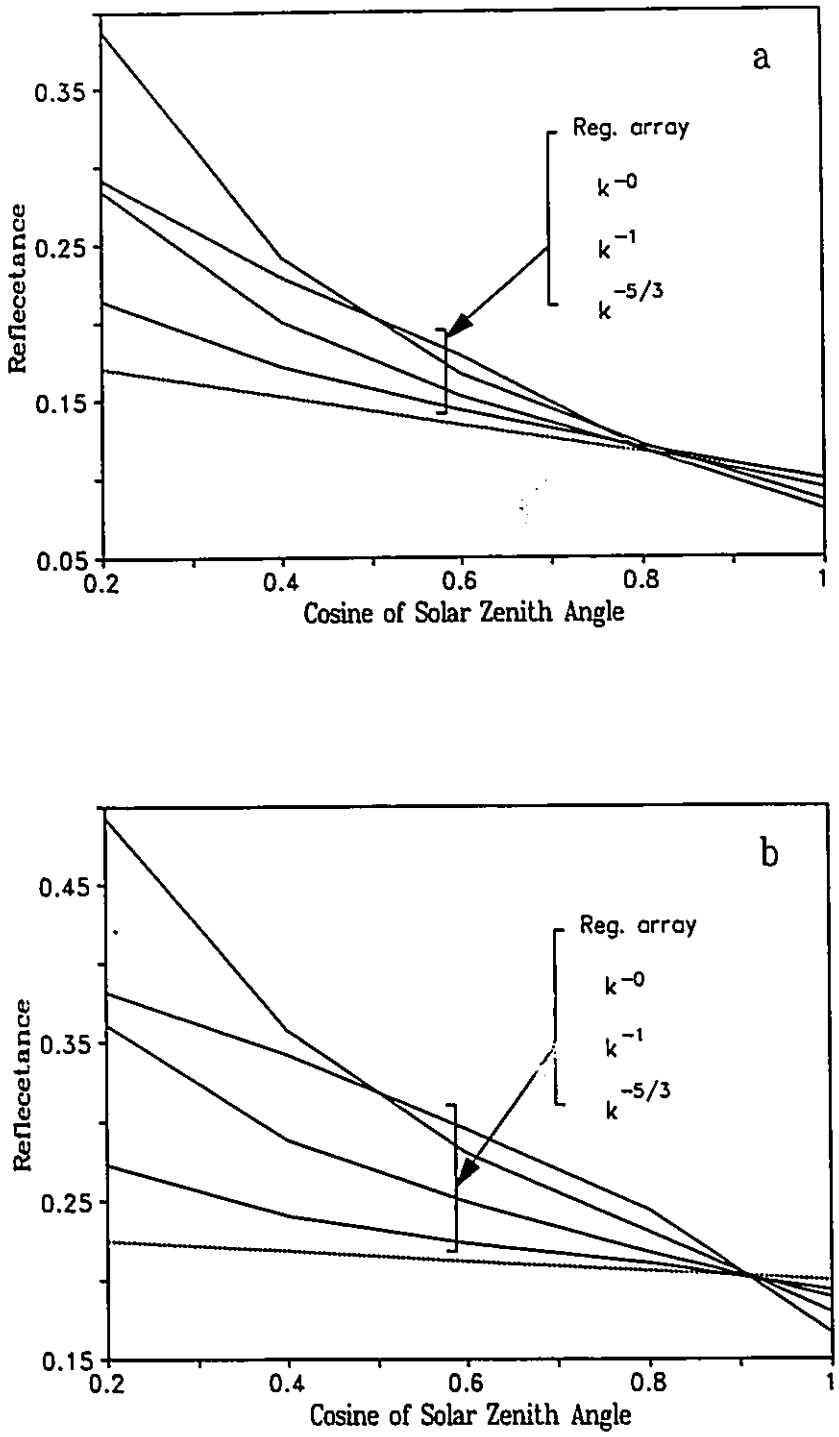

Fig.5.8. (a) Reflectance as a function of μ_0 for several different cloud fields each with $A_c = 0.25$, vertical optical depth of 10, and individual cubic cells. The scaling fields are of the identical format. Dashed line is plane–parallel reflectance. (b) As in (a) except $\tau = 50$. (c) As in (a) except $\tau = 10$ and $A_c = 0.45$. (d) As in (c) except $\tau = 50$...

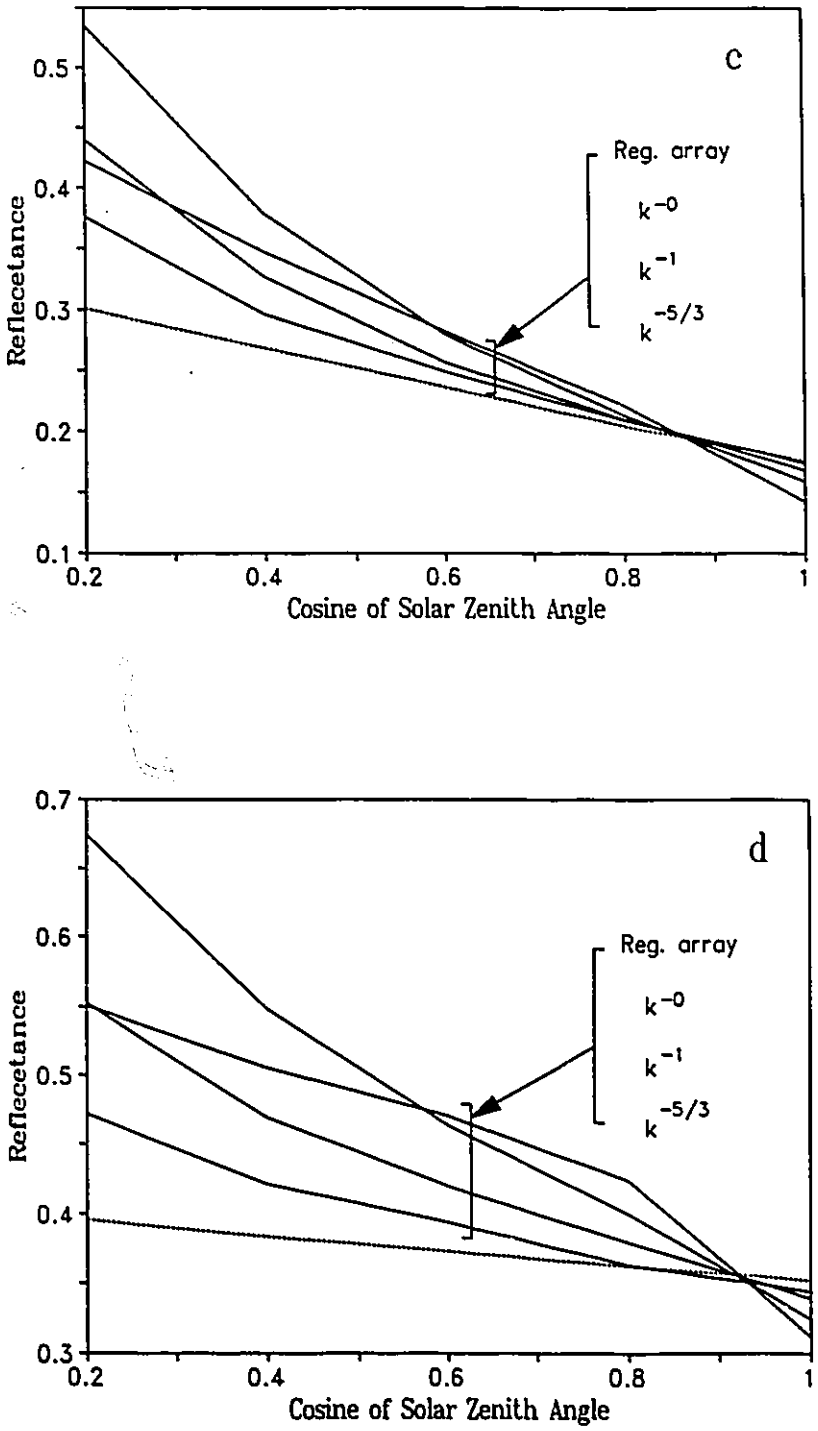

Fig.5.8. Continued

albedo cannot be reduced by side leakage. A significant number of photons that exit the sides of finite clouds would still be in a plane–parallel cloud and, therefore, have a greater probability of being scattered eventually through the top of the cloud.

While random arrays of clouds (k^{-0}) have no coherent patterns, there are some large clouds that have aspect ratio less than 1.0. As such, the random field is slightly more plane–parallel than the regular array. The examples in Fig.2.12 to 2.14 show that, as scaling exponent increases, clouds tend to conglomerate or coagulate. This reduces the area of cloud sides and hence the regionally integrated aspect ratio. Therefore, as scaling exponent increases, cloud fields become more plane–parallel. This explains the increase in reflectance with scaling exponent at high sun. Also, as scaling exponent increases, the average separation distance between clouds increases. Therefore, photons that leak through cloud sides have less chance of entering another cloud and possibly being reflected. This effect, however, is minor compared to the decrease in aspect ratio.

As the solar zenith angle increases, side illumination of finite clouds comes into play. Hence, an increasing fraction of incident radiation is intercepted by clouds and given at least a chance to be reflected. This effect has been documented extensively for individual clouds and regular arrays (e.g. McKee and Cox, 1974; Davies, 1978; Kobayashi, 1988). Plane–parallel clouds have no sides so as μ_0 decreases their reflectance increases slowly, only because photons stand a greater chance of being redirected into an upward direction near cloud–top. Note that for $\mu_0 \lesssim 1$, reflectance of the regular array with $\tau = 50$ increases very quickly. This is because each cloud is isolated and enhanced side illumination is very effective.

As μ_0 decreases further, reflectance by the regular array increases at a rate which is substantially less than its rate of increase at μ_0 near 1 and substantially less than the rates at which reflectances due to the k^{-0} and k^{-1} fields increase. As

the solar zenith angle increases, the sun reaches a point [$\theta_0 = \tan^{-1}(A_c^{-1/2} - 1)$] for the regular array where all clouds begin to cast shadow on their neighbour. When this occurs, enhanced side illumination ceases to increase and the cloud field presented to the solar beam is effectively a set of infinitely long bars. In all four graphs, reflectance due to the scaling and random cloud fields increase steadily as μ_0 decreases because, unlike the regular array where enhanced illumination reaches a maximum quite quickly, side illumination of scaling fields continues to increase for larger ranges of μ_0. However, as the scaling exponent increases, reflectance increases at a much reduced rate with decreasing μ_0. This is attributed to the increased number of large cloudless regions between cloud clusters which even at very low μ_0 can still admit to the surface a significant fraction of directly incident photons. This effect becomes so prevailent that even for fields that scale like $k^{-5/3}$, reflectances at most μ_0 are only slightly higher than the corresponding plane–parallel values. On the other hand, side illumination is so effective for the k^{-1} case that by $\mu_0 = 0.2$ reflectance either rivals ($A_c = 0.25$) or exceeds ($A_c = 0.44$) reflectances due to the regular array. Enhanced illumination is so effective in the k^{-0} case that reflectance exceeds that due to the regular array for all $\mu_0 < 0.5$ to 0.6.

Figure 5.9 shows the ratio of broken cloud field reflectance to plane–parallel reflectance as a function of A_c. This is the ratio which some researchers believe may be useful in parameterization for it relates broken cloud fluxes back to easily calculated plane–parallel fluxes. Again, only the identical cloud fields are used. The scaling cloud fields used to create Fig.5.9 were all created with the same initial white noise but using different scaling exponents and threshold values of f_{crit} to set A_c. While the optical depth of clouds in the field is 20 (intermediate to those used to create Fig.5.8), the results in Fig.5.9 augment those just discussed. For example, Fig.5.9a shows that for $\mu_0 = 0.5$ the random array has the largest

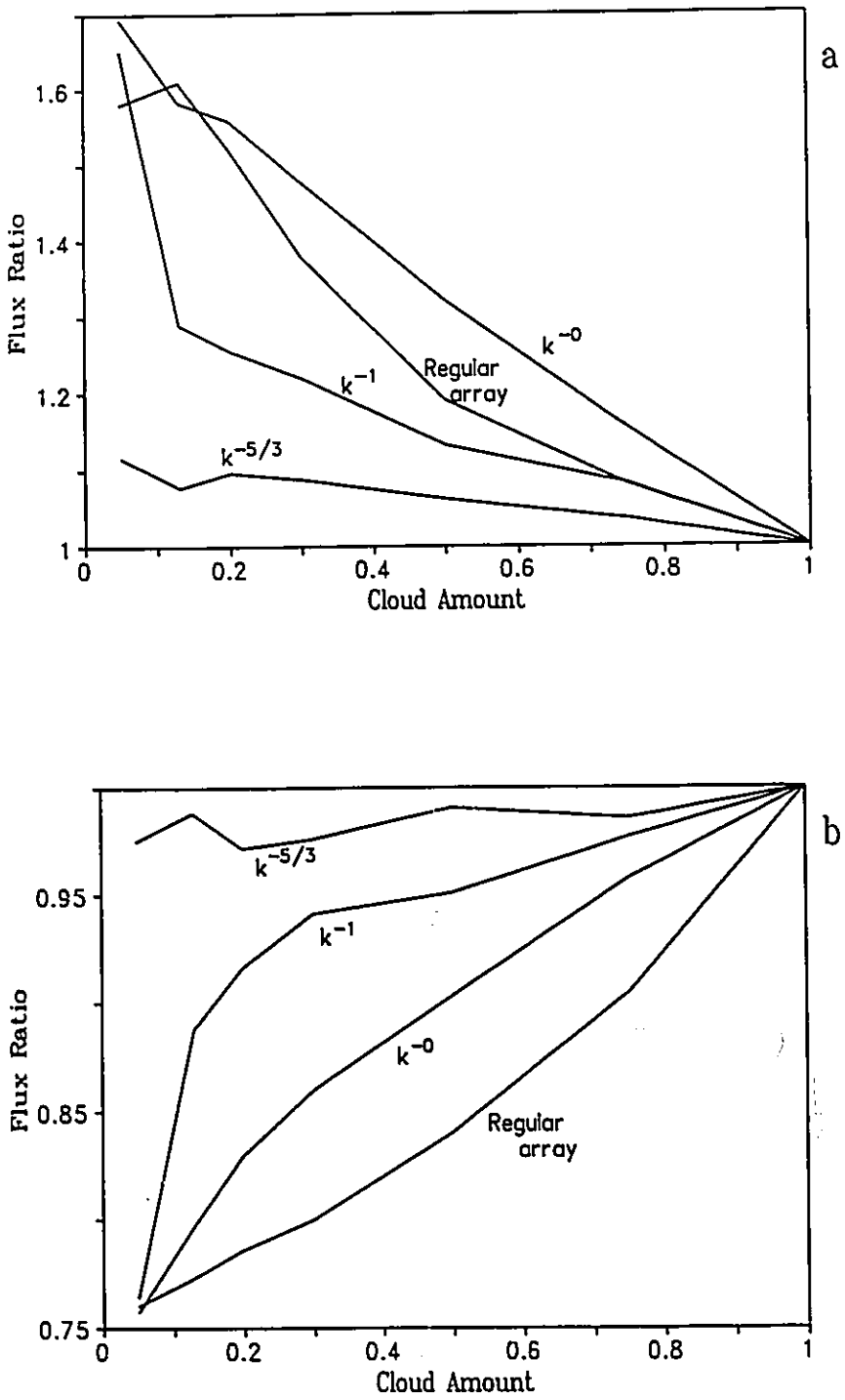

Fig.5.9. (a) Ratio between broken cloud field reflectances and plane–parallel reflectances as a function of A_c. Scaling cloud fields are of the identical cloud format and were all created with the same white noise. $\tau = 20$ and $\mu_0 = 0.5$. (b) As in (a) except $\mu_0 = 1.0$.

reflectance for essentially all A_c due to substantially enhanced side illumination. Figure 5.10 explicitly shows the value of enhanced cloud amount for $\mu_o = 0.2$ and 0.5. This is calculated by setting ω_o to 0 so that cloud absorptance equals approximately the fraction of the direct beam intercepted by cloud. For k^{-0}, at $\mu_o = 0.2$ and $A_c > 0.4$, enhanced cloud amount is almost overcast and very little direct beam gets throught to the surface.

Figure 5.9b shows that at $\mu_o = 1.0$, the regular array is the most effective at trapping photons for $A_c > 0.1$. The sudden increase (decrease) in flux ratio for the k^{-1} field for $\mu_o = 0.5$ (1.0) at $A_c < 0.1$ is due to the cloud model. At $A_c = 0.05$, 95% of the initially generated k^{-1} field is set to zero. As such, much information is lost and the field has fairly little to do with a '1/f noise'. The very large f_{crit} value has produced a field whose power spectrum is approximately $k^{-0.3}$. This 'whitening' of the field at low A_c (see section 2.4.3) is a shortcoming of the model. Regardless the general result is that as the scaling exponent increases, side leakage and illumination become less important, and therefore, reflectances approach the plane–parallel limit.

Figure 5.11 shows reflectances for the variable cloud versions of the identical cloud fields used to produce the reflectances shown in Fig.5.8. Again, the basic pattern is that for $\mu_o \gtrsim 0.8$ to 0.9, reflectance increases with scaling exponent while for smaller μ_o, reflectance decreases with scaling exponent. The explanation for this is exactly the same as that for the identical cloud case: as scaling exponent increases, finite clouds behave more like plane–parallel clouds. Figure 5.12, however, shows that horizontal variability in optical depth reduces albedo below that due to the identical cloud fields by between 10 – 15%. This is because of the non–linear nature of reflectance as a function of optical depth (see Stephens, 1988, and Appendix A) and also because the probability of photons encountering mass is reduced. The identical cloud field reflectances exceed the plane–parallel values for

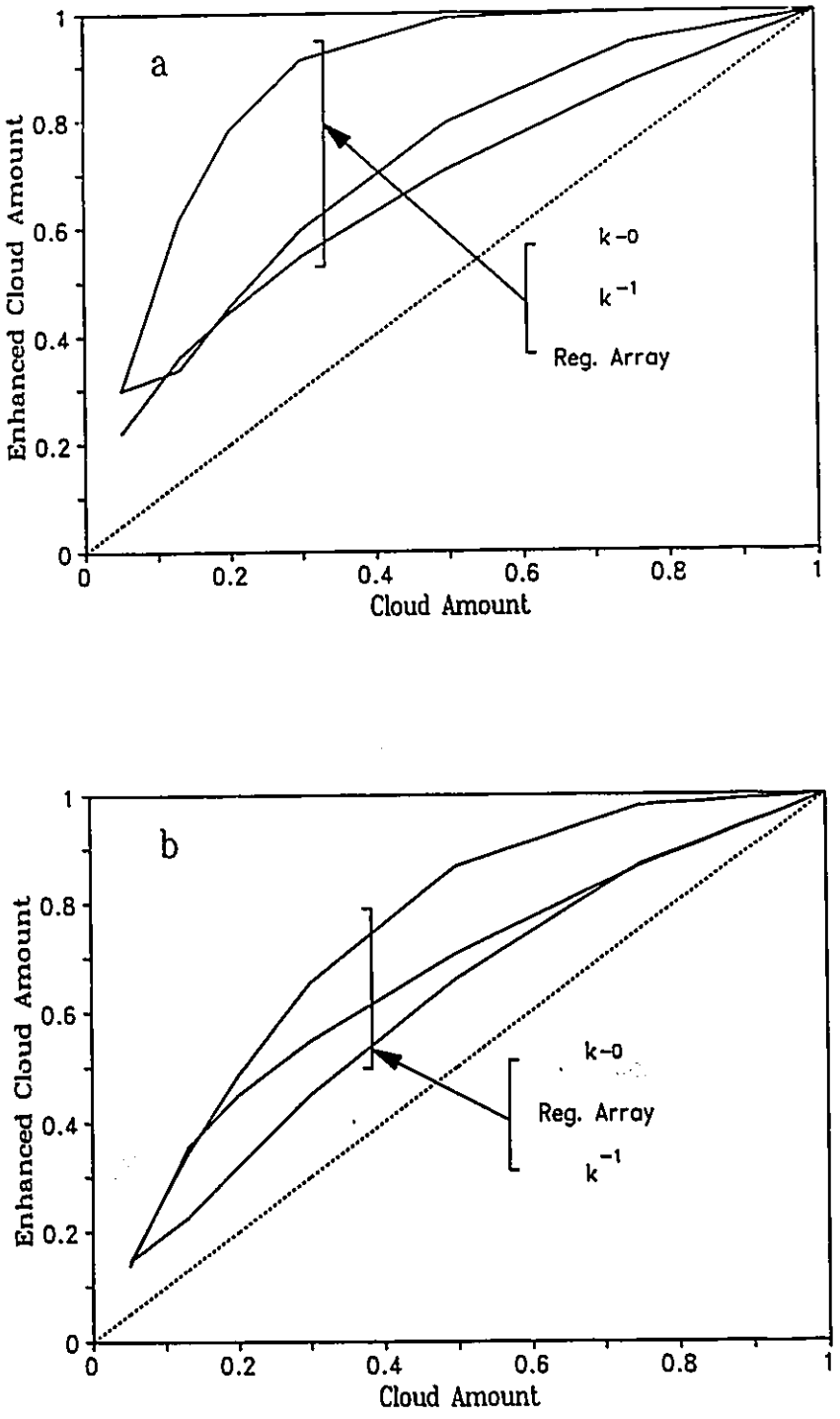

Fig.5.10. Enhanced cloud fraction for the fields used in Fig. 5.9 but for (a) $\mu_o = 0.2$ and (b) $\mu_o = 0.5$. Enhanced cloud fraction was determined by setting $\omega_o = 0$ in which case cloud absorptance is approximately equivalent to enhanced cloud fraction.

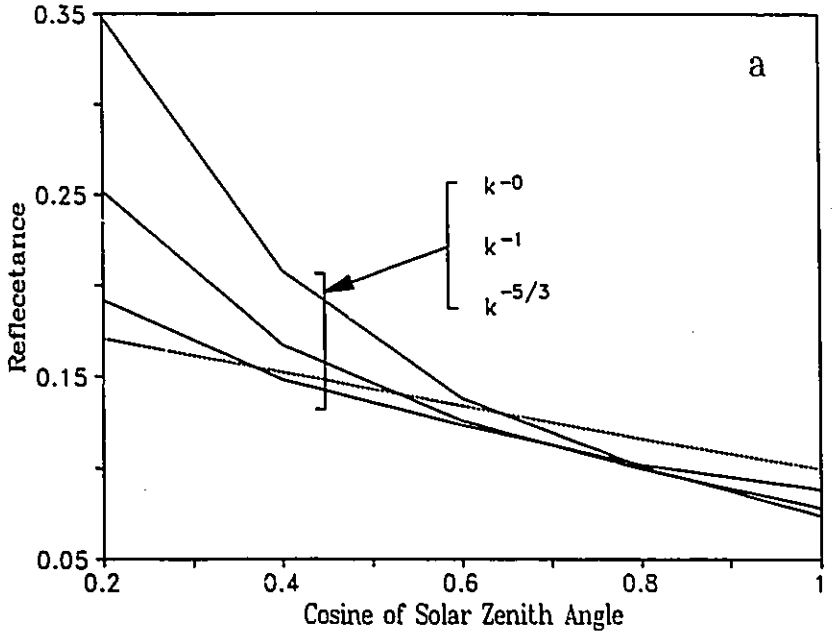

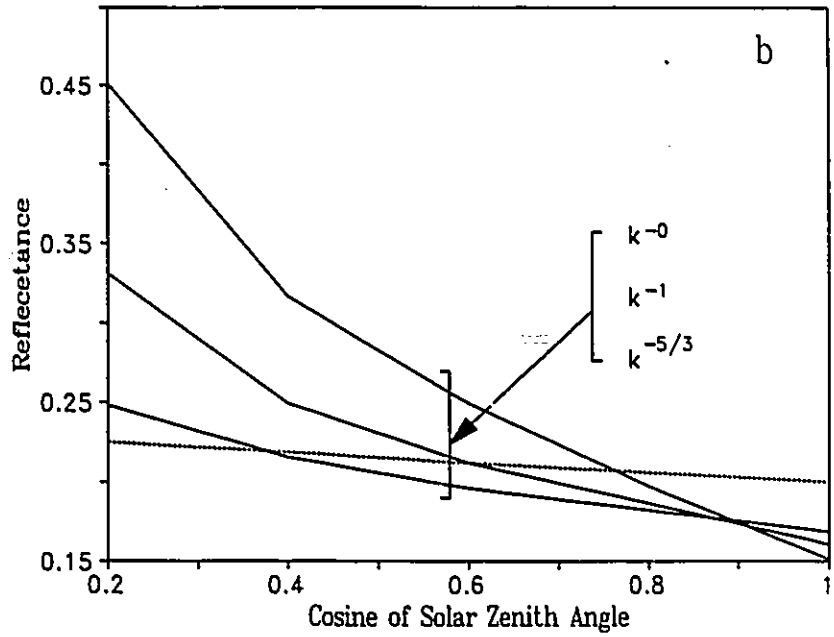

Fig.5.11..(a–d) Reflectances for the variable cloud field counterparts of the identical cloud fields used in Fig.5.8.

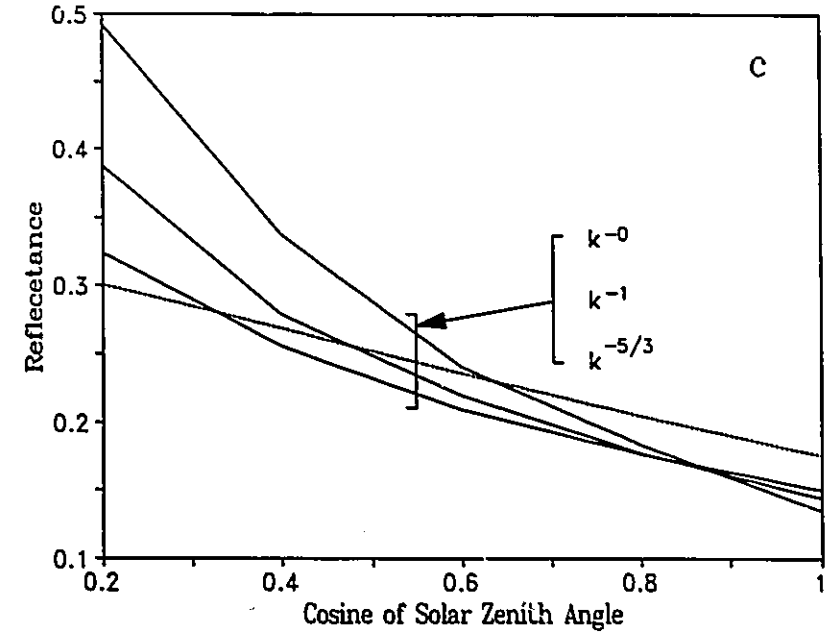

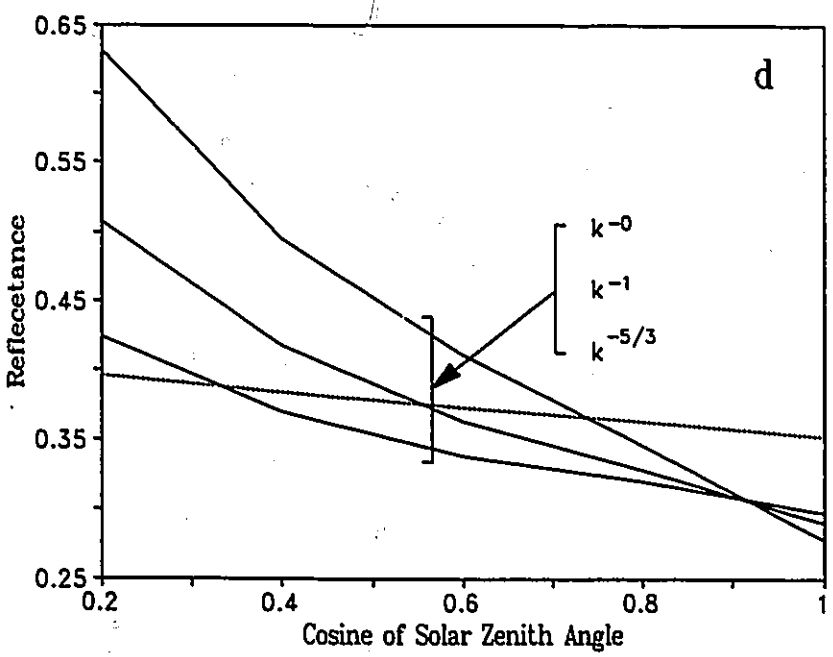

Fig.5.11. Continued.

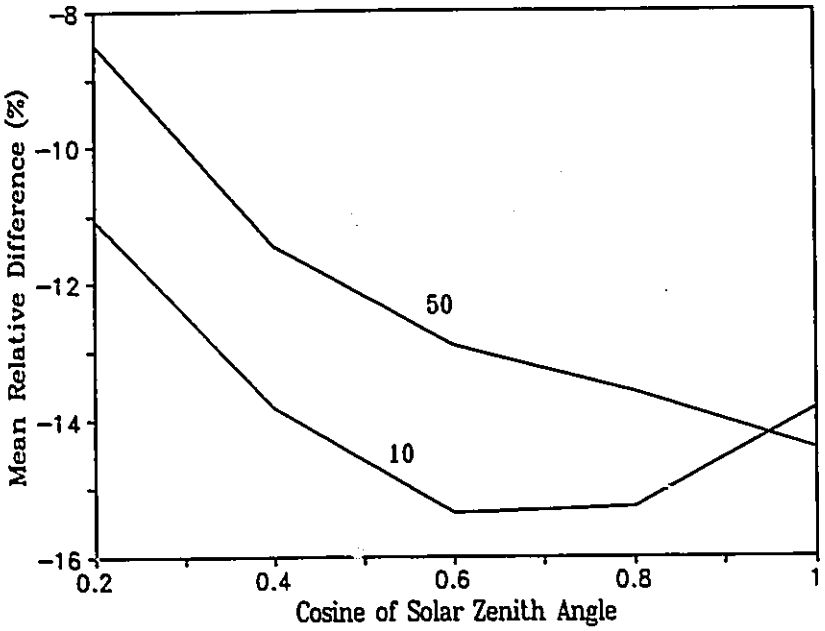

Fig.5.12. Percentage reduction in reflectance when going from the identical scaling clouds used in Fig.5.8 to the variable scaling clouds used in Fig.5.11. Regardless of cloud amount and solar zenith angle, all reflectances are grouped into the respective optical depth. Standard deviation of the curves are about ± 2%.

$\mu_o \leq 0.9$. With horizontal variability, scaling cloud field reflectances exceed the plane–parallel estimates for $\mu_o \leq 0.7$ (k^{-0}), $\mu_o \leq 0.55$ (k^{-1}), and $\mu_o \leq 0.35$ ($k^{-5/3}$). This is quite a dramatic qualitative difference: accounting for broken clouds but no horizontal variation in τ primarily enhances cloud albedo, but when variable τ is admitted, broken cloud albedo is smaller than albedo for the plane–parallel case (especially for large scaling exponents and small cloud amounts).

5.2.2 Radiative Properties of Scaling Cloud Fields

In this section, some properties of fluxes associated with scaling cloud fields are examined.

Figures 5.13, 5.14, and 5.15 show how identical and variable scaling cloud fields reflect azimuthally averaged direct–beam radiation as a function of cloud field scaling exponent d; that is, the cloud field behaves as $\langle S_k \rangle \sim k^{-d}$. For all cases in Fig.5.13, averaged vertical optical depth $\langle \tau \rangle$ is 20 and A_c is 0.25. The cloud cells in Fig.5.13a are cubes while in Fig.5.13b they are horizontally square rectangles with aspect ratio 3.33 with $\langle \tau \rangle = 20$. The same distinction applies to Fig.5.14a and b except $\langle \tau \rangle = 10$ and $A_c = 0.5$. Cloud cells in Fig.5.15 are cubes with $\langle \tau \rangle = 50$ and $A_c = 0.3$. Each cloud field in Fig.5.13 and 5.14 was generated with a different white noise. The cloud fields in Fig.5.15 were all generated with the same white noise.

All five plots reveal that the reflectance of cloud fields with continuous spectra are bounded between random, white noise arrays of clouds at one extreme ($d = 0$) and plane–parallel clouds at the other ($d \to \infty$). In all cases, reflectance for the identical cloud fields approach the plane–parallel limit defined as $R_{pp}(\mu_o)*A_c$, where $R_{pp}(\mu_o)$ is plane–parallel cloud reflectance. Note that because of the finite nature of the clouds in the generated fields, the plane–parallel limit is not approached strictly. In the cases considered here, cloud aspect ratio beyond $d = 4$

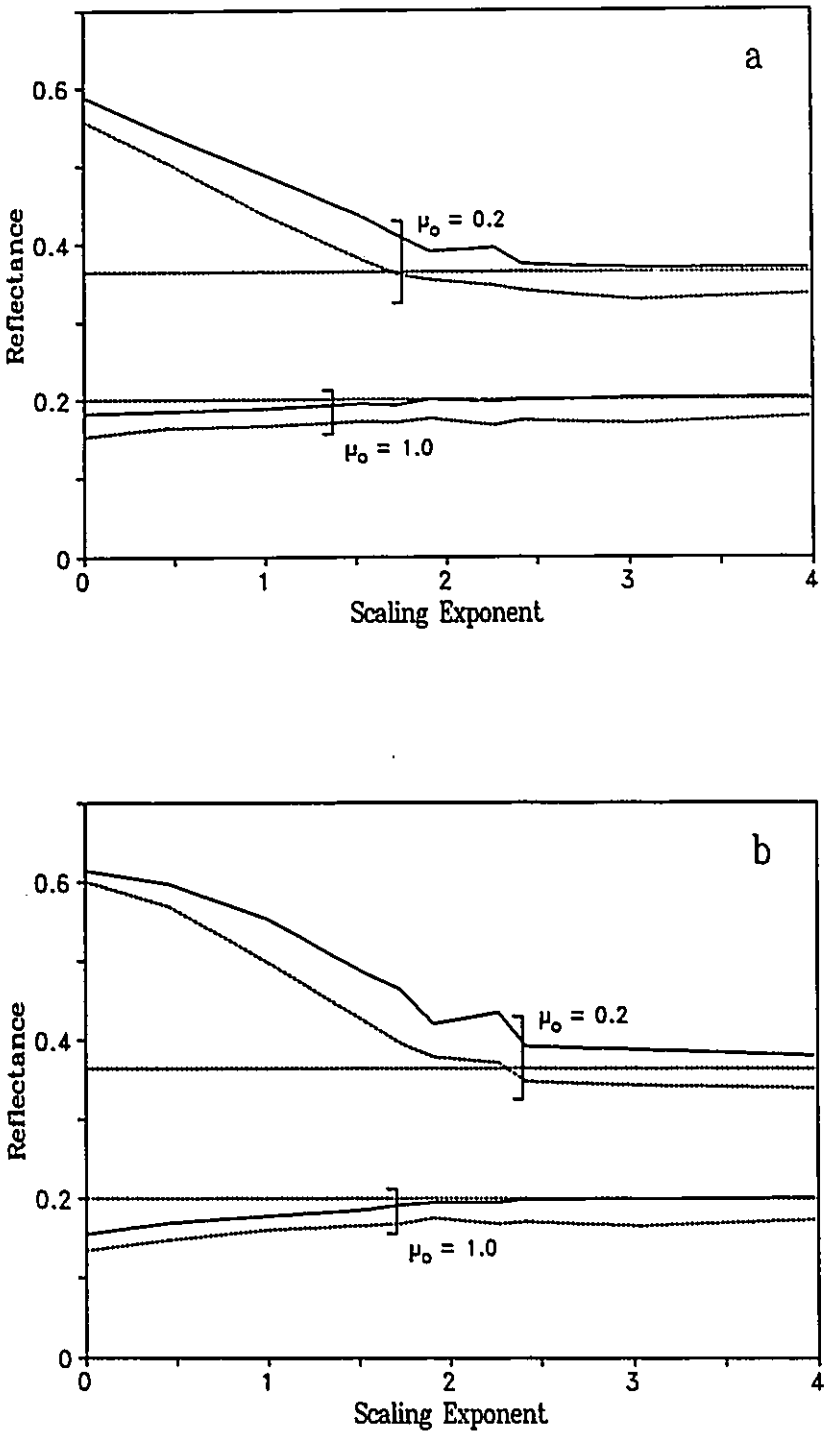

Fig.5.13. (a) Reflectance for 256x256 arrays of clouds as a function of scaling exponent d ($\langle S_k \rangle \sim k^{-d}\ \forall\ k$). For all cases, $A_c = 0.25$ and average vertical optical depth $\langle \tau \rangle = 20$. Dashed and solid lines refer to variable and identical clouds. Individual cells have aspect ratio of 1. (b) As in (a) except individual cells have aspect ratio of 3.33.

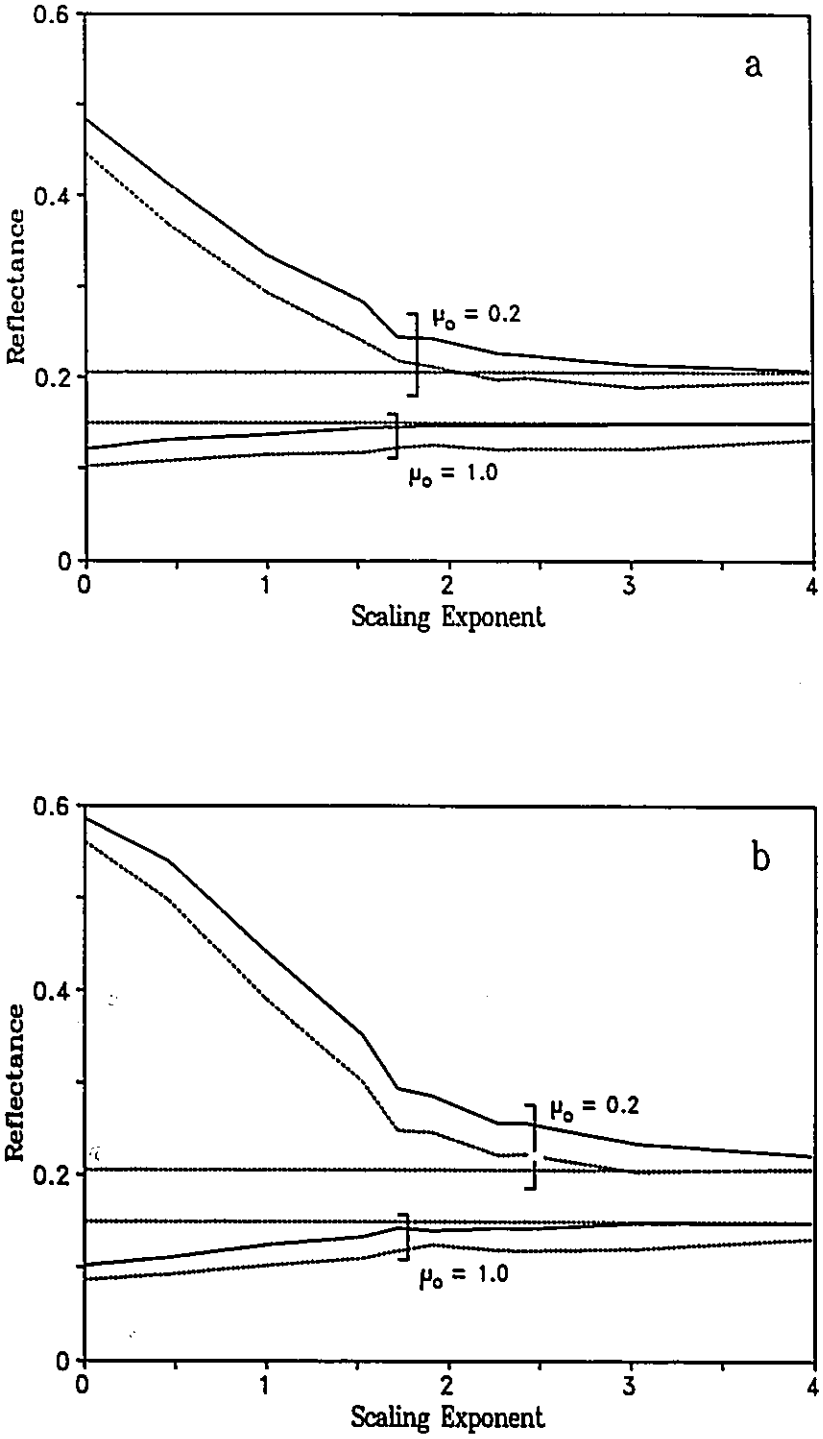

Fig.5.14. As in Fig.5.13 except $A_c = 0.5$ and $\langle \tau \rangle = 10$.

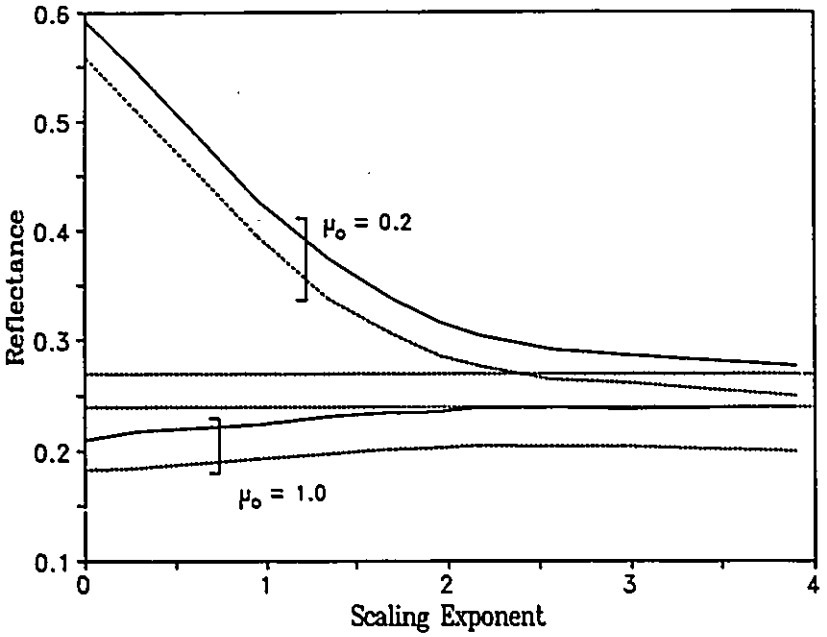

Fig.5.15. As in Fig.5.13a except $A_c = 0.3$ and $\langle \tau \rangle = 50$.

is about 1/100 which yields very nearly plane–parallel results (Davies, 1978). The variable cloud fields appear to at least level off at reflectances less than the plane–parallel values. It is presumed that as the scaling exponent approaches infinity the variable cloud field will cease to be variable for virtually all oscillations will be damped out. Thus, in the true limit of infinite scaling exponent, the variable field reflectances may asymptote to the plane–parallel values. The greatest deviations from plane–parallelism occur at d = 0; white noise. All cloud fields with intermediate scaling exponents, and thus probably all realistic values, have reflectances that fall between these extremes. This was also implied by the results in the previous section. These results are reasonable for as scaling exponent increases the size distribution of clouds narrows, the mean area of individual clouds increases, mean separation between clouds increases, and variability across individual clouds decreases. All of these factors act to produce plane–parallel–like clouds.

In all plots for both $\mu_0 = 0.2$ and 1.0, reflectance for both identical and variable cloud fields varies almost linearly for $d \lesssim 1.5$ to 2.0. Then, there is a transition regime out to about d = 2.5 (most visible for $\mu_0 = 0.2$) and beyond $d \simeq 2.5$, reflectance appears to approach the limits asymptotically. With fairly remarkable consistency, reflectances of the variable cloud fields are less than the identical cloud field reflectances by a constant *amount*. Hence, at small d for $\mu_0 = 1.0$ and large d for $\mu_0 = 0.2$, the fractional differences between the reflectances for the two cloud types are greatest.

Based on the satellite radiances and aircraft samplings presented in Chapter 2, it is conjectured that at scales greater than about 0.5 km to 4 km and less than about 50 to 100 km, vertically integrated optical depth of cumulus cloud fields scale between $\langle S_k \rangle \sim k^{-0.5}$ and k^{-2}. If this is true, the results in Fig.5.13, 5.14, and 5.15 show that reflectances can vary substantially in this range and that the

range of reflectances may often be significantly different from those due to white noise and plane–parallel arrays of cloud. Furthermore, the cloud field shown in Cahalan and Snider's (1989) Fig.3 has a near infrared spectrum like $\langle S_k \rangle \sim k^{-0.6}$. They referred to this field as a 'nearly wavenumber independent (white noise) spectrum' (p.104). While their statment is not incorrect, Fig.s 5.13 through 5.15 show that with a scaling exponent of 0.6, reflectance at $\mu_0 = 1.0$ can be at least 10% greater than the white noise value and at $\mu_0 = 0.2$ it can be at least as much as 20% smaller than the white noise value. These are significant and important differences.

The next set of experiments concern the effects of vertical texturing on cloud field reflectances. All fields in these experiments are arrays of 128x128 cells in the horizontal. Figure 5.16a shows reflectance as a function of μ_0 for three cloud fields all created with the same white noise, scaled with $|k|^{-2}$, $A_c = 0.25$, and $\langle \tau \rangle = 20$. The maximum vertical optical depth in the variable and textured cases is 99.6. Each field consists of cubes of equal volume. The clouds (or parts of clouds) in the textured case with the greatest vertical geometric thickness are 5 times thicker than the clouds in the variable and identical fields. The average cloud thickness in the textured case is about 1.5 times thicker than the other fields.

As in previous experiments, reflectances for the identical cloud field exceed those of the variable cloud field by about 10 to 20% for all μ_0. At overhead sun, reflectance due to the textured field is slightly less than that due to the variable field. Thus, at high sun, the overall effect of texture is to trap photons and reduce albedo. Photons tend to leak out the sides of the towering parts of cloud and shower down on shallower clouds at an effective zenith angle greater than 0°. Thus, photons tend to escape from regions of large vertical optical depth easier than if the massive columns were compressed to a single cell thick. Also, photons reflected by shallower clouds cannot escape as easily as in the single layer variable

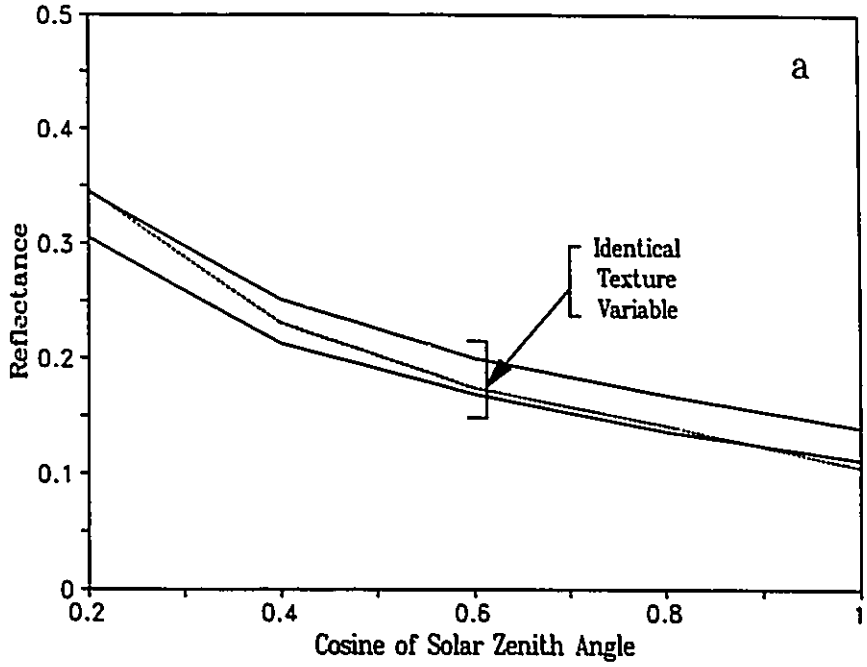

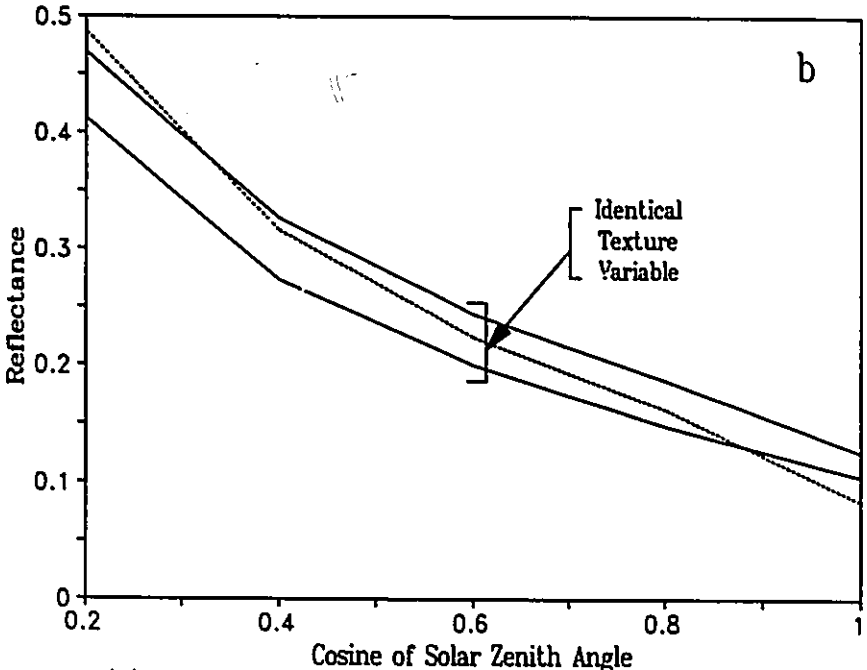

Fig.5.16. (a) Cloud reflectance as a function of μ_0. Identical and variable cloud fields are 128x128x1 arrays. Textured field has some clouds that are five cells deep. All fields have vertically integrated τ that go like $\langle S_k \rangle \sim k^{-1} \forall k$, $A_c = 0.25$, and $\langle \tau \rangle = 20$. Individual cells have aspect ratio of 1. (b) As in (a) except individual cells have aspect ratio of 3.33.

cloud case due to interception by towering clouds. Enhanced solar zenith angle due to photon leakage through cloud sides is an insignificant reflection enhancement mechanism compared with the albedo reduction mechanisms just mentioned.

Van Blerkom (1971) and Wendling (1976) found that periodic striations on top of plane–parallel clouds reduced albedo, especially at $\mu_0 = 1.0$. (Though not reported, their results where reproduced). However, they found that striations reduced slightly the albedo for all μ_0 since they only considered overcast. The cloud field used to produce reflectances in Fig.5.16a is more cumulus–like than stratocumulus. Hence, as μ_0 decreases, reflectance of the textured field quickly exceeds that due to the variable field as side enhanced illumination becomes rapidly a factor. By $\mu_0 = 0.2$ the textured reflectance exceeds the identical cloud reflectance. This is due simply to super–enhancement of the illuminated area of the textured field as μ_0 decreases and easier escape upwards as photons exit the sides of towering clouds.

Figure 5.16b shows reflectances for the same cloud fields used to produce Fig.5.16a except that the cells are rectangles (not cubes) with x, y, and z lengths 0.3, 0.3, and 1.0 times those of the cubes in the first experiment. Thus, the cloud fraction and average vertical optical depth are the same, but the clouds used to create Fig.5.16b are narrower and have an effective aspect ratio 3.33 times that of the clouds in the first experiment. Figure 5.16b shows that for overhead sun, texture suppresses reflectance below that due to the variable field by the same amount as the identical field's reflectance exceeds that due to the variable field. Hence, photon trapping by texture has been amplified. The enhanced illuminated area effect has been amplified as well since textured reflectance exceeds that due to identical clouds for $\mu_0 \lesssim 0.3$ as oppossed to 0.2 in the first experiment. In fact, note that at $\mu_0 = 1.0$ all reflectances are reduced slightly in the second example while for most μ_0 reflectance is increased. Welch and Wielicki (1984) have already

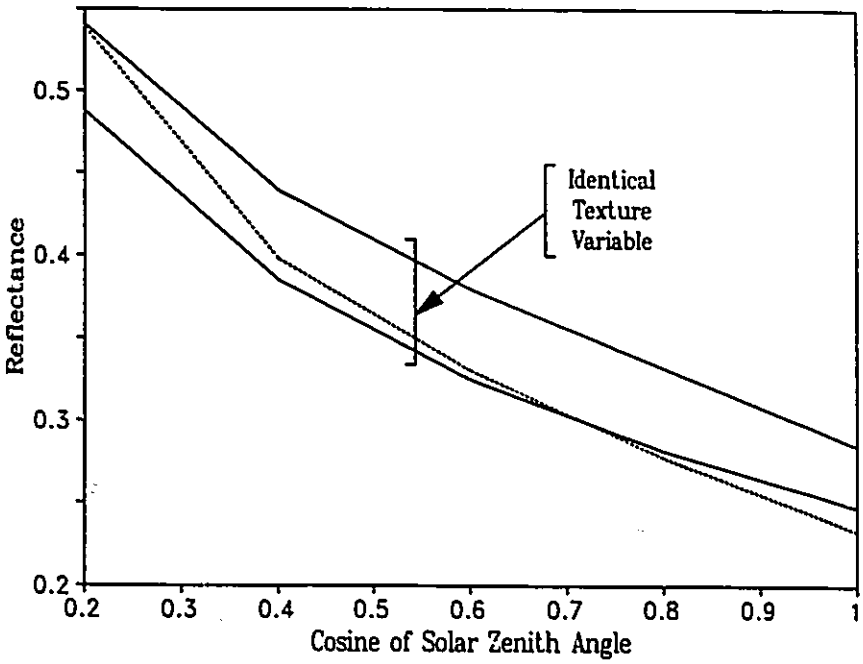

Fig.5.17. As in Fig.5.16a except $\langle S_k \rangle \sim k^{-1.66}$ for $k > 5$ and k^{-0} for $k \leq 5$ and $A_c = 0.5$.

documented this effect for regular arrays. It is due to enhanced trapping and illuminated area respectively as aspect ratio increases. Thus, the effect of texturing can be easily understood by referring to experiments that have investigated how aspect ratio affects cloud field reflectance since texturing is a more subtle, but realistic, way of exploring the effects of aspect ratio.

Figure 5.17 is like Fig.5.16a and b except that the cloud field was produced by scalings $|\mathbf{k}|^{-0}$ for $k \leq 5$ and $|\mathbf{k}|^{-2.66}$ ($\langle S_k \rangle \sim k^{-5/3}$) for $k \geq 5$, $A_c = 0.5$, and $\langle \tau \rangle = 20$. The pattern of reflectances in Fig.5.16a and b is preserved: texturing reduces reflectance below that for the variable model at large μ_o ($\geq$0.85) and enhances reflectance to match or exceed the identical cloud reflectances for $\mu_o \leq$ 0.2. Since reflectances for the textured case can excced the others by more than 10%, accounting for texture may be desirable, especially in simulations of photon transport through towering tropical cumuli.

The final experiment in this section concerns the reflectance effects of applying different scaling factors to different scales. This experiment was motivated by the satellite radiance power spectra shown in Section 2.4.1.2. For example, it may be that clouds in scene A scale as k^{-1} but vertical integral of liquid water across cloud cells scales closer to k^{-4}. This kind of variable scaling can be accounted for with the cloud models and reflectances investigated with the Monte Carlo codes.

Figure 5.18 shows four cloud fields created with the same white noise matrix. All images have $A_c = 0.25$ and $\langle \tau \rangle = 30$ and are single layer cloud fields consisting of cubes. Field A was created by applying $|\mathbf{k}|^{-2}$ $\forall$ $|\mathbf{k}|$ to the white noise. Field B was created the same way except with $|\mathbf{k}|^{-4}$ for $|\mathbf{k}| \geq 70$. Thus, the vertical optical depth spectrum, especially $\langle S_k \rangle$, of field B is very similar to the radiance spectra of AVHRR scene A (if cell size is assumed to be about 1 km). Note that field B has smoother edged clouds and fewer small clouds relative to

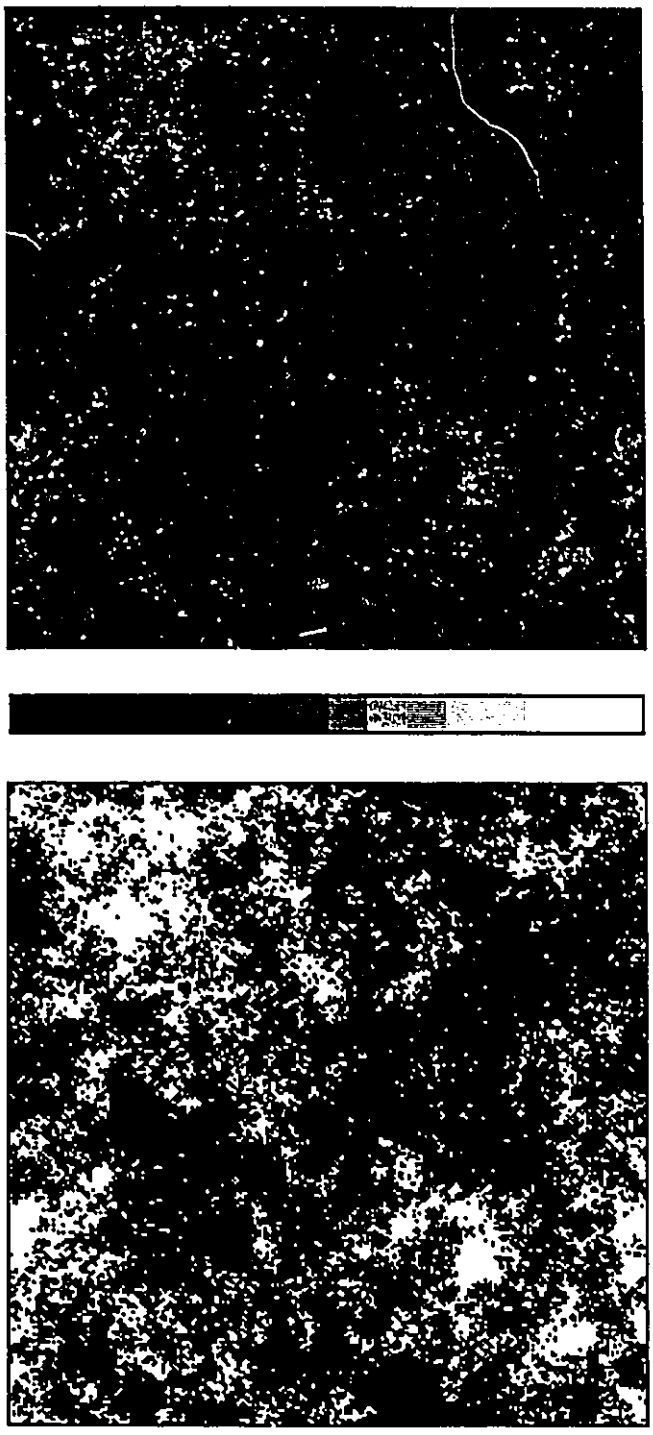

Fig.5.18. Four images of 256x256 arrays of clouds each created with the same white noise and having $A_c = 0.25$ and $\langle \tau \rangle = 30$. (a) $\langle S_k \rangle \sim k^{-1}$ $\forall$ k; maximum τ is 209.

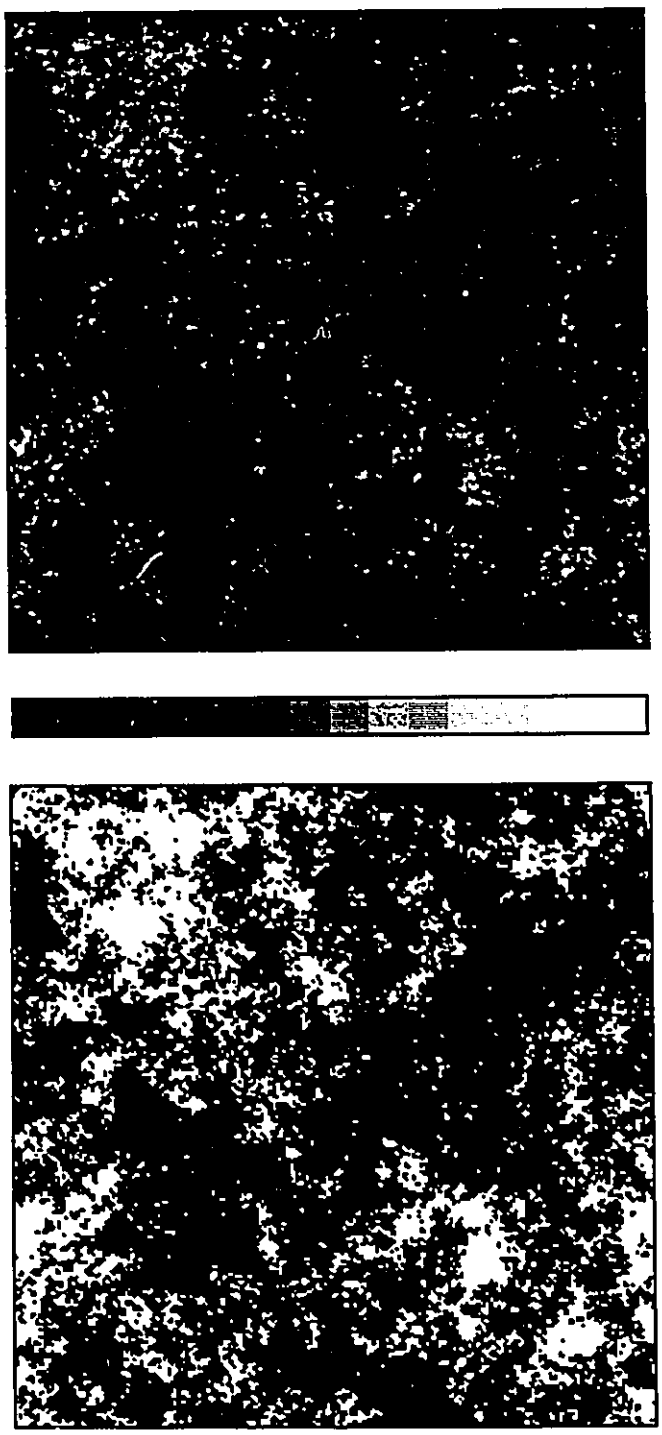

Fig.5.18. (b) As in (a) except $\langle S_k \rangle \sim k^{-3}$ for $k \geq 70$; maximum τ is 206.

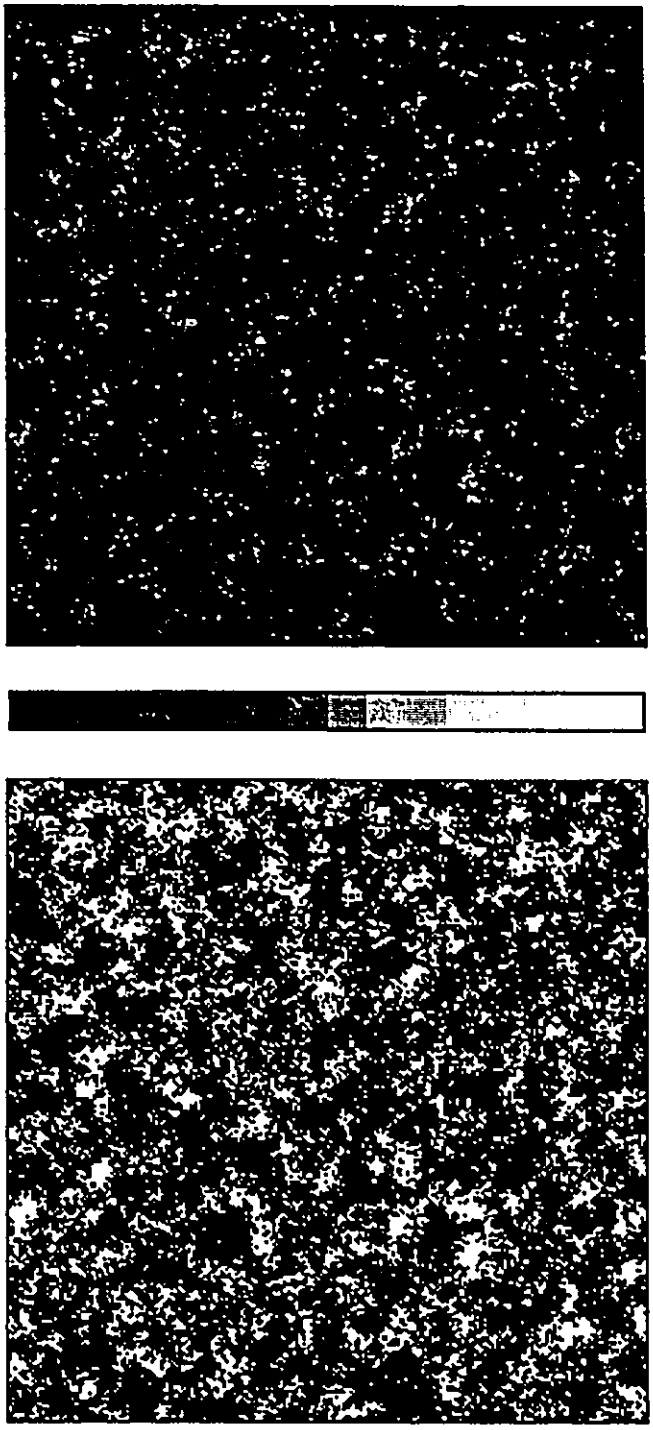

Fig.5.18. (c) As in (a) except $\langle S_k \rangle \sim k^{-0}$ for $k \leq 10$; maximum τ is 220.

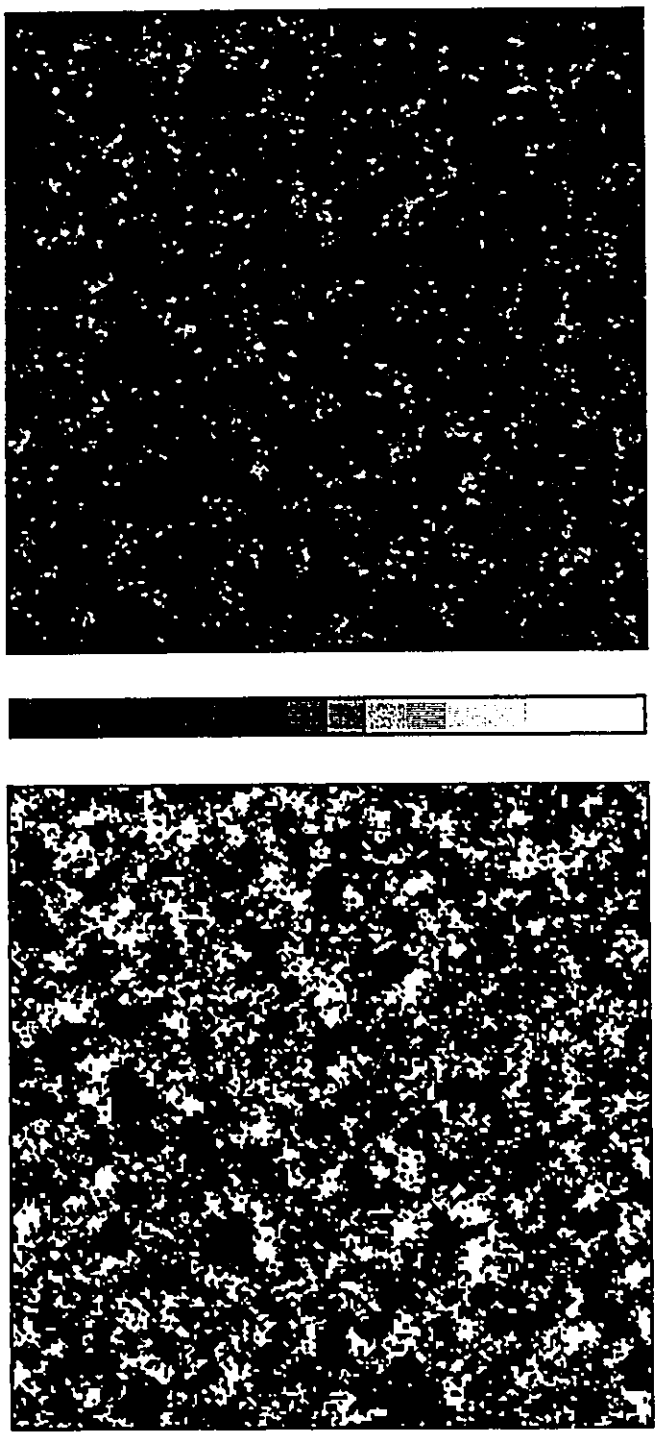

Fig.5.18. (d) As in (c) except $\langle S_k \rangle \sim k^{-3}$ for $k \geq 70$; maximum τ is 221.

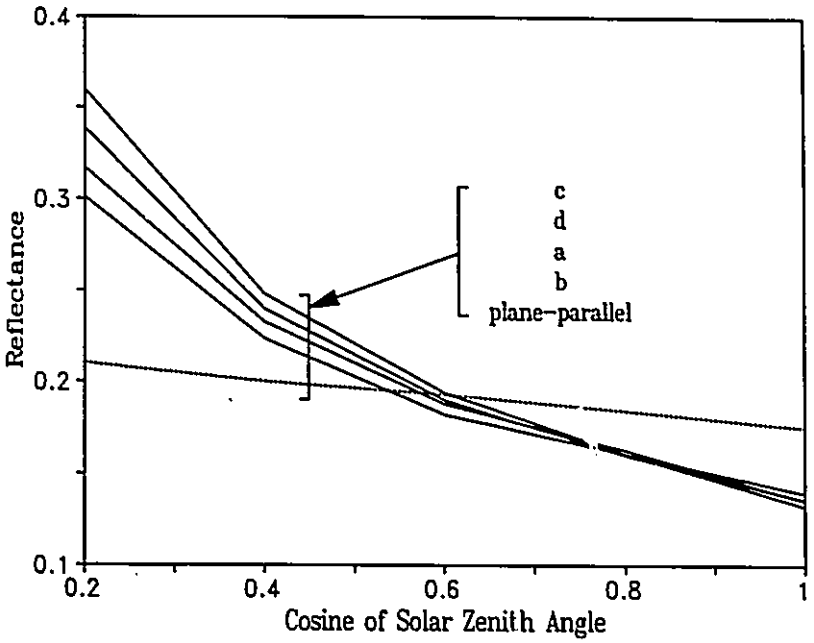

Fig.5.19. Reflectance as a function of μ_0 for the images in Fig.5.18.

field A. Field C was created with $|\mathbf{k}|^{-1}$ for $|\mathbf{k}| \leq 10$ and $|\mathbf{k}|^{-2}$ for $|\mathbf{k}| > 10$. This field differs significantly from fields A and B though some general similarities are discernable. The most distinguishing feature of field C is the lack of extensive clouds and cloud–free regions. Field D is created like field C except that $|\mathbf{k}|^{-4}$ is applied to $|\mathbf{k}| > 70$. Thus, like field B relative to A, field D is similar to field C but cloud edges are smoother, fewer small clouds exist and as a result, spaces between clouds are on averaged greater in field D than in field C.

Figure 5.19 shows reflectance for the four cloud fields discribed above. For $\mu_0 > 0.7$, differences are small and reflectances are less than plane–parallel reflectances. For $\mu_0 < 0.7$, reflectances of the four fields begin to diverge. For this range of sun angles, the $|\mathbf{k}|^{-1}$ scaling at low frequencies tends to enhance illuminated area and thus reflectance by about 15% over the counterpart with $|\mathbf{k}|^{-2}$ low frequency scaling. On the other hand, over the same range of sun angles, the $|\mathbf{k}|^{-4}$ scaling at high frequencies tends to reduce reflectance by about 8% below the counterpart with $|\mathbf{k}|^{-2}$ high frequency scaling. Therefore, it is most likely that accounting for low frequency 'whitish' noise is more important than accounting for attenuation of detail at high frequency.

5.3 Radiative Fluxes for Broken Clouds Above Reflecting Surfaces

Almost all previous studies of solar radiative transfer in broken cloud have considered single layer fields of identical, homogeneous clouds irradiated from above by a direct beam with an underlying black surface. Including a reflecting surface or multiple cloud layers complicates the problem significantly. This section investigates some aspects of solar radiative transfer for broken clouds above realistic reflecting surfaces. It consists of three main parts. The first assesses the applicability of the Lambertian surface approximation for calculating fluxes in broken cloud. The second tests the validity of the geometric sum form of flux

calculation in a multiple reflecting system. Both approximations are ubiquitous in climate studies (e.g. Schneider and Dickenson, 1976; Fouquart, 1988; Barker and Davies, 1989a,b). The third examines the phenomenon of system albedo reduction by non–absorbing clouds.

5.3.1 Applicability of a Lambertian Surface for Flux Calculations

When using remotely–sensed radiance data to infer properties about reflecting surfaces or to extrapolate flux estimates, it is very important to account for the bi–directional reflectance nature of surfaces (Gerstl and Simmer, 1985; Pinty *et al.*, 1990). This section explores the question: how important is it to include explicit bi–directional surface reflection functions when calculating solar fluxes for broken cloud? To do this, a non–Lambertian surface, whose qualitative reflectance characteristics do not differ much from natural surfaces, and two Lambertian surfaces are considered. While examination of one surface does not provide a definitive answer, it is at least a stringent test and settles the question for many surfaces.

5.3.1.1 Non–Lambertian Test Surface

The bi–directional reflecting surface for this study is assumed to be plane–parallel, homogeneous, and consisting of particles (e.g. individual or consolidated grains). Reflectance is accounted for by the statistical bi–directional model (see section 3.3.2). The effective single–scattering albedo of the particles is $\omega_s = 0.6$, and the effective scattering phase function is given by

$$P_s(\cos\psi) = 1 + \omega_1 \cos\psi \ ,$$

or

$$P_s(-\mu,\varphi;\mu_z) = 1 + \omega_1 \left[-\mu\mu_z + \sqrt{(1-\mu^2)(1-\mu_z^2)}\,\cos\varphi \right] \ , \qquad (5.1)$$

where all terms are explained in section 3.3.3 and ω_1=–1.0 which implies that the effective asymmetry factor of the particles is –1/3.

Figure 5.20 shows the normalized intensity function $I(-\mu,\varphi;\mu_z,\varphi_z)/I(-1,\varphi;\mu_z,\varphi_z)$ [Eq.(3.70)] for this surface in the solar–zenith plane for a number of different μ_z values. The surface zenith angle dependent albedo $\alpha_s(\mu_z)$ shows (Fig.5.21) a greater dependence on μ_z than expected for many natural surfaces (e.g. Barker and Davies, 1989). The formula

$$\alpha_s(\mu_z) = \frac{0.25107 + 0.90206\mu_z}{0.70416 + \mu_z(3.78902 + \mu_z)}\ , \tag{5.2}$$

fits the curve in Fig.5.21 with maximum error of 0.8% at μ_z = 0.1 and average error of 0.24%. The spherical albedo of the surface is 0.236. Equation (5.2) is used in the Monte Carlo code to decide whether a photon incident at the surface is reflected or absorbed (see section 3.4).

Figure 5.22 shows the cumulative density function for reflected photon zenith angle [Eq.(3.73)] with ω_s =0.6 and ω_1=–1.0 for several values of μ_z. This plot shows the values of a random number RN which satisfies a particular θ_r. For the non–Lambertian surface with μ_z=1.0, the expression for the reflected angle θ_r is almost identical to the Lambertian formula given in Eq.(3.44) (dashed line in Fig.5.22). This implies that for the test surface, normal incident photons undergo near isotropic reflection. The family of curves produced by Eq.(3.73) (of which those in Fig.5.22 are a subset) have been parameterized such that θ_r of reflected photons is given by

$$\theta_r = \cos^{-1}\left\{-\mathrm{RN}^{[a(\mu_z) + b(\mu_z)\ln(\mathrm{RN})]}\right\}, \tag{5.3a}$$

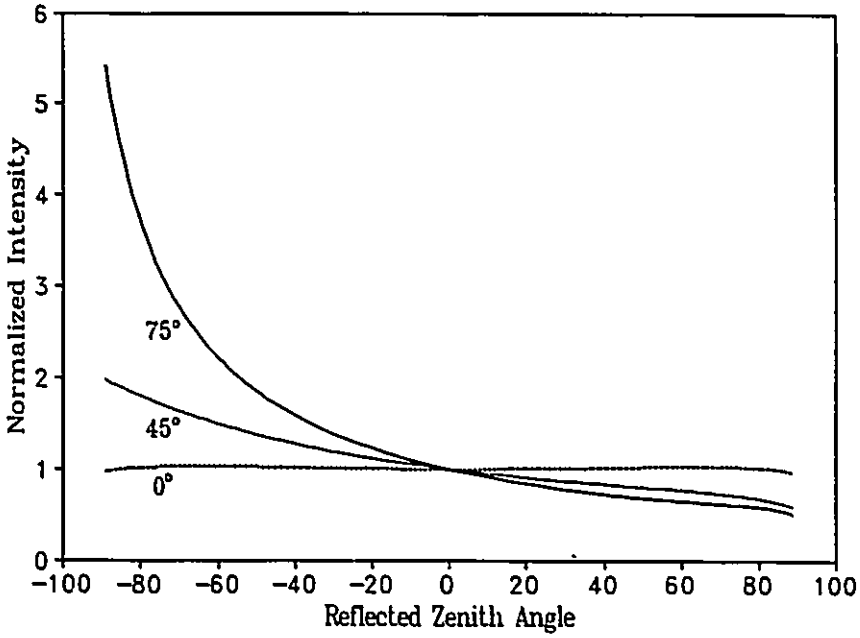

Fig.5.20. Normalized reflected intensity in the solar plane for the test surface defined by Eq.(5.1) as a function of $\pi-\theta_r$ for several incident angles θ_z. Right side of the plot corresponds to forward scattered radiation and the left side corresponds to backscattered radiation.

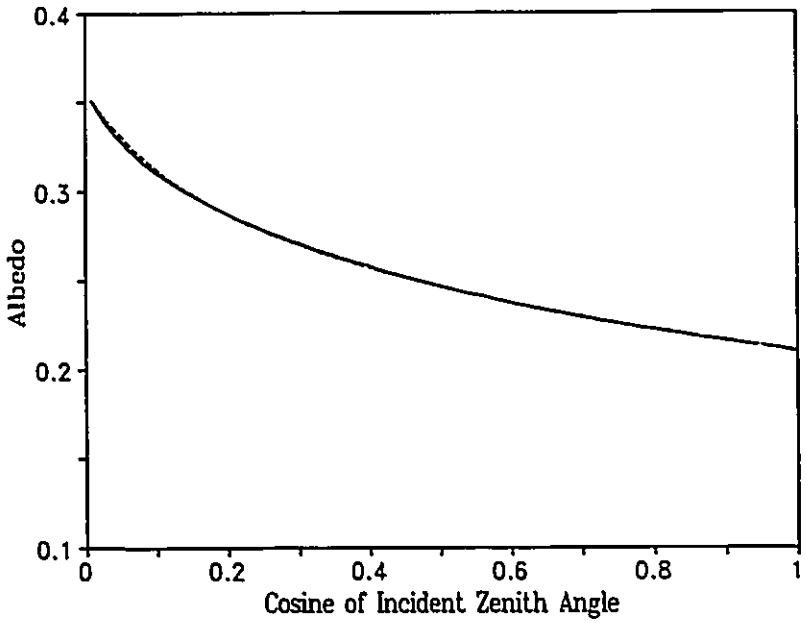

Fig.5.21. Zenith angle dependent albedo for the test surface. Solid line is actual albedo while dashed line is the approximation givenby Eq.(5.2).

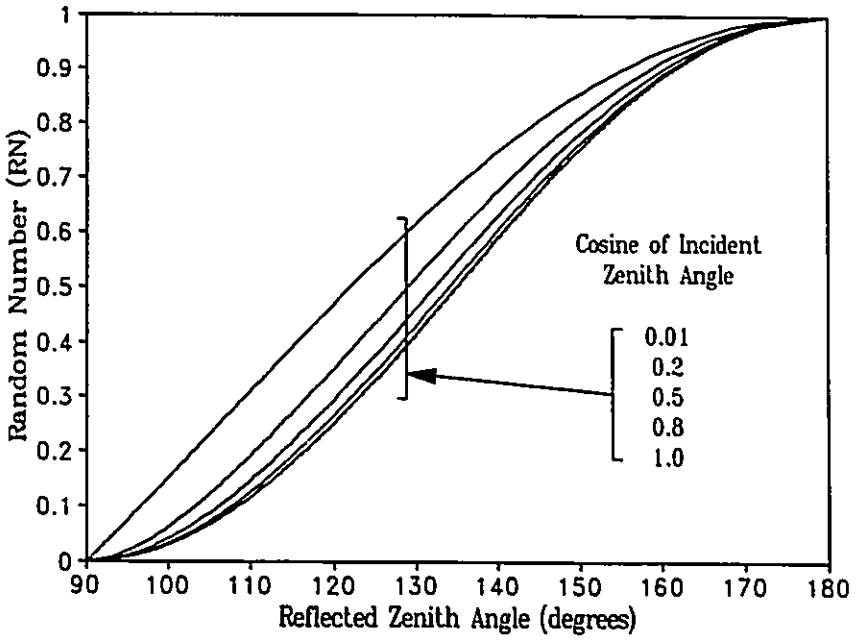

Fig.5.22. Random number RN that satisfies $\mu = -\cos(\theta_r)$ in Eq. (3.73) when $\omega_0 = 0.6$ and $\omega_1 = -1.0$. The dashed line is the solution for the Lambertian surface [Eq.(3.44)].

where

$$a(\mu_z) = \frac{\sum_{n=1}^{3} a_n \mu_z^n}{\sum_{n=1}^{4} b_n \mu_z^n} \; ; \quad b(\mu_z) = \frac{\sum_{n=1}^{4} c_n \mu_z^n}{\sum_{n=1}^{5} d_n \mu_z^n} \; , \tag{5.3b}$$

and the constants a_n, b_n, c_n, and d_n are listed in Table 5.1. The maximum absolute error in using Eq.(5.3) is approximately 0.345° for $\mu_z \geq 0.03$. These errors are tolerable given that the alternative is to numerically solve Eq.(3.73) each time a photon is reflected by the surface

The reflection azimuth angle φ_r is calculated by Eq.(3.76). This is done by generating a random number RN and solving Eq.(3.76) by the Newton–Raphson root–finding method. For the surface under consideration, only about six iterations are required to calculate φ_r to an accuracy of 0.065°. Due to the nature of Eq.(3.76), this solution is very efficient and reliable.

5.3.1.2 Non–Lambertian verses Lambertian Surfaces

In this section, radiative fluxes for broken clouds computed with the non–Lambertian surface are compared with fluxes computed with two versions of the Lambertian surface. The albedo of Type 1 Lambertian surface is given by Eq.(5.2) evaluated with the zenith angle of the solar beam incident at cloudtop and applies to all photons incident at the surface regardless of μ_z. Reflection for all photons, however, is still isotropic. This is the type of surface most likely to be used by the next generation of solar radiation codes in global climate models. Type 2 Lambertian surface is characterized by isotropic reflection and albedo of 0.236 (the spherical albedo of the non–Lambertian surface) for all incident angles and all initial solar beams. This surface is currently used by global climate models. The

Table 5.1

Coefficients for $a(\mu_z)$ and $b(\mu_z)$ in Eq.(5.3).

n	a_n	b_n
1	−1.5352009	−1.6915608
2	−4.1125995	−9.3491408
3	3.6841510	6.1237881
4	0.0	1.0

n	c_n	d_n
1	−3.4940378E−06	2.9685703E−04
2	2.3009754E−03	6.3977135E−02
3	3.2009885E−03	6.3105142E−01
4	−4.1986237E−03	3.5494985E−02
5	0.0	1.0

cloud fields used in this section are random arrays of identical cubic clouds with base heights equal to cloud thickness.

Table 5.2 indicates the differences in cloud/surface reflectance when non–Lambertian and Lambertian surfaces are used. The table contains a representative sample of a large number of computations. Clearly, the reflectance differences between surfaces are small; less than 5% with maximum differences occurring with no cloud. It is important to note that although the differences between non–Lambertian and Lambertian surfaces could be greater than those portrayed in this case, they are probably typical of many surfaces. Compared with the non–Lambertian surface, results for the Type 1 Lambertian surface underestimated reflectance at large cloud amounts and small θ_0 and over estimated reflectance at large cloud amounts and large θ_0. The reason for this is simply that the Type 1 Lambertian surface albedo is strictly $\alpha_s(\theta_0)$. In the non–Lambertian case, clouds diffuse radiation such that as cloud amount increases, the effective surface albedo approaches the intermediate spherical albedo. Thus, the corresponding surface albedo for the Type 1 Lambertian surface is too large at high θ_0 and too low at small at low θ_0. For small cloud amount the differences are negligible.

The opposite is true for the Type 2 Lambertian surface which has constant albedo equal to the intermediate spherical albedo. Hence, for large cloud amounts (with $\tau > \sim 5$), differences between the non–Lambertian and Type 2 Lambertian surfaces are negligible. But for small cloud amounts the surface and system albedos for Type 2 Lambertian are larger than the non–Lambertian case for small θ_0 and smaller for large θ_0.

It should be mentioned that the experiments for which results are listed in Table 5.2 were also conducted using the Monte Carlo method of photon transport in the surface (section 3.3.1). Scattering by soil grains was described by the

Table 5.2

Cloud/surface reflectances for random arrays of clouds above three different surfaces. NL is the non–Lambertian surface defined by Eq.(5.1); L1 is Type 1 Lambertian with albedo given by Eq.(5.2) evaluated only at the zenith angle of the initial solar beam θ_0; L2 is Type 2 Lambertian with albedo equal to 0.236 which is the Bond albedo of the NL surface. Cloud fields consist of identical, homogeneous, non–absorbing, 1 km cubic clouds of optical depth τ, arranged at random over a 10×10×1 cyclic generater. Cloudbase height is 1 km. A_c is the fraction of the generator filled with clouds. Errors in reflectances range from 0.001–0.003.

$\tau = 10$

θ_0(deg.)	A_c	NL	L1	L2
0	0	0.2100	0.2100	0.2360
60	0	0.2465	0.2465	0.2360
0	0.1	0.2238	0.2227	0.2452
60	0.1	0.2981	0.2959	0.2893
0	0.3	0.2632	0.2572	0.2787
60	0.3	0.3946	0.3975	0.3913
0	0.5	0.3115	0.3071	0.3135
60	0.5	0.4796	0.4914	0.4872
0	0.8	0.4075	0.3929	0.4145
60	0.8	0.5944	0.5956	0.5927
0	1.0	0.4774	0.4675	0.4727
60	1.0	0.6394	0.6469	0.6367

$\tau = 50$

θ_0(deg.)	A_c	NL	L1	L2
0	0	0.2100	0.2100	0.236
60	0	0.2465	0.2465	0.236
0	0.1	0.2444	0.2449	0.2679
60	0.1	0.3321	0.3326	0.3250
0	0.3	0.3356	0.3300	0.3506
60	0.3	0.4934	0.5015	0.4943
0	0.5	0.4500	0.4426	0.4601
60	0.5	0.6389	0.6389	0.6271
0	0.8	0.6523	0.6461	0.6512
60	0.8	0.7906	0.7944	0.7929
0	1.0	0.8137	0.8018	0.8125
60	1.0	0.8659	0.8716	0.8698

Henyey–Greenstein phase function [Eq.(3.30)] with g = –1/3 and ω_s = 0.6. Thus, the surface was very similar to that defined in Eq.(5.1) through (5.3). As expected, the results using the Monte Carlo surface are virtually identical to the non–Lambertian values listed in Table 5.2.

In conclusion, this comparison shows that for many cases of broken cloud, use of either type of Lambertian surface is adequate. This is very convenient for both analyses and parameterization of fluxes for broken clouds and for climate modelling. In the rest of the thesis, Type 2 Lambertian surface wili be used exclusively.

5.3.2 Multiple Reflections of Radiation Between Surface and Broken Clouds

Attention is now turned toward multiple reflections of photons between reflecting surfaces and broken cloud fields. First, a review of the multiple reflection process is given. Second, a method is developed and implemented for demonstrating the ranges of applicability of the multiple reflection geometric sum formulae for conditions of broken cloud above Lambertian surfaces.

5.3.2.1 Review of Multiple Reflections Between Atmosphere and Surface

Consider a reflecting and transmitting layer, such as a layer of broken clouds, situated over a reflecting ground surface. For simplicity, scattering and absorption by molecules between the layer and the surface are neglected. Assume that the layer is irradiated from above by a collimated beam of monochromatic solar radiation of unit intensity and that fractions R_c and T_c of this beam are reflected and transmitted respectively. Designate the albedo of the underlying surface to the initially transmitted flux (diffuse and direct beams) as $\alpha_{s,1}$. Thus, $T_c\alpha_{s,1}$ of the original beam irradiates the base of the layer. Assume that the layer reflects a fraction r_1 of the upwelling radiation back towards the surface and

transmits a fraction t_1 out its top. Therefore, $T_c\alpha_{s,1}t_1$ emerges out the top while the return flow of radiation downwards, $T_c\alpha_{s,1}r_1$, is reflected again by the surface which this time has an albedo of $\alpha_{s,2}$. Reflectance and transmittance of the layer to the second stream of upwelling radiation are denoted r_2 and t_2. The reason why surface albedo and layer albedo and transmittance may differ on each internal reflection is because the angular and spatial distribution of the radiation fields may differ. Allowing this process to repeat indefinitely leads to overall system reflectance and surface irradiance of

$$R = R_c + T_c\alpha_{s,1}t_1 + T_c\alpha_{s,1}\alpha_{s,2}t_2r_1 + \cdots + T_ct_n\prod_{j=1}^{n}\alpha_{s,j}\prod_{i=1}^{n-1}r_i + \cdots$$

$$= R_c + T_c\sum_{k=1}^{\infty}\left\{t_k\prod_{j=0}^{k-1}\alpha_{s,j+1}r_j\right\} \quad \Big| \; r_0 = 1 \;, \tag{5.4a}$$

and

$$T = T_c + T_c\alpha_{s,1}r_1 + T_c\alpha_{s,1}\alpha_{s,2}r_1r_2 + \cdots + T_c\prod_{j=1}^{n}\alpha_{s,j}r_j + \cdots$$

$$= T_c\sum_{k=1}^{\infty}\left\{\prod_{j=1}^{k}\alpha_{s,j}r_j\right\} . \tag{5.4b}$$

If the conditions

$$\left.\begin{aligned}\alpha_{s,i} &= \alpha_{s,j} = \alpha_s \\ r_i &= r_j = \langle r\rangle \\ t_i &= t_j = \langle t\rangle\end{aligned}\right\} \forall\, i \neq j, \tag{5.5}$$

are satisfied, then Eqs.(5.4a) and (5.4b) become geometric series conveniently expressed as

$$R = R_c + \frac{T_c \langle t \rangle \alpha_s}{1 - \alpha_s \langle r \rangle} , \tag{5.6a}$$

and

$$T = \frac{T_c}{1 - \alpha_s \langle r \rangle} . \tag{5.6b}$$

These expressions are used throughout climate studies and implicitly assume that clouds are either distributed evenly across the sky or completely overcast. The plane–parallel forms of Eq.(5.6) are obtained by letting $R_c = A_c R_{pp}$, $T_c = A_c T_{pp}$, $\langle r \rangle = A_c \langle r_{pp} \rangle$, and $\langle t \rangle = A_c \langle t_{pp} \rangle$, where A_c is cloud amount and terms with subscript 'pp' are plane–parallel values (e.g. Schnieder and Dickinson, 1976). For true plane–parallel slabs of cloud, multiple reflections are confined to regions beneath clouds and Eq.(5.6) becomes

$$R = A_c R_{pp} + (1 - A_c)\alpha_s + \frac{A_c T_{pp} \langle t_{pp} \rangle \alpha_s}{1 - \alpha_s \langle r_{pp} \rangle} , \tag{5.7a}$$

$$T = (1 - A_c) + \frac{A_c T_{pp}}{1 - \alpha_s \langle r_{pp} \rangle} . \tag{5.7b}$$

The differences between Eq.(5.6) and (5.7) are very small; generally $\leq 2\%$. It is not known yet, however, whether the conditions listed in Eq.(5.5) are satisfied for true broken cloud. If the leap from Eq.(5.4) to Eq.(5.6) is valid, the geometric sum formulation can be applied in climate models using parameterizations of fluxes for broken cloud. This seems more desirable than including the effects of surface

albedo in some other manner (e.g. Welch and Wielicki, 1989).

5.3.2.2 Applicibility of the Multiple Reflection Geometric Sum Formulae for Broken Clouds

This section examines the range of validity of Eq.(5.6a) and Eq.(5.6b) for broken cloud conditions. A technique is presented for verifying Eq.(5.6a) and (5.6b) using the Monte Carlo code developed earlier. The technique is then employed using examples which illustrate the applicability of Eq.(5.6a) and (5.6b).

To test the applicability of Eqs.(5.6a) and (5.6b), the Monte Carlo models are used with $\alpha_s = \omega_0 = 1.0$ and reflectances of a cloud field to upwelling photons that have encountered the surface 1, 2, 3, ..., M times are calculated. If the conditions in Eq.(5.5) hold, all reflectances should be equal to within experimental error.

Besides being a satisfactory approximation to realistic surfaces, the Lambertian surface leads to the following property which helps simplify experiments. Equation (3.48) defined the albedo of a cloud layer irradiated by a field of radiation that varied only as a function of zenith angle. Radiation incident on cloudbase after having been reflected by the surface can vary in both zenith and azimuth angle as well as in space. This is because of shadows cast by broken clouds and perhaps inhomogeneous surface. The reflectance of a cloud field to upwelling radiation that has interacted with the surface n times is a surface area integral over a hemispheric integral and given by

$$r_n = \frac{\int_{\mathcal{A}} \int_{2\pi} R_c(\Omega, \sigma) K_n(\Omega, \sigma) \, d\Omega d\sigma}{\int_{\mathcal{A}} \int_{2\pi} K_n(\Omega, \sigma) \, d\Omega d\sigma}, \qquad (5.8)$$

where $\mathcal{A}$ signifies the surface and $d\sigma$ is an elemental area of $\mathcal{A}$, $d\Omega$ represents elemental solid angle, R_c is cloud reflectance to radiation incident from the Ω direction reflected at $d\sigma$, and K_n defines the areal and angular distribution of radiation reflected by the surface for the n^{th} time. A similar expression can be written for cloud transmittance t_n. For the simple Lambertian surface, radiation reflected at $d\sigma$ is equal in all directions and albedo α_s is constant and independent of incident angle. Thus, for a Lambertian surface

$$K_n(\Omega,\sigma) = \alpha_s L_n(\sigma) \ , \tag{5.9}$$

where L_n defines the areal distribution of radiative flux *incident* at the surface for the n^{th} time. Substituting Eq.(5.9) into Eq.(5.8) shows that r_n is independent of α_s when the surface is Lambertian. Note that for a Lambertian surface below a plane–parallel overcast cloud, $L_n(\sigma)$ is constant over $\mathcal{A}$ for any given n and Eq.(5.8) reduces to Eq.(3.48). In broken cloud conditions, however, $L_n(\sigma)$ varies over $\mathcal{A}$ especially for n=1 due to cloud shadows. The point of this demonstration is that for a Lambertian surface, r_n and t_n do not depend on α_s; any variation in them is due to spatial distribution of radiation.

The overall reflectance of a cloud/Lambertian surface system to a monochromatic solar beam in a Monte Carlo simulation can be expressed as

$$R = \left\{ \frac{1}{N} \sum_{i=1}^{N} \omega_o^{n_i} \cdot \delta_{0m_i} \right\} + \left\{ \frac{1}{N} \alpha_s \sum_{i=1}^{N} \omega_o^{n_i} \cdot \delta_{1m_i} \right\} + \cdots \tag{5.10}$$

$$\cdots + \left\{ \frac{1}{N} \alpha_s^k \sum_{i=1}^{N} \omega_o^{n_i} \cdot \delta_{km_i} \right\} + \cdots$$

$$= \frac{1}{N} \sum_{k=0}^{\infty} \left\{ \alpha_s^k \sum_{i=1}^{N} \omega_o^{n_i} \cdot \delta_{km_i} \right\},$$

where N is the total number of photons used, n_i and m_i are the numbers of scattering events and surface encounters experienced by the i^{th} photon, and δ_{ij} is the Kronecker delta. The first term on the right hand side of Eq.(5.10) represents the fraction of incident photons weighted for droplet absorption that are reflected without ever encountering the surface. This is equivalent to cloud reflectance to the initial direct beam; R_c in Eq.(5.4a). Subsequent terms on the right hand side of Eq.(5.10) represent the weighted fraction of reflected photons that have encountered the surface at least once. Thus, Eq.(5.10) is just a term–by–term discrete analog of Eq.(5.4a) provided the first condition in Eq.(5.5) is satisfied.

Having established a term–by–term correspondance betweem Eq.(5.4a) and Eq.(5.10), the quotients between successive terms in both equations are

$$\frac{\alpha_s^k \sum_{i=1}^{N} \omega_o^{n_i} \cdot \delta_{km_i}}{\alpha_s^{k-1} \sum_{i=1}^{N} \omega_o^{n_i} \cdot \delta_{(k-1)m_i}} \equiv \frac{T_c t_k \, \alpha_s^k \prod_{i=1}^{k-1} r_i}{T_c t_{k-1} \alpha_s^{k-1} \prod_{i=1}^{k-2} r_i} = \alpha_s \frac{t_k}{t_{k-1}} r_{k-1} \,. \tag{5.11}$$

Dividing this expression by α_s leaves

$$\frac{t_k}{t_{k-1}} r_{k-1} \equiv \frac{\sum_{i=1}^{N} \omega_o^{n_i} \cdot \delta_{km_i}}{\sum_{i=1}^{N} \omega_o^{n_i} \cdot \delta_{(k-1)m_i}} \,. \tag{5.12}$$

From the second term on the right hand side of both Eq.(5.41) and Eq.(5.10), when $\omega_o = 1.0$,

$$T_c t_1 \equiv \frac{1}{N} \sum_{i=1}^{N} \delta_{1m_i} \quad . \tag{5.13}$$

Also for $\omega_o = 1.0$,

$$T_c \equiv 1 - R_c = 1 - \frac{1}{N} \sum_{i=1}^{N} \delta_{0m_i} \quad , \tag{5.14}$$

and

$$r_k = 1 - t_k \quad . \tag{5.15}$$

Therefore, it follows from Eq.(5.13) and Eq.(5.14) that

$$t_1 = \frac{\frac{1}{N} \sum_{i=1}^{N} \delta_{1m_i}}{\left[1 - \frac{1}{N} \sum_{i=1}^{N} \delta_{0m_i}\right]} = \frac{\sum_{i=1}^{N} \delta_{1m_i}}{\left[N - \sum_{i=1}^{N} \delta_{0m_i}\right]} \quad . \tag{5.16}$$

Hence, substituting Eq.(5.16) into (5.15) gives r_1. Substituting Eq.(5.15) into Eq.(5.12) with $\omega_o = 1.0$ gives the recursive formula for cloudbase reflectance as

$$r_k = 1 - \left[\frac{1 - r_{k-1}}{r_{k-1}}\right] \frac{\sum_{i=1}^{N} \delta_{km_i}}{\sum_{i=1}^{N} \delta_{(k-1)m_i}} \quad . \tag{5.17}$$

This is calculated easily in the Monte Carlo code. From this, the set $\{r_1, r_2, \ldots, r_k\}$ can be generated and if $r_i \simeq r_j$ for all $i \neq j$ then the geometric sums are applicable. Errors associated with estimates of r_k are given as

$$\Delta r_k \simeq \pm \left[\frac{r_k(1 - r_k)}{N \left\{ \prod_{n=0}^{k-1} r_n \right\}} \right]^{1/2} , \tag{5.18a}$$

where r_0 designates

$$r_0 \equiv 1 - \frac{1}{N} \sum_{i=1}^{N} \delta_{0m_i} = 1 - R_c = T_c \ . \tag{5.18b}$$

Note that the denominator in brackets in Eq.(5.18a) is just the number of photons that experienced at least k encounters with the surface.

Before applying this technique to broken cloud fields, it is demonstrated for plane–parallel homogeneous overcast cloud layers above a Lambertian surface defined by I_L [see Eq.(3.42)]. For this case it is known *a priori* that all r_k should be within experimental error of each other. In this test, as in all that follow, only six internal multiple reflections are considered because the flux leaving cloud–top that has undergone at least six internal reflections is almost always less than 0.01 of the initial input. Table 5.3 shows the results for a cloud of $\tau = 5$, ω_o=1.0, and μ_o=1.0. As expected the values of r_k all very similar. Furthermore, direct–beam reflectances of the cloud $R_c(\mu_o)$ were determined for 10 values of μ_o. The points were fitted with a cubic polynomial ($r^2 = 0.999$) and the spherical albedo was computed to be 0.371 which is in excellent agreement with the values of r_k in Table 5.3. This demonstrates the validity of both the method of finding r_k and the

Table 5.3

Demonstration of the procedure developed in Eqs.(5.10) through (5.17) for estimating the reflectance of a cloud field to upwelling radiation r_k on successive orders of internal multiple reflections. Cloud is of infinite horizontal extent, homogeneous, and has an optical depth of 5 and $R_c(\mu)$ is the zenith angle dependent albedo of the cloud.

k	$r_k \pm \Delta r_k$
1	0.3710 ± 0.002
2	0.3702 ± 0.004
3	0.3791 ± 0.007
4	0.3690 ± 0.011
5	0.3877 ± 0.017
6	0.4034 ± 0.028

$$\langle r \rangle = 2\int_0^1 R_c(\mu)\mu d\mu = 0.371$$

use of I_L to describe a Lambertian surface.

Figure 5.23 shows cloud layer reflectance to upwelling radiation for the first six internal reflections for three broken cloud fields. The cloud fields consist of cubic clouds 1 km thick, average vertical optical depth of 30, and $A_c = 0.25$. Figure 5.23a applies to a cloud field produced by the variable cloud model scaled with $|\mathbf{k}|^{-2}\ \forall\ |\mathbf{k}|$ and Fig.5.23b applies to its identical cloud field counterpart. Figure 5.23c applies to a regular array of identical cubic clouds. Solar zenith angles of 0° anf 60° and cloudbase heights of 0, 1, and 5 km are considered.

The curves in Fig.5.23a and b are similar. The most striking feature is that, even at base height of 5 km, r_k is not independent of k. Hence, strictly speaking, the geometric sum forms are not applicable. Later on it is shown that this, however, is not a serious problem. First, the curves in Fig.5.23 have some interesting properties that deserve mentioning.

The reflectance of the scaling cloud fields to radiation that has encountered the surface once r_1 increases with base height. This is because most radiation reflected by the surface is direct–beam radiation that is incident on cloudless parts of the surface. Because the surface is Lambertian, reflected radiation spreads out as it travels upwards. If the clouds are high, a large fraction of surface reflected radiation spreads out and encounters cloud. If, on the other hand, base height is low, a relatively large fraction of reflected photons escape through the cloudless space they entered by. This is also why r_1 for $\theta_0 = 60°$ is slightly greater than for $\theta_0 = 0°$. At $\theta_0 = 60°$, some direct–beam is incident below clouds and proportionaly less irradiates surface below cloudless areas.

Cloudbase reflectance to radiation that has encountered the surface twice r_2 is much greater than r_1. This is because initially incident radiation reflected by regions of surface beneath cloudless sectors is easily lost leaving much of the radiation still involved in multiple reflections directly beneath clouds. Hence, layer

Fig.5.23. Cloud field reflectance for the first six up–welling streams of surface reflected radiation. Clouds are 1 km thick and base heights are indicated on the plots. Solid and dashed lines correspond to $\mu_0 = 1.0$ and 0.5. Cloud fields are characterized by: (a) Variable clouds with $\langle S_k \rangle \sim k^{-i} \forall k$, $A_c = 0.25$, and $\langle \tau \rangle = 30$; (b) Identical cloud field counterpart to (a); (c) Regular array of identical cubes with $A_c = 0.25$ and $\tau = 30$. Short horizontal lines indicate the spherical albedo of the cloud fields (for (c) it lies on top of the 1 and 5 km curves).

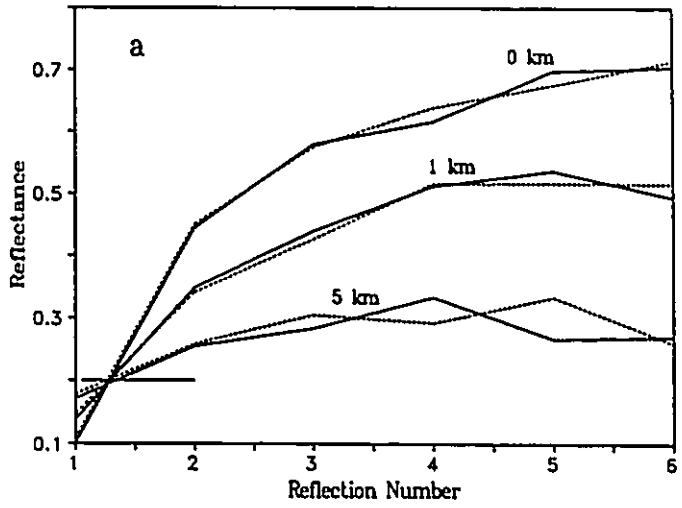
a
0 km
1 km
5 km
Reflectance
0.7
0.5
0.3
0.1
1
2
3
4
5
6
Reflection Number

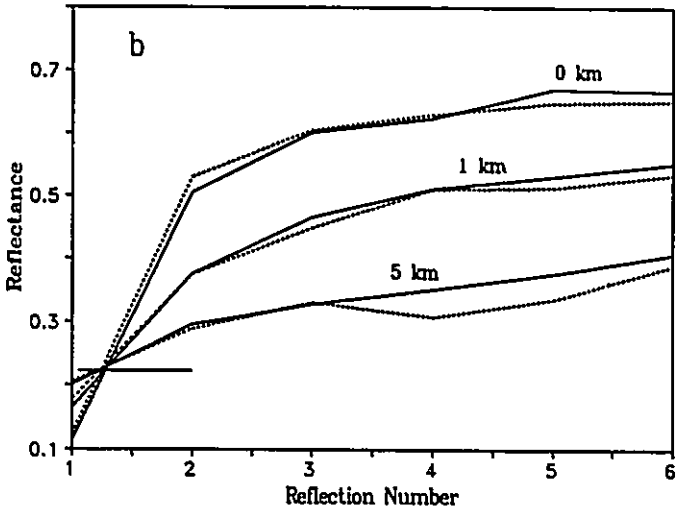
b
0 km
1 km
5 km
Reflectance
0.7
0.5
0.3
0.1
1
2
3
4
5
6
Reflection Number

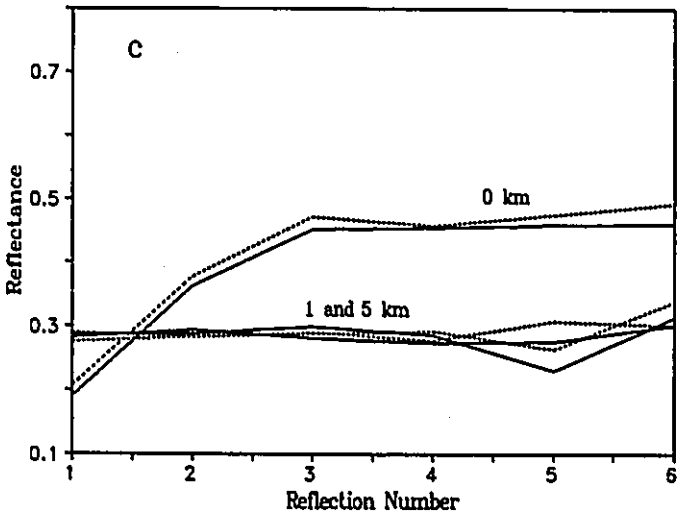
c
0 km
1 and 5 km
Reflectance
0.7
0.5
0.3
0.1
1
2
3
4
5
6
Reflection Number

reflectance to the second upwelling stream of radiation is governed to a greater extent by cloud optical attributes than by cloud amount. As base height increases, the spreading out of up– and down–welling radiation is quite efficient and the difference between r_2 and r_1 decreases. For subsequent internal reflections, r_k increases at an attenuating rate for all base heights and levels off at $k \simeq 5$, and memory of θ_0 is lost. The magnitude of the limiting reflectance is governed by cloudbase height: 0 km base has the largest reflectance because radiation involved in multiple reflections is almost exclusively beneath extensive (horizontal and vertical) cloud. For 5 km base height, the internal reflecting radiation field is well diffused, hence, a significant fraction of upwelling radiation escapes on each encounter with the cloud field.

The horizontal line on Fig.5.23a and b signifies the spherical albedo of the cloud fields. If internally reflected radiation was perfectly diffused, this would be the cloudbase reflectance. Though the reflectance values on the plots have been joined with lines, regions between the integer reflection numbers are meaningless. It may, therefore, be a coincidence that the reflectance curves for different cloudbase heights intersect at the value of the cloud field spherical albedo.

Figure 5.23c shows that for base height of 0 km, reflectance of the regular array depends on reflection number but less than it does for the scaling cloud fields. By base height of 1 km, however, r_k is independent of k and θ_0 and equals the regular array's spherical albedo of 0.287. This is because of the regularity of the array: radiation reflected by the surface is sufficiently diffused after only one reflection and remains as such due to the regular spacing of non–extensive clouds.

The geometric form of the flux equation [Eq.(5.6a)] can be rearranged to solve for the effective cloudbase albedo required for the geometric formula to be true as

$$\langle r \rangle_{eff} = \frac{[1 - R_c(\mu_o)]\alpha_s - R(\mu_o) + R_c(\mu_o)}{\alpha_s[1 - R(\mu_o)]} \quad . \tag{5.19}$$

$\langle r \rangle_{eff}$ is plotted in Fig.5.24 as a function of α_s for the identical scaling cloud field used to produce Fig.5.23b. Figure 5.24a shows that for base height of 0 km, $\langle r \rangle_{eff}$ depends on α_s for all μ_o. It has already been shown that r_k does not depend on α_s for a Lambertian surface, hence, the fact that $\langle r \rangle_{eff}$ depends on α_s is just another indication that the geometric forms are imperfect descriptions. Note that the values of $\langle r \rangle_{eff}$ at small α_s are almost identical to the values of r_1 shown in Fig.5.23b. This is because with α_s so low, internal reflections beyond the first one are insignificant. For large α_s, however, $\langle r \rangle_{eff}$ has increased to approximately the cloud fields spherical albedo. This is because more radiation is undergoing multiple reflections and so the larger valued higher order cloudbase reflectances are more important. The same can be said for $\langle r \rangle_{eff}$ with cloudbase height of 5 km (Fig.5.24b) except that the dependance of $\langle r \rangle_{eff}$ on α_s is much reduced. The dependence of of $\langle r \rangle_{eff}$ on θ_o is governed primarily by the dependence of r_1 on θ_o as discussed above.

What value of $\langle r \rangle_{eff}$ should be used in multiple reflection calculations for broken cloud? If a simple procedure for choosing an appropriate $\langle r \rangle_{eff}$ cannot be found, the usefulness of the geometric formulae is reduced. Before attempting to broach this question, consider how others have dealt with it. Welch and Wielicki (1984) parameterized albedo for a regular array of identical, homogeneous, non–absorbing cuboidal clouds irradiated with direct solar beam parallel to cloud sides (shining down clear rows between clouds) as

$$R_{cf}(\mu_o) = A_e R_{pp}(\mu_o) \quad , \tag{5.20}$$

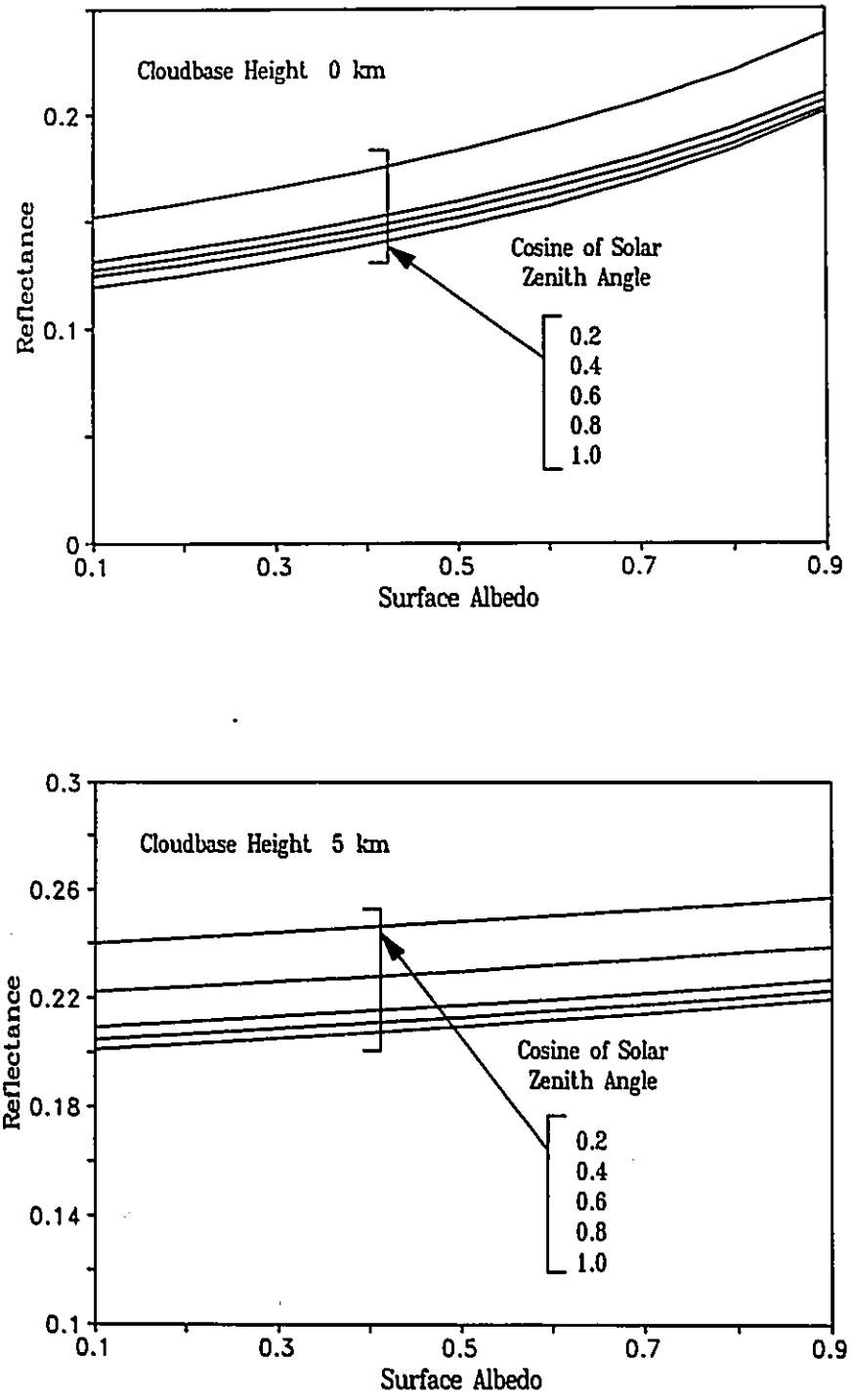

Fig.5.24. $\langle r \rangle_{eff}$ as a function of α_s for the identical scaling cloud field used in Fig.5.23b at several values of μ_0 and cloudbase height of 0 and 5 km.

where R_{pp} is plane–parallel cloud albedo using the vertical optical depth of the cuboids and A_e is effective cloud fraction. They parameterized A_e, by extending a procedure by Weinman and Harshvardhan (1982), as a function of A_c, cloud τ and aspect ratio, and θ_o. Welch and Weilicki (1989) accounted for surface albedo by

$$R_{cf}(\mu_o) = A_e R_{pp}(\mu_o) + (1 - N'')\alpha_s \ , \tag{5.21}$$

where

$$N'' = \frac{A_c}{2}\left[1 + \begin{cases} 1 + (H/D)\tan\theta_o, & A_c \le A^* \\ A_c^{1/2}, & A_c > A^* \end{cases}\right] \ ,$$

and A^* depends on cloud aspect ratio and θ_o. In Eq.(5.20), $A_e R_{pp}(\mu_o)$ is equivalent to $R_c(\mu_o)$ in Eq.(5.6a). Therefore,

$$(1 - N'') \equiv \frac{T_c(\mu_o)\langle t\rangle}{1 - \alpha_s \langle r\rangle_{eff}} \ . \tag{5.22}$$

Thus, Eq.(5.22) does not account explicitly for multiple reflections. Furthermore, it applies to regular arrays with $\tau \lesssim 50$ and $\varphi_o = n\pi/2$ (n=0,1,2,3) only.

Kobayashi (1989) explicitly accounts for multiple reflections and used random arrays of clouds. His fundamental equation is the same as Eq.(5.6a) in which he defines

$$R_c(\mu_o) \equiv I_a E_f A_c R(1) \ , \tag{5.23}$$

where R(1) is albedo of an isolated cuboidal cloud with $\alpha_s = 0$, and I_a and E_f are cloud–cloud interaction and area enhancement ratios (Kobayashi, 1988), respectively. He uses the following approximations:

$$I_a = 1 + \left[\frac{R_{pp}(\mu_o)}{R(1)} - 1\right] A_c \ ,$$

$$R_{pp}(\mu_o) = c + d\mu_o \ , \tag{5.24}$$

and

$$R(1) = e - f\mu_o \ ,$$

where c, d, e, and f are parametric constants. He defines $\langle r \rangle_{eff}$ as (his notation)

$$R_b = \frac{2}{\pi}\int_0^{\pi/2} I_a E_f A_c R(1) d\theta \ , \tag{5.25a}$$

where θ is zenith angle. He then maintains that Eq.(5.25a) is

$$R_b = gA_c + g(h-1)A_c^2 \ , \tag{5.25b}$$

where

$$g = (e + f)\langle E_f \rangle \ ,$$

and

$$h = \frac{2}{\pi}\int_0^{\pi/2} \left[\frac{c + d\cos\theta}{e - f\cos\theta}\right] d\theta \ ,$$

in which $\langle E_f \rangle$ is the hemispherically–averaged area enhancement ratio. The author has not been able to reproduce Eq.(5.25b). Not knowing exactly what Kobayashi means by $\langle E_f \rangle$, his expressions cannot be accepted or rejected. What is important, however, is that in his notation, the parameterization requires six parametric constants and one numerical integration. His parameterization requires more work than is necessary and warranted.

For the same identical cloud field used in Fig.s 5.23 and 5.24, Fig.5.25a shows the fractional error, as a function α_s, between system reflectance calculated by the Monte Carlo code and the geometric sum flux equation using $\langle r \rangle_{eff}$ equal to the cloud field spherical albedo (0.227) with base altitude of 0 km. Maxmimal errors of $\sim -5\%$ occur at high sun near $\alpha_s = 0.3$. Use of $\langle r \rangle_{eff} = R_c(\mu_o{=}0.5) = 0.25$ generally shifted down all the curves in Fig.5.25a resulting in a maximum error of –6.5%. Figure 5.25b is the same as Fig.5.25a except that cloudbase height is 5 km. This time, use of cloud spherical albedo in the geometric sum formula produces errors that are generally less than 1%. Use of $\langle r \rangle_{eff} = R_c(\mu_o{=}0.5)$ pushed down all curves in Fig.5.25b resulting in maximum error of –2.5%.

To augment these results, consider a scaling variable cloud field consisting of cubes with $\langle S_k \rangle \sim k^{-1.35}$ for $k > 5$ and $\sim k^{-0}$ for $k \leq 5$, $\langle \tau \rangle = 10$, $A_c = 0.4$, and base height equal to cloud thickness. Figure 5.26 shows reflectance of this cloud field as a function of α_s for three solar zenith angles. Solid lines are Monte Carlo results and the dashed lines are from the geometric sum formula using Monte Carlo results with $\alpha_s = 0$. Figure 5.25a used $\langle r \rangle_{eff}$ equal to the spherical albedo of the cloud field which is 0.20. Figure 5.25b used $\langle r \rangle_{eff}$ equal to cloud fields direct–beam albedo for $\mu_o = 0.5$ which is 0.226. Clearly, both estimates of $\langle r \rangle_{eff}$ yield accurate results. Maximum relative errors due to the geometric sum formula with $\langle r \rangle_{eff}$ of 0.20 and 0.226 are –1.9% and –3.6% respectively. Based on these results, representing $\langle r \rangle_{eff}$ in the geometric sum flux equations by either a cloud field's spherical albedo or its direct–beam albedo evaluated at $\mu_o \simeq 0.5$ is adequate in most cases. The most troublesome cases involve broken clouds at the surface which is unrealistic.

Fig.5.25. Fractional error in system reflectance due to use of the spherical albedo of the cloud field used in Fig.5.23b and 5.24 ($\langle r \rangle = 0.227$) in the geometric sum multiple reflection equation [Eq.(5.6a)]. Fractional error is defined as FE = $100[R(\langle r \rangle) - R(MC)]/R(MC)$, where $R(\langle r \rangle = 0.227)$ and R(MC) are system reflectances due to Eq.(5.6a) using the spherical cloud albedo and the Monte Carlo model respectively.

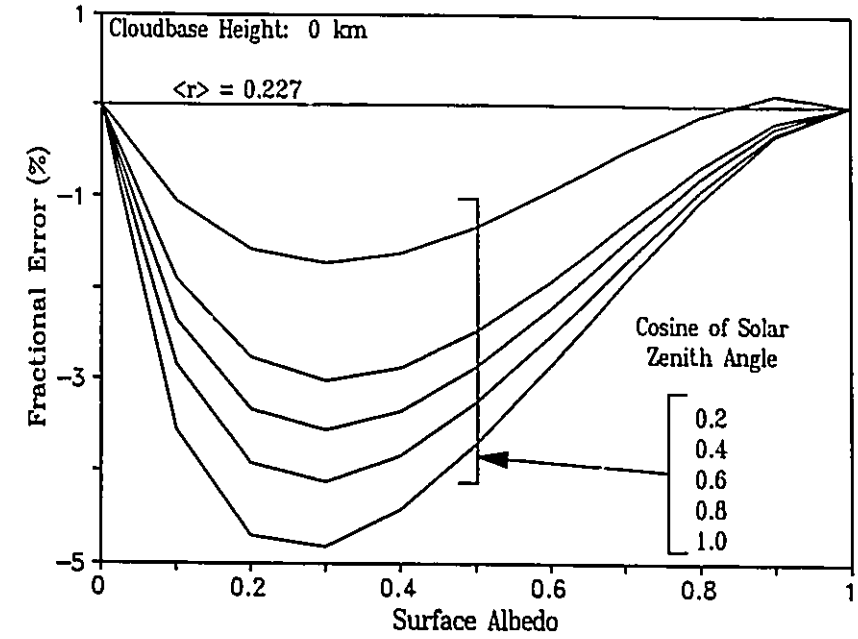
Cloudbase Height: 0 km
<r> = 0.227
Fractional Error (%)
1
−1
−3
−5
0
0.2
0.4
0.6
0.8
1
Surface Albedo
Cosine of Solar Zenith Angle
0.2
0.4
0.6
0.8
1.0

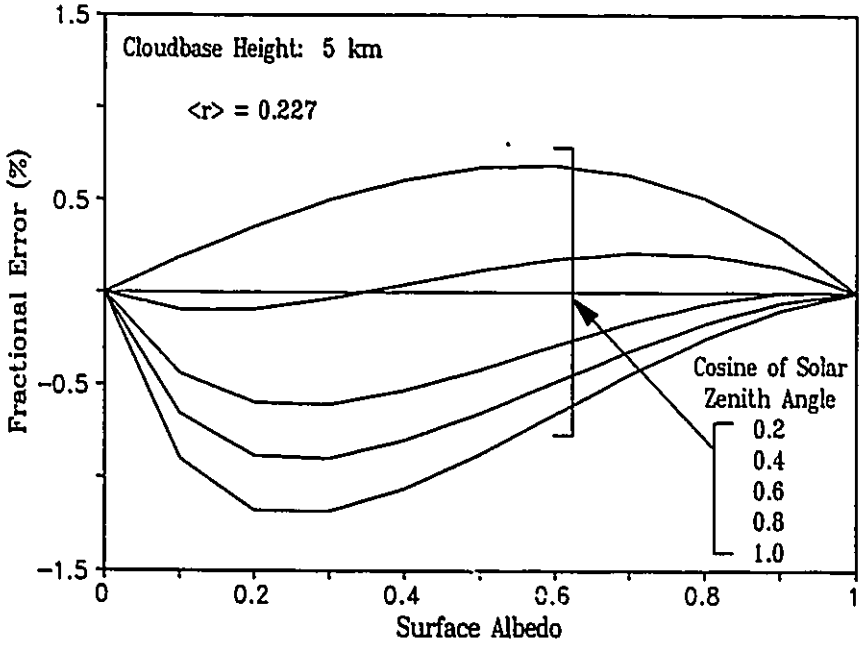
Cloudbase Height: 5 km
<r> = 0.227
Fractional Error (%)
1.5
0.5
−0.5
−1.5
0
0.2
0.4
0.6
0.8
1
Surface Albedo
Cosine of Solar Zenith Angle
0.2
0.4
0.6
0.8
1.0

Fig.5.26. System reflectance of a variable cloud field consisting of cubes with $\langle S_k \rangle \sim k^{-1.35}$ fo $k > 5$ and k^{-0} for $k \leq 5$, $A_c = 0.4$, and $\langle \tau \rangle = 10$. Cloud base height equals cloud thickness. Solid lines are Monte Carlo results. Dashed lines are the geometric sum formula using a) $\langle r \rangle = 0.20$ (cloud field spherical albedo) and b) $\langle \bar{r} \rangle = 0.226$ (cloud field reflectance at $\mu_0 = 0.5$). Labels on curves indicate solar zenith angle.

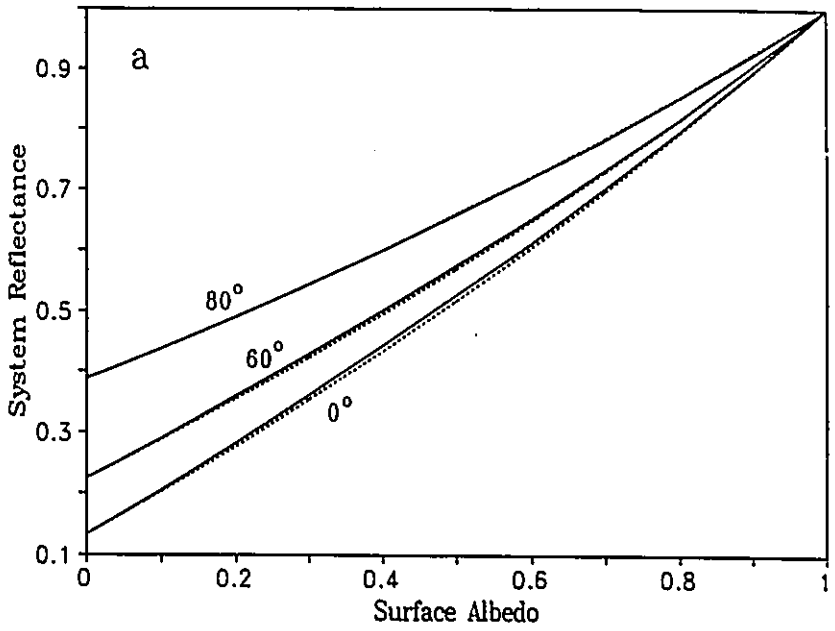
a
0.9
0.7
0.5
0.3
0.1
System Reflectance
80°
60°
0°
0
0.2
0.4
0.6
0.8
1
Surface Albedo

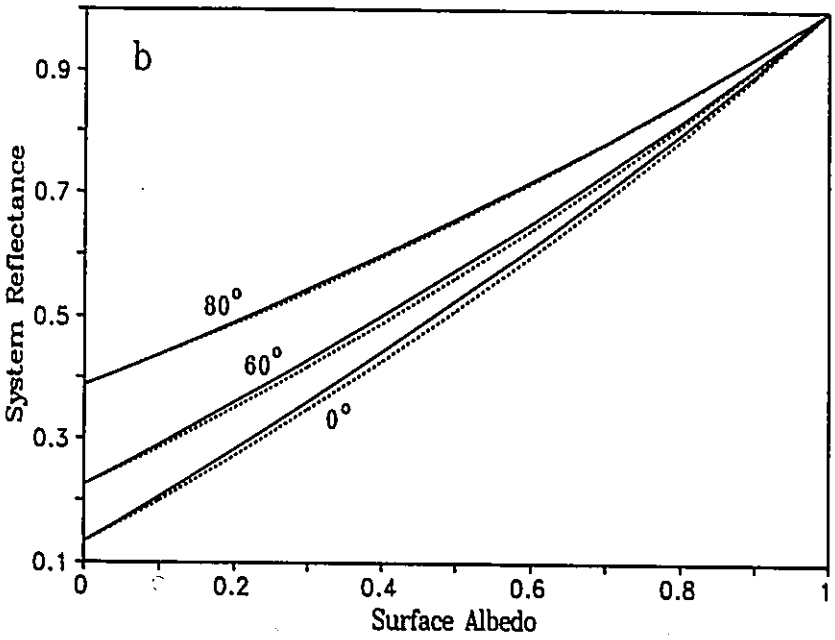
b
0.9
0.7
0.5
0.3
0.1
System Reflectance
80°
60°
0°
0
0.2
0.4
0.6
0.8
1
Surface Albedo

5.4 System Albedo Reduction due to Non–Absorbing Clouds

Welch and Wielicki (1989) noted that conservative scattering, broken clouds can reduce system albedo below surface albedo. They referred to this situation as "extremely counterintuitive" and examined it at length. They concluded that reduced albedo is due to enhanced surface irradiance and hence absorption. This point is raised for three reasons: first, this phenomenon has been studied for sometime with regard to aerosols; second, it is not necessarily counterintuitive as it follows directly from the multiple reflection geometric sum formula; and third, it is not restricted to broken cloud but applies to overcast as well.

It has been known for sometime (e.g. Rasool and Schnieder, 1971; Chýlek and Coakley, 1974; Russell and Grams, 1975) that introduction of an aerosol into the atmosphere can reduce (increase) or increase (reduce) the albedo (temperature) of Earth. What surprised Welch and Wielicki (1989) was the system albedo reduction (warming) produced by non–absorbing broken clouds. The geometric form of the multiple reflection flux equation provides an approximate indication of whether system albedo is reduced by cloud (or any atmospheric constituent that attenuates solar radiation).

If $R_c(\mu_o)$ is albedo of a cloud field to direct beam radiation and $R(\mu_o)$ is albedo of the cloud/surface system, albedo reduction below the case with no cloud is mathematically stated as $R(\mu_o) < \alpha_s$, where α_s is surface albedo. Assuming that the geometric flux equation [Eq.(5.6a)] holds, this implies that

$$R(\mu_o) = R_c(\mu_o) + \frac{T_c(\mu_o)\langle t\rangle \alpha_s}{1 - \alpha_s\langle r\rangle} < \alpha_s \ , \tag{5.26}$$

where $\langle t\rangle$ and $\langle r\rangle$ can assumed to be equivalent to $\langle t\rangle_{eff}$ and $\langle r\rangle_{eff}$ as used in the

previous section. For non–absorptive clouds, this inequality can be rearranged to give

$$R(\mu_o) < \alpha_s \quad \Leftrightarrow \quad \frac{R_c(\mu_o)}{\langle r \rangle} < \alpha_s \ . \tag{5.27}$$

For large μ_o ($\gtrsim 0.6$), it is common to have $R_c(\mu_o)/\langle r \rangle < 1$ for both overcast and broken cloud conditions. Hence, for large α_s values, it would not be surprising to find $R(\mu_o) < \alpha_s$. Quite simply, the presence of any cloud (absorbing or not) serves to reflect a fraction of surface reflected photons back to the absorbing surface where they have additional opportunities of being absorbed. Therefore, under certain conditions, approximately those in Eq.(5.27), non–absorbing clouds can be expected to reduce system albedo. The conditions are small solar zenith angle and high underlying albedo. Simultaneous occurence of these conditions, however, are rare on Earth.

CHAPTER 6

Summary and Conclusion

The primary objective of this study was to investigate solar radiative transfer through realistic fields of broken cumulus with horizontal dimensions similar to GCM gridboxes. The thesis consists of three main components: empirical evidence demostrating the 'scaling', fractal–like nature of cloud liquid water distribution and the presentation of a model to generate such fields; development and validation of three–dimensional atmospheric and underlying reflecting surface Monte Carlo photon transport models; and numerical exploration of radiative fluxes for scaling cloud fields using the models just mentioned.

In the first part, several AVHRR satellite images of broken, single–layer cloud fields were examined for scaling properties primarily. Spectra of shortwave reflectance and longwave emission showed very similar form. Of particular interest was the finding that one–dimensional spectra $\langle S_k \rangle$ of both waveband images exhibit distinct changes in slope at space scales corresponding to ~3 to 4 km. This appears to be typical cloud cell diameter. These changes in slope are remarkably similar to those found by Cahalan and Snider (1989) in LANDSAT near–infrared imagery from the FIRE experiment. They, however, found that the changes in slope occurred at less than 1 km (but still typical cloud cell size). For scales larger than ~ 4 km, $\langle S_k \rangle$ can range from at least $k^{-0.5}$ to $k^{-5/3}$. It is likely that for scales greater than perhaps 50 km, cloud fields (especially stratoform clouds) may

be completely random. For scales less than typical cloud cell size, it appears that radiance fields are generally smoother than k^{-3}. The fact that the AVHRR VIS and IR spectra display the same form suggests that the scaling changes are due to dynamics, as hypothesized by Cahalan and Snider, and are not entirely a radiative phenomenon. However, since Cahalan and Snider's explanation for the scaling changes stem from two–dimensional turbulence theory, it is difficult to see how it could apply at scales less than a few kilometers where the atmosphere is not even approximately two–dimensional.

Examination of cloud liquid water content (LWC) and temperature time series obtained by aircraft flying through fairweather cumulus showed that these fields tend to follow a single scaling law, often very close to $k^{-5/3}$, from at least ~50 km down to ~120 m. While slight increases in slope are seen below 1 km, the change in slope seems much less pronounced than those seen for satellite radiance fields. It may be that LWC follows closely a three–dimensional turbulence law at most scales greater than the viscous cut–off and that the vertical integral of liquid water is much smoother. If the radiation fields are represented by the vertical integral of liquid water more so than by the LWC, this, in conjunction with smoothing by multiple scattering, may explain the relatively smooth radiation fields at scales less than typical cloud cell size.

Of the four spectra of upwelling inter–cloud flux of UV radiation examined, three of them showed remarkably similar spectra ($\sim k^{-3.6}$) at scales which appear to be less than typical cloud cell size. This scaling structure is similar to that observed for shortwave satellite radiances.

Clearly, a comprehensive explanation of the spectral structure of satellite imagery does not exist. It is widely recognized that detailed coordinated observations of cloud fields by satellite (radiances), aircraft (radiances, irradiances, and microphysics), microwave radiometers (columnar mass of water), and lidar

(cross–section of LWC) may be required to solve the problem.

As a result of the scaling behaviour of one and two–dimensional fields of LWC and thermal radiances, and the observation that for large transects LWC = 0 when temperature is above a fairly well defined critical value, a stochastic, phenomonological, scaling, broken cloud field model was proposed. The basic model produces two–dimensional fields of vertically integrated optical depth with significant horizontal variability. Cloud fields have constant vertical extent and, hence, variable LWC. These are referred to as variable scaling fields. A second type of field can be produced in which all cells in the variable field with non–zero optical depth have optical depth set to the grid average. These fields are called identical scaling. By extension, a third field can be produced in which the original field is drawn upwards creating a new field with variable geometric thickness of clouds but near constant LWC. These fields are referred to as textured. All three fields possess the same cloud cover fraction and spatial distribution of vertical optical depth. Several examples of the models were shown. The fields are clearly distinguishable from random, regular, and plane–parallel clouds and tend to resemble non–oriented fields of cumuli.

In the second part of the thesis, a Monte Carlo atmospheric photon transport model was presented which is capable of computing solar radiances and fluxes for extremely variable and extensive three–dimensional cloud fields. Also, two underlying reflecting surface models were developed. The first was a trimmed down version of the atmospheric Monte Carlo model and the second was a general statistical bi–directional model. It was shown that the surface used by Welch and Wielicki (1989) and Kobayashi (1989) was not Lambertian. A semi–analytic correction, however, can be applied to their results. Fortunately, in most cases the correction to the system albedo is small. In Chapter 4, the Monte Carlo models

were validated by comparing their flux estimates with accepted published results for standard cloud scenarios.

In the third part of the thesis, model generated scaling cloud fields were used as input for the Monte Carlo transport models. The objective was to compare fluxes for various models of broken cloud fields and to explore some radiative properties of scaling cloud fields. First, however, it was demonstrated that statistically meaningful *fluxes* for extensive cloud fields are attainable with as few as 50,000 photons/simulation and that an individual realization of a cloud field represents its population well. These are important points especially for parameterization purposes.

An intercomparison of reflectances for scaling, random, regular, and plane–parallel arrays of clouds was conducted. Only cloud fields with constant vertical optical and geometric depth were considered. The findings showed that the cloud fields considered transfer solar radiation very differently. The governing factors seem to be enhanced illuminated area of cloud sides and effective aspect ratio of the cloud field. Cloud fields that are strongly scaling (e.g. $k^{-5/3}$) reflect radiation like a plane–parallel cloud. This is because many clouds are fairly extensive in the horizontal and often large tracts of cloud–free space exist between them. Random arrays of cloud and weakly scaling fields differ significantly from plane–parallel. This is because few clouds are extensive (large aspect ratio) and most spacings between clouds are small ($\lesssim$ 2 cloud diameters).

Introduction of horizontal variability into the scaling cloud fields tended to reduce reflectance by between 10 to 15%. This is due to the non–linear transfer of radiation in clouds and also to the fact that the probability of a photon not encountering liquid water is enhanced. This is in accord with results due to Cahalan (1990) and Davis *et al.* (1990). Clearly, the extent to which horizontal variability is introduced is somewhat arbitrary at this stage. Taken to the absurd

extreme, there would be a fractal set of points of infinite LWC which would give rise to zero reflectance because the probability of a photon encountering a denumerable set of points is zero. Furthermore, because the horizontal distribution of vertical optical depth is not attainable from satellite radiances, we must rely, for the time being, on one–dimensional time series of vertically integrated LWC obtained by microwave emission. It is suspected, however, that for the scales considered in this study, the scaling cloud models probably provide a fair estimate of horizontal variability in fairweather cumuli.

Next, the dependence of cloud field reflectance on the scaling exponent of optical depth was studied. Here it was clearly demonstrated that scaling cloud fields span a spectrum from white noise to plane–parallel and that only a minor degree of scaling in optical depth (e.g. $k^{-0.6}$) is required to produce reflectances that differ substantially from those produced by white noise and plane–parallel fields. Since all cloud fields exhibit scaling to some extent, it is likely that neither extreme is a good approximation.

The effects of vertical texture on reflectance was predictable in terms of existing studies which examined the effects of cloud aspect ratio. At high sun, towering clouds have an overall trapping effect on photons while at low sun, the enhanced illumination on the sides of towers leads to enhanced reflectance. In some cases, most notably in tropical fields containing some very tall clouds, inclusion of vertical texture may be important for properly accounting for the feedback between solar heating of the surface and cloud development.

The fact that the break in scaling of satellite radiances occurred at ~4 km in the AVHRR data (afternoon) and at ~1 km in the LANDSAT data (mid–morning) may be due to coalescence of individual cloud cells later in their life cycle. If the only difference between clouds in the morning and afternoon is average cloud size, then based on the results in Fig.5.18 and 5.19, there will be a slight reduction

(enhancement) in reflectance (surface absorptance). Given, however, that other variables such as vertical extent, cloud fraction, and optical depth will change over the same period, diurnal migration downward in wavenumber of the scaling change (increased cloud diameter) is likely to be a minor factor only. In fact, for grid–averaged flux calculations it is probably more important to account for low frequency white noise.

The final set of experiments involved reflecting surfaces beneath broken cloud fields. First, it was demonstrated that for a wide variety of surfaces, the Lambertian approximation will lead to accurate estimates of system fluxes. Next, a method was developed for estimating cloud base reflectance in a Monte Carlo simulation as a function of the number of internal reflections k between surface and cloud. It was shown that for scaling broken cloud fields, cloudbase reflectance depends very much on k due to efficient depletion of radiation out extensive cloud–free regions: photons that undergo multiple reflections are confined to regions beneath extensive clouds; even when base altitude is five times the cloud thickness. While this condition violates that needed to use the geometric sum formulae for flux calculation, it turns out that use of the cloud field's spherical albedo, or its direct–beam albedo evaluated near $\mu_0 = 0.5$, to represent cloudbase albedo in the geometric formulae often, though fortuitously, leads to small errors ($< 2\%$) in overall reflectance. This is fortunate for climate models that employ the geometric formulae already. When a comprehensive parameterization of direct–beam cloud albedo is developed, it should, therefore, be a much simpler task to parameterize cloud field spherical albedo. Last, it was shown that the geometric sum formula for system albedo predicts that in some cases non–absorbing cloud will reduce system albedo below surface albedo. The necessary conditions required for this phenomenon to occur, however, are rare and not important to climate modelling.

There are several recommendations for future research. First, a concerted effort should be made to develop a flux parameterization for broken clouds for GCMs. Several avenues were followed during the course of this thesis but none were sufficiently satisfactory to report. Due to the clear theoretical and observational indications that clouds are intimately related to the turbulent state of the atmosphere, sub–grid distribution of cloud should be accounted for by some kind of scaling law. It may be possible to parameterize radiative flux from scaling cloud fields as a function of scaling exponent (e.g. Fig.5.13 to 5.15). Also, radiative transfer in extremely inhomogeneous three–dimensional clouds should be studied carefully. Such experiments were beyond the scope of this thesis. Finally, effects on fluxes for broken inhomogeneous cloud fields due to absorption by cloud droplets and water vapour should be investigated, for ultimately broadband fluxes are desired. To date, only conservative scattering has been examined.

REFERENCES

Aida, M., 1977: Reflection of solar radiation from an array of cumuli. *J. Meteor. Soc. Japan*, 55, 174–181.

Barker, H.W. and J.A. Davies, 1989a: Surface albedo estimates from Nimbus–7 ERB data and a two–stream approximation of the radiative transfer equation. *J. Appl. Climate*, 2, 409–418.

——— and ———, 1989b: Multiple reflections across a linear discontinuity in surface albedo. *Int. J. Climat.*, 9, 203–214.

Berge, P., Y. Pomeau and C. Vidal, 1984: Order within chaos: Towards a deterministic approach to turbulence. Wiley and Sons, 329pp.

Blanchet, J.–P. and J.–J. Morcrette, 1985: Radiative processes in the AES/CCC multi–level spectral general circulation model. *AES/CCC report* No.85–6, CCRN16, 83p.

Bradley, S.G., 1981: The relation between cumulus albedo and extinction coefficient and its application to remote sensing. *J. Atmos. Sci.*, 38, 2243–2256.

Busygin, V.P., N.A. Yevstratov, and E.M. Feigelson, 1973: Optical properties of cumulus and radiant fluxes for cumulus cloud cover. *Izv. Atmos. Ocean Phys.*, 9, 1142–1151.

Cahalan, R.F. and J.M. Joseph, 1989: Fractal statistics of cloud fields. *Mon. Wea. Rev.*, 117, 261–272.

——— and J.B. Snider, 1989: Marine stratocumulus structure. *Remote Sens. Environ.*, 28, 95–107.

———, 1989: Overview of fractal clouds. In Advances in Remote Sensing. Deepak Publ., p371 – 389, 515pp.

Cess, R.D., G.L. Potter *et al.*, 1989: Intercomparison of cloud–climate feedback as produced by 14 atmospheric general circulation models. *Science*, 245, 513–516.

——— and I.L. Vulis, 1989: Intercomparison and interpretation of satellite–derived directional albedos over deserts. *J. Appl. Clim.*, 2, 393–407.

Chandrasekhar, S., 1960: Radiative Transfer. Dover, N.Y., 393p.

Charney, J.G., 1971: Geostrophic turbulence. *J. Atmos. Sci.*, 28, 1087–1095.

Claussen, M., 1982: On the radiative interaction in three–dimensional cloud fields. *Contrib. Atmos. Phys.*, 55, 158–169.

Coakley, J.A. and P. Chylek, 1975: The two–stream approximation in radiative transfer:Including the angle of the incident radiation. *J. Atmos. Sci.*, 32, 409–418.

——— and F.P. Bretherton, 1982: Cloud cover from high–resolution scanner data: Detecting and allowing for partially filled fields of view. *J. Geophys. Res.*, 87, 4917–4932.

———, 1983: Properties of multilayered cloud systems from satellite imagery. *J. Geophys. Res.*, 88, 10,818–10,828.

Cretel. D., M. Herman, and D. Tanre, 1988: Fluxes and directional effects of broken clouds. IRS '88: Current Problems in Atmospheric Radiation, Eds. J. Lenoble and J.–F. Geleyn, Deepak Publ., Hampton VA., 652p.

Davies, R., 1978: The effect of finite geometry on the three–dimensional transfer of solar irradiance in clouds. *J. Atmos. Sci.*, 35, 1712–1725.

Davis, A, P. Gabriel, S. Lovejoy, D. Schertzer and G.L. Austin, 1990: Discrete angle radiative transfer – Part III: Numerical results and applications. T appear in *J. Geo. Res.*

Deirmendjian, D, 1969: Electromagnetic scattering on spherical polydispersions. Elsevier, 290p.

Diner, D.J. and J.V. Martonchik, 1984: Atmospheric transfer of radiation above an inhomogeneous non–Lambertian reflective ground– I. Theory. *J. Quant. Spectrosc. Radiat. Trans.*, 32, 97–125.

Fouquart, Y. and B. Bonnel, 1980: Computation of solar heating of the Earth's atmosphere. *Contrib. Atmos. Phys.*, 53, 35–62.

———, J.C. Buriez, M. Herman, and R.S. Kandel, 1990: The influence of clouds on radiation. *Rev. Geophys.*, 28, 145–166.

Frisch, U., P.L. Sulum, and M. Nelkin, 1978: A simple dynamical model of intermittency in fully developed turbulence. *J. Fluid. Mech.*, 87, 719–736.

——— and G. Parisi, 1985: A multifractal model of intermittancy. In Turbulence and predictability in geophysical fliud dynamics and climate dynamics, eds. M. Ghil, R. Benzi and G. Parisi. Elsevier North–Holland, 84–88

Gabriel, P., S. Lovejoy, D. Schertzer, and G.L. Austin, 1988: Multifractal analysis of resolution dependence in satellite imagery. *Geophys. Res. Let.*, 15, 1373–1376

———, ———, A. Davis, G.L. Austin, and D. Schertzer, 1990: Discrete angle radiative transfer– PartII: Renormalization approach for homogeneous and fractal clouds. *J. Geophys. Res.*, to appear.

Gage, K.S. and G.D. Nastrom, 1986: Theoretical interpretation of atmospheric wavenumber spectra of wind and temperature observed by commercial aircraft during GASP. *J. Atmos. Sci.*, 43, 729–740.

Garand, L., 1986: Automated recognition of oceanic cloud patterns and its application to remote sensing of meteorological parameters. Ph.D. thesis, Univ. of Wisconsin (Madison), 231p.

Gerstl, S.A.W. and C. Simmer, 1986: Radiation physics and modeling of off–nadir satellite–sensing of non–Lambertian surfaces. *Remote Sens. Environ.*, 20, 1–29.

Grant, I.P. and G.E. Hunt, 1969: Discrete space theory of radiative transfer I.Fundamentals. *Proc. Roy. Soc. London*, a313, 183–197.

Hapke, B.W., 1981: Bidirectional reflectance spectroscopy I. Theory. *J. Geophys. Res.*, 86, 3039–3054.

Harshvardhan and R.W.L. Thomas, 1984: Solar reflection fron interacting and shadowing cloud elements. *J. Geophy. Res.*, 89, 7179–7185.

Henyey, L.C. and J.L. Greenstein, 1941: Diffuse radiation in the galaxy. *Astrophys. J.*, 93, 70–83.

Johnson, T.H., 1976: Failure testing: A proposal for increasing confidence in the results of numerical simulations. *J. Comp. Phys.*, 21, 245–250.

Joseph, J.H., W.J. Wiscombe, and J.A. Weinman, 1976: The delta–Eddington approximation for radiative transfer. *J. Atmos. Sci.*, 33, 2452–2459.

King, W.D., C.T. Maher, and G.A. Hepburn, 1981: Further performance tests on the CSIRO liquid water probe. *J. Clim. Appl. Met.*, 20, 195–202.

King, M.D. and Harshvardhan, 1986: Comparitive accuracy of selected multiple scattering approximations. *J. Atmos. Sci.*, 43, 784–801.

Kite, A., 1987: The albedo of broken cloud fields. *Q. J. R. Meteorol. Soc.*, 113, 517–531.

Kobayashi, T., 1988: Parameterization of reflectivity for broken cloud. *J. Atmos. Scl.*, 45, 3034–3045.

———, 1989: Radiative properties of finite cloud fields over a reflecting surface. *J. Atmos. Sci.*, 46, 2208–2214.

Kolmogorov, A.N., 1941: The local structure of turbulence in compressible turbulence for very large Reynold's numbers. *C. R. Akad. Nauk. SSR*, 30, 301–305.

Kraichnan, R.H., 1967: Inertial ranges in two–dimensional turbulence. *Phys. Fliuds*, 10, 1417–1423.

———, 1971: Inertial–range tansfer in two– and three–dimensional turbulence. *J. Fliud Mech.*, 47, 525–535.

Kratz, D.P. and R.D. Cess, 1986: Solar absorption by atmospheric water vapor: A comparison of radiation models. *Tellus*, 37B, 53–63.

Lacis, A.A, and J.E. Hansen, 1974: A parameterization of the absorption of solar radiation in the Earth's atmosphere. *J. Atmos. Sci.*, **31**, 118–133.

Lenoble, J. (ed.), 1977: Standard procedures to compute radiative transfer in a scattering atmosphere. IAMAP Radiation Commission, Boulder, CO, 125p.

Lorenz, E.N., 1969: Three approaches to atmospheric predictability. *Bull Am. Met. Soc.*, 50, 345–349.

Lovejoy, S., 1982: Area–perimeter relation for rain and cloud areas. *Science*, 216, 185–187.

———, A. Davis, P. Gabriel, G.L. Austin, and D. Schertzer, 1990: Discrete angle radiative transfer – Part I: Scaling and similarity, universality and diffusion. Accepted for publication in *J. Geophys. Res.*

———, and D. Schertzer, 1990: Multifractals, universality classes and satellite and radar measurements of cloud and rain fields. Accepted for publication in *J. Geophys. Res.*

Mandelbrot, B., 1974: Intermittant turnulence in self–similar cascades: Divergence of high moments and dimension of the carrier. *J. Fluid Mech.*, 62, 331–350.

McKee, T.B. and S.K. Cox, 1974: Scattering of visible radiation by finite clouds. *J. Atmos. Sci.*, 31, 1885–1892.

Meador, W.E. and W.R. Weaver, 1980: Two–stream approximations to radiative transfer in planetary atmospheres: A unified description of existing methods and a new improvement. *J Atmos. Sci.*, 37, 630–643.

Mie, G., 1908: *Ann. der Physik*, 25, 377–445.

Mitchell, J.F.B., 1989: The 'greenhouse' effect and climate change. *Rev. Geophys.*, 27, 115–139.

———, C.A. Senoir, and W.J. Ingram, 1990: CO_2 and climate: amissing feedback? *Nature*, 341, 132–134.

Nastrom, G.D. and K.S. Gage, 1985: A climatology of atmospheric wavenumber spectra observed by commercial aircraft. *J. Atmos. Sci.*, 42, 950–960.

Oke, T.R., 1978: Boundary layer climates. Methuen, 372p.

Parker, L., R.M. Welch, 1986: Analysis of spatial inhomogeneities in cumulus clouds using high spatial resolution Landsat data. *J. Clim. Appl. Met.*, 25, 1301–1314.

Pinty, B., M.M Verstraete and R.E. Dickinson, 1989: A physical model for predicting bidirectional reflectances over bare soil. *Remote Sens. Environ.*, 27, 273–288.

Plank, V.G., 1969: The size distribution of cumulus clouds in representative Florida populations. *J. Appl. Met.*, 8, 46–67.

Preisendorfer, R.W. and G.L. Stephens, 1984: Multimode radiative transfer in finite optical media. I: Fundamentals. *J. Atmos. Sci.*, 41, 709–724.

Press, W.H., B.P Flannery, S.A. Teukolsky, and W.T. Vetterling, 1986: Numerical Recipes. Cambridge Press, 702p.

Pruppacher, H. and J. Klett, 1978: Microphysics of cloud and precipitation. D. Reidel, 714pp.

Ramanathan, V., 1987: The role of Earth radiation budget studies in climate and general circulation research. *J. Geophys. Res.*, **92**, 4075–4095.

———, 1988: The greenhouse theory of climate change: A test by an inadvertant global experiment. *Science*, 240, 293–299.

Randall, D.A. and G.J. Huffman, 1980: A stochastic model of cumulus clumping. *J. Atmos. Sci.*, 37, 2068–2078.

Rawlins, F., 1990: A note on 'The albedo of broken cloud fields' by A.J. Kite (1987). *Q. J. R. Meteorol. Soc.*, 116, 243–244.

Richardson. L.F., 1926: Atmospheric diffusion shown on a distance neighbor graph. *Proc. R. Soc. London.* A110, 709–722.

Roeckner, E., 1988: Cloud–radiation feedbacks in a climate model. *Atmos. Res.*, 21, 293–303.

Rogers, R.R., 1976: A short course in cloud physics. Pergamon Press, 227p.

Rosenfeld, A. and A.K. Kak, 1982: Digital picture processing. 2nd Ed., vol. 1, Academic Press, 435p.

Ruelle, D., 1989: Chaotic evolution and strange attractors. Cambridge Press. 96p.

Sasamori, T., 1975: A statistical model for stationary atmospheric cloudiness, liquid water content, and rate of precipitation. *Mon. Wea. Rev.*, 103, 1037–1049.

Schertzer, D. and S. Lovejoy, 1985: On the dimension of atmospheric motions. In Turbulence and chaotic phenomena in fluids, ed. T. Tatsumi. Elsevier, 505–511.

——— and ———, 1987: Physical modelling and analysis of rain and clouds by anisotropic scaling multiplicative processes. *J. Geo. Res.*, 92, 9693–9714.

Schmetz, J., 1984: On the parameterization of radiative properties of broken cloud. *Tellus*, 36A, 417–432.

Schnieder, S.H. and R.E. Dickinson, 1976: Parameterization of fractional cloud amounts in climate models: The importance of modelling multiple reflections. *J. Appl. Met.*, 15, 1050–1056.

Slingo. A., R.C. Wilderspin and R.N.B. Smith, 1989: Effect of improved physical parameterization of cloudiness and the Earth's radiation budget. *J. Geo. Res.*, 94, 2281–2301.

Smith, R.N.B., 1990: A scheme for predicting layer clouds and their water content in a general circulation model. *Q. J. R. Meteorol. Soc.*, 116, 435–460.

Smith, G.L., 1988: Radiative transfer solutions in cylinders. IRS' 88: Current problems in atmospheric radiation. Ed. J. Lenoble abd J.F. Geleyn. Deepak Publ., 88–90.

Somerville, R.C.J. and L.A. Remer, 1984: Cloud optical thickness feedbacks in the CO_2 climate problem. J. Geo. Res., 89, 9668–9672.

———, 1987: The predictability of weather and climate. *Climatic Change*, 11, 239–246.

Spanier, J. and E.M. Gelbard, 1969: Monte Carlo principles and neutron transport. Addison–Wesley, 234p.

Stephens, G.L., 1985: Reply. *Mon. Wea. Rev.* 113, 1834–1835.

———, 1988a: Radiative transfer through arbitrary shaped optical media. PartI: A general method of solution. *J. Atmos. Sci.*, 45, 1818–1836.

———, 1988b: Radiative transfer through arbitrary shaped optical media. PartII: Group theory and simple closure. *J. Atmos. Sci.*, 45, 1837–1848.

Sundqvist, H., 1978: A parameterization scheme for non–convective condensation including prediction of cloud water content. *Q. J. R. Met. Soc.*, 104, 677–690.

Van Blerkhom, D.J., 1971: Diffuse reflection from clouds with horizontal inhomogeneities. *Astro. J.*, 166, 235–242.

Van de Hulst, H.C., 1957: Light scattering by small particles. Wiley and Sons, 470p.

Warner, J., 1969: The microstructure of cumulus cloud. Part II: The effect on droplet size distribution of the cloud nucleusspectrum and updraft velocity. *J. Atmos. Sci.*, 26, 1272–1282.

———, 1970: The microstructure of cumulus cloud. Part III: The nature of the updraft. J. Atmos. Sci., 27, 682–688.

Weinman, J.A. and Harshvardhan, 1982: Solar reflection from a regular array of horizontally finite clouds. *Appl. Optics*, 21, 2940–2944.

Wendling, P., 1976: Albedo and reflected radiance of horizontally inhomogeneous clouds. *J. Atmos. Sci.*, 34, 642–650.

Welch, R.M., S.K. Cox, and J.M. Davis, 1980: Solar radiation and clouds. Met. Monograph, AMS, 92p.

——— and W.G. Zdunkowski, 1981: The radiative characteristics of non–interacting cumulus cloud fields. Part II: Calculations for cloud fields. *Cont. Atmos. Phys.*, 54, 273–285.

———, and B.A. Wielicki, 1984: Stratocumulus cloud field reflected fluxes: The effect of cloud shape. *J. Atmos. Sci.*, 41, 3085–3103.

——— and ———, 1985: A radiative parameterization of stratocumulus cloud fields. *J. Atmos. Sci.*, 42, 2888–2897.

———, K.S. Kuo, B.A. Wielicki, S.K. Sengupta, and L. Parker, 1988: Marine stratocumulus cloud fields off the coast of Southern California observed using LANDSAT imagery: Part I: Structural characteristics. *J. Appl. Met.*, 27, 341–362.

——— and ———, 1989: Reflected fluxes for broken clouds over a Lambertian surface. *J. Atmos. Sci.*, 46, 1384–1395.

Wielicki, B.A. and R.M. Welch, 1986: Cumulus cloud properties using LANDSAT satellite data. *J. Clim. Appl. Met.*, 25, 261–276.

Wiscombe, W.J., 1977: The delta–Eddington approximation for a vertically inhomogeneous atmosphere. NCAR Tech. Note, TN–121+STR, 66p.

———, 1980: Improved Mie scattering algorithms. *Appl. Optics*, 19, 1505–1509.

———, R.M. Welch and W.D. Hall, 1984: The effect of very large drops on cloud absorption: Part I: Parcel models. *J. Atmos. Sci.*, 41, 1336–1335.

Zdunkowski, W.G., R.M. Welch and G. Korb, 1980: An investigation of the structure of typical two–stream methods for the calculation of solar fluxes and heating rates in clouds. *Cont. Atmos. Phys.*, 53, 147–166.

APPENDIX A

Cloud Inhomogeneity and Reduced Cloud Reflectance

This appendix presents a simple proof showing that the introduction of inhomogeneity into a plane–parallel cloud leads to reduced reflectance.

Let the extinction coefficient β be distributed in a horizontally infinite cloud in such a manner that the optical depth τ along trajectories of the incident beam has a density function $p(\tau)$ where

$$\tau = \int_0^{h_c} \beta(z)\frac{dz}{\mu_o} \ , \tag{A.1}$$

h_c is cloud geometric thickness, and $\mu_o = \cos\theta_o$ where θ_o is solar zenith angle. The direct beam transmittance averaged over the entire cloud is, therefore,

$$\langle t \rangle = \int_0^{\infty} e^{-\tau} p(\tau) d\tau \ . \tag{A.2}$$

For homogeneous (plane–parallel) media, $p(\tau) = \delta(\tau - \tau_o)$ where $\tau_o\mu_o$ is the vertically integrated cloud optical depth. Thus, for plane–parallel clouds, Eq.(A.2) becomes

$$\langle t \rangle = \int_0^\infty e^{-\tau} \delta(\tau - \tau_0) d\tau = \exp[-\tau_0] \ , \tag{A.3}$$

which is simply Beer's law.

Now, introduce inhomogeneity into the cloud and represent it as

$$p(\tau) = \begin{cases} \frac{1}{2\epsilon} \ ; \ \tau \epsilon [\tau_0 - \epsilon, \ \tau_0 + \epsilon] \\ 0 \ ; \ \text{elsewhere} \end{cases} . \tag{A.4}$$

This is the 'top–hat' approximation of the Dirac function. In the limit as $\epsilon \to 0$, Eq.(A.4) approaches $\delta(\tau - \tau_0)$; homogeneity. Note that the average optical depth of the cloud is the same as in the plane–parallel case. Substituting Eq.(A.4) into Eq.(A.2) gives

$$\langle t \rangle = \exp[-\tau_0] \frac{\sinh(\epsilon)}{\epsilon} \ . \tag{A.5}$$

For all possible ϵ, $\sinh(\epsilon)/\epsilon > 1$ and $\lim_{\epsilon \to 0} \sinh(\epsilon)/\epsilon = 1$. Hence, this shows that the slightest inhomogeneity leads to enhanced direct beam transmittance relative to that associated with plane–parallel conditions.

If the cloud is scattering conservatively, enhanced direct beam transmittance implies less scattered (diffuse) radiation. Since a diffuse radiation field is just infinitely many direct beams, then by the same argument, the proportion of scattered radiation transmitted through a plane–parallel cloud of optical depth τ_0 will be less than the proportion of scattered radiation transmitted through all heterogeneous clouds of average optical depth τ_0. Since less diffuse radiation is produced by inhomogeneous clouds, and a greater proportion of that is transmitted, inhomogeneity reduces reflected flux. This is in accord with Cahalan's

(1989) and Davis *et al.*'s (1990) study's Monte Carlo simulations of photon transport in heterogeneous clouds.

APPENDIX B

Systematic Bias in Retrieved Cloud Amount: The Role of the Black Cloud Assumption

The purpose of this appendix is to show that the spatial coherence method underestimates systematically cloud amount. Assume all quantities apply to a narrow waveband. Let I_c be the Planck radiance received by a sensor at the top of the atmosphere looking at an isothermal sea–surface at the nadir. Let I_o be the Planck radiance received by the same sensor but associated with the temperature of an isothermal cloud. If ϵ and τ are cloud emissivity and vertically integrated optical depth respectively, then the radiance measured by the sensor is approximately

$$I(\tau) = I_c e^{-\epsilon\tau} + I_o(1 - e^{-\epsilon\tau}) \ . \qquad \text{(B.1)}$$

If $p(\tau)$ is the normalized density function of cloud optical depth over an area A, the measured radiance for A is

$$\begin{aligned} I &= \int_0^\infty p(\tau) I(\tau) d\tau \\ &= I_o + (I_c - I_o) \int_0^\infty p(\tau) e^{-\epsilon\tau} d\tau \ , \end{aligned} \tag{B.2a}$$

where

$$\int_0^\infty p(\tau) d\tau = 1 \ , \tag{B.2b}$$

has been used.

Assume that a fraction $(1 - A_c)$ of A has $\tau = 0$ (no cloud). Therefore,

$$p(\tau) = (1 - A_c)\delta(\tau) + \hat{p}(\tau) \ , \tag{B.3a}$$

where $\hat{p}(0) = 0$ and by Eq.(B.2b)

$$\int_0^\infty \hat{p}(\tau) d\tau = A_c \ . \tag{B.3b}$$

Thus, A_c is the true cloud fraction. Hence, Eq.(B.2a) becomes

$$\begin{aligned} I &= (1 - A_c) I_c + A_c I_o + (I_c - I_o) \int_0^\infty \hat{p}(\tau) e^{-\epsilon\tau} dt \\ &= (1 - A_c) I_c + A_c I_o + (I_c - I_o) \mathscr{L}[\hat{p}(\tau); \epsilon] \ , \end{aligned} \tag{B.4}$$

where $\mathscr{L}[\cdots]$ is the Laplace transform of the optical depth density function.

If it is assumed that

$$I = (1 - \hat{A}_c) I_c + \hat{A}_c I_o \ , \tag{B.5}$$

where $\hat{A}_c$ is cloud amount retrieved by the spatial coherence method, it is implicitly assumed that $\mathcal{L}[\hat{p}(\tau);\epsilon] \simeq 0$ and that $\hat{p}(\tau)$ is of a form like

$$\hat{p}(\tau) = \begin{cases} 0 & ; \tau < \tau^* \\ f(\tau) & ; \tau \geq \tau^* \end{cases} , \tag{B.6}$$

where $e^{-\epsilon\tau^*} << 1$. Thus, the assumption in Eq.(B.6) is stating that there is no thin cloud, only extremely thick cloud. This is rarely true.

Equating Eq.(B.4) and Eq.(B.5), because regardless of any assumptions the measured radiance I is unchanged, and rearranging gives

$$A_c = \hat{A}_c + \mathcal{L}[\hat{p}(\tau);\epsilon] \ . \tag{B.7}$$

Since $\hat{p}(\tau) \geq 0$, so to is its Laplace transform, and so

$$A_c \geq \hat{A}_c \ . \tag{B.8}$$

Hence, assuming Eq.(B.6) leads to a systematic underestimation in cloud amount.

APPENDIX C

Additional AVHRR Images

In this Appendix, five of the eight AVHRR images examined in this study are presented. Table C.1 summarizes the imagery. The images are shown in Fig.C1a – C1e along with their spatial coherence scatter–plots created using AVHRR IR radiances in 4x4 pixel arrays. Note that the scatter–plot for image E appears to indicate the presence of two cloud layers (two cold arches). When the scatter–plot generates on the screen, however, the cooler arch forms right at the end of the plot. Therefore, it is due to the single layer of clouds in the upper $1/8^{th}$ of the image.

Figure C2 shows $\langle S_k \rangle$ for the VIS and IR fields of each image. Each $\langle S_k \rangle$ curve was created using ten scan lines. Note the remarkable similarity between these spectra and those in Fig.2.10.

Table C.1

NOAA–9 (AVHRR) satellite information

	Scene D	Scene E	Scene F
Date	5/3/86	5/3/86	8/3/86
Time (GMT)	1939	1940	1908
Orbit Number	6325	6325	6367
Latitude (N)	30.0°	31.2°	35.5°
Longitude (W)	73.5°	72.8°	71.3°
Solar Zenith Angle	52.7°	53.3°	51.5°
Viewing Zen. Angle	45.3°	45.2°	14.7
Relative Azimuth	30.9°	31.9°	36.3°

Table C.1 (cont'n.)

NOAA–9 (AVHRR) satellite information

	Scene G	Scene H
Date	13/3/86	13/3/86
Time (GMT)	1639	1639
Orbit Number	6436	6436
Latitude (N)	58.5°	56.6°
Longitude (W)	54.5°	48.8°
Solar Zenith Angle	63.0°	62.0°
Viewing Zen. Angle	36.2°	23.2°
Relative Azimuth	130.3	131.9

Fig.C1. (a) Relative brightness image of scene D using AVHRR VIS imagery. Minimum and maximum reflectances are 0.036 and 0.61. Beneath the image is its spatial coherence scatter–plot using AVHRR IR imagery (4x4 pixel arrays).

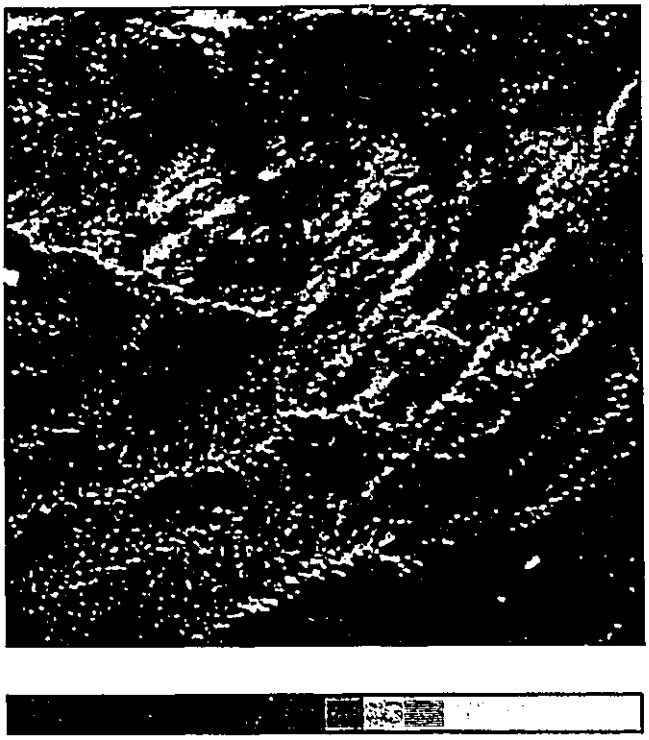

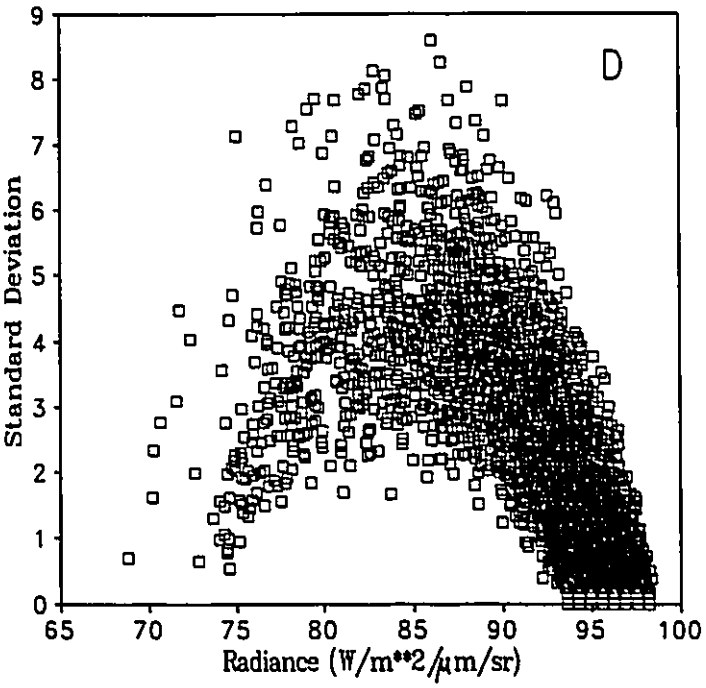
D
Standard Deviation
0
1
2
3
4
5
6
7
8
9
65
70
75
80
85
90
95
100
Radiance (W/m**2/μm/sr)

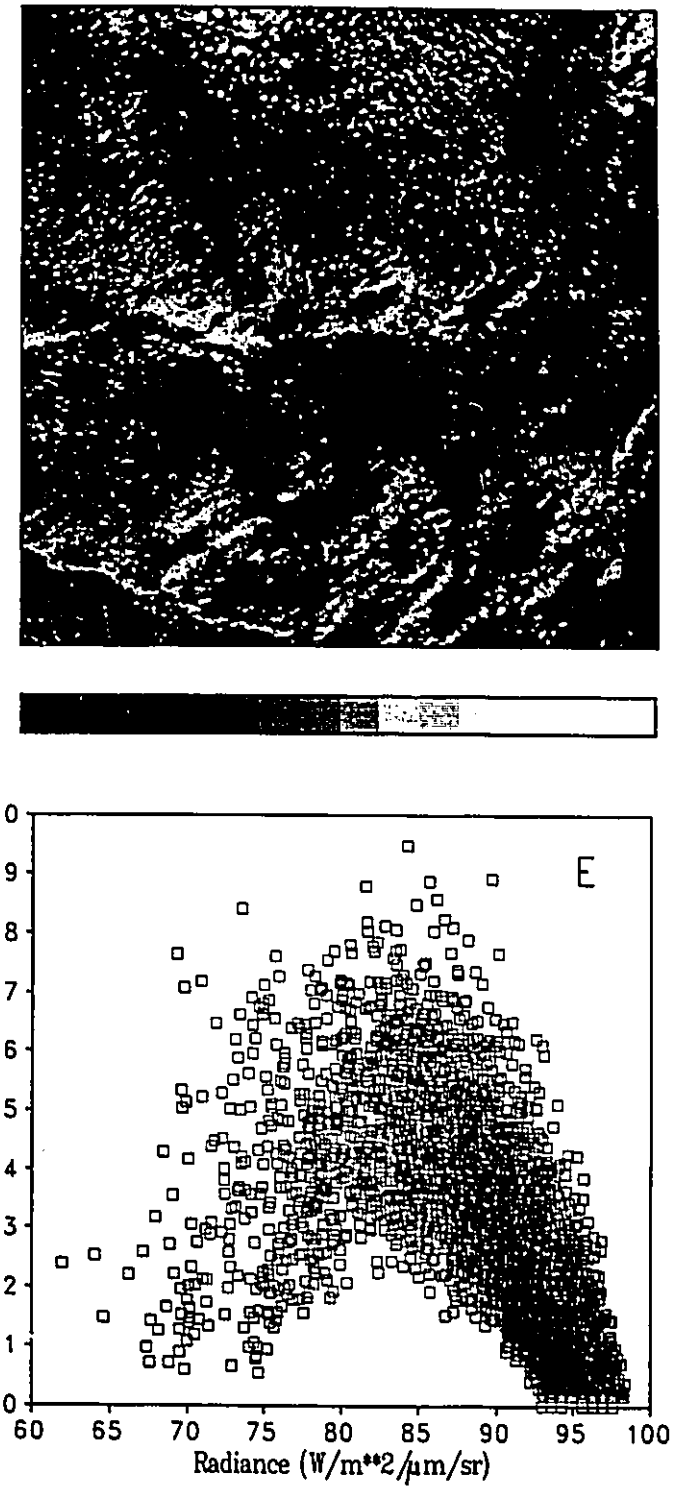

Fig.C1. (b) As in (a) except for scene E where minimum and maximum reflectances are 0.036 and 0.657.

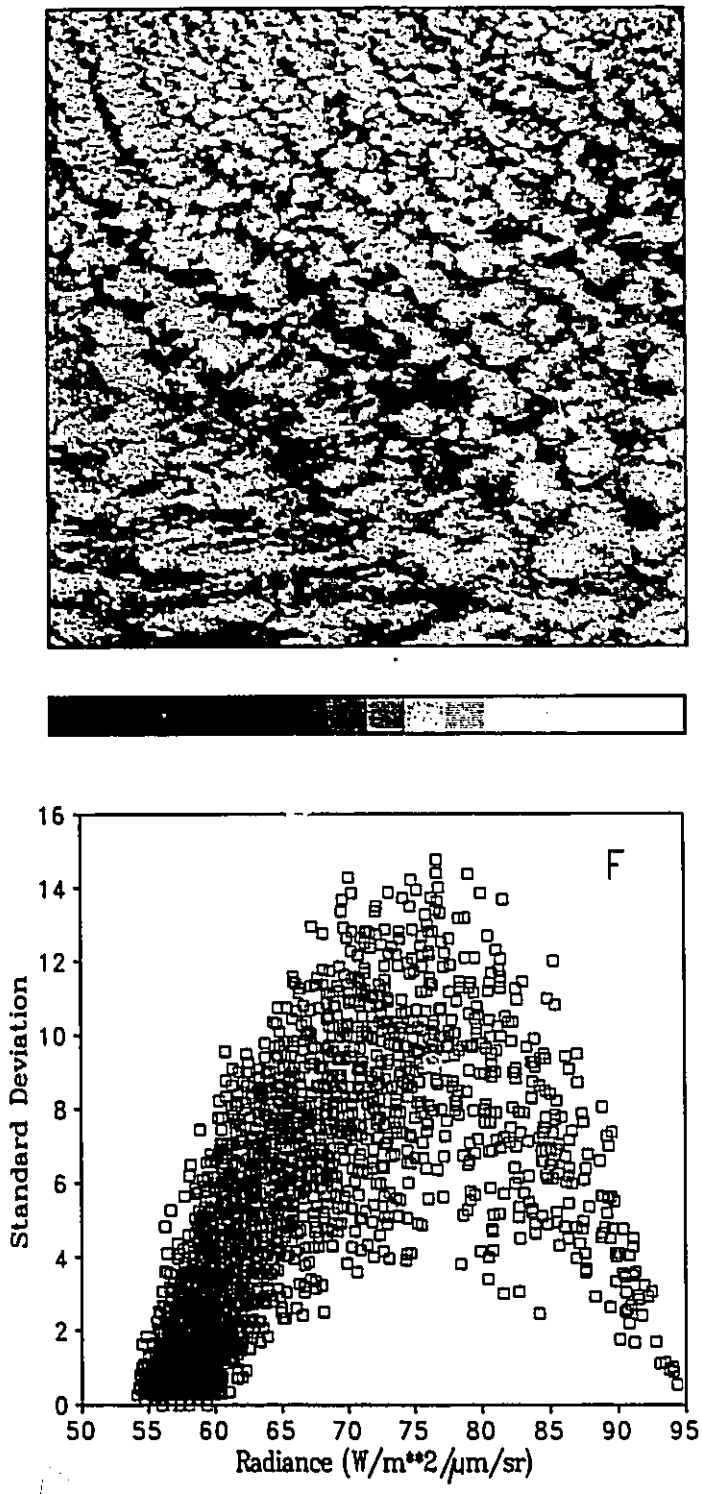

Fig.C1. (c) As in (a) except for scene F where minimum and maximum reflectances are 0.036 and 0.668.

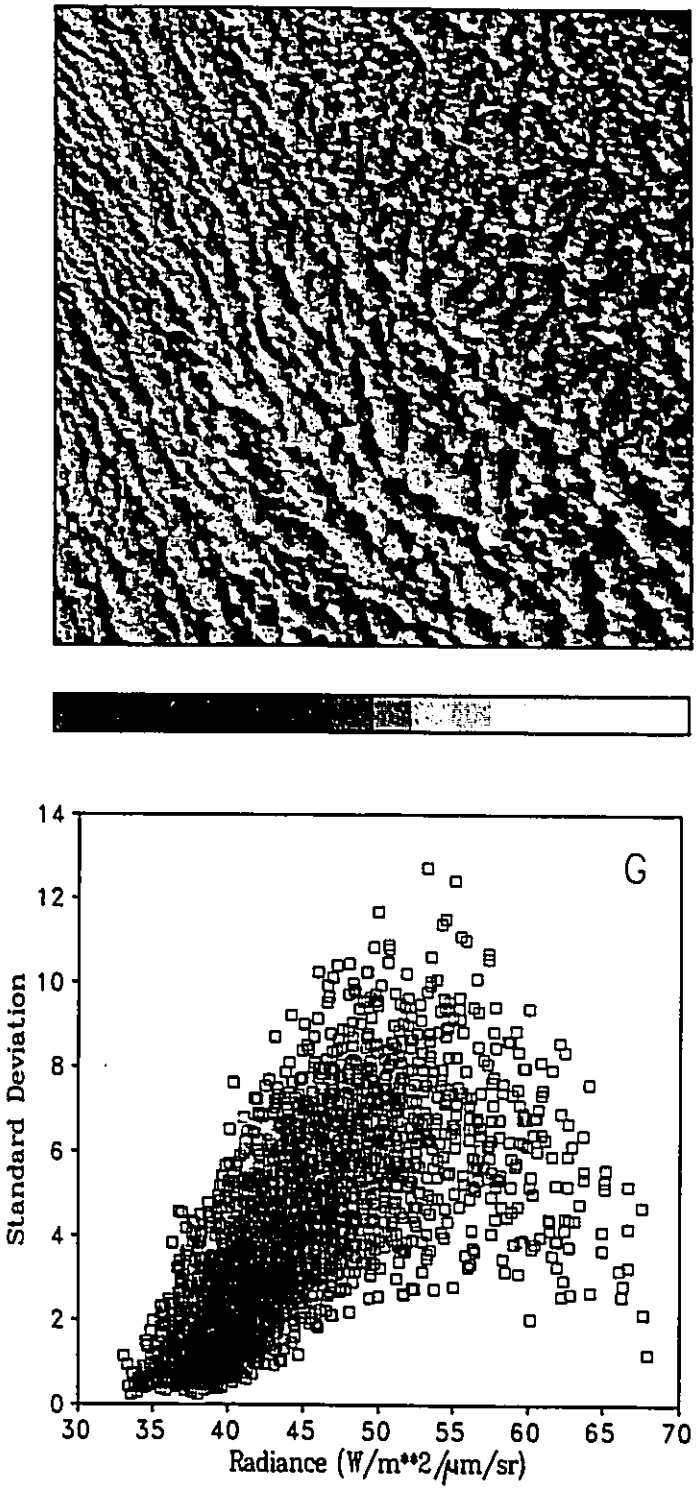

Fig.C1. (d) As in (a) except for scene G where minimum and maximum reflectances are 0.034 and 0.473.

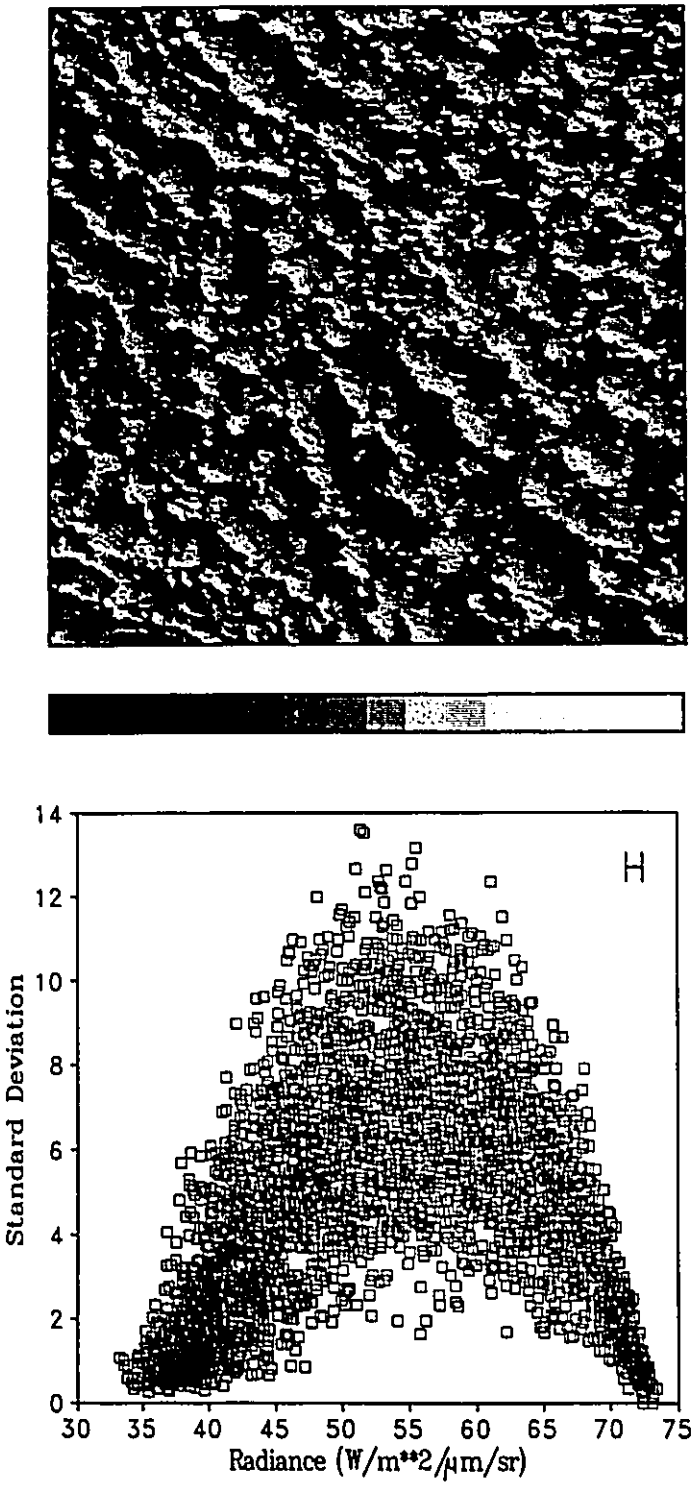

Fig.C1. (e) As in (a) except for scene H where minimum and maximum reflectances are 0.022 and 0.551.

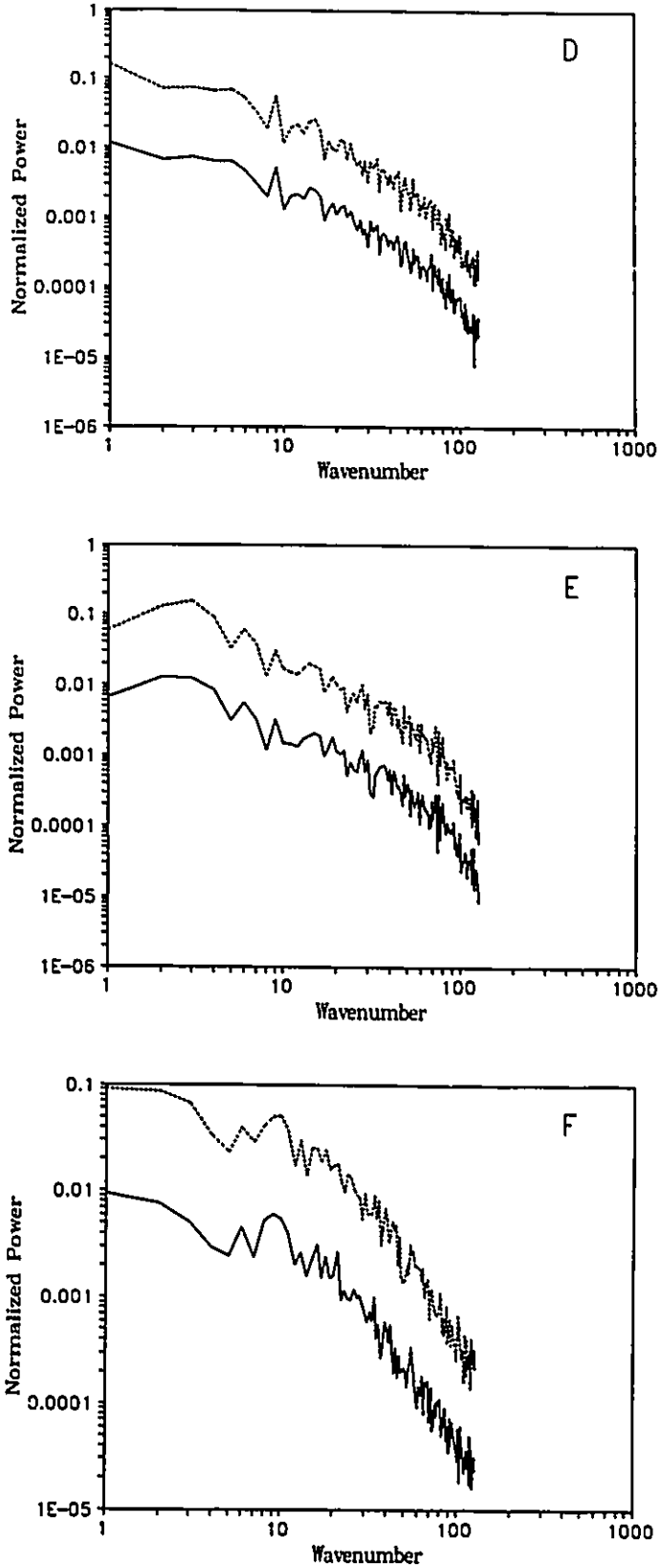

Fig.C2. Normalized ensemble–average one–dimensional wavenumber spectra for scenes D–H. Solid and dashed lines are for VIS and IR imagery respectively. The IR spectra are shifted up by one decade.

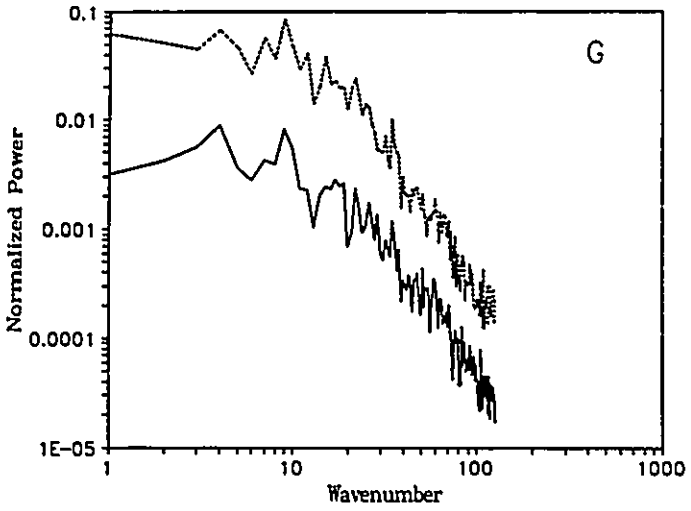
G
Normalized Power
0.1
0.01
0.001
0.0001
1E-05
1
10
100
1000
Wavenumber

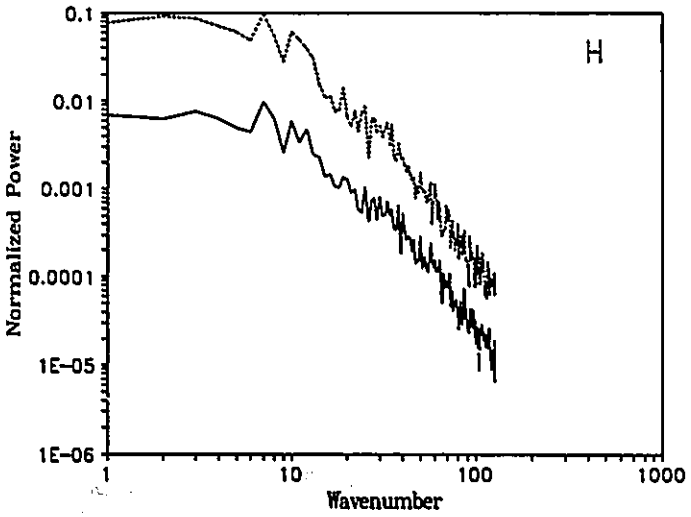
H
Normalized Power
0.1
0.01
0.001
0.0001
1E-05
1E-06
1
10
100
1000
Wavenumber

APPENDIX D

Graphical Technique for Estimation of Parameters in the Codimension Function of a Multiplicative Cascade

This appendix presents a graphical technique for estimating the parameters in the codimension function associated with a multiplicative cascade model. Schertzer and Lovejoy (1986) showed that the codimension function of the bare quantities of a multiplicative cascade is given by

$$c(\gamma) = c_0\left[\frac{\gamma}{\gamma_0} + 1\right]^{\alpha'} , \tag{D.1}$$

where c_0, γ_0, and α' are constants that must be determined empirically. Since c_0 is just $c(0)$, it can be estimated easily from the graph of points $(\gamma, c(\gamma))$ obtained by evaluation of Eq.(2.35).

Differentiating Eq.(D.1) with respect to γ results in

$$c'(\gamma) = \frac{\alpha' c(\gamma)}{\gamma + \gamma_0} . \tag{D.2}$$

From this equation, $c'(\gamma) = 1$ at

$$\hat{\gamma} = \alpha' c(\hat{\gamma}) - \gamma_o \ , \tag{D.3a}$$

and

$$c'(0) = \frac{\alpha' c_o}{\gamma_o} \ . \tag{D.3b}$$

Plotting the approximate derivative (finite difference) of the points $(\gamma, c(\gamma))$, again obtained by evaluation of Eq.(2.35), makes for simple estimation of $\hat{\gamma}$ and $c'(0)$.

Using Eq.(D.3),

$$c(\hat{\gamma}) = c_o \left[\frac{c'(0)c(\hat{\gamma})}{c_o}\right]^{\alpha'} \ , \tag{D.4}$$

which upon solving for α' gives

$$\alpha' = \frac{\ln\left[\frac{c(\hat{\gamma})}{c_o}\right]}{\ln\left[\frac{c'(0)c(\hat{\gamma})}{c_o}\right]} \ . \tag{D.5}$$

γ_o can be obtained from Eq.(D.3a) by

$$\gamma_o = \alpha' c(\hat{\gamma}) - \hat{\gamma} \ . \tag{D.6}$$

Since all of the variables in Eq.(D.5) and Eq.(D.6) have been estimated graphically, first order estimates of all the parameters in $c(\gamma)$ now exist. At this point, one may be satisfied with the estimates of c_o, γ_o, and α' or use them as initial guesses in a non–linear regression attempt to find more accurate estimates.